Aerodynamic and structural modeling for vortex-excited vibrations in bundled conductors

Himanshu Verma

Aerodynamic and structural modeling for vortex-excited vibrations in bundled conductors

Dem Fachbereich Maschinenbau

an der Technischen Universität Darmstadt

zur

Erlangung des Grades eines Doktor-Ingenieurs (Dr.-Ing.)

eingereichte

D i s s e r t a t i o n

vorgelegt von

Himanshu Verma, M.Tech.

aus Ambah (M.P.), Indien

Berichterstatter:	Prof. Dr. Peter Hagedorn
Mitberichterstatter:	Prof. Dr. rer. nat. Michael Schäfer
Tag der Einreichung:	29. Februar 2008
Tag der mündlichen Prüfung:	18. Juni 2008

Darmstadt, 2008

D 17

This book is approved as a doctoral dissertation by:
Prof. Dr. Peter Hagedorn, Professor, Technische Universität Darmstadt.

Ph.D. oral examination was held on June 18th 2008.

Members of the examination committee were:

Prof. Dr. Peter Hagedorn,	*Referent*
Prof. Dr. rer. nat. Michael Schäfer,	*Korreferent*
Prof. Dr.-Ing. Rainer Nordmann,	*Vorsitzer*
Prof. Dr.-Ing. Wilfried Becker,	*1. Beisitzer*
Prof. Dr.-Ing. Samuel Schnabel,	*2. Beisitzer*

Verma, Himanshu
Aerodynamic and structural modeling for vortex-excited vibrations in bundled conductors
Dynamics and Vibrations Group, Technische Universität Darmstadt
Darmstadt, Germany

Zugl.: Darmstadt, Techn. Univ., Diss., 2008

Keywords: Vortex-excited vibrations, Transmission line, Bundled conductors, Stockbridge damper, Spacer damper, Energy balance principle, Computational Fluid Dynamics

ISBN 978-90-9023741-1

Printed by PrintPartners Ipskamp in the Netherlands.

Front and back cover of this book, and the bookmark illustrate twin-, triple- and quad-spacer dampers produced by Ribe Electrical Fittings GmbH, Schwabach, Germany. AutoCAD picture on the front cover represents the schematic model of quad-bundle transmission line conductor with N-spacer dampers, taken from chapter 2 of this book.

Acknowledgements

I would like to express my gratitude to all those who, directly or indirectly, have given me their valuable support in the course of this work.

My utmost gratitude goes to my thesis supervisor Prof. Dr. Peter Hagedorn for his continuous support, kindness, and his patience towards me. Since my first days in Germany as a DAAD scholar, you have been a source of inspiration to me. Whether it is *10 o'clock coffee meeting* or any technical discussion, you always managed to find time for your people and inspire everyone in the group. I cannot but once again commend your wonderful hospitality towards each new comer in the group. Truly it's your sincere efforts which have kept the whole group as a family.

I would like to express my gratitude to my co-supervisor Prof. Dr. rer. nat. Michael Schäfer, his former colleague Dr.-Ing. Sebastian Meynen and colleagues of FNB for their support regarding Computational Fluid Dynamics part of my work.

I greatly appreciate the interest of Prof. Goutam Chakraborty, Prof. Satya Chakravarthy, Prof. Anirvan DasGupta, Prof. Dr.-Ing. Richard Markert, Dr. Nandan Kumar Sinha, Dr.-Ing. Nils Wagner and Prof. Dr.-Ing. Utz von Wagner, and would like to thank them for the technical discussions I had with them in different stages of my work.

Thanks to DFG (*Deutsche Forschungsgemeinschaft*) and our industrial partner Ribe Electrical Fittings GmbH for financially supporting this research work. Special thanks to Hans-Jörg Krispin for our telephonic conversations and regular meetings, which were a great opportunity for me to learn the industrial perspective of the transmission line vibrations problem.

Now to the *Mechanik* group, where I spent five memorable years of my life, and met some of the most wonderful people. I would like to thank my colleagues: Kathrin Baumann, Anke Böttcher, Ana Costa Conrado, Ashish Dighe, Uli Ehehalt, Florian Fischer, Stefenie Gutschmidt, Daniel Hochlenert, Thira Jearsiripongkul, Martin Kreschel, Alexander Lünenschloß, Jhon Malta, Sandeep Kumar Parashar, Roland Platz, Daniel Sauter, Martin Schönecker, Nobert Skricka, Gottfried Spelsberg-Korspeter, Alireza Tofangchi and Tobias Vomstein. Thanks you all for your support and for providing such a fantastic work environment. I would also like to thank gorgeous ladies-Renate Schreiber and Maria Rauck. Without you, I wouldn't have had my appointments set, my housing problems sorted out and other administrative tasks neatly done. It were you who made the group complete. Thank you all! I will always cherish the moments I spent with you.

My stay in Germany would have never been so comfortable, homely and memo-

rable without many of my friends. I would like to thank all my folks: Rajni Kumar Akula, Atul Athavale, Poonam and Debasish Banerjee, Arijit and Tanali Bhattacharya, Abhay Davesthale, Masum Düman, Ashwini and Rahul Harshe, Pragya and Chirag Jain, Kamalpreet Kaur, Orio Kieboom, Monika Luca, Divya and Bhaskar Mehta, Ioannis Michailidis, Sunil Kumar Omar, Kalpana and Sandeep Kumar Parashar, Ileana Petroniu, Anita Singh, Karelle and Prashant Soni, Pallavi Thiagarajan and Manu Anna Thomas. My life outside India wouldn't have been as exciting and happening without you people. In fact, you all are the reason that has made Germany my second home over these years.

I would also like to thank all my teachers, who provided a good foundation for my development. I owe a lot to the Department of Civil and Applied Mechanics at S.G.S.I.T.S. Indore, where I did my Graduation, learned a lot, and spent some of the best days of my life. A special thanks to my supervisor at IIT Bombay, Prof. Yogesh M. Desai, who encouraged me to go for higher research.

A heart-filled thanks to my love and life-partner Swati Gehlot, who has been an inspirer and motivator to me for last many years. Without you, I would have never been able to finish this research work. It was you who has always provided her unconditional support and encouragement in my tough days. You were the one knowing all my weaknesses and still accepting me for what I am. Thank you Swati for always being with me.

In India, the parents never say "I Love You" to their kids, as they breathe, think and love for their kids: *Mummy* and *Papa* (Shashi Bala and Surendra Kumar Verma), you have played a huge role in bringing me up to where I am today. It would be too artificial if I have to thank you, but without your sacrifices and the opportunities you provided me during my life's journey, I wouldn't have been able to achieve so much and come this far. I consider myself fortunate for the freedom that you provided to me taking some of life's crucial decisions. Even if you were seldom physically near me through these years in Europe, your thoughts and blessings have always been a lighthouse for me, guiding me in the right direction. I cannot thank you enough but just dedicate this book to you both. Please accept it!

And finally but most importantly, I thank the Almighty for everything I have, every opportunity I have been given, all right ideas and desired support given at the right time. I thank You for your blessings for me. Without You, this journey would have been an unlived dream...

Hamburg, 15. November 2008 Himanshu Verma

Contents

Abstract

Wind excited vibrations generated by the vortex shedding are very common in high-voltage overhead transmission lines. Although such vibrations are barely perceptible due to their low amplitudes (less than a conductor diameter), controlling them, however, is extremely important since they may lead to conductor fatigue. Mathematical models are therefore necessary for the computation of these vibrations, not only to evaluate the risk of potential damage to the transmission line but also for studying the efficiency of the damping measures. For single conductor transmission lines, the so-called energy-balance method (e.g., [1, 2, 3, 4, 5]) gives fairly good results for the estimation of vibration amplitudes. However, the problem becomes more involved for the conductor bundles attached with different damping devices. A modified form of the energy-balance method is thus needed.

This thesis presents a mathematical-mechanical model for modeling the vibrations of the conductor bundles with many spacer dampers and STOCKBRIDGE dampers, by considering subconductors as continuous systems. External damping devices are incorporated into the model by means of their complex impedance matrices. The presented model results in a smaller system matrix in comparison to what is obtained while modeling the conductor as a discrete system.

This modeling procedure yields a complex non-polynomial transcendental eigenvalue problem (TEVP). Solving such a TEVP is simple for smaller systems, e.g., for single conductor transmission lines. However, for a comparatively bigger system like the one in case of conductor bundles, it is a formidable task to obtain all the system eigenvalues in a certain frequency domain. The first goal of the presented thesis is to find efficient numerical methods for obtaining the solutions of TEVPs. Different numerical techniques are discussed and their results are compared. NEWTON's approach for the solution of the eigenvalue problem is found to be an efficient solution technique for obtaining the complex eigenvalues of a TEVP of the current type.

After obtaining the complex eigenvalues and eigenmodes of the system, an energy balance principle is presented in order to obtain the actual vibration amplitudes in the subconductors. In energy balance the energy input from the wind is equated with the energy loss due to external damping and the conductor's self damping. Wind power input is normally obtained using data from the wind tunnel experiments (e.g., [6, 7, 8, 9, 10]) or from the experiments carried out with transmission lines in the field (e.g., [11, 12]), for laminar and turbulent wind speeds. Wind power input data is only available for single oscillating rods/cylinders, as obtaining such data via experiments for different configurations of multi-cylinders, is a difficult task.

The second goal of the presented work is to numerically obtain the wind power

input for the oscillating cylinders in a tandem arrangement. A finite-volume approach is used for the solution of the NAVIER-STOKES equations. Moving grids are used to incorporate the movements of the cylinders. Firstly, accuracy and feasibility of the numerical results are verified by solving the flow around a single cylinder, and comparing the obtained results with the available experimental data. For similar setups as used in the experiments from different researchers, numerical wind power input for a single oscillating cylinder is obtained. Good agreement with the experimental results is found. The numerical approach is subsequently further extended to obtain the wind power input for two oscillating cylinders in a tandem arrangement.

A considerable difference between the wind power inputs for the downstream cylinder in a cylinder-tandem and for a single oscillating cylinder is observed. The newly obtained wind power input is utilized for the energy balancing in a bundled conductor benchmark problem, and results are discussed.

Kurzfassung

Winderregte Schwingungen, die durch Wirbelablösung erzeugt werden sind in Hochspannungsleitungen sehr verbreitet. Obwohl solche Schwingungen wegen ihrer niedrigen Amplituden (kleiner als der Leiterdurchmesser) kaum wahrnehmbar sind, ist es dennoch extrem wichtig, sie unter Kontrolle zu halten, da sie zur Leiterermüdung führen können. Mathematische Modelle für die Berechnung dieser Schwingungen sind daher nicht nur für die Ermittlung des Risikos von potentiellen Beschädigungen der Hochspannungsleitung notwendig, sondern auch um die Effektivität der Dämpfungsmaßnahmen zu untersuchen. Für Einzelleiter gibt die so genannte Energiebilanzmethode (z.B. [1, 2, 3, 4, 5]) recht gute Ergebnisse für die Abschätzung von Schwingungsamplituden. Allerdings wird das Problem komplizierter für Leiterbündel, die an unterschiedliche Dämpfermodelle angeschlossen sind. Daher wird eine modifizierte Form der Energiebilanzmethode benötigt.

Diese Dissertation präsentiert ein mathematisch-mechanisches Modell für die Modellierung von Schwingungen von Leiterbündeln mit mehreren dämpfenden Abstandshaltern und STOCKBRIDGE Dämpfern in dem die Teilleiter als kontinuierliche Systeme betrachtet werden. Externe Dämpfer werden in dem Modell durch ihre komplexen Impedanzmatrizen berücksichtigt. Das Modell führt zu einer kleineren Systemmatrix als es bei einer Disktretisierung mit FEM der Fall wäre.

Diese Vorgehensweise bei der Modellierung führt zu einem komplexen nicht-polynomialen transzendenten Eigenwertproblem (TEVP). Ein solches Eigenwertproblem ist für kleinere Systeme einfach numerisch zu lösen, z.B. für Einzelleiter. Allerdings ist es für größere Systeme, wie im Fall von Leiterbündeln schwierig, alle Systemeigenwerte in einem bestimmen Frequenzbereich zu erhalten. Das erste Ziel der vorgestellten Dissertation ist es, effiziente numerische Methoden zur Bestimmung der Lösungen des TEVP zu finden. Unterschiedliche numerische Techniken werden diskutiert und ihre Ergebnisse verglichen. NEWTON's Ansatz für die Lösung des Eigenwertproblems stellt sich als effiziente Lösungstechnik zur Bestimmung von komplexen Eigenwerten von TEVP des aktuellen Typs heraus.

Nach der Bestimmung der komplexen Eigenwerte und Eigenmoden des Systems, wird ein Energiebilanzprinzip vorgestellt um die eigentlichen Schwingungsamplituden des Subleiters zu erhalten. In der Energiebilanz wird der durch die mittlere Leistung der aerodynamischen Kräfte gleich der Dämpfungsleistung gesetzt. Die Windleistung wird in der Regel aus Daten von Windkanalversuchen (z.B. [6, 7, 8, 9, 10]) oder aus Messungen an Hochspannungsleitungen in Feldern (z.B. [11, 12]) für laminare und turbulente Windgeschwindigkeiten bestimmt. Windenergieeingangsdaten sind nur verfügbar für einzeln oszillierende Zylinder. Es ist schwierigsolche Daten durch Experimente für un-

terschiedliche Konfigurationen von Multizylindern zu erhalten.

Das zweite Ziel dieser Arbeit ist die numerische Ermittlung der Windleistung für oszillierende Zylinder in Tandemanordnung. Für die numerische Lösung der Navier-Stokes-Gleichungen wird ein Finite-Volumen Ansatz angewendet. Bewegliche Gitterwerden verwendet, um die Bewegungen der Zylinder zu berücksichtigen. Zunächst werden die Genauigkeit und Machbarkeit der numerischen Ergebnisse verifiziert, indem der Fluß um einen einzelnen Zylinder herum gelöst und die erhaltenen Ergebnisse mit den verfügbaren experimentellen Daten verglichen werden. Für ähnliche Konfigurationen, wie die bei Experimenten anderer Forscher verwendeten, wird die numerische Windleistung für einen einzeln oszillierenden Zylinder gefunden. Die numerischen Resultate weisen gute Übereinstimmung mit den experimentellen Ergebnissen auf. Anschließend wird der numerische Ansatz erweitert, um den Windenergieeintrag für oszillierende Zylinder in einer Tandemanordnung zu erhalten.

Es wird ein erheblicher Unterschied zwischen der Windleistung für den nachgeschalteten Zylinder in einem Zylindertandem und einem einzeln oszillierenden Zylinder beobachtet. Die neu erhaltene Windleistungwird für die Energiebilanz an einem Benchmarkproblem für Leiterbündel verwendet. Die Ergebnisse werden diskutiert.

Chapter 1

Introduction

1.1 General

High voltage overhead electrical power transmission in the past has commonly involved three voltage phases operated in the range of 110 kV to 230 kV. In such installations, it had been customary to utilize the single, multi-strand conductors for each phase of the transmission. When transmitting electrical power by such single conductor transmission lines there is, however, a practical upper limit to the voltages that can be transmitted due to the problems of higher reactance and corona effect [13]. The energy is also limited by the combined effects of the conductance and the capacitance of the conductor system.

Continuous growth in the demand of electric power, together with the effects of technical and economical factors, are leading to an increased use of bundled conductors comprising a plurality of spaced-apart subconductors for each voltage phase. Bundle conductors are used to increase the amount of the power that may be carried in a line. Due to the skin effect, ampacity of subconductors is not proportional to the cross section [13], for the larger sizes. Therefore, bundle conductors may carry more current for a given weight. Moreover, they result in lower reactance, compared to a single conductor. Bundle conductors are normally used for voltages over 220 kV in order to avoid corona losses and audible noise. Customarily two or more subconductors[1] are provided per phase in order to increase the power transmitting capacity of a transmission line circuit. Previously, bundle conductors were thought to be useful only for very high voltage, such as 500 kV. More recently, the advantage has been proven, and they are more common, for 230 kV and 115 kV. To prevent contacts among individual subconductors under normal operating conditions, they are held apart by placing the nonconducting spacers or clamped rigid frames at suitable intervals, which maintain a uniform bundle geometry along the whole span.

Bundled conductor transmission lines suffer from many of the similar mechanical problems as the single conductor transmission lines do. Of the different dynamical phenomena in the high-voltage overhead transmission lines, wind-excited oscillations of the conductors constitute a major issue. These wind-excited oscillations can, for example, be classified with respect to the dominant frequencies. The most common wind-excited conductor oscillations are *galloping* and *aeolian vibrations* [14]. In contrast to galloping, which is a rare phenomenon occurring under special climatic conditions, the vortex-induced aeolian vibrations are observed very commonly and are the main focus of the current work. Cross-winds of low velocities (i.e., from 1 to 7 m/sec) tend to induce the aeolian vibrations in the conductors due to VON KÁRMÁN vortex shedding [15] in the frequency range of 3-150 Hz [14], mainly in the vertical plane. Figure 1.1

[1] e.g., for 220 kV lines: 2-subconductors; for 380 kV: 3 or 4-subconductors.

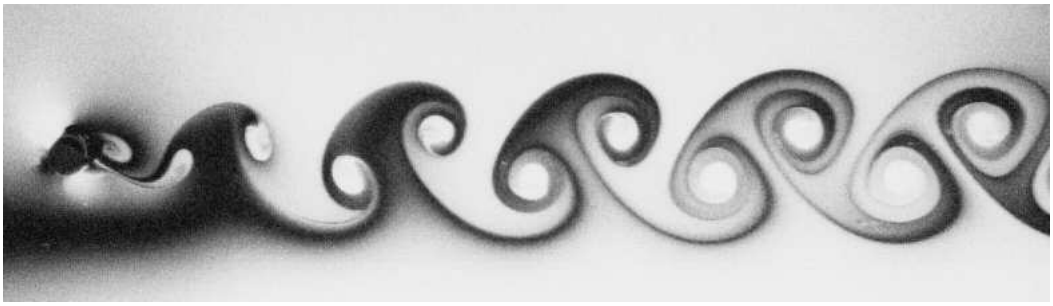

Figure 1.1: von Kármán vortex street past a stationary cylinder under laminar flow

illustrates a typical von Kármán vortex street formed past a stationary cylinder, causing harmonic aerodynamic forces on it. However, in the case of conductor bundles, interaction of the spacers leads to a coupling of vibrations in the vertical plane with those in the horizontal plane.

Transmission line engineers are mainly concerned with the physical consequences of the aeolian vibrations in the conductor bundles. It causes a continuous and sever flexure at the points of subconductor attachments to the suspension clamps and to the spacer clamps, which may lead to an early fatigue failure of the subconductors at these points, limiting the lifespan of the subconductors or the fittings attached to it. This problem is further aggravated by the modern tendency to string the conductors at increasingly higher mechanical tensions. Due to high axial tensions, damping due to the internal friction in taut-wired subconductors undergoing the bending vibrations is negligible. Hence, subconductor's self damping is normally not enough to mitigate the wind-excited vibrations, and high mechanical stresses may develop in the conductors at critical locations.

Additional vibration controlling devices are, hence, required to keep the subconductor stresses in the desirable limits. Commonly used vibration controlling devices in the transmission lines are passive in nature. The most successful control of aeolian vibrations in single conductor transmission lines has been achieved through the Stockbridge dampers [14]. A *spacer damper* was first mentioned by Edwards and Boyd in [16], which is potentially used for controlling the aeolian vibrations in the conductor bundles. A modern spacer damper consists of a rigid aluminium frame, and a number of arms having different orientations. Depending on the number of subconductors in a conductor bundle, attached spacer dampers have different number of arms. Figure 1.2 illustrates typical twin, triple and quad spacer dampers produced by Ribe Electrical Fittings GmbH, Germany [17]. Arms are attached to the central rigid frame by means of the special flexible joints containing rubber elements. Disintegrated view of a typical quad-bundle spacer damper is shown in figure 1.3. In-addition to its primary function of maintaining the desired spacing between the subconductors, a spacer damper also provides a mean of absorbing the mechanical vibration energy of the subconductors through its viscoelastic joints. It serves to limit the bending stresses, and hence the strains, in the subconductors to a safe level, resulting in extended lifespan of the

(a) (b) (c)

Figure 1.2: Typical spacer dampers (Courtesy: Ribe Electrical Fittings GmbH [17])
(a): twin spacer damper, (b): triple spacer damper, (c): quad spacer damper

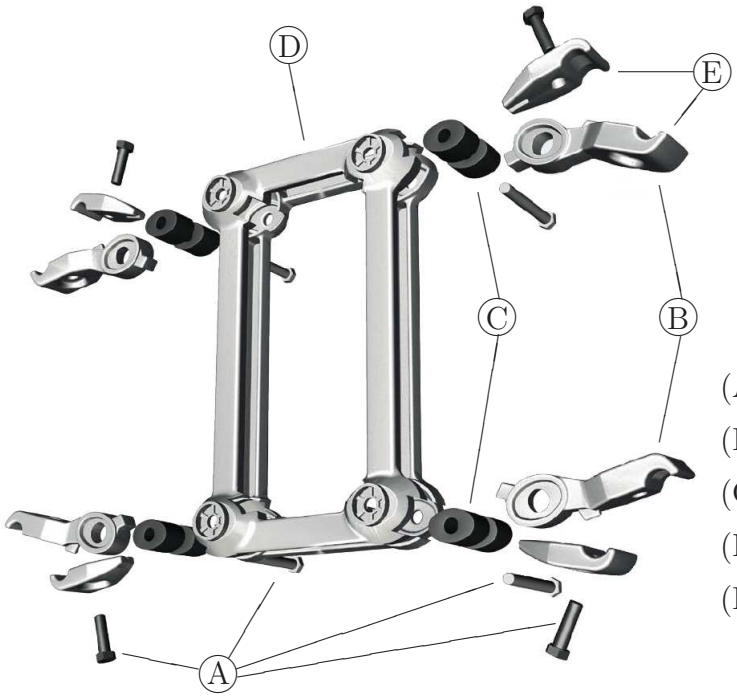

Figure 1.3: Disintegrated view of a typical quad spacer damper (Courtesy: Ribe Electrical Fittings GmbH [17])

conductor bundles exposed to the aeolian vibrations.

Ideally, spacer dampers should eliminate the need for separate vibration dampers (e.g., STOCKBRIDGE damper). However, it is not yet clear under which conditions this goal can actually be achieved completely by the spacer dampers in the market. Imperfect design of the spacer dampers, in absence of good understanding of the physics behind its effect on the conductor bundle vibrations, leads to the requirement of additional STOCKBRIDGE dampers to damp-out the localized subspan vibrations, specially in the case of long-span bundled conductors. There have been reported cases for high vibration amplitudes and fatigue failures in the subconductors [18, 19], due to poor

designs of the conductor bundles. Mathematical models are therefore necessary for the computation of aeolian vibrations, in order to evaluate the risk of potential damage to the line as well as for studying the efficiency of the damping measures. They could be extremely useful in providing the insight into the basic phenomena, permitting the optimization of the parameters and leading to the improved designs.

According to [20]: "*The increase in number of subconductors which may be envisaged in condition with future development of overhead transmission lines, has made it necessary to carry out more detailed research on the response of bundle system to wind induced motion.*"

Also, Anderson and Hagedorn mentioned in their work [21]: "*It is, of course, clear that a mathematical-mechanical model of a bundled line with spacer damper can completely replace neither the field tests nor the laboratory experiments. However, it can be a valuable tool in the design of spacer dampers and in deciding if, for a given line, sufficient damping can be achieved without additional damping devices. Such a model may also be useful in defining the minimum number of spacers dampers per span as well as in optimizing their spacing.*"

The energy balance principle (EBP) [1, 2, 5] is well established for estimating the vibration amplitudes, and hence, the strain levels in the single conductor transmission lines. A similar energy balance principle is developed in the current work to estimate the vibration levels in conductor bundles with spacer dampers and/or Stockbridge dampers. Besides the parameters of the conductor and of the damping devices, the aerodynamic forces acting on the vibrating conductor are the main input data required for energy balancing. For the wind power input, researchers still depend on the experimental data of drag and lift forces of a vibrating cylinder obtained from the wind tunnel testing. Experimental wind power input curves for a single vibrating cylinder are used for the analysis of the single conductor transmission line vibrations. However, it is not clear if the same can be used for conductor bundles, as the wind interacts differently with the bundled subconductors.

1.2 State of the art: literature review

1.2.1 Modeling of the aeolian vibrations in transmission line conductors

Current work focuses at the aeolian vibrations of the conductor bundle system within a frequency range of 3-150 Hz [14]. This frequency range, for a bundle conductor with a span length of the order of 100-500 m with few spacer dampers, typically corresponds to the range between the system's 500th and 5000th eigenfrequency. A very large number of modes are, therefore, required to be considered in the Ritz-Galerkin method, in order to obtain acceptable results. Moreover, mode shapes that are obtained from the Ritz-Galerkin method or discrete methods like the FEM, are not adequate for the determination of the dynamic stresses and strains at critical points, as it is well known that the computational error of approximate methods increases rapidly with the rise in the order.

Studies for the analysis of the vibrations of conductors and dampers were carried out by many researchers during the decade of 1940's [22, 23]. By the end of 1970's many researchers had directed their attention to the mathematical-mechanical modeling of a long span single conductor transmission lines with attached dampers. Many papers presenting study of the transverse conductor vibrations by modal analysis using RITZ-GALERKIN's method appeared, e.g., [24, 25, 26]. But the determination of the mode shapes from such approximate methods did not yield good results from the industrial point of view. In order to design the transmission lines with more operational safety, two directions of thought evolved by the end of 1980. In the first direction, the aeolian vibrations level of the span were determined by energy balance [27, 1, 2, 11, 5], by using the quantitative relationship between the vibration level and the power input from wind, the power dissipated from conductor's self damping and from other external damping devices. In the second direction of thought, the behavior of the wind excited lift was assumed to satisfy the empirical models based on the experimental data. Significant research in this direction was carried out in [28, 29, 30, 10, 20, 31, 32]. However, most of the work in this field was limited to the single conductor transmission lines with one or more STOCKBRIDGE dampers installations.

As compared to the single conductor transmission lines, only a few papers have so far been devoted to the mathematical-mechanical modeling of the conductor bundles. The method of modal analysis was applied to the modeling of the quad-conductor bundles in [33]. In [34] a transfer matrix method was introduced for the calculation of the free and the forced vibrations in conductor bundles with spacer dampers, resulting in a complicated eigenvalue problem. In [26] the eigenfrequencies and the eigenfunctions of the conductor bundles were calculated using the dynamical stiffness matrix. In [35] a traveling-wave approach, together with the energy-balance method was suggested. In regard to only aeolian vibrations in the conductor bundles with spacer dampers, a mathematical model was developed using the energy balance principle in [36, 21, 37, 38, 39], where individual subconductors are mechanically modeled as taut strings and their vibrations were described by the wave equations. Bending stiffness of the subconductors was not considered in the first approximation for simplicity. It was, however, considered later in order to obtain the strains at the critical locations. Conductor's vibrations were assumed to be harmonic and the spacer dampers were modeled as linear systems.

Practical evaluation of the performance of the spacer dampers via field tests is normally carried out by the utilities and the manufacturers. However, it is time consuming, and long experiments are required to be carried out under different meteorological and mechanical conditions (refer [40, 41]). [42] used an experimental modal analysis to determine the dynamical properties of the spacer dampers. HAGEDORN in [36] and [43] presented a mathematical model for a twin-spacer damper, by modeling it as a multi-body system. Experimental determination of the dynamical properties of the spacer dampers as a function of the vibration frequency, was also shown in [36] and [43]. In such a model the spacer damper was considered as a combination of rigid bodies (i.e., central frame and spacer arms) connected to each other via flexible joints. Such modeling of the spacer dampers was further extended in [21] for a quad-spacer damper and was used in the mathematical model of the conductor bundles, using the energy balance approach. Spacer dampers in this model were incorporated in the form of their complex impedance matrices, which were determined using the multi-body model [21].

First results of the obtained strain levels at the critical points on the subconductors using such modeling of the conductor bundles were presented in [37, 44, 38].

1.2.2 Power input from the wind

To perform an energy balance analysis, one not only needs to know the geometric and the damping characteristics of the conductor and of the damping devices, but also needs an estimate on the power imparted by the wind to the conductors. It was recognized as early as in 1930 that controlling the conductor vibrations involves the dissipation of the vibration energy at a greater rate than it could be accumulated in the span of a conductor from the wind. Some efforts were made to evaluate the energy relationships involved, but most of these investigations were limited in scope or hampered by the lack of fully adequate instrumentations. At the same time, theoretical relationships were sought for clarifying the behavior of the wind, the conductor and the damping devices during vibrations.

Among the first successful efforts made are the wind tunnel experiments performed by Farquharson and McHugh at the University of Washington [28]. They determined the power delivered by the wind using wind tunnel experiments on a vibrating cylinder. Bishop and Hassan in [7] experimentally investigated the forced oscillations of a circular cylinder in the cross-flow direction, with special attention to the hydrodynamic forces exerted on the body, over a wide range of the driving frequencies and the oscillation amplitudes. Their experiments revealed the magnification of the mean drag and the lift-force amplitudes when the excitation frequency is close to the natural shedding frequency. A sudden change in the phase angle between the lift force and cylinder displacement was noticed by them, when the oscillation frequency is varied around the shedding frequency.

Since then many researchers obtained the wind power input experimentally from tests carried out in wind tunnels and in water channels, with oscillating rigid cylinders or flexible rods. Most significant work in this direction can be found in [10, 11, 45, 46, 47, 48, 49]. Recently a comparative study was reported in [49], which shows an overall state of the wind tunnel data from different studies, for a single vibrating cylinder. A similar plot is shown in figure 5.11 of the current work. However, the obtained wind power input data vary considerably among different studies.

Rawlins mentioned in [11]: "*There is considerable uncertainty about wind power supplied even under conditions of steady or so-called laminar wind. All laboratory investigations of wind input during aeolian vibration have been carried out under conditions that correspond to steady wind. The list of references cites fourteen such investigations. There is a more than 2 to 1 spread in reported results for comparable conditions.*"

Also, according to Brika and Laneville in [45] "*Even in the simple case of an isolated cylinder, the agreement between the results of the various investigations is poor.*"

As mentioned in section 1.2.1, the mathematical model to estimate the vibration levels in the bundled conductors, also uses energy balancing. In such a case, the energy balance is applied to the complex eigenmodes of each subconductor of the vibrating bundle. Obviously the wind flow around an individual subconductor is affected by the

presence of other subconductors in the bundle. Therefore, wind power inputs for a single oscillating cylinder, as shown in figure 5.11, may not directly be used for the conductor bundles. Because of the influence of the upstream cylinder, the wind power imparted to the downstream cylinder may change considerably. In such a case, the power imparted by the wind on the downstream cylinder depends on various factors, e.g., separation between two cylinders, different planes and the phases of their oscillations and different bundle inclination with respect to the flow direction. Many experimental studies were performed in this regard (i.e., [50, 47, 48]). Specially the pioneer work by Brika and Laneville in [51, 52, 53, 54] sets the landmark. Other significant studies in this direction are presented in [55, 56, 57]. Numerous numerical studies using computational fluid dynamics (CFD) are also available in the literature, which deal with the flow around a vibrating cylinder (e.g., [58, 59, 60, 61, 62]) or look at the interaction of the wake of the upstream cylinder to the downstream cylinder (e.g., [63]). Most of the CFD studies are based on the two-dimensional Navier-Stokes equations and they employ the finite difference, the finite element or the finite volume schemes. However, no attempt has so far been made to obtain numerically the wind power input on the vibrating downstream cylinder in a cylinder tandem. It should be noted that besides the aeolian vibrations many other types of vibrations are possible in bundled conductors. They are, however, not the subject of this work.

1.3 Motivation

Modeling of the transmission line as a continuous system leads to a transcendental system matrix, having infinitely many eigenvalues. In order to apply the energy balance principle, one needs to obtain all eigenvalues of the system matrix in the frequency range of interest. For the single conductor transmission lines, obtaining the solution of the transcendental eigenvalue problem (TEVP) is comparatively easy, as it involves a smaller system matrix and simpler compatibility conditions at the damper attachment points. However, in the case of bundled conductors with many spacer dampers, the system matrix shows a poor numerical behavior because of its bigger size, very dense spectrum of the system eigenvalues and complicated constitution of the impedance matrix for the spacer dampers. This leads to an inadequate optimization criterion for iterative solution techniques. Hence, many eigenvalues are missed[2] when conventional methods are used for solving the TEVP. First goal of the current work is to present more efficient numerical techniques for the solution of the TEVP, which are able to find most, if not all, the system eigenvalues of conductor bundle with many spacer dampers and Stockbridge dampers.

Another significant difference between the energy balance analysis of the single conductor transmission lines and of the bundled conductors is the power input from the wind. It is clear from the experimental data, that flow around a downstream cylinder in a tandem configuration may be significantly different from the flow around an isolated cylinder. Hence, the power inputs from the wind for both cases may differ too. However, there is still not enough wind tunnel data available, which can directly be used

[2]Missing eigenvalues are clearly noticeable in the results presented by Hadulla [44], page 82, Mitra [64], page 77 and Ranmale [65], page 53.

for the energy balance in the conductor bundles. Many possible configurations regarding the number of the conductors, their spacing and their orientations, make the wind tunnel tests very expensive and formidable. Hence, it is practical to replace the wind tunnel tests by numerical simulations using CFD, which may yield a good insight into the aerodynamical behavior of the problem. Moreover, the numerical solutions provide a good description of the flow parameters throughout the solution domain, a task which is difficult to be accomplished experimentally, specially in the unsteady flows. However, the accuracy of the numerical results depends on various factors such as the method of solution, the mesh refinement and the boundary conditions etc. Second goal of the present work is to numerically obtain the power input from the wind on the bundled conductor configuration.

1.4 Organization of the thesis

As described in the last section, the present thesis is devoted to two main objectives:

1. to present efficient numerical solution techniques for transcendental eigenvalue problems, which can find most of the complex eigenvalues of the conductor bundle system with many spacer dampers and STOCKBRIDGE dampers,

2. to numerically obtain the power input from the wind using CFD, on the oscillating downstream cylinder in a tandem, vibrating under the wakes from oscillating upstream cylinder.

In chapter 2 the problem of a conductor bundle attached with many spacer dampers and STOCKBRIDGE dampers is formulated. Motion of the subconductors in each subspan were represented by the traveling waves in vertical and horizontal planes. Spacer dampers and STOCKBRIDGE dampers, are incorporated in the mathematical-mechanical model in the form of their complex impedance matrices. In order to obtain the frequency-dependent impedance matrix of the spacer dampers, a linear multi-body model is presented in appendix B, which was developed in [36] and extended in [21]. Additionally, an impedance matrix is formulated for a combination of the twin spacer dampers installed on a quad conductor bundle, attached in horizontal and vertical configuration alternately. The formulation results in a TEVP in the complex domain.

Chapter 3 fulfills the first objective of the present work. Several solution techniques are discussed in detail for solving the non-polynomial TEVP, resulted from the formulation in chapter 2. Efficiencies of the presented solution techniques are later compared by solving a smaller benchmark problem, defined in the section 3.6.1. Another representative real-life conductor bundle problem is formulated in section 3.6.2, for which the obtained eigenvalues are shown in the last part of chapter 3. A second benchmark problem is further analyzed in the next chapters. Additionally, a method is mentioned which gives an estimate of the number of eigenvalues presented in the desired frequency range.

Chapter 4 presents the theoretical background behind the energy balancing, by comparing the power input in the system to the power losses, in order to obtain the vibration level of the system. This chapter also describes the dependency of power

input from the wind and of different power losses, on the subconductor's amplitude. In section 4.4 different design parameters for the transmission lines are discussed. Section 4.4.2 describes how to compute the resultant amplitudes of two orthogonally oscillating waves, in order to obtain the maximum amplitudes for the conductor bundle. A similar approach is also used to obtain the resultant conductor strains, as described in section 4.4.1. Energy balance is applied to the second benchmark problem, and the results are shown in the last part of chapter 4.

Chapter 5 fulfills the second objective of the present work, which is to numerically obtain the wind power input, using CFD. Transmission line conductors are treated as circular cylinders and flow around them is simulated using the finite-volume method. The first part of this chapter describes the elementary equations of fluid dynamics (viz., Navier-Stokes equations). Block structured grids are used for the discretization of the fluid domain. A moving grid approach is used, where the grids around the cylinder move together with it. In this chapter, flow around a single stationary and then moving cylinder are simulated. The obtained results are compared to the experimentally available wind-tunnel data. Wind power input on a single oscillating cylinder is obtained numerically, and compared to the experimental analysis by different researchers. After finding a good agreement with the experimental results, the same approach is further extended to simulate the flow around two stationary cylinders in a tandem arrangement. Time-averaged drag and lift forces are obtained on the downstream cylinder, and are compared with the experimental data. In the last step, the flow around two oscillating cylinders is simulated. The wind power input on the oscillating downstream cylinder is obtained for different vibration amplitudes. The obtained results are discussed in the last part of chapter 5.

Chapter 6 evaluates the results obtained from chapter 3 and chapter 5, and gives the concluding remarks. A brief description of the scope for the future work is also included.

Chapter 2

Mathematical model for a conductor bundle

Summary: This chapter presents a mathematical-mechanical modeling of a conductor bundle with many spacer dampers and Stockbridge *dampers. In section 2.2 the modeling is further extended to incorporate twin spacer dampers with different orientations in a quad conductor bundle. Such formulation results in a transcendental eigenvalue problem (TEVP) (2.25) in the complex domain, which is required to be solved in order to obtain the complex system eigenvalues and eigenvectors.*

2.1 Modeling the conductor bundle

A conductor bundle consists of more than one subconductors spanned together and with a number of spacers or spacer dampers, as shown in figure 2.1. Sometimes additional groups of Stockbridge dampers are also attached to the conductor bundle, as will be discussed in section 2.1.3. We first consider a conductor bundle consisting of M subconductors, as shown in figure 2.1, where a quad bundle (i.e., $M = 4$) is shown. N spacer dampers, each having M number of arms, are attached at different locations on the conductor bundle. Spacer dampers are placed at positions $x = l_n$, where $n = 1, 2, 3, \ldots, N$, from the left end. They divide the total span length L, into $N+1$ subspans of lengths Δl_1, Δl_2, $\ldots \Delta l_{N+1}$, as shown in figure 2.1. To model the conductor bundle, the subconductor motions are first mathematically represented and the end-boundary conditions are implemented, as shown in the next section. Additional compatibility conditions will be incorporated at the points of spacer damper attachments in the section 2.1.2.

2.1.1 Equation of motion for the subconductors

In early days of electrical transmission, copper was used extensively as a conductor, but now virtually all conductors are made of aluminum. Each conductor is made of many strands (1-5 mm in diameter) combined to give an overall diameter of 4-50 mm. In most conductors, a steel or a high-strength aluminum alloy is used for the core strands to give the conductor an added strength for medium and high voltage lines. A detailed mathematical description of conductors is difficult due its standard construction. Hence, the problem is simplified in the current study by treating conductor as a solid, homogeneous cylindrical body whose physical properties, i.e., mass per unit length and flexural rigidity, are constant.

Let us consider a conductor with diameter D, cross sectional area A and moment of

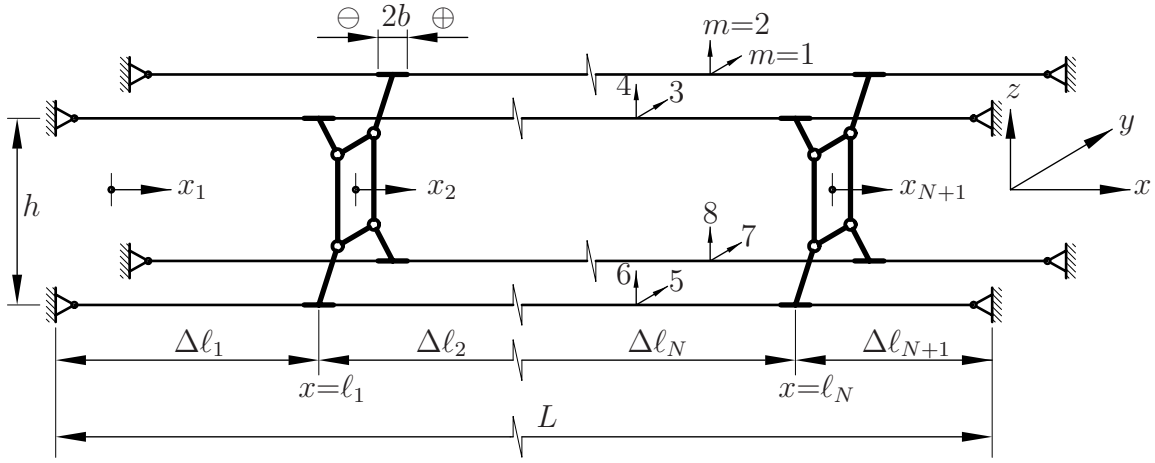

Figure 2.1: Schematic diagram of a quad bundle attached with N spacer dampers

inertia I. The mass density of the conductor material is ρ and its YOUNG's modulus is E. Since, sag to span length ratio in a normal overhead transmission line is small ($\approx 3-4\%$), conductor's sag is disregarded in the current study. Although, transmission line conductor possess a finite value of flexural rigidity EI, yet in the eigenvalue problem and in energy balance it is considered as a string, with no flexural rigidity. Considering the conductor as a string significantly reduces the size of the eigenvalue problem. Such consideration is reasonable as the conductor's flexural rigidity has a very little influence on the eigenfrequencies and the eigenmodes of the system, as shown in appendix A. In the determination of the bending strains, on the other hand, EI plays an essential role.

It is usually assumed that the aeolian vibrations in single conductors occur predominantly in the vertical plane [1, 2, 5], as the wind blowing transversely in a horizontal direction gives rise to vertical lift-forces on a conductor [15, 66]. The presence of spacers or spacer dampers in case of conductor bundles, however, complicates the subconductor motion. In such a case not only the vortex shedding differs from that in the single conductor, as the vortex-wake coming from the upstream subconductor hits the downstream subconductor, but also the spacer itself complicates the situation further. Hence, a spacer damper design, like the one shown in figure 1.2, provides coupling of the vibrations in different directions, i.e., a vertical force on one of the spacer damper arm will cause rotation of the arm together with a compression of the flexible joints in the longitudinal direction of the arm. Hence, subconductors, to which the spacer damper is attached, will not move purely in the vertical plane. To take this into account, transverse displacements of the conductor in both vertical as well as in the horizontal directions are considered in the present model. The transverse motion of any subconductor in the v-th subspan ($v = 1, 2, 3, \ldots, N+1$) is expressed by the wave equation as shown in (A.12),

$$\rho A \ddot{w}_{m,v}(x,t) - T_m w''_{m,v}(x,t) = f_W(x,t) + f_D(w_{m,v}, \dot{w}_{m,v}, t) \qquad (2.1)$$
$$\forall\ v = 1, 2, 3, \ldots, N+1$$
$$\forall\ m = 1, 2, 3, \ldots, 2M$$

where m represents the plane of motion of the subconductors in v-th subspan and T_m

is the tension values in different subconductors. Odd values of m correspond to the horizontal displacement and even values correspond to the vertical displacements of the subconductors (e.g., figure 2.1). Of course, the tension in any subconductor is the same for vertical and for horizontal motion, i.e. $T_{2k-1} = T_{2k}$, where $k = 1, 2, 3..., M$. In (2.1) f_W stands for the aerodynamic forces acting over the profile of the subconductors and f_D for their structural damping. The f_W term is dependent on the wind speed, which is only defined within a large tolerance level. It is difficult to know the exact values of wind forces acting on the conductors, firstly because of its variation along the transmission line span, and secondly because of its stochastic variation in time and geographic profile of land where transmission line is laid. The basic philosophy in current analysis of the vortex excited vibrations is to obtain the vibration levels, which are based on a worst case hypothesis [1, 2]. These are, in fact, the vibrations corresponding to a constant wind speed directed transversally to the transmission line. Hence, in the beginning we neglect the forcing terms f_W and f_D, and solve an eigenvalue problem in order to obtain the system eigenfrequencies and the corresponding mode shapes. The obtained mode shapes are then scaled using the energy balance between input and dissipated energies, as is shown in the chapter 4. Details on the wind power input and on the different energy dissipations are discussed in the chapter 4 and 5. Neglecting the forcing terms leads us to a set of homogeneous equations of motion

$$\begin{aligned} \rho A \ddot{w}_{m,v}(x,t) - T_m w''_{m,v}(x,t) = 0, & \qquad (2.2)\\ \forall\ v &= 1, 2, 3, \ldots, N+1;\\ \forall\ m &= 1, 2, 3, \ldots, 2M. \end{aligned}$$

Conductors are normally suspended between the towers via the insulators, which allow small movements at the hanging points. However, it is assumed here that the span under consideration is symmetrical with respect to the adjacent spans, and hence, the suspension points do not undergo large motions. Using this fact the conductors can be assumed to be clamped at the span ends, resulting simplified boundary conditions. In order to reduce the complexity of the problem, it is also assumed that both towers are at the same level and the wind speed is uniform throughout the span length. A relatively low overall damping of the bundle systems reduces any possible coupling between modes having different frequencies. Hence, it is assumed that the deformation along the span in the case of aeolian vibrations is due only to one mode of vibration. The above mentioned conditions assure that the transmission line system can be modeled as always vibrating in one of its eigenmodes and exhibiting a synchronous motion[3].

The subconductors are considered to be clamped at both ends. With homogeneous boundary conditions at the clamped supports

$$w_{m,1}(0,t) = 0, \qquad (2.3)$$

$$w_{m,N+1}(L,t) = 0. \qquad (2.4)$$

Equations (2.2–2.4) define a boundary value problem. New local coordinates x_v are introduced for each subspan, which are defined as

$$x_v = x - l_{v-1}, \qquad v = 1, 2, 3, \ldots, N+1; \text{ with } l_0 = 0, \qquad (2.5)$$

[3]A synchronous motion is defined as the motion in which ratio of the vibration amplitudes at any two points remain constant with time.

which gives $0 < x_v < \Delta l_v$. In the new coordinate system the equation of motion (2.2) will be

$$\rho A \ddot{w}_{m,v}(x_v,t) - T_m w''_{m,v}(x_v,t) = 0, \qquad (2.6)$$
$$\forall\ v = 1,2,3,\ldots,N+1;$$
$$\forall\ m = 1,2,3,\ldots,2M.$$

Since the transmission line is considered to vibrate in synchronous motion, space and time dependent components of the displacement quantity can be separated

$$w_{m,v}(x_v,t) = \mathbf{Re}\left[W_{m,v}(x_v)\mathrm{e}^{st}\right]. \qquad (2.7)$$

Substituting in (2.6), leads to

$$W_{m,v}(x_v) = A_{m,v}\mathrm{e}^{\left(\frac{sx_v}{c_m}\right)} + B_{m,v}\mathrm{e}^{\left(\frac{-sx_v}{c_m}\right)} \qquad (2.8)$$

where c_m is the wave velocity in m-th direction defined as $c_m = \sqrt{T_m/\rho A}$. $A_{m,v}$ and $B_{m,v}$ are the integration constants for the vibration of v-th subspan in the m-th direction. According to (2.8) the displacement of the conductor at any position is the summation of two traveling waves; one traveling in the negative x_v-direction with an amplitude $A_{m,v}$ and another in the positive x_v-direction with an amplitude $B_{m,v}$. It is clear from (2.8) that, if the parameter s is a purely imaginary quantity (i.e., for the undamped system) the $W_{m,v}$ will have constant amplitudes over each subspan and hence two traveling waves will result in a standing wave. However, if the parameter s is complex (i.e., for the damped system) $W_{m,v}$ will be a traveling wave, which will show the direction of flow of the energy in any particular subspan. Substituting (2.8) in the boundary conditions (2.3 and 2.4) gives

$$A_{m,1} + B_{m,1} = 0, \qquad (2.9)$$
$$A_{m,N+1}\mathrm{e}^{\frac{s\Delta l_{N+1}}{c_m}} + B_{m,N+1}\mathrm{e}^{\frac{-s\Delta l_{N+1}}{c_m}} = 0. \qquad (2.10)$$

2.1.2 Incorporating the spacer dampers

In the modeling of the conductor bundle, the effect of spacer dampers is incorporated by means of their respective impedance matrices. The impedance matrix for any spacer damper is obtained by considering its mass, geometric and damping properties. In doing so, the spacer damper is treated as a multi-body system with linear elastic joints and damping (e.g., for a quad spacer damper 4-arms and a central frame are treated as five interconnected rigid bodies). The formulation (as described in [36] and [21]) results in a square impedance matrix, elements of which are the functions of the spectral parameter s. The detailed formulation for the impedance matrix of a spacer damper is shown in appendix B.

Figure 2.2 represents the multi-body models for the twin, triple and quad spacer dampers shown in figure 1.2. Figure 2.2 also shows the clamp of effective width[4] $2b$.

[4]Effective clamp width $2b$ is the sum of actual physical clamp width and the conductor's characteristic length due to bending at both sides of the clamp, i.e., $2b = b_{physical} + 2l_{char}$, where $l_{char} = \sqrt{EI/T}$.

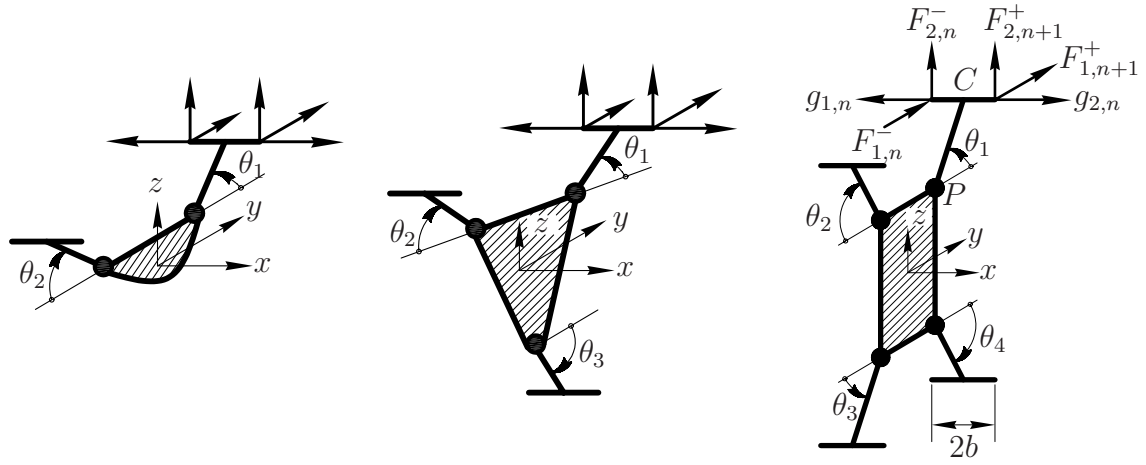

(a) (b) (c)

Figure 2.2: Forces acting at the clamp of a spacer damper

Four transverse forces acting at one clamp are illustrated in figure 2.2c. In this figure only forces acting on one clamp are shown, although the same applies for all the clamps. In figure 2.2c one of the four arms is shown attached to the central frame via a viscoelastic joint at the point P. Forces in the transverse directions to the conductor are denoted by $F^-_{m,n}$ or $F^+_{m,n+1}$, $m = 1, 2, 3, \ldots, 2M$ and $n = 1, 2, 3, \ldots, N$. Here, $(\ )^+$ and $(\ )^-$ are used to show whether the point of interest is in positive or in negative x-direction from the point of spacer damper attachment on the conductor bundle. Forces in the axial conductor direction are denoted by $g_{j,n}$, $j = 1, 2$ and $n = 1, 2, 3, \ldots, N$.

The generalized transverse force and velocity vectors at the n-th spacer damper are

$$\mathbf{F}_n(t) = \begin{bmatrix} F^-_{1,n} \\ F^-_{2,n} \\ F^+_{1,n+1} \\ F^+_{2,n+1} \\ F^-_{3,n} \\ F^-_{4,n} \\ \vdots \\ F^+_{2M-1,n+1} \\ F^+_{2M,n+1} \end{bmatrix}, \qquad \dot{\mathbf{w}}_n(t) = \begin{bmatrix} \dot{w}^-_{1,n}(\Delta l_n - b, t) \\ \dot{w}^-_{2,n}(\Delta l_n - b, t) \\ \dot{w}^+_{1,n+1}(b, t) \\ \dot{w}^+_{2,n+1}(b, t) \\ \dot{w}^-_{3,n}(\Delta l_n - b, t) \\ \dot{w}^-_{4,n}(\Delta l_n - b, t) \\ \vdots \\ \dot{w}^+_{2M-1,n+1}(b, t) \\ \dot{w}^+_{2M,n+1}(b, t) \end{bmatrix}, \tag{2.11}$$

which can be expressed as

$$\begin{aligned} &\mathbf{F}_n(t) = \mathbf{Re}[\widehat{\mathbf{F}}_n \mathrm{e}^{st}], \\ \text{and} \quad &\dot{\mathbf{w}}_n(t) = \mathbf{Re}[\widehat{\dot{\mathbf{w}}}_n \mathrm{e}^{st}]. \end{aligned} \tag{2.12}$$

The impedance matrix of the spacer damper relates the $4M$ velocities at the clamps to the $4M$ transverse forces. The detailed formulation in the appendix B also shows that the impedance matrix is of the size $4M \times 4M$. Here we assume that the impedance matrix $\mathbf{Z}_n(s)$ for the n-th spacer damper is known. The amplitudes $\widehat{\mathbf{F}}_n$ and $\widehat{\dot{\mathbf{w}}}_n$ are related to each other by the relation

$$\widehat{\mathbf{F}}_n = \mathbf{Z}_n(s)\widehat{\dot{\mathbf{w}}}_n, \qquad n = 1, 2, 3, \ldots, N. \tag{2.13}$$

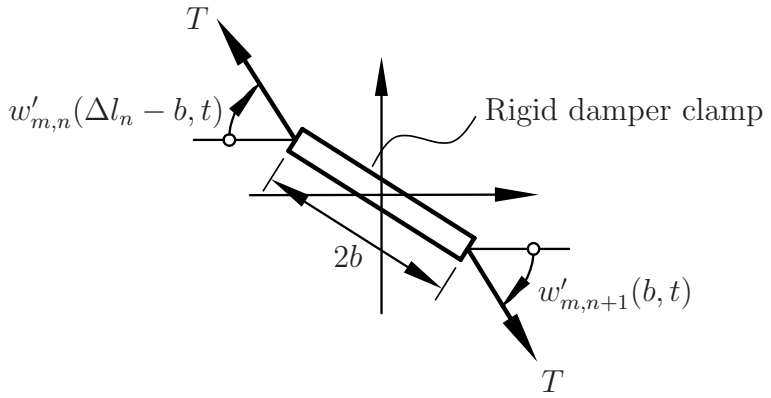

Figure 2.3: Rotation of the spacer damper clamp about y- or z-axis

The forces at the clamp ends of any spacer damper are in equilibrium with the transverse components of the tensile forces on both the sides of the clamp (refer figure 2.3). Assuming small displacements, the transverse components of T are

$$\widehat{F}^{-}_{m,n}(t) = -T_m w'_{m,n}(\Delta l_n - b, t), \tag{2.14}$$

$$\widehat{F}^{+}_{m,n+1}(t) = T_m w'_{m,n+1}(b, t). \tag{2.15}$$

Using (2.7) and (2.8) gives

$$\widehat{F}^{-}_{m,n} = -\frac{T_m s}{c_m}\left[A_{m,n}\mathrm{e}^{\left(\frac{s\Delta l_n}{c_m}\right)}\mathrm{e}^{\left(\frac{-sb}{c_m}\right)} - B_{m,n}\mathrm{e}^{\left(\frac{-s\Delta l_n}{c_m}\right)}\mathrm{e}^{\left(\frac{sb}{c_m}\right)}\right], \tag{2.16}$$

$$\widehat{F}^{+}_{m,n+1} = \frac{T_m s}{c_m}\left[A_{m,n}\mathrm{e}^{\left(\frac{sb}{c_m}\right)} - B_{m,n}\mathrm{e}^{\left(\frac{-sb}{c_m}\right)}\right]. \tag{2.17}$$

For $\xi^{\pm}_m = \mathrm{e}^{\left(\pm\frac{sb}{c_m}\right)}, \chi^{\pm}_{m,n} = \mathrm{e}^{\left(\pm\frac{s\Delta l_n}{c_m}\right)}$, the expressions for the force and the velocity amplitudes at the spacer damper clamp can be written as

$$\widehat{F}^{-}_{m,n} = -\frac{T_m s}{c_m}\left(A_{m,n}\chi^{+}_{m,n}\xi^{-}_m - B_{m,n}\chi^{-}_{m,n}\xi^{+}_m\right), \tag{2.18}$$

$$\widehat{F}^{+}_{m,n+1} = \frac{T_m s}{c_m}\left(A_{m,n+1}\xi^{+}_m - B_{m,n+1}\xi^{-}_m\right), \tag{2.19}$$

and

$$\widehat{\dot{w}}_{m,n}\Big|_{x_n=(\Delta l_n - b)} = s\left(A_{m,n}\chi^{+}_{m,n}\xi^{-}_m + B_{m,n}\chi^{-}_{m,n}\xi^{+}_m\right), \tag{2.20}$$

$$\widehat{\dot{w}}_{m,n+1}\Big|_{x_{n+1}=b} = s\left(A_{m,n+1}\xi^{+}_m + B_{m,n+1}\xi^{-}_m\right). \tag{2.21}$$

Equations (2.18) and (2.19) express the forces as a product of the tension and the slope; whereas (2.13) expresses them as a product of the velocity and the impedance. Let us only consider the first element of the force vector from (2.13)

$$\widehat{F}^{-}_{1,n} = [Z_{1,1} \quad Z_{1,2} \quad \dots \quad Z_{1,4M}]\, \widehat{\dot{\mathbf{w}}}_n, \tag{2.22}$$

and the same element from (2.18) is

$$\widehat{F}^{-}_{1,n} = -\frac{T_1 s}{c_1}\left(A_{1,n}\chi^{+}_{1,n}\xi^{-}_{1} - B_{1,n}\chi^{-}_{1,n}\xi^{+}_{1}\right). \tag{2.23}$$

Since (2.22) and (2.23) show the same clamp force $\widehat{F}^{-}_{1,n}$, equating their right hand terms and rearranging them results in

$$\begin{aligned} 0 \;=\; & A_{1,n}\chi^{+}_{1,n}\xi^{-}_{1}\left(Z_{1,1} + \frac{T_1}{c_1}\right) + B_{1,n}\chi^{-}_{1,n}\xi^{+}_{1}\left(Z_{1,1} - \frac{T_1}{c_1}\right) \\ & +(A_{2,n}\chi^{+}_{2,n}\xi^{-}_{2} + B_{2,n}\chi^{-}_{2,n}\xi^{+}_{1})Z_{1,2} \\ & +(A_{1,n+1}\chi^{+}_{1,n+1}\xi^{-}_{1} + B_{1,n+1}\chi^{-}_{1,n+1}\xi^{+}_{1})Z_{1,3} \\ & +(A_{2,n+1}\chi^{+}_{2,n+1}\xi^{-}_{2} + B_{2,n+1}\chi^{-}_{2,n+1}\xi^{+}_{1})Z_{1,4} \\ & \quad \vdots \\ & +(A_{2M,n+1}\chi^{+}_{2M,n+1}\xi^{-}_{2M} + B_{2M,n+1}\chi^{-}_{2M.n+1}\xi^{+}_{2M})Z_{1,4M}. \end{aligned} \tag{2.24}$$

Similarly the other clamp forces of the n-th spacer damper can also be obtained by equating other elements of (2.18), (2.19) and (2.13). Similar equations can be obtained using the other force vector elements. Corresponding to each spacer damper one will have $4M$ equations of this type. Hence, N-spacer dampers will result in $4MN$ equations. From the boundary conditions in (2.9) and (2.10) one additionally has $4M$ equations (i.e., $2M$-equations for the left-end boundary and $2M$ equations for the right-end boundary). These $4M$ equations from boundary conditions assembled together with $4MN$ equations from the force compatibility at the spacer damper clamps result in the set of equations

$$\mathbf{J}(s)\mathbf{a} = \mathbf{0}, \tag{2.25}$$

where

$$\begin{aligned} \mathbf{a} = \langle & A_{1,1}, B_{1,1}, A_{2,1}, B_{2,1}, ..., A_{2M,1}, B_{2M,1}, ..., \\ & A_{1,v}, B_{1,v}, A_{2,v}, B_{2,v}, ..., A_{2M,v}, B_{2M,v}, ..., \\ & A_{1,N+1}, B_{1,N+1}, A_{2,N+1}, B_{2,N+1}, ..., A_{2M,N+1}, B_{2M,N+1}\rangle^{T}. \end{aligned} \tag{2.26}$$

Since the matrix $\mathbf{J}(s)$ contains the system parameters we will refer to it as the *system matrix*. the system matrix for a conductor bundle system with N spacer dampers has the following form

$$\mathbf{J}(s) = \left[\begin{array}{l} \mathbf{L} \leftarrow \text{Due to left boundary } (2M \times 4M) \\ \mathbf{S}_1 \\ \quad \mathbf{S}_2 \\ \quad\quad \ddots \\ \quad\quad\quad \mathbf{S}_n \\ \quad\quad\quad\quad \ddots \\ \text{Due to } n\text{-th spacer damper } (4M \times 8M) \quad\quad \mathbf{S}_N \\ \text{Due to right boundary } (2M \times 4M) \rightarrow \mathbf{R} \end{array}\right], \tag{2.27}$$

where $\mathbf{L}$ and $\mathbf{R}$ are the matrices due to left and right boundary conditions, each of size $2M \times 4M$; and $\mathbf{S}_1, \mathbf{S}_2, ..., \mathbf{S}_n$ are due to the inclusion of spacer dampers, each having a size of $4M \times 8M$. Eventually the complete size of the system matrix is $4M(N+1)$. Different elements of the system matrix $\mathbf{L}$, $\mathbf{S}_n$ and $\mathbf{R}$ are shown below. The matrix $\mathbf{L}$ corresponds to the left-end homogeneous boundary conditions and has the form

$$\mathbf{L} = \begin{bmatrix} 1 & 1 & 0 & 0 & \dots & 0 & 0 & 0 & 0 \\ 1 & 1 & 0 & 0 & \dots & 0 & 0 & 0 & 0 \\ 0 & 0 & 1 & 1 & \dots & 0 & 0 & 0 & 0 \\ \vdots & \vdots & \vdots & \vdots & \ddots & \vdots & \vdots & \vdots & \vdots \\ 0 & 0 & 0 & 0 & \dots & 1 & 1 & 0 & 0 \\ 0 & 0 & 0 & 0 & \dots & 0 & 0 & 1 & 1 \end{bmatrix}. \tag{2.28}$$

The complex matrix $\mathbf{S}_n$ emerges because of the presence of the n-th spacer damper, and has the form

$$\begin{aligned} \mathbf{S}_n = [\mathbf{P}_{1,n}\ \mathbf{P}_{2,n}\ ...\ \mathbf{P}_{p,n}\ .....\ \mathbf{Q}_{3,n}\ \mathbf{Q}_{4,n}\ ...\ \mathbf{Q}_{q,n}\ .....], \\ \forall\ p = 1, 2, 5, 6, 9, 10, ..., (4M-3), (4M-2), \\ \forall\ q = 3, 4, 7, 8, 11, 12, ..., (4M–1), 4M \end{aligned} \tag{2.29}$$

where

$$\mathbf{P}_{p,n} = \begin{bmatrix} \chi^+_{p,n}\xi^-_p\left(Z_{1,p} + \frac{T_1}{c_1}\delta_{1p}\right) & \chi^-_{p,n}\xi^+_p\left(Z_{1,p} - \frac{T_1}{c_1}\delta_{1p}\right) \\ \chi^+_{p,n}\xi^-_p\left(Z_{2,p} + \frac{T_2}{c_2}\delta_{2p}\right) & \chi^-_{p,n}\xi^+_p\left(Z_{2,p} - \frac{T_2}{c_2}\delta_{2p}\right) \\ \chi^+_{p,n}\xi^-_p Z_{3,p} & \chi^-_{p,n}\xi^+_p Z_{3,p} \\ \chi^+_{p,n}\xi^-_p Z_{4,p} & \chi^-_{p,n}\xi^+_p Z_{4,p} \\ \chi^+_{p,n}\xi^-_p\left(Z_{5,p} + \frac{T_5}{c_5}\delta_{5p}\right) & \chi^-_{p,n}\xi^+_p\left(Z_{5,p} - \frac{T_5}{c_5}\delta_{5p}\right) \\ \chi^+_{p,n}\xi^-_p\left(Z_{6,p} + \frac{T_6}{c_6}\delta_{6p}\right) & \chi^-_{p,n}\xi^+_p\left(Z_{6,p} - \frac{T_6}{c_6}\delta_{6p}\right) \\ \vdots & \vdots \\ \chi^+_{p,n}\xi^-_p Z_{4M-1,p} & \chi^-_{p,n}\xi^+_p Z_{4M-1,p} \\ \chi^+_{p,n}\xi^-_p Z_{4M,p} & \chi^-_{p,n}\xi^+_p Z_{4M,p} \end{bmatrix}, \tag{2.30}$$

and

$$\mathbf{Q}_{q,n} = \begin{bmatrix} \xi_q^+ Z_{1,q} & \xi_q^- Z_{1,q} \\ \xi_q^+ Z_{2,q} & \xi_q^- Z_{2,q} \\ \xi_q^+ \left(Z_{3,q} - \frac{T_3}{c_3}\delta_{3q}\right) & \xi_q^- \left(Z_{3,q} + \frac{T_3}{c_3}\delta_{3q}\right) \\ \xi_q^+ \left(Z_{4,q} - \frac{T_4}{c_4}\delta_{4q}\right) & \xi_q^- \left(Z_{4,q} + \frac{T_4}{c_4}\delta_{4q}\right) \\ \xi_q^+ Z_{5,q} & \xi_q^- Z_{5,q} \\ \xi_q^+ Z_{6,q} & \xi_q^- Z_{6,q} \\ \vdots & \vdots \\ \xi_q^+ \left(Z_{4M-1,q} - \frac{T_{4M-1}}{c_{4M-1}}\delta_{(4M-1)q}\right) & \xi_q^- \left(Z_{4M-1,q} + \frac{T_{4M-1}}{c_{4M-1}}\delta_{(4M-1)q}\right) \\ \xi_q^+ \left(Z_{4M,q} - \frac{T_{4M}}{c_{4M}}\delta_{(4M)q}\right) & \xi_q^- \left(Z_{4M,q} + \frac{T_{4M}}{c_{4M}}\delta_{(4M)q}\right) \end{bmatrix}. \quad (2.31)$$

Matrix $\mathbf{R}$ corresponds to the right-end homogeneous boundary conditions and is a complex matrix having the form

$$\mathbf{R} = \begin{bmatrix} \chi_{1,n+1}^+ & \chi_{1,n+1}^- & 0 & 0 & \dots & 0 & 0 \\ 0 & 0 & \chi_{2,n+1}^+ & \chi_{2,n+1}^- & \cdots & 0 & 0 \\ \vdots & \vdots & \vdots & \vdots & \ddots & \vdots & \vdots \\ 0 & 0 & 0 & 0 & \dots & 0 & 0 \\ 0 & 0 & 0 & 0 & \dots & \chi_{2M,n+1}^+ & \chi_{2M,n+1}^- \end{bmatrix}. \quad (2.32)$$

2.1.3 Incorporating the Stockbridge dampers

In long-span conductor bundles with many spacer dampers, the probability of "localized modes" is higher. Attaching groups of in-span STOCKBRIDGE dampers, in addition to the spacer dampers, proves to be an effective mean to withhold the higher local amplitudes in the subconductors. The inclusion of additional STOCKBRIDGE damper is modeled in this section. In order to keep the modeling simple and understandable, let us first assume that wherever STOCKBRIDGE dampers are attached to the subconductors, one damper is fastened to each subconductor at the same location. This means that STOCKBRIDGE dampers are mounted as groups of M dampers, as shown in figure 2.4. Let us, for the moment, treat a group of M STOCKBRIDGE dampers as one system, and depending upon its location on the span, the corresponding $\mathbf{S_n}$ matrix in (2.27) will be updated. In what follows, the updated $\mathbf{S_n}$ matrix for a group of STOCKBRIDGE dampers is formulated.

A STOCKBRIDGE damper is primarily effective in suppressing the vertical oscillations only. Although it also has a limited direct effect on the horizontal oscillations, this effect is neglected here. At the point of attachment of the STOCKBRIDGE damper the displacement compatibility will be fulfilled in the horizontal and the vertical plane. Considering the negligible clamp width of the STOCKBRIDGE damper, the displacement compatibility gives the following set of equations

$$w_{m_1,v}(\Delta l_v, t) = w_{m_1,v+1}(0,t), \qquad \forall \quad m_1 = 1,3,5,...,(2M-1) \quad (2.33)$$

$$w_{m_2,v}(\Delta l_v, t) = w_{m_2,v+1}(0,t), \qquad \forall \quad m_2 = 2,4,8,...,2M. \quad (2.34)$$

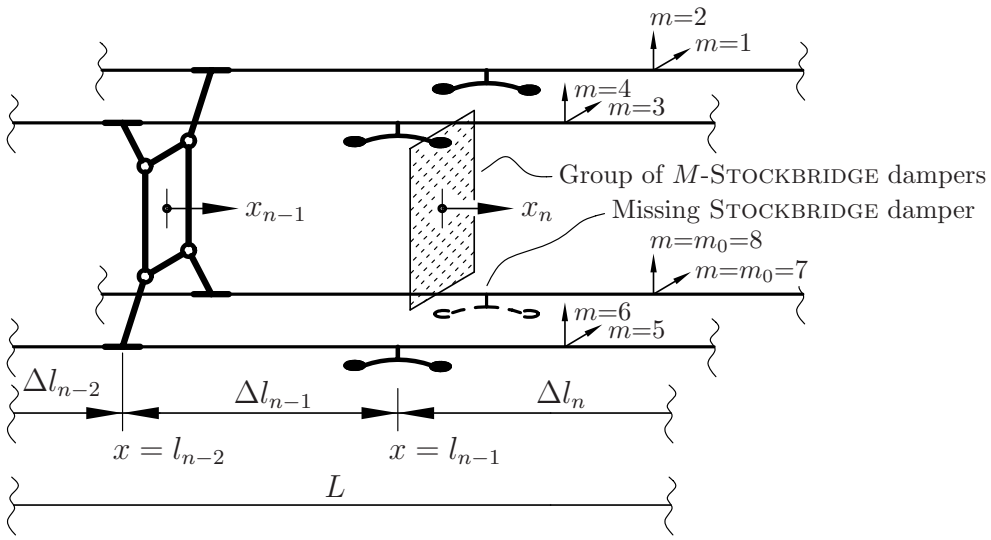

Figure 2.4: Schematic diagram of a quad bundle with Stockbridge damper groups

Here, m_1 and m_2 are the indices corresponding to the horizontal and the vertical plane respectively. Equations (2.33) and (2.34) respectively give

$$A_{m_1,v}\mathrm{e}^{\frac{s\Delta l_v}{c_{m_1}}} + B_{m_1,v}\mathrm{e}^{\frac{-s\Delta l_v}{c_{m_1}}} - A_{m_1,v+1} - B_{m_1,v+1} = 0, \tag{2.35}$$

$$A_{m_2,v}\mathrm{e}^{\frac{s\Delta l_v}{c_{m_2}}} + B_{m_2,v}\mathrm{e}^{\frac{-s\Delta l_v}{c_{m_2}}} - A_{m_2,v+1} - B_{m_2,v+1} = 0. \tag{2.36}$$

The force compatibilities at the point of damper attachments must also be fulfilled in the horizontal as well as in the vertical plane. In the horizontal plane, since the Stockbridge damper is assumed to be ineffective, it will exert no additional force on the conductor[5]. In the horizontal plane, forces from the conductor tensions will simply be equal for left and right subspans at the damper attachment points, i.e.,

$$T_{m_1} w'_{m_1,v}(\Delta l_v, t) = T_{m_1} w'_{m_1,v+1}(0, t). \qquad \forall \quad m_1 = 1, 3, 5, ..., (2M-1) \tag{2.37}$$

which leads to

$$A_{m_1,v}\mathrm{e}^{\frac{s\Delta l_v}{c_{m_1}}} - B_{m_1,v}\mathrm{e}^{\frac{-s\Delta l_v}{c_{m_1}}} - A_{m_1,v+1} + B_{m_1,v+1} = 0. \tag{2.38}$$

In the vertical plane, the Stockbridge damper exerts a complex external force ($f_D(t) = \hat{F}_D \mathrm{e}^{st}$). The complex amplitude of this force $\hat{F}_D$ is defined using the complex impedance $Z_D(s)$ of the Stockbridge damper, as shown in [67]. It relates the harmonic damper clamp force f_D and the harmonic damper clamp velocity ($\dot{w}_D = \mathbf{Re}\,[sW_D\mathrm{e}^{st}]$) according to the relation

$$f_D(t) = Z_D \dot{w}_D(x_D, t), \tag{2.39}$$

where $\hat{F}_D$ and W_D are the complex amplitudes of the force and the displacement at the damper clamp. The complex representation used in (2.39) takes into account the

[5]Here it is assumed that the mass of the Stockbridge damper in small compared to the mass per unit length of subconductors.

phase angle between the force and the velocity at the damper clamp. For the force equilibrium in the vertical plane at the damper attachment points, the damper force f_D should be compatible with the forces from the conductor tensions, i.e.,

$$T_{m_2}\left[w'_{m_2,v+1}(0,t) - w'_{m_2,v}(\Delta l_v, t)\right] = Z_D(s)\dot{w}_{m_2,v+1}(0,t), \quad \forall m_2 = \ 2,4,6,...,2M \tag{2.40}$$

which finally leads to

$$A_{m_2,v}\mathrm{e}^{\frac{s\Delta l_v}{c_{m_2}}} - B_{m_2,v}\mathrm{e}^{\frac{-s\Delta l_v}{c_{m_2}}} + A_{m_2,v+1}\left[\frac{Z_D c_{m_2}}{T_{m_2}} - 1\right] + B_{m_2,v+1}\left[\frac{Z_D c_{m_2}}{T_{m_2}} + 1\right] = 0. \tag{2.41}$$

Assembling (2.35), (2.36), (2.38) and (2.41) gives the $\mathbf{S_n}$ matrix for the n-th group of M Stockbridge dampers, one attached to each subconductor. The matrix $\mathbf{S_n}$ for such a system consists of two matrices $\mathbf{S_{n_1}}$ and $\mathbf{S_{n_2}}$, each of size $4M \times 4M$,

$$\mathbf{S_n} = \left[\mathbf{S_{n_1}} \quad \mathbf{S_{n_2}}\right], \tag{2.42}$$

where

$$\mathbf{S_{n_1}} = \begin{bmatrix} \Lambda^+_{1,n} & \Lambda^-_{1,n} & 0 & 0 & 0 & 0 & \dots & 0 & 0 \\ \Lambda^+_{1,n} & -\Lambda^-_{1,n} & 0 & 0 & 0 & 0 & \dots & 0 & 0 \\ 0 & 0 & \Lambda^+_{2,n} & \Lambda^-_{2,n} & 0 & 0 & \dots & 0 & 0 \\ 0 & 0 & \Lambda^+_{2,n} & -\Lambda^-_{2,n} & 0 & 0 & \dots & 0 & 0 \\ 0 & 0 & 0 & 0 & \Lambda^+_{3,n} & \Lambda^-_{3,n} & \dots & 0 & 0 \\ 0 & 0 & 0 & 0 & \Lambda^+_{3,n} & -\Lambda^-_{3,n} & \dots & 0 & 0 \\ \vdots & \vdots & \vdots & \vdots & \vdots & \vdots & \ddots & \vdots & \vdots \\ 0 & 0 & 0 & 0 & 0 & 0 & \dots & \Lambda^+_{2M,n} & \Lambda^-_{2M,n} \\ 0 & 0 & 0 & 0 & 0 & 0 & \dots & \Lambda^+_{2M,n} & -\Lambda^-_{2M,n} \end{bmatrix}, \tag{2.43}$$

and

$$\mathbf{S_{n_2}} = \begin{bmatrix} -1 & -1 & 0 & 0 & 0 & 0 & 0 & 0 & \dots & 0 & 0 \\ -1 & 1 & 0 & 0 & 0 & 0 & 0 & 0 & \dots & 0 & 0 \\ 0 & 0 & -1 & -1 & 0 & 0 & 0 & 0 & \dots & 0 & 0 \\ 0 & 0 & \Gamma^-_2 & \Gamma^+_2 & 0 & 0 & 0 & 0 & \dots & 0 & 0 \\ 0 & 0 & 0 & 0 & -1 & -1 & 0 & 0 & \dots & 0 & 0 \\ 0 & 0 & 0 & 0 & -1 & 1 & 0 & 0 & \dots & 0 & 0 \\ 0 & 0 & 0 & 0 & 0 & 0 & -1 & -1 & \dots & 0 & 0 \\ 0 & 0 & 0 & 0 & 0 & 0 & \Gamma^-_4 & \Gamma^+_4 & \dots & 0 & 0 \\ \vdots & \vdots & \vdots & \vdots & \vdots & \vdots & \vdots & \vdots & \ddots & \vdots & \vdots \\ 0 & 0 & 0 & 0 & 0 & 0 & 0 & 0 & \dots & -1 & -1 \\ 0 & 0 & 0 & 0 & 0 & 0 & 0 & 0 & \dots & \Gamma^-_{2M} & \Gamma^+_{2M} \end{bmatrix}, \tag{2.44}$$

with

$$\Lambda_{m,n}^{\pm} = \mathrm{e}^{\frac{\pm s\Delta l_n}{c_m}}, \text{ and } \quad \Gamma_m^{\pm} = \left[\frac{Z_D c_m}{T_m} \pm 1\right]. \tag{2.45}$$

Once having obtained the $\mathbf{S_n}$ matrix corresponding to a group of STOCKBRIDGE dampers, (2.42) can simply be modified if the STOCKBRIDGE dampers are attached only at fewer subconductors than M. For example in the figure 2.4 one damper is missing in the group of STOCKBRIDGE dampers. In such a case, the only change will be in the $\mathbf{S_{n_2}}$ part of the matrix shown in (2.44). For the subconductor (e.g., the fourth subconductor in figure 2.4) in which there is no STOCKBRIDGE damper, the corresponding damper-impedance Z_D can simply be equated to zero. Hence, corresponding to such a group of STOCKBRIDGE dampers $\mathbf{S_n}$ is generated using

$$\Lambda_{m,n}^{\pm} = \mathrm{e}^{\frac{\pm s\Delta l_n}{c_m}}, \text{ and } \quad \Gamma_m^{\pm} = \begin{cases} \left[\frac{Z_D c_m}{T_m} \pm 1\right] & \text{for } m \neq m_0 \\ \\ \pm 1 & \text{for } m = m_0 \end{cases} \tag{2.46}$$

where m_0 is the index of the subconductor which does not carry a STOCKBRIDGE damper.

2.2 Different orientations of the spacer dampers

When designing a transmission line system, consideration is given to the total number and also to the number of different types of damping devices. It is always preferred to use the same type of spacer/spacer-damper in order to reduce the overall cost of the project. Sometimes more economical twin spacer dampers are used in quad conductor bundles, oriented in such a way that they have an overall effect of a quad spacer damper. To achieve this, groups of two twin-spacer dampers are attached alternately in the horizontal plane and in the vertical plane in a quad conductor bundle, as shown in figure 2.5. Such a configuration can easily be incorporated in the mathematical model by changing the corresponding impedance matrix $\mathbf{Z_n}$ for the spacer dampers at the n-th location. One can easily generate the local impedance matrix of a two armed spacer damper with the same procedure as shown in appendix B. Let $\mathbf{Z}_{ht}$ be the impedance matrix for a twin spacer damper attached horizontally, and $\mathbf{Z}_{vt}$ be the impedance matrix when it is attached vertically to the subconductors (e.g., figure 2.5). Reassembling two such impedance matrices one can easily generate a new impedance matrix which corresponds to the group of these two twin-spacer dampers. Let $\mathbf{Z}_{hq}$ be the impedance matrix of two twin spacer dampers when they are horizontally attached on the quad conductor bundle and $\mathbf{Z}_{vq}$ be the impedance matrix for the group when they are attached vertically. Obviously, $\mathbf{Z}_{ht}$ and $\mathbf{Z}_{vt}$ are of dimension 8×8, and $\mathbf{Z}_{hq}$ and $\mathbf{Z}_{vq}$ are of dimension 16×16.

We first consider the case when the twin spacer damper group is attached horizontally on the conductor bundle. The impedance matrix of each individual twin spacer damper in this group is divided into four square matrices each of size 4×4 as

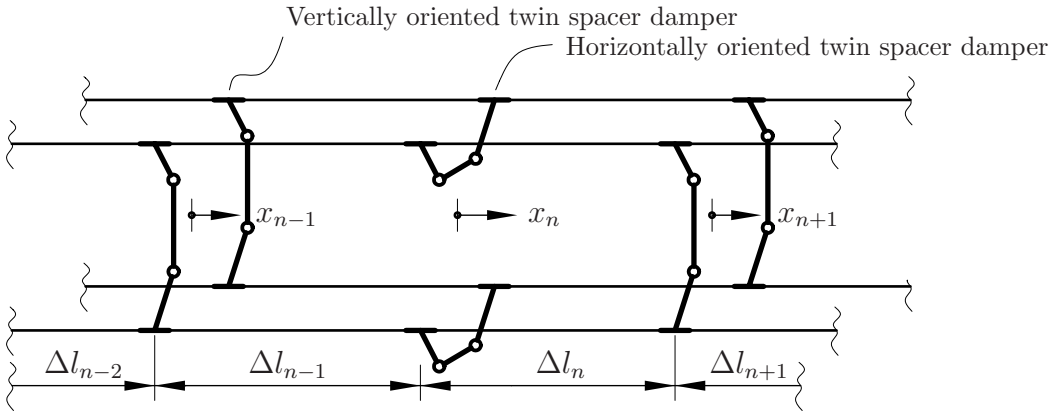

Figure 2.5: Alternate vertically and horizontally oriented twin spacer dampers attached on the quad conductor bundle

$$\mathbf{Z}_{ht}^{i} = \begin{bmatrix} \mathbf{Z}_{ht,11}^{i} & \mathbf{Z}_{ht,12}^{i} \\ \mathbf{Z}_{ht,21}^{i} & \mathbf{Z}_{ht,22}^{i} \end{bmatrix}, \qquad i = 1, 2 \tag{2.47}$$

with $i = 1$ for the upper twin-spacer damper (in the positive z-direction) and $i = 2$ for the lower twin-spacer damper (in the negative z-direction), where

$$\mathbf{Z}_{ht,11}^{i} = \begin{bmatrix} Z_{ht}^{i}(1,1) & \dots & Z_{ht}^{i}(1,4) \\ Z_{ht}^{i}(2,1) & \dots & Z_{ht}^{i}(2,4) \\ \vdots & \ddots & \vdots \\ Z_{ht}^{i}(4,1) & \dots & Z_{ht}^{i}(4,4) \end{bmatrix}, \; \mathbf{Z}_{ht,12}^{i} = \begin{bmatrix} Z_{ht}^{i}(1,5) & \dots & Z_{ht}^{i}(1,8) \\ Z_{ht}^{i}(2,5) & \dots & Z_{ht}^{i}(2,8) \\ \vdots & \ddots & \vdots \\ Z_{ht}^{i}(4,5) & \dots & Z_{ht}^{i}(4,8) \end{bmatrix},$$
$$\mathbf{Z}_{ht,21}^{i} = \begin{bmatrix} Z_{ht}^{i}(5,1) & \dots & Z_{ht}^{i}(5,4) \\ Z_{ht}^{i}(6,1) & \dots & Z_{ht}^{i}(6,4) \\ \vdots & \ddots & \vdots \\ Z_{ht}^{i}(8,1) & \dots & Z_{ht}^{i}(8,4) \end{bmatrix}, \; \mathbf{Z}_{ht,22}^{i} = \begin{bmatrix} Z_{ht}^{i}(5,5) & \dots & Z_{ht}^{i}(5,8) \\ Z_{ht}^{i}(6,5) & \dots & Z_{ht}^{i}(6,8) \\ \vdots & \ddots & \vdots \\ Z_{ht}^{i}(8,5) & \dots & Z_{ht}^{i}(8,8) \end{bmatrix}. \tag{2.48}$$

The impedance matrix corresponding to a quad spacer damper equivalent of a combination of two twin-bundles attached horizontally to the conductors, as shown in figure 2.5, is

$$\mathbf{Z}_{qh} = \begin{bmatrix} \mathbf{Z}_{ht,11}^{1} & \mathbf{Z}_{ht,12}^{1} & \mathbf{0} & \mathbf{0} \\ \mathbf{Z}_{ht,21}^{1} & \mathbf{Z}_{ht,22}^{1} & \mathbf{0} & \mathbf{0} \\ \mathbf{0} & \mathbf{0} & \mathbf{Z}_{ht,22}^{2} & \mathbf{Z}_{ht,21}^{2} \\ \mathbf{0} & \mathbf{0} & \mathbf{Z}_{ht,12}^{2} & \mathbf{Z}_{ht,11}^{2} \end{bmatrix}, \tag{2.49}$$

where $\mathbf{0}$ is a zero-matrix of size 4×4.

Similarly, when the twin-spacer dampers are attached vertically to the conductor bundles, then one needs to first generate the impedance matrices for individual twin spacer dampers using the procedure shown in appendix B. Let the impedance matrix for the first spacer damper (in positive y-direction) be $\mathbf{Z}^1_{vt}$ and the for the second spacer damper (in negative y-direction) be $\mathbf{Z}^2_{vt}$. The impedance matrix of each individual twin spacer damper in this group can be divided into four square matrices in the similar way as shown in (2.47):

$$\mathbf{Z}^i_{vt} = \begin{bmatrix} \mathbf{Z}^i_{vt,11} & \mathbf{Z}^i_{vt,12} \\ \mathbf{Z}^i_{vt,21} & \mathbf{Z}^i_{vt,22} \end{bmatrix}, \qquad i = 1, 2 \tag{2.50}$$

where $i = 1$ is for the spacer damper in the positive y-direction and $i = 2$ is for the damper attached in the negative y-direction. The impedance matrix corresponding to a group of two twin-bundles attached vertically to the quad conductor bundle as shown in figure 2.5, is

$$\mathbf{Z}_{qv} = \begin{bmatrix} \mathbf{Z}^1_{vt,11} & \mathbf{0} & \mathbf{0} & \mathbf{Z}^1_{vt,12} \\ \mathbf{0} & \mathbf{Z}^2_{vt,11} & \mathbf{Z}^2_{vt,12} & \mathbf{0} \\ \mathbf{0} & \mathbf{Z}^2_{vt,21} & \mathbf{Z}^2_{vt,22} & \mathbf{0} \\ \mathbf{Z}^1_{vt,21} & \mathbf{0} & \mathbf{0} & \mathbf{Z}^1_{vt,22} \end{bmatrix}, \tag{2.51}$$

with $\mathbf{0}$ again being a zero-matrix of size 4×4.

After having obtained the corresponding impedance matrices for the groups of twin spacer dampers as shown in (2.49) and (2.51), $\mathbf{S_n}$ can now be generated using (2.29)-(2.31).

2.3 Transcendental eigenvalue problem (TEVP)

In order to obtain the values of the integration constants $A_{m,v}$, $B_{m,v}$ with $m = 1, 2, ..., 2M$, $v = 1, 2, ..., (N + 1)$ of (2.26) one needs to solve the homogeneous set of $4M(N + 1)$ non-polynomial equations, of the form (2.25) as an eigenvalue problem. It is to be noted from the constitution of the system matrix that its elements are *transcendental functions* of the spectral parameter s, and so will be the values of the integration constants $A_{m,v}$ and $B_{m,v}$. The parameter s is a complex number ($s = -\delta + \mathrm{i}\omega$), where the imaginary part (i.e., ω) represents a circular frequency and the real part (i.e., δ) represents a decay coefficient.

Since the elements of the system matrix can not be exactly written in the form of polynomials, they are non-polynomial functions of the parameter s. Hence, the degree of the eigenvalue problem in (2.25) is infinite, and consequently so is the number of system eigenvalues. However, we are interested in obtaining only few system eigenvalues in the frequency range where vortex shedding prevails (i.e., $\approx 3 - 150$ Hz [14, 66]). Numerical iteration techniques need to be used in order to obtain the eigenvalues and the eigenfunctions of (2.25). Different solution techniques and detailed comparisons of the obtained results are discussed in Chapter-3.

Chapter 3

Solution of the transcendental eigenvalue problem (TEVP)

Summary: This chapter explains the solution of the transcendental eigenvalue problem (TEVP) that appeared in (2.25), after the mathematical-mechanical modeling of the conductor bundle. Section 3.1 describes the standard eigenvalue problem and its different forms. Section 3.2 gives details on the non-polynomial TEVP. Section 3.3 gives an overview of the solution techniques which are used for the non-polynomial TEVP. In the current work three solution techniques are compared by solving an representative conductor bundle problem, which is shown in the section 3.6.1. NEWTON*'s approach is found to be an efficient solution technique for the TEVP of the current type. After obtaining the complex eigenvalues s, corresponding eigenvectors are obtained.*

3.1 Introduction

Large-scale problems of engineering and scientific computing often require solutions of eigenvalue and related problems. The algebraic eigenvalue problem refers to finding a set of characteristic values associated with a matrix or matrices. Eigenvalues and eigenvectors are important, when the corresponding equations model a physical situation. The eigenvalue problem (EVP) can take several different forms. A small introduction to the standard eigenvalue problem and its different forms are presented in this section.

3.1.1 Standard EVP

Consider a matrix $\mathbf{A} \in \mathcal{C}^{n\times n}$. The standard (or *linear* or *algebraic*) EVP is the determination of those values of λ for which the set of n homogeneous linear equations in n unknowns [68]

$$\mathbf{A}\mathbf{x} = \lambda\mathbf{x}, \tag{3.1}$$

has a nontrivial solution. Equation (3.1) may be written in the form

$$(\mathbf{A} - \lambda\mathbf{I})\mathbf{x} = 0, \tag{3.2}$$

and for arbitrary λ this set of equation has only the solution $\mathbf{x} = 0$. The general theory of simultaneous equations shows that there is a nontrivial solution if, and only if the matrix $(\mathbf{A} - \lambda\mathbf{I})$ is singular, i.e.

$$\det(\mathbf{A} - \lambda\mathbf{I}) = 0. \tag{3.3}$$

The determinant of the left hand side of (3.3) gives the explicit polynomial equation

$$\alpha_0 + \alpha_1\lambda + ... + \alpha_{n-1}\lambda^{n-1} + (-1)^n\lambda^n = 0. \tag{3.4}$$

(3.4) is called as the *characteristic equation* of the matrix $\mathbf{A}$ and the polynomial on the left hand side of (3.4) is called the *characteristic polynomial*. Since coefficient of λ^n is not zero, (3.4) has n roots. In general the roots are complex and are called *eigenvalues*, *latent roots*, *characteristic values* or *proper values* of the matrix $\mathbf{A}$. Corresponding to any eigenvalue λ, the set of equations (3.2) has at least one nontrivial solution $\mathbf{x}$. Such a solution is called *eigenvector*, *latent vector*, *characteristic vector* or *proper vector* corresponding to that eigenvalue. A pair $(\mathbf{x}, \lambda)$ satisfying relation (3.2) is called an *eigenpair* of the matrix $\mathbf{A}$. It is evident that if $\mathbf{x}$ is a solution of (3.2), then $k\mathbf{x}$ is also a solution for any value of k, the eigenvector corresponding to λ is arbitrary to the extent of a constant multiplier. It is convenient to choose this multiplier so that the eigenvector has some desirable numerical property, and such vectors are called *normalized* vectors.

3.1.2 Forms of standard EVP

This section shows different forms of EVP's which are convertible to the standard EVP. Solution techniques which are used for the standard EVP, can also be adopted for solving these different forms.

Generalized EVP

If $\mathbf{A}, \mathbf{B} \in \mathcal{C}^{n\times n}$ are nonsingular matrices, generalized EVP's are of the form $\mathbf{Ax} = \lambda\mathbf{Bx}$. Such problems are very common in the structural analysis. The pair $(\mathbf{A}, \mathbf{B})$ is often called as *matrix pencil*. Generalized EVP can be transformed into standard EVP as

$$\mathbf{Ax} = \lambda\mathbf{Bx} \quad \Longrightarrow \quad \mathbf{B}^{-1}\mathbf{Ax} = \lambda\mathbf{x}. \tag{3.5}$$

In practice, matrix $\mathbf{B}^{-1}\mathbf{A}$ is never obtained. Instead, $\mathbf{y} = \mathbf{B}^{-1}\mathbf{Ax}$ is computed by solving the system of linear equations $\mathbf{By} = \mathbf{u}$, where $\mathbf{u} = \mathbf{Ax}$.

Quadratic EVP

If $\mathbf{A}, \mathbf{B}, \mathbf{C} \in \mathcal{C}^{n\times n}$ are nonsingular matrices, one defines the matrix equation

$$\left[\lambda^2\mathbf{A} + \lambda\mathbf{B} + \mathbf{C}\right]\mathbf{x} = \mathbf{0}, \tag{3.6}$$

as *quadratic EVP* of the order n. Clearly the characteristic polynomial is of degree n^2 and there are $2n$ possible eigenvalues. Such problems are common in the nonclassically damped systems. The quadratic EVP can also be transformed into a standard EVP as follows. Let

$$\lambda\mathbf{x} = \mathbf{y}. \tag{3.7}$$

From (3.6) we have

$$\lambda\mathbf{Ay} + \mathbf{By} + \mathbf{Cx} = \mathbf{0}. \tag{3.8}$$

Pre-multiplying (3.8) with $\mathbf{A}^{-1}$ gives,

$$\lambda \mathbf{A}^{-1}\mathbf{A}\mathbf{y} + \mathbf{A}^{-1}\mathbf{B}\mathbf{y} + \mathbf{A}^{-1}\mathbf{C}\mathbf{x} = \mathbf{0}, \tag{3.9}$$

or

$$-\mathbf{A}^{-1}\mathbf{C}\mathbf{x} - \mathbf{A}^{-1}\mathbf{B}\mathbf{y} = \lambda \mathbf{y}. \tag{3.10}$$

A new equivalent EVP can now be written from (3.7) and (3.10) as

$$\begin{bmatrix} \mathbf{0} & \mathbf{I} \\ -\mathbf{A}^{-1}\mathbf{C} & -\mathbf{A}^{-1}\mathbf{B} \end{bmatrix} \begin{pmatrix} \mathbf{x} \\ \mathbf{y} \end{pmatrix} = \lambda \begin{pmatrix} \mathbf{x} \\ \mathbf{y} \end{pmatrix}. \tag{3.11}$$

There are many other possible techniques mentioned in [69, 70, 71] to transform the quadratic EVP's in either the generalized or in the standard EVP form.

Matrix polynomials

If $\mathbf{A}_0, \mathbf{A}_1, ..., \mathbf{A}_l \in \mathcal{C}^{n\times n}$ are nonsingular matrices, an EVP using matrix polynomial is of the form

$$\mathbf{L}(\lambda)\mathbf{x} = \left[\sum_{i=0}^{l} \mathbf{A}_i \lambda^i\right] \mathbf{x} = \left[\mathbf{A}_0 + \lambda \mathbf{A}_1 ... + \lambda^l \mathbf{A}_l\right] \mathbf{x} = \mathbf{0}. \tag{3.12}$$

Equation (3.12) describes an eigenvalue problem of degree l. $\mathbf{L}(\lambda)$ is called the matrix polynomial of l-th degree. For $\mathbf{A}_l = \mathbf{I}$, $\mathbf{L}(\lambda)$ is said to be *monic*, whereas if $\mathbf{A}_0 = \mathbf{I}$ it is called to be *comonic* . Matrix polynomials often occur in differential equations with constant coefficients. If the size of $\mathbf{A}_i$ is $n \times n$, then $\mathbf{L}(\lambda)$ can be linearized by defining its *companion polynomial* $\mathbf{C}_L(\lambda)$ of size $nl \times nl$ as [72]

$$\mathbf{C}_L = \mathbf{S}_0 + \lambda \mathbf{S}_1, \tag{3.13}$$

if

$$\begin{bmatrix} \mathbf{L}(\lambda) & \mathbf{0} \\ \mathbf{0} & \mathbf{I}_{n(l-1)} \end{bmatrix} = \mathbf{E}(\lambda)\mathbf{C}_L(\lambda)\mathbf{F}(\lambda), \tag{3.14}$$

for some $nl \times nl$ matrix polynomials $\mathbf{E}(\lambda)$ and $\mathbf{F}(\lambda)$ with constant nonzero determinants. Matrices $\mathbf{S}_0$ and $\mathbf{S}_1$ are given by

$$\mathbf{S}_0 = \begin{bmatrix} \mathbf{0} & -\mathbf{I} & \mathbf{0} & \dots & \mathbf{0} \\ \mathbf{0} & \mathbf{0} & -\mathbf{I} & \dots & \mathbf{0} \\ \vdots & \vdots & \vdots & \ddots & \vdots \\ \mathbf{0} & \mathbf{0} & \mathbf{0} & \dots & -\mathbf{I} \\ \mathbf{A}_0 & \mathbf{A}_1 & \mathbf{A}_2 & \dots & \mathbf{A}_{l-1} \end{bmatrix}; \quad \text{and} \quad \mathbf{S}_1 = \begin{bmatrix} \mathbf{I} & \mathbf{0} & \dots & \mathbf{0} & \mathbf{0} \\ \mathbf{0} & \mathbf{I} & \dots & \mathbf{0} & \mathbf{0} \\ \vdots & \vdots & \ddots & \vdots & \vdots \\ \mathbf{0} & \mathbf{0} & \dots & \mathbf{I} & \mathbf{0} \\ \mathbf{0} & \mathbf{0} & \dots & \mathbf{0} & \mathbf{A}_l \end{bmatrix}. \tag{3.15}$$

It turns out that $\mathbf{C}_L(\lambda)$ is a linearization of $\mathbf{L}(\lambda)$, more detailed description of which can be found in [72]. In particular, every regular matrix polynomial has a linearization, though it is not unique. Thus, the l-th degree matrix polynomial problem in (3.12) is linearized to a standard or generalized EVP of size $nl \times nl$ as

$$\mathbf{C}_L(\lambda)\widetilde{\mathbf{x}} = \mathbf{0}. \tag{3.16}$$

Matrix of the transcendental form

Consider a matrix polynomial $\mathbf{T}(\lambda)$, the elements of which are transcendental functions of the parameter λ. We define the matrix polynomial as

$$\mathbf{T}(\lambda) = \sum_{i=0}^{\infty} \mathbf{A}_i \lambda^i = \mathbf{0}, \quad \forall \mathbf{A}_i \in \mathcal{C}^{n\times n}, \quad \lambda \in \mathcal{C}. \tag{3.17}$$

Now, if one wishes to linearize the matrix polynomial, it will be of size $\infty \times \infty$. Nevertheless, it is possible to truncate the polynomial by considering only the terms till certain degree, e.g., $\leq l$, then one can linearize the matrix polynomial to the size $nl \times nl$. However, in many cases it is not possible to truncate the series due to the high contributions from the higher order terms. For some cases such truncation might even be feasible, but linearization leads to very big matrices.

3.2 Nonlinear transcendental matrix

In the current case the nonlinear TEVP as shown in (2.25) is required to be solved, where $\mathbf{J}(s) \in \mathcal{C}^{[4M(N+1)]\times[4M(N+1)]}$ is the system matrix. The elements of $\mathbf{J}(s)$ in (2.27) are analytical functions of the complex spectral parameter s. It is not possible to expand the complicated exponential terms of the system matrix $\mathbf{J}(s)$ in a matrix polynomial form, as the one shown in the last section. Moreover, even if it could be done, one also would have required to include the empirical impedances of the STOCKBRIDGE dampers and of the spacer dampers, in the form of polynomials in s. Hence, we conclude that it is not possible to linearize the $\mathbf{J}(s)$ to a standard or a generalized EVP. Specialized solution techniques are, therefore, required for the current type of nonlinear non-polynomial EVP.

3.3 Solution of the nonlinear TEVP

Many classical methods are available for solving the linear eigenvalue problems, such as the power method, spectral transformation, inverse iterations, shift-and-inverse, the QR-method, explicitly or implicitly shifted QR-method, ARNOLDI factorization, explicitly or implicitly shifted ARNOLDI method, JACOBI-DAVIDSON method etc. [73, 74, 75, 76, 77, 78, 65, 79, 80, 81]. In the case of linear EVP, most of the useful algorithms are based on similarity transformations. In the case of nonlinear EVP, however, it is no longer possible to transform $\mathbf{J}(\lambda)$ into a condensed form (e.g., Hessenberg or tridiagonal), and therefore the very successful LR and QR algorithms [68] have no counterpart

for the nonlinear EVP. There is a variant of the QR algorithm that does not transform the matrix [82]. Starting with an algorithm proposed by KUBLANOVSKAJA [83, 84], RUHE [85] developed an algorithm for the nonlinear case. He showed that his approach was equivalent to a certain form of inverse iteration for the linear case, which was also shown by PARLETT and KAHAN [86]. Different solution techniques for nonlinear EVP have been discussed in detail in [87, 88]. Every method has its own advantages and limitations. They are useful for the solution of problems for certain classes of the involved matrices. Moreover, for the linear or the nonlinear polynomial EVP's, as the number of eigenvalues are finite it is comparatively easy to solve them. In contrast to it, for the nonlinear non-polynomial TEVP (e.g., in (2.25)), there is no generalized solution technique for the solution. Specially in the current case, when the behavior and the size of the system matrix is dependent on the number, locations and the types of damping devices (or other conductor fittings [89]) attached to the conductor bundle, it is difficult to find a generalized solution technique which can guarantee to find all system eigenvalues in the desired frequency domain.

The calculation of the eigenvalues for the transcendental non-polynomial EVP has benefited greatly from the WITTRICK-WILLIAMS (W-W) algorithm [90, 91, 92], because it enabled the development of many other logical procedures which guarantee the convergence to all the required eigenvalues with certainty and to any desired accuracy. The W-W algorithm is a reliable and efficient tool to obtain the real eigenvalues (natural frequencies in free vibration problems or critical load factors in buckling problems) of TEVP to any required accuracy, in contrast to other methods which can miss to find some eigenvalues. The algorithm does not directly compute the eigenvalues, but instead simply finds the total number of eigenvalues below an arbitrarily given trial value. In this way the upper and the lower bounds are established on each required eigenvalue, after which various iterative procedures can be used to converge to the eigenvalue to the desired accuracy. An important feature of W-W algorithm is that it permits substructuring [90, 91, 92], including powerful multi-level sub-structuring [93, 94]. A recent advancement [95] uses the W-W algorithm extremely efficiently, which is analogous to the inverse iteration for the linear EVP. The procedures using W-W algorithms are limited only to self-adjoint matrices with real system eigenvalues. However, in the current case, the system matrix is not self-adjoint, and has complex system eigenvalues. Moreover, the calculation of the eigenvectors in W-W algorithms lacks the precision and the elegance which, on the other hand, are paramount requirements for the current case, as we are eventually interested in knowing the mode shapes of conductor bundle vibrations corresponding to each eigenvalue in order to compute the amplitudes and the strains.

Considering this, we now look for a method which can solve the nonlinear non-polynomial eigenvalue problem in a complex domain. Classically, a "determinant search method" is used to solve such problems, as mentioned in [34, 64]. Few simpler approaches are discussed by VERMA in [96, 39], which includes a new "alternate approach" by transforming the homogeneous set of transcendental equations in to a nonhomogeneous set. The alternate approach was found to be fast and very useful for the comparatively simpler problems of single conductor transmission lines, or of a bundle conductor with only very few spacer dampers attached. As shown later that for the vibration problems of conductor bundles, the system eigenfrequencies are very closely spaced in the complex

domain. Hence, with different iterative procedures it is very likely to miss many of the frequencies even for very closely spaced initial guesses, because the optimization functions are not good enough, as described in sections 3.3.1 and 3.3.2.

Taking advantage of closely spaced system eigenvalues of the transmission line bundle systems, an engineering approach was presented by VERMA, named as *continuous spectrum approach* [96, 39]. The continuous spectrum approach is very useful to obtain the *engineering solution* for a big conductor bundle attached with many spacer dampers attached. In case of the conductor bundles, it is always difficult to define the exact system parameters e.g., span length, location of the spacer dampers or the STOCKBRIDGE dampers on the conductors, conductor tensions etc. Apart from it, the wind velocity is another stochastic factor which varies even along the span of long span conductor bundles. Because of these uncertainties, the design of conductor bundle is always done for the worst possible conditions. Though, the continuous spectrum method does not predict the exact system frequencies or the exact mode shapes, it can, on the other hand, roughly estimate the maximum strains/stresses the conductors undergo in the course of their life span.

YANG [97] developed a NEWTON eigenvalue iteration method for solving nonlinear TEVP's, which was later used and further extended by SINGH and RAM [98] in order to obtain the solution of non-polynomial EVP's. SINGH and RAM in [98] presented a higher order approximation technique which leads to accelerated convergence. The technique is specially useful for systems where eigenvalues are very closely spaced, such as our system of conductor bundle. This technique is used in the current work and extended further, in section 3.3.4, to obtain the solution of nonlinear non-polynomial EVP in the complex domain. In what follows, first the approaches presented by VERMA in [96, 39] are discussed. NEWTON's eigenvalue iteration method is described next, results from which are later compared with the obtained solutions using other mentioned techniques.

3.3.1 Determinant search method

A classical way of solving a TEVP is using the determinant search method [34, 38, 5], in which one searches for such values of s for which

$$\det\left[\mathbf{J}(s)\right] = 0. \tag{3.18}$$

Since the parameter s is a complex number, the search domain is two dimensional. Finding all of the eigenvalues with this approach is possible only for relatively small systems, e.g., short-span single conductor problems. Due to very closely spaced eigenvalues for the conductor bundle, it is easy to miss many values of s for which actually the determinant of $\mathbf{J}(s)$ is zero. Although, normalization of the basic variables leads to a better conditioned system matrix (as shown in [5]), difficulties are faced when solving the TEVP for bigger system matrices using the determinant search method [5]. The major difficulty is that, for a big system matrix the optimizer does not converge to zero, rather it sticks to a minimum value. The prime reason for this difficulty is the large variation in the order of numerical values of the elements of the system matrix, which, together with the large number of algebraic operations (i.e., multiplications) involved in calculating the determinant, lead to such numerical problems. Mathematically, when a

zero is multiplied with any number, no matter how big the number is, the multiplication results in a zero. However, when a "numerical zero", e.g., $\approx 10^{-10}$, is multiplied with a number of the higher order, e.g., of 10^8, it no more results a number close to "numerical zero". The situation gets worse when such many multiplications take place, as happens while computing the determinant. Hence, additional checks are required to confirm if the obtained values are actual eigenvalues of the system or they are just the values of parameter s corresponding to local minima of the determinant of the system matrix.

3.3.2 Alternate approach

To overcome the difficulties arose in the determinant search method, an *alternate approach* was presented by VERMA [5], in which the homogeneous system of $4M(N+1)$ simultaneous equations, given by (2.25), was first transformed into a nonhomogeneous system by using any $\{4M(N+1)-1\}$ equations. A simple and better-conditioned optimization criterion is thus defined for the remaining equation. The detailed steps for the alternate approach are described as follows:

1. In (2.26), let us assume that $A_{1,1} = 1$.
2. Substitute the value of $A_{1,1}$ into any $\{4M(N+1)-1\}$ homogeneous equations of (2.25), so as to transform them into a set of nonhomogeneous equations. Determine other system variables, i.e. $B_{1,1}, A_{2,1}, B_{2,1}, ..., A_{2M,N+1}, B_{2M,N+1}$ (refer (2.26)), by solving these $\{4M(N+1)-1\}$ nonhomogeneous simultaneous equations with the Gauss elimination technique.
3. Substitute the values of $B_{1,1}, A_{2,1}, B_{2,1}, ..., A_{2M,N+1}, B_{2M,N+1}$ back into the remaining one [say l-th] equation. Since, perviously assumed $A_{1,1}$ was not the correct one, these values will not satisfy the l-th equation and will result in an error ε as

$$\begin{aligned} J_{l,1} + B_{1,1}J_{l,2} + A_{2,1}J_{l,3} + B_{2,2}\ J_{l,4} + ... \\ +A_{2M,N+1}\ J_{l,\{4M(N+1)-1\}} + B_{2M,N+1}\ J_{l,4M(N+1)} = \varepsilon. \end{aligned} \tag{3.19}$$

The optimization criterion, now, is to search such values of s, in the complex domain, for which $|\varepsilon|$ equals (or tends to) zero. This approach leads to a well-behaving numerical optimization criterion, which converges faster than the one in the determinant search method [5]. It gives most, if not all, of the eigenvalues if good initial guesses are used. Moreover, one can always be sure that the found value of s after minimizing the error ε, is an eigenvalue of the system in (2.25). However, this approach requires good initial guesses, otherwise it fails to find very closely spaced eigenvalues, specially in the case of a two dimensional complex search domain.

3.3.3 Newton's eigenvalue iteration method

Consider a $n \times n$ matrix $\mathbf{T}(\lambda)$ whose elements are the functions of parameter λ and are differentiable at least once. Assume that, at present, the elements of the matrix $\mathbf{T}$ and the parameter λ are real numbers. We shall try to find iteratively an eigenvalue λ^* of

the matrix $\mathbf{T}(\lambda)$ if an initial estimate λ_0 is sufficiently close to λ^*. If the first derivative of the matrix $\mathbf{T}(\lambda)$ with respect to parameter λ is $\mathbf{T}'(\lambda)$, the Taylor's series expansion reads

$$\mathbf{T}(\lambda + \Delta\lambda) = \mathbf{T}(\lambda) + e\mathbf{T}'(\lambda) + \mathcal{O}\left(e^2\right), \tag{3.20}$$

where $\mathcal{O}\left(e^2\right)$ includes the second and higher order terms. Neglecting the higher order terms an approximate expression can be written from (3.20) as

$$\mathbf{T}(\lambda + \Delta\lambda) \approx \mathbf{T}(\lambda) + \Delta\lambda\mathbf{T}'(\lambda). \tag{3.21}$$

Let $e = \Delta\lambda$. Now, for a given initial estimate of λ, we seek a correction e which satisfies

$$\det\left(\mathbf{T}(\lambda + \Delta\lambda)\right) = 0, \tag{3.22}$$

which means that for an appropriate value of e

$$\det\left(\mathbf{T}(\lambda) + e\mathbf{T}'(\lambda)\right) = 0. \tag{3.23}$$

This is equivalent to solving an eigenvalue problem of the form (3.5) as

$$\mathbf{A}x = e\mathbf{B}x. \tag{3.24}$$

where, $\mathbf{A} = \mathbf{T}(\lambda)$ and $\mathbf{B} = -\mathbf{T}'(\lambda)$. There are many good methods to solve the matrix EVP in (3.24), e.g. [88]. However, for our purpose only the smallest value of $|e|$ is needed, for which a very efficient method using LU-factorization is described by Yang in [97].

For a given λ_k, it is always possible to factorize $T(\lambda_k)$ into a product of three matrices with suitable choice of a permutation matrix $\mathbf{P}$ such that

$$\mathbf{T}(\lambda_k) = \mathbf{P}^T\mathbf{L}\mathbf{U}, \tag{3.25}$$

where, $\mathbf{L}$ is a lower triangular matrix with unit diagonal and $\mathbf{U}$ is an upper triangular matrix. If one or more diagonal elements of $\mathbf{U}$ equal zero, then λ_k is an eigenvalue of $\mathbf{T}$, because of the fact

$$\det\left(\mathbf{T}(\lambda_k)\right) = \prod_{i=1}^{n} t_{ii}. \tag{3.26}$$

However, we shall start with assuming that $t_{ii} \neq 0, i = 1, 2, \ldots, n$. As long as the determinant of $(\mathbf{T}(\lambda_k))$ does not vanish, the eigenvalue is not found and $\mathbf{T}\left(\lambda_k\right))$ has to be invertible. Equation (3.23) can be written in the form

$$\det\left(\mathbf{I} + e\mathbf{G}\right) = 0, \tag{3.27}$$

where, $\mathbf{G} = \mathbf{L}^{-1}\mathbf{P}\mathbf{T}'\mathbf{U}^{-1}$ and $\mathbf{I}$ is an identity matrix.

The matrix $e\mathbf{G}$ may be regarded as a small perturbation of the identity matrix for a small value of e. The effect of the perturbation on the determinant may be expressed by

$$\det\left(\mathbf{I} + e\mathbf{G}\right) \approx \det\left(\mathbf{I}\right) + \sum_{j=1}^{n}\sum_{i=1}^{n} \frac{\partial}{\partial d_{ij}} \det\left(\mathbf{I}\right) e\ g_{ij} \tag{3.28}$$

where d_{ij} and g_{ij} are the elements of the matrices $\mathbf{I}$ and $\mathbf{G}$ respectively. In (3.28) we may denote the partial derivative by

$$\frac{\partial}{\partial d_{ij}} \det(\mathbf{I}) = \lim_{\Delta d_{ij} \to 0} \left\{ \frac{1}{\Delta d_{ij}} \left[\det\left(\mathbf{I} + \Delta d_{ij}\ g_i g_j^T\right) - \det(\mathbf{I}) \right] \right\}, \tag{3.29}$$

where g_i and g_j are the unit base vectors in $\mathbf{G}^n$. Note that

$$\det\left(\mathbf{I} + \Delta d_{ij}\ g_i g_j^T\right) = \det(\mathbf{I}) \qquad \text{for} \quad i \neq j. \tag{3.30}$$

Hence, it can be simply deduced that

$$\frac{\partial}{\partial d_{ij}} \det(\mathbf{I}) = \begin{cases} 0 & i \neq j, \\ 1 & i = j. \end{cases} \tag{3.31}$$

So, (3.29) can be reduced to

$$1 + e \sum_{i=1}^{n} g_{ii} = 0. \tag{3.32}$$

Hence, we obtain

$$e(\lambda_k) = -\left(\sum_{i=1}^{n} g_{ii} \right)^{-1}. \tag{3.33}$$

One can now improve the approximate eigenvalue by

$$\lambda_{k+1} = \lambda_k + e(\lambda_k) \qquad k = 0, 1, 2, \ldots \tag{3.34}$$

Thus, with each iteration one gets closer to the right value of λ. Convergence of each iteration obviously depends on the initial guess value of λ_0. We use the KANTOROVIC theorem [99] to establish a convergence criterion for the algorithm. Let us denote the determinant as a function

$$f(\lambda) = \det(\mathbf{T}(\lambda)). \tag{3.35}$$

For a given λ_0 we may compute $e_0 = e(\lambda_0)$. In the process we have computed

$$f_0 = f(\lambda_0) = \prod_{i=1}^{n} u_{ii}. \tag{3.36}$$

Then obtain

$$f_0' = f'(\lambda_0) = -\frac{f_0}{e_0}, \tag{3.37}$$

and $\lambda_1 = \lambda_0 + e_0$. We still need an estimate for $f''(\lambda_0)$ which can be expressed in the form

$$f_0'' = f''(\lambda_0) = (1 + e'(\lambda_0)) \frac{f_0}{e_0^2}. \tag{3.38}$$

Unfortunately, $e'(\lambda_0)$ is not obtainable exactly. An approximation can be computed as

$$e'(\lambda_0) \approx \frac{1}{\varepsilon}\left[e\left(\lambda_0+\varepsilon\right)-e(\lambda_0)\right], \tag{3.39}$$

where ε is a small number. It requires an additional LU-factorization of the matrix $T(\lambda_0+\varepsilon)$.
We state the KANTOROVIC theorem [99], that if

$$h_0 = \frac{|\lambda_1-\lambda_0| \,.\, |f''(\lambda_0)|}{|f'(\lambda_0)|} \leq \frac{1}{2}, \tag{3.40}$$

then the NEWTON's sequence (3.34) starting from λ_0 converges to a solution λ^* which exists in neighborhood, defined by

$$|\lambda-\lambda_0| \leq \frac{1-\sqrt{1-2h_0}}{h_0}|\lambda_1-\lambda_0| \tag{3.41}$$

The above mentioned statement is a sufficient condition for the convergence. If the condition (3.40) is not satisfied, the convergence can not be guaranteed. In some instances, when λ_0 does not satisfy (3.40), NEWTON's iteration actually converges with a subsequent iterate satisfying condition (3.40). It is the case when the initial guess is too far from the system eigenvalue. However, because of its closely spaced system eigenvalues, NEWTON's eigenvalue iteration method is very suitable for the conductor bundle problems. In the current case, even if the initial guess is far from an eigenvalue, it converges to another eigenvalue which is closer to the initial guess.

Algorithm

1. Assume an initial estimate λ_0 and compute λ_1 by iteration (3.34).
2. Compute $e'(\lambda_0)$ by (3.39) and test the adequacy of λ_0 by the criterion (3.40).
3. If (3.40) is satisfied, continue. Otherwise, assume another λ_0 and go to step 1.
4. At a subsequent iteration k-th iteration ($k = 2, 3, 4, ...$), if diagonal elements of $\mathbf{U}$ satisfy $|u_{ii}|_{max}.|u_{ii}|_{min} \leq \varepsilon_d$, where ε_d is a properly chosen small number, go to step 6. Otherwise continue.
5. If $\frac{e(\lambda_k)}{\lambda_k} \leq \varepsilon_\lambda$, where $\lambda_k \neq 0$ and ε_λ is a properly chosen, go to step 6. Otherwise increase k by 1 and go back to step 4.
6. Set $\lambda^* = \lambda_k$.

3.3.4 Extension for the complex system matrix

The approach shown above can be modified for a complex system matrix, resulting in complex eigenvalues. One can convert the complex domain problem into two real

domain problems as shown below. If our system matrix $\underline{\mathbf{T}}(\lambda)$ is a complex matrix, we can write it and its derivate as

$$\underline{\mathbf{T}}(\underline{\lambda}) = \mathbf{T}_R(\underline{\lambda}) + \mathrm{i}\mathbf{T}_I(\underline{\lambda}) \tag{3.42}$$
$$\underline{\mathbf{T}}'(\underline{\lambda}) = \mathbf{T}_R^D(\underline{\lambda}) + \mathrm{i}\mathbf{T}_I^D(\underline{\lambda}) \tag{3.43}$$

where $\mathbf{T}_R(\underline{\lambda})$ and $\mathbf{T}_I(\underline{\lambda})$ respectively are the real and the imaginary part of complex system matrix; and $\mathbf{T}_R^D(\underline{\lambda})$ and $\mathbf{T}_I^D(\underline{\lambda})$ are the real and the imaginary part of the derivative of the system matrix. Obviously, the system eigenvalue $\underline{\lambda} = \lambda_R + \mathrm{i}\lambda_I$ is also a complex number. Note that in this section $(\underline{\ \cdot\ })$ denotes complex terms. Hence, the eigenvalue problem to be solved in (3.24) becomes

$$\left[\mathbf{T}_R(\underline{\lambda}) + \mathrm{i}\mathbf{T}_I(\underline{\lambda})\right] x = -e\left[\mathbf{T}_R^D(\underline{\lambda}) + \mathrm{i}\mathbf{T}_I^D(\underline{\lambda})\right] x. \tag{3.44}$$

This, on the other hand, means solving two linear eigenvalue problems simultaneously, which are

$$\mathbf{T}_R(\underline{\lambda})x = -e\mathbf{T}_R^D(\underline{\lambda})x, \tag{3.45}$$
$$\mathbf{T}_I(\underline{\lambda})x = -e\mathbf{T}_I^D(\underline{\lambda})x. \tag{3.46}$$

That means for each iteration, one now needs to solve an eigenvalue problem in the real domain of the size $2n \times 2n$

$$\mathbf{T}_{new}(\underline{\lambda})\tilde{x} = -e\mathbf{T}_{new}^D(\underline{\lambda})\tilde{x}, \tag{3.47}$$

with

$$\tilde{x} = \begin{bmatrix} x \\ x \end{bmatrix}, \tag{3.48}$$

where

$$\mathbf{T}_{new}(\underline{\lambda}) = \begin{bmatrix} \mathbf{T}_R(\underline{\lambda}) & \mathbf{0} \\ \mathbf{0} & \mathbf{T}_I(\underline{\lambda}) \end{bmatrix} \quad \text{and} \quad \mathbf{T}_{new}^D(\underline{\lambda}) = \begin{bmatrix} \mathbf{T}_R^D(\underline{\lambda}) & \mathbf{0} \\ \mathbf{0} & \mathbf{T}_I^D(\underline{\lambda}) \end{bmatrix}. \tag{3.49}$$

Now, we choose two initial guesses $\lambda_{R,0}$ and $\lambda_{I,0}$, which form a complex initial guess $\underline{\lambda}_0 = \lambda_{R,0} + \mathrm{i}\lambda_{I,0}$. The complex system matrix $\underline{\mathbf{T}}(\underline{\lambda}_0)$ and its derivative $\underline{\mathbf{T}}'(\underline{\lambda}_0)$ corresponding to $\underline{\lambda}_0$ are computed; and real matrices $\mathbf{T}_R(\underline{\lambda}_0)$, $\mathbf{T}_I(\underline{\lambda}_0)$, $\mathbf{T}_R^D(\underline{\lambda}_0)$, $\mathbf{T}_R^D(\underline{\lambda}_0)$ are numerically obtained, as defined in (3.42) and (3.43). Matrices $\mathbf{T}_{new}(\underline{\lambda})$ and $\mathbf{T}_{new}^D(\underline{\lambda})$ are then formed, as defined in (3.49). Now, we solve an EVP (3.47) of double the size, by the same procedure as shown in the last section, in order to obtain λ_R^* and λ_I^*, and ultimately the complex system eigenvalue $\underline{\lambda}^* = \lambda_R^* + \mathrm{i}\lambda_I^*$.

Using ready-made optimization functions:

Highly sophisticated optimization functions have been developed in many programming languages. MATLAB has become a very powerful tool for engineering computations because of its variety of toolboxes using advanced mathematical algorithms. The approach defined in section 3.3.3 can be used with MATLAB even in the case of a complex system matrix. In the current work the MATLAB function `polyeig` has been used in order to obtain the solution of (3.24) during each iteration. In the `polyeig` function different algorithms are merged together, depending on the behavior of the matrices under consideration the best suitable solution type is chosen [100]. MATLAB uses LAPACK routines to compute eigenvalues and eigenvectors. More information about different solution algorithms `polyeig` function uses, can be found in [101].

Using MATLAB, the algorithm described in section 3.3.3 can be very simply applied to obtain the solution of nonlinear eigenvalue problems in the complex domain. For optimization in the complex domain the nonlinear optimization function `fsolve` is used, whereas, for the linear eigenvalue problem (3.24) the function `polyeig` is used. The simple procedure which is followed in order to obtain the solution of (2.25) using MATLAB functions, is as follows:

Constitution of the system matrix $\mathbf{J}(s)$ in (2.27) and (2.43) shows that it is differentiable at least once with respect to the complex parameter s. One can also obtain the derivative of the impedance (i.e., the matrix $\mathbf{Z}(s)$ for the spacer damper and Z_D for the STOCKBRIDGE damper). The impedance of the STOCKBRIDGE damper can be differentiated using its rational polynomial form, as shown in [44]. It is assumed here that the derivative of the system matrix $\mathbf{J}'(s)$ is known. TAYLOR's series expansion of the complex system matrix $\mathbf{J}(s)$ for a complex initial guess $\underline{s}^{(0)}$ gives

$$\underline{\mathbf{J}}\left(\underline{s}^{(0)}+\underline{e}\right)=\underline{\mathbf{J}}\left(\underline{s}^{(0)}\right)+\underline{e}\,\underline{\mathbf{J}}'\left(\underline{s}^{(0)}\right)+\mathcal{O}\left(\underline{e}^{2}\right), \tag{3.50}$$

where

$$\underline{\mathbf{J}}'\left(\underline{s}^{(0)}\right)=\left.\frac{\mathrm{d}\underline{\mathbf{J}}\left(s\right)}{\mathrm{d}s}\right|_{s=\underline{s}^{(0)}}, \tag{3.51}$$

and $\mathcal{O}\left(\underline{e}^{2}\right)$ includes the terms of order $\underline{e}^{2}$ and higher. The small perturbation $\underline{e}$ is a complex number. Ignoring the second and higher ordered terms in $\underline{e}$ gives

$$\det\left[\underline{\mathbf{J}}\left(\underline{s}^{(0)}+\underline{e}\right)\right]=\det\left[\underline{\mathbf{J}}\left(\underline{s}^{(0)}\right)+\underline{e}\,\underline{\mathbf{J}}'\left(\underline{s}^{(0)}\right)\right]. \tag{3.52}$$

Hence, in the neighborhood of a complex eigenvalue $\underline{s}$ of (2.25)

$$\underline{s}=\underline{s}^{(0)}+\underline{e}, \tag{3.53}$$

we have

$$\left[\underline{\mathbf{J}}\left(\underline{s}^{(0)}\right)+\underline{e}\,\underline{\mathbf{J}}'\left(\underline{s}^{(0)}\right)\right]\mathbf{a}=0. \tag{3.54}$$

The value of the small complex perturbation $\underline{e}$ can now be determined by the solution of linear EVP in (3.54) with the use of the MATLAB function `polyeig`. Hence, starting with an initial guess $\underline{s}^{(0)}$, the p-th iteration gives a new approximation of $\underline{s}$ as

$$\underline{s}^{(p)}=\underline{s}^{(p-1)}+\underline{e}^{(p)}. \tag{3.55}$$

An algorithm of finding the complex eigenvalues using the ready-made optimization functions in NEWTON's eigenvalue iteration method, is as follows:

Algorithm:

1. Choose a complex initial guess $\underline{s}^{(0)}$.
2. Compute the system matrix and its derivative with respect to $\underline{s}$ at $\underline{s} = \underline{s}^{(p-1)}, \forall p = 1, 2, ...$, i.e., obtain $\underline{\mathbf{J}}\left(\underline{s}^{(p-1)}\right)$ and $\underline{\mathbf{J}}'\left(\underline{s}^{(p-1)}\right)$.
3. Solve the linear EVP (3.54) using MATLAB function `polyeig` and get the minimum eigenvalue, which is $e^{(p-1)}$.
4. Check if $|e^{(p-1)}| < \varepsilon$, where $\varepsilon \leq 10^{-6}$. If the condition is satisfied, go to step 6.
5. If condition in step 4 is not satisfied, get the next value of complex parameter by (3.55) and repeat steps 1-4.
6. If the condition in the step 4 is satisfied, then the obtained value of $\underline{s}^{(p-1)}$ is an eigenvalue $\underline{s}^*$ of the transcendental non-polynomial EVP, corresponding to the given initial guess $\underline{s}^{(0)}$.

3.3.5 Higher order approximation

SINGH and RAM [98] showed that by using a higher order approximation for (3.20) or for (3.50) one can improve the convergence of NEWTON's eigenvalue iteration method. Using the higher order approximation is especially useful for the solution in the complex domain, as the convergence takes more time because of the two dimensional search. This section shows the higher order NEWTON approach for the solution of EVP. Taylor series expansion of (3.50), of an order p gives

$$\underline{\mathbf{J}}\left(\underline{s}^{(0)} + \underline{e}\right) = \underline{\mathbf{J}}\left(\underline{s}^{(0)}\right) + \sum_{k=1}^{p} \frac{\underline{e}^k}{k!} \left.\frac{\mathrm{d}^k \mathbf{J}(s)}{\mathrm{d}s^k}\right|_{s=\underline{s}^{(0)}} + \mathcal{O}\left(\underline{e}^{p+1}\right). \tag{3.56}$$

Neglecting the $(p+1)$-th and higher order terms, $\left(\underline{s}^{(0)} + \underline{e}\right)$ is an eigenvalue of the system if

$$\det\left[\underline{\mathbf{J}}\left(\underline{s}^{(0)} + \underline{e}\right)\right] = 0, \tag{3.57}$$

which means

$$\det\left[\underline{\mathbf{J}}\left(\underline{s}^{(0)}\right) + \underline{e}\ \underline{\mathbf{J}}_1\left(\underline{s}^{(0)}\right) + \underline{e}^2\ \underline{\mathbf{J}}_2\left(\underline{s}^{(0)}\right) + ... + ... + \underline{e}^p\ \underline{\mathbf{J}}_p\left(\underline{s}^{(0)}\right)\right] = 0, \tag{3.58}$$

where

$$\underline{\mathbf{J}}_k\left(\underline{s}^{(0)}\right) = \frac{1}{k!} \left.\frac{\mathrm{d}^k \mathbf{J}(s)}{\mathrm{d}s^k}\right|_{s=\underline{s}^{(0)}}, \qquad \forall\ k = 1, 2, 3, ..., p. \tag{3.59}$$

So, one now needs to solve the following p-th order matrix polynomial EVP in order to determine the iterative correction for $\underline{e}$ in each step, which is the smallest eigenvalue of the problem:

$$\left[\underline{\mathbf{J}}\left(\underline{s}^{(0)}\right) + \underline{e}\ \underline{\mathbf{J}}_1\left(\underline{s}^{(0)}\right) + \underline{e}^2\ \underline{\mathbf{J}}_2\left(\underline{s}^{(0)}\right) + ... + ... + \underline{e}^p\ \underline{\mathbf{J}}_p\left(\underline{s}^{(0)}\right)\right] \mathbf{a} = 0. \tag{3.60}$$

The procedure is easy to follow if one uses the `polyeig` function, which enables obtaining the solution of (3.60) faster. Otherwise, one can always convert the system in (3.60) to linear problem of size $pn \times pn$ as shown in section 3.1.2, where n is the size of square system matrix $\mathbf{J}(s)$.

3.4 Obtaining the eigenvectors

In order to estimate the critical design parameters (e.g., conductor strains and stresses, maximum sub-span amplitudes etc.), we are interested in knowing the mode shapes corresponding to each system eigenvalue. Mode shapes can be obtained by computing the eigenvectors $\mathbf{a}$ for each eigenvalue $\underline{s}^*$. After finding the system eigenvalues using the above mentioned approaches, corresponding eigenvectors are obtained by solving an equivalent algebraic eigenvalue problem of the form

$$[\underline{\mathbf{J}}\,(\underline{s}^*) - \lambda_1 \mathbf{I}]\,\mathbf{a} = 0. \tag{3.61}$$

Obviously, if $\underline{s}^*$ is an eigenvalue of the system (2.25), the determinant of the system matrix, i.e., $\det[\underline{\mathbf{J}}\,(\underline{s}^*)] = 0$ vanishes. Hence, as described in (3.26), one of the eigenvalues λ_1 of the equivalent algebraic EVP (3.61) equals zero. The eigenvector corresponding to any eigenvalue $\underline{s}^*$ of the TEVP in (2.25) is obtained by finding the eigenvector associated to $\lambda_1 = 0$ in the equivalent algebraic EVP (3.61), where $\underline{s}^*$ is determined beforehand by using techniques defined in previous sections. The smaller the convergence criteria for ε one satisfies (refer section 3.3.4), the closer is the determinant of the system matrix $\underline{\mathbf{J}}\,(\underline{s}^*)$ to zero, and so is the minimum eigenvalue of equivalent algebraic EVP, i.e., λ_1. However, setting $\varepsilon = 10^{-3}$ results in $|\lambda_1|_{min} \approx 10^{-8}$, which is good enough for our purposes.

3.5 Obtaining the number of eigenvalues

Using above mentioned approaches does not guarantee to find all the eigenvalues in the desired frequency domain. It is required to make initial guesses finer and to compare the obtained results for two subsequent step sizes, in order to check if most of the eigenvalues are found. This is particularly the problem in the case of complex eigenvalues. In such a case, initial guesses should be well distributed in the complex domain (i.e., in both the real and the imaginary domain) in order to obtain most of the eigenvalues. Hence, an optimal step size for the initial guesses in both the real and the imaginary domain is an important decision to make.

Kartyshov in [102, 103] proposed a numerical method, which can not only obtain the number of eigenvalues present in a certain domain, but also can get better initial guesses in order to iteratively compute those eigenvalues. His approach was further modified in [104], and made numerically stable for the bigger problems. The basis of the algorithm searching for the initial approximations to all eigenvalues of a complex matrix situated in a complex domain $\mathbf{\Omega}$ is presented in this section.

Let $\mathbf{T}(\lambda)$ be a complex $n \times n$ matrix whose elements are analytical functions of a complex parameter λ. We seek values of eigenvalues $\lambda \in \mathcal{C}$ and the left and the right

eigenvectors $\mathbf{x}$ and $\mathbf{y}$ respectively, which satisfy the equations

$$\mathbf{T}(\lambda)\mathbf{x} = \mathbf{0}, \tag{3.62}$$
$$\mathbf{y}\mathbf{T}(\lambda) = \mathbf{0}. \tag{3.63}$$

We consider a function $f(\lambda)$ defined as

$$f(\lambda) = \det\left[\mathbf{T}(\lambda)\right], \tag{3.64}$$

which has n zeros $\lambda_1, \lambda_2, ..., \lambda_n$ (counted with their multiplicities) in a complex domain $\mathbf{\Omega}$ and has no zeros on the boundary $\mathbf{\Gamma}$ of $\mathbf{\Omega}$. If

$$s_k = \frac{1}{2\pi \mathrm{i}} \int_{\mathbf{\Gamma}} \lambda^k \frac{f'(\lambda)}{f(\lambda)} \mathrm{d}\lambda, \qquad k = 0, 1, 2, ... \tag{3.65}$$

the following relation holds from the *argument theorem* [105, 102, 103, 104, 106]

$$\sum_{j=1}^{n} \lambda_j^k = s_k, \qquad k = 0, 1, 2, ... \tag{3.66}$$

The number of eigenvalues enclosed by boundary $\mathbf{\Gamma}$ can be obtained by substituting $k = 0$ in (3.66), $s_0 = 1 + 1 + ... + 1 = n$. The main difficulty in using (3.65) is not only to obtain the analytical function $f(\lambda)$ but also its derivative $f'(\lambda)$ [107]. Some numerical results on eigenvalue counting methods are given in [108, 109]. Kartyshov in [102, 103] suggested to use the *trace theorem* given in [110], which states: If the elements of a square matrix $\mathbf{T}(\lambda)$ are differentiable functions of λ, then for any λ such that $f(\lambda) = \det\left[\mathbf{T}(\lambda)\right] \neq 0$

$$f'(\lambda) = f(\lambda)\mathrm{trace}\left\{\mathbf{T}^{-1}(\lambda)\mathbf{T}'(\lambda)\right\}. \tag{3.67}$$

Hence, the ratio $f'(\lambda)/f(\lambda)$ can be replaced in (3.65) using (3.67). Here, "trace" of any matrix, e.g. $\mathbf{A}$ of size $m \times m$ is defined as the summation of its diagonal terms, i.e.,

$$\mathrm{trace}\left\{\mathbf{A}\right\} = \sum_{i=1}^{m} a_{ii}. \tag{3.68}$$

Hence, (3.65) takes the form

$$s_k = \frac{1}{2\pi \mathrm{i}} \int_{\mathbf{\Gamma}} \lambda^k \ \mathrm{trace}\left\{\mathbf{T}^{-1}(\lambda)\mathbf{T}'(\lambda)\right\} \mathrm{d}\lambda, \qquad k = 0, 1, 2, ... \tag{3.69}$$

Obtaining the integral in (3.65) is the main computational difficulty. It was proposed in [102, 103] to choose a circular domain $\mathbf{\Omega}$ and use the rectangular quadrature rule for calculating the s_k. Consider a circle $\mathbf{\Omega}(\lambda_0, r)$ with the center at point λ_0 and the radius r as the domain $\mathbf{\Omega}$ bounded by the contour $\mathbf{\Gamma}$. After the substitution $\lambda = \lambda_0 + r\mathrm{e}^{2\pi \mathrm{i}t}$, integrals (3.69) become

$$s_k = \int_0^1 \left(\lambda_0 + r\mathrm{e}^{2\pi \mathrm{i}t}\right)^k \varphi(t) r\mathrm{e}^{2\pi \mathrm{i}t} \mathrm{d}t, \qquad k = 0, 1, 2, ... \tag{3.70}$$

where

$$\varphi(t) = \text{trace}\left\{\mathbf{T}^{-1}\left(\lambda_0 + re^{2\pi it}\right)\mathbf{T}'\left(\lambda_0 + re^{2\pi it}\right)\right\}, \tag{3.71}$$

is a slowly varying complex function of the real variable t.

When the eigenvalues of a transcendental matrix are closely spaced, i.e. when n is a big number, the integrand in (3.70) is a rapidly oscillating function. System (3.66) is such that, for n ranging from 20 to 30, even a small relative error in the calculated right-hand sides s_k may result in a strong distortion of the solution; in some cases, it is even possible that the iteration process diverges. In such cases, it is inefficient to calculate the integrals with the use of a circular domain as the reasonable size of circle is very small, and one will need to consider many such circles in order to obtain the eigenvalues in the desired domain. The type of nonlinear EVP (2.25) also has such properties that make the use of a circular domain inefficient. Kartyshov in [104] suggested a method using $\mathbf{\Omega}$ as a rectangular domain, which makes it possible to increase the dimension of the problem. In most of the applied problems it is convenient to use the rectangular domain. The method is more reliable than the one using circular domains, because of its stability for higher n-values.

Considering $\mathbf{\Omega}$ as a rectangular domain:

Considering a rectangular domain defined by four straight lines, $x = a, x = b, y = c$ and $y = d$, where x is the real axis and y is the imaginary axis. The integrals (3.70) can be represented as sum of four integrals taken along the sides of the rectangle defined by these four straight lines:

$$s_k^1 = \int_a^b (x + \mathrm{i}c)^k \varphi(x + \mathrm{i}c)\,\mathrm{d}x, \qquad s_k^2 = -\int_a^b (x + \mathrm{i}d)^k \varphi(x + \mathrm{i}d)\,\mathrm{d}x,$$
$$s_k^3 = \mathrm{i}\int_c^d (\mathrm{i}x + b)^k \varphi(\mathrm{i}x + b)\,\mathrm{d}x, \qquad s_k^4 = -\mathrm{i}\int_c^d (\mathrm{i}x + a)^k \varphi(\mathrm{i}x + a)\,\mathrm{d}x. \tag{3.72}$$

Integrations of s_k^j are carried out over real variable for $j = 1, 2$, and carried out over imaginary variable for $j = 3, 4$. We divide the interval $[a, b]$ into n_r equal parts and interval $[c, d]$ into n_i equal parts. Functions $\varphi(\cdot)$ in (3.72) are approximated by linear polynomials in the interval $[x_{q-1}, x_q]$, and integrals are obtained, which finally results in

$$s_k^j = \sum_{q=1}^{n_r} \left\{ \frac{1}{(k+2)} \frac{n_r}{(b-a)} \left[\varphi(\alpha_q) - \varphi(\alpha_{q-1})\right]\left(\alpha_q^{k+2} - \alpha_{q-1}^{k+2}\right) \right.$$
$$\left. + \frac{1}{(k+1)} \frac{n_r}{(b-a)} \left[\alpha_q\varphi(\alpha_{q-1}) - \alpha_{q-1}\varphi(\alpha_q)\right]\left(\alpha_q^{k+1} - \alpha_{q-1}^{k+1}\right) \right\} + \mathcal{O}\left(\frac{1}{n_r}\right)$$
$$\forall j = 1, 2, 3, 4 \tag{3.73}$$

where

$$\text{for } s_k^1,\ \alpha_q = (\mathrm{i}c + a) + (b - a)\frac{q}{n_r}, \qquad \text{for } s_k^2,\ \alpha_q = (\mathrm{i}d + a) + (b - a)\frac{q}{n_r},$$
$$\text{for } s_k^3,\ \alpha_q = (b + \mathrm{i}c) + \mathrm{i}(d - c)\frac{q}{n_i}, \qquad \text{for } s_k^4,\ \alpha_q = (a + \mathrm{i}c) + \mathrm{i}(d - c)\frac{q}{n_i}. \tag{3.74}$$

In order to obtain the s_k values from (3.73) and (3.74) it is necessary to evaluate the function $\varphi(\alpha_q)$ at the nodes. For this purpose the *trace theorem* (3.67) is used again, where

$$\varphi(\alpha_q) = \text{trace}\left\{\mathbf{T}^{-1}(\alpha_q)\mathbf{T}'(\alpha_q)\right\}, \tag{3.75}$$

for $\det[\mathbf{T}(\alpha_q)] \neq 0$, meaning that on the boundaries of the rectangular domain $\mathbf{\Omega}$ there should lie no system eigenvalue and the matrix $\mathbf{T}(\alpha_q)$ is invertible. Now, one can either use the standard subroutines or reduce the evaluation of trace $\{\mathbf{T}^{-1}(\alpha_q)\mathbf{T}'(\alpha_q)\}$ to solve the systems of linear equations by employing the method presented in [103]. In the present analysis, a function of MATLAB, namely `inv` is utilized, for the evaluation of inverse of matrix $\mathbf{T}(\alpha_q)$. Finally the s_k value in the rectangular domain $\mathbf{\Omega}$ can be obtained by summing up all s_k^j values.

$$s_k = \sum_{j=1}^{4} s_k^j. \tag{3.76}$$

Using (3.76), one can now obtain the number of eigenvalues in the circular domain $\mathbf{\Omega}(\lambda_0, r)$ by obtaining s_k value for $k = 0$.

3.6 Benchmark problems

Two benchmark problems are presented in this section. In the first benchmark problem, a conductor bundle problem with one spacer damper is considered. The idea is to compare the obtained results from different solution techniques for TEVP described in section 3.3. The second benchmark problem, which is considerably bigger, is a real life example. The second benchmark problem is analyzed further in chapter 4 using energy balancing, in order to obtain the actual vibration amplitudes and strains at critical positions. In the current chapter, the solution of TEVP for the second benchmark problem is shown at the end.

Both benchmark problems have the same system parameters except for the number of spacer dampers. A quad bundled transmission line is considered (i.e. M=4). All four subconductors of 25 mm diameter have same mass, stiffness and damping characteristics. Each subconductor is subjected to an equal tension. Various geometric and other relevant data for the benchmark problems are shown in table 3.1.

The normal range of wind speed for the aeolian vibrations is from 1 m/s to 7 m/s [14]. The corresponding frequency range of interest is obtained using STROUHAL relation $f = SU/D$, where f is the vortex shedding frequency in Hz, S is the STROUHAL number, U is the wind velocity in m/s and D is the conductor diameter in meters. Using an average STROUHAL number of 0.2 for flow around a circular cylinder [15], the frequency range of interest for the aeolian vibrations ranges from $0.2/D$ Hz to $1.4/D$ Hz. Hence, for the current conductor diameter of 25 mm, our interest lies in analyzing the system behavior in the frequency range of 8 Hz to 56 Hz.

It is shown in section 4.5 that the provided combination of the quad spacer dampers in the second benchmark problem is good enough to keep the transmission line design

Table 3.1: Data for the benchmark problems

Parameter	**Value**
Number of subconductors	4
Span length	500 m
Tension in all subconductors	9000 N
Conductor Type	339-AL1/30-ST1A (Al-St 340/30)
Conductor diameter	25 mm
Mass per unit length of conductors	1.171 kg/m
Number of spacer dampers	Problem-1: 1 Problem-2: 6
Type of spacer dampers	`RIBE-454-465-3`
Spacer dampers locations [m]	Problem-1: 250 Problem-2: 70, 143, 213, 277, 350, 429

parameters (i.e. strains at the critical points, amplitude of conductor vibrations etc.) within the desired limits.

3.6.1 Benchmark problem-1

This benchmark problem considers a quad conductor bundle having a span length of 500 m. Only one spacer damper (of the type `RIBE-454-465-3`) [17] is attached at the center of the conductor span (i.e., at 250 m). Mass, stiffness and damping characteristics of the spacer damper are provided by RIBE Electrical Fittings, Germany [17]. Further details of the spacer damper `RIBE-454-465-3` are shown in table B.2, and its impedance matrix as a function of the frequency is generated in appendix B.

The system matrix is formed using the formulation described in (2.27-2.32). According to the formulation shown in the section 2.1 the size of the transcendental system matrix $\mathbf{J}$ for this benchmark problem (with $M = 4$ and $N = 1$) is 32×32. TEVP in (2.25) is solved next in order to obtain the system eigenvalues ($s = -\delta + \mathrm{i}\omega$).

The approximate number of the system eigenvalues in the desired frequency range can be obtained using the method described in section 3.5. Let us consider a rectangular domain ranging from $a = -4$ to $b = 0$ rad/s in the real domain; and 8 to 56 Hz in the imaginary domain (i.e., $c = 50.24$ rad/s to $d = 351.68$ rad/s). Using $n_r = n_i = 100$ equal parts in the real as well as in the imaginary domain, the coefficients of (3.66) are obtained using relations (3.73) for $k = 0$. It results in approximately 2550 eigenvalues in the range of 8 Hz to 56 Hz. This means that system eigenfrequencies are so closely spaced that in the range of 1 Hz there are approximately 54 system eigenfrequencies.

The TEVP, as described in (2.25), is solved using the following methods:

1. Determinant search method;
2. Alternate approach by converting the homogenous set of equations into a nonhomogenous set; and
3. First order (FO) NEWTON's method.

For a better comparison, the same initial guesses are used for obtaining the solution with each of the mentioned methods. Each initial guess is a complex number given by the sum of one real and one imaginary part. The step size in the imaginary domain is taken as 0.005 Hz (i.e., 0.0314 rad/s) and, hence, the initial guesses in the imaginary domain are multiples of 0.0314 rad/s. Each guess value in the imaginary domain is summed-up with -0.3, -0.15, -0.01 respectively in the real domain in order to produce three complex initial guesses. Hence, in 1 Hz there are 600 initial guesses[6], which should result in approximately 54 individual eigenvalues. Due to different optimizations criterions and their numerical limitations, different solution techniques might converge to different eigenvalues for the same initial guess. For a conductor bundle, since the eigenvalues are so closely spaced, it is very likely that many subsequent initial guesses converge to the same eigenvalue, and eventually miss another very closely spaced one. Hence, there are few eigenvalues which subsequently remain undetected because no initial guess converged to them. In fact, missing of many eigenvalues is clearly noticeable in the results presented by HADULLA [44], page 82, MITRA [64], page 77 and RANMALE [65], page 53. For the current benchmark problem same was the case for the results obtained using the determinant search method and the alternate approach.

The solution of TEVP via the determinant search method, the alternate approach and the first order NEWTON's method are shown in figure 3.1, 3.2 and 3.3 respectively, which show a typical dense frequency spectrum for a conductor bundle. Eigenfrequencies ($\omega/2\pi$) in Hertz are plotted with respect to corresponding damping ratios ($\delta/\text{abs}(s)$). Due to finding repeated eigenvalues and eventually missing many others, the determinant search method results only in 1005 eigenvalues. For the same initial guesses the alternate approach results in 1786 eigenvalues, whereas, the first order NEWTON's method results in 2546 frequencies. In figure 3.4a and 3.4b results from three approaches are plotted together in different frequency ranges in order to show the comparison of the obtained solutions from different methods. Because of a large variation in their numerical order, the damping ratios are plotted on the log-scale in figure 3.5. There are 8 distinct pattern curves noticeable in figure 3.5, which correspond mainly to 8 degrees of freedom (i.e., horizontal and vertical motion of each subconductor) of the transmission line system. These 8 curves are made-up of sets of 8 adjacent eigenvalues, one situated on each curve.

In order to present a comparative study, this part of the section states the results for a set of initial guesses, which converged to different eigenvalues with different solution methods. Details of the solution convergence using the same initial guesses for 8 adjacent system eigenvalues in the range of 34.20 Hz to 34.35 Hz are shown in tables 3.2-3.9, for three solution methods. Values in the intermediate iteration steps are

[6] [1/0.005 (step size)] $\times$ 3 (for each imaginary guess)=600

also shown in the tables. Let us call these 8 finally obtained eigenvalues as "*first*", "*second*", ..., "*eighth*" eigenvalues. It can be seen in the tables 3.2-3.9 that the same initial guesses converge to different system eigenvalues for different solution methods, e.g., $-0.15 + 214.81$i in table 3.2 converges to the *second* eigenvalue by the determinant search method, to the *third* eigenvalue by the alternate method and to the *first* eigenvalue by the FO NEWTON's method. Similarly $-0.3 + 214.97$i and $-0.01 + 215.08$i result in the same eigenvalue (i.e., *third* eigenvalue) for the determinant search method and for alternate approach, whereas the same initial guesses resulted in two different (i.e., the *third* and the *forth*) eigenvalues when solving using FO NEWTON's method. Similar patterns are seen for other initial guesses.

The results obtained for these 8 eigenvalues are plotted together in figure 3.6. In this figure 8 initial guesses are shown by the dots ($\bullet$). The finally obtained 8 eigenvalues are shown by the squares ($\square$). Results obtained by different solution methods are shown using $\bigcirc$, $+$ and $\times$. Different line-types in the figure show the convergence paths using different solution methods. Among the current set of 8 system eigenvalues, the determinant search method is able to find only 2 (the *third* and the *sixth*) eigenvalues, the alternate approach finds 6 (except the *forth* and the *fifth*) eigenvalues and the FO NEWTON's method finds all 8 eigenvalues.

It is observed in the tables 3.2-3.9 that FO NEWTON's method requires approximately half the number of iterations compared to the determinant search method and approximately three less iterations than the alternate approach. Because of the fewer required iterations, NEWTON's method is approximately 2 times faster than determinant search method and approximately 1.25 times faster than the alternate approach. In addition of being faster than the other two methods, the FO NEWTON's method is also able to find closely spaced eigenvalues efficiently. Knowing the suitability of the FO NEWTON's method, the same solution method is used for obtaining the eigenvalues for the second benchmark problem, as explained in the next section.

3.6.2 Benchmark problem-2

In the second benchmark problem six similar spacer dampers of the type `RIBE-454-465-3` are attached respectively at 70 m, 143 m, 213 m, 277 m, 350 m and 429 m from one end of the conductor bundle having a span length of 500 m. This results in 6 approximately equal subspans, having span-lengths of 70 m, 73 m, 70 m, 64 m, 73 m, 79 m and 71 m respectively. Other geometric and damping data are shown in the table 3.1. Mass, geometry, stiffness and damping characteristics of the conductor remain the same as in the first benchmark problem.

The system matrix for this benchmark problem is again formed using the formulation described in (2.27-2.32). The size of the transcendental system matrix $\mathbf{J}$ for a quad bundle (i.e., M=4) with six spacer dampers (i.e., N=6) is 112×112. The TEVP in (2.25) is solved using FO NEWTON's method to compute the system eigenvalues ($s = -\delta + \mathrm{i}\omega$). Using the current conductor diameter of 25 mm TEVP is solved in the frequency range of 8 Hz to 56 Hz. However, because of such a big size of the transcendental system matrix, more closely spaced complex initial guesses are used than in the benchmark problem-1. The step size in the imaginary domain is taken as 0.0025 Hz (i.e., 0.0157

Table 3.2: Intermediate iteration steps for: -1.50e-001 +214.81i

Iteration	Determinant search	Alternate approach	FO Newton's method
1.	-1.5000e-001 +214.81i	-1.5000e-001 +214.81i	-1.5000e-001 +214.81i
2.	-1.0844e-001 +215.02i	-1.3247e-002 +214.86i	4.2470e-003 +214.90i
3.	-1.7563e-001 +214.95i	-1.0457e-002 +214.91i	-5.6749e-005 +214.94i
4.	-2.1352e-001 +215.19i	-3.3446e-003 +214.92i	3.2098e-008 +214.95i
5.	-2.2563e-001 +215.14i	-7.2345e-005 +214.99i	-1.4901e-009 +214.95i
6.	-1.8236e-001 +214.99i	-6.1046e-007 +214.98i	-1.4889e-009 +214.95i
7.	-2.1035e-001 +215.17i	-8.3485e-008 +214.96i	-1.4895e-009 +214.95i
8.	-2.0947e-001 +215.02i	-3.0037e-008 +214.95i	-1.4900e-009 +214.95i
9.	-1.8623e-001 +215.06i	-7.1680e-009 +214.95i	-1.4904e-009 +214.95i
10.	-2.0624e-001 +215.16i	-2.3340e-009 +214.95i	**-1.4904e-009 +214.95i**
11.	-2.0358e-001 +215.08i	-2.4650e-009 +214.95i	-
12.	-1.8979e-001 +215.12i	-2.4430e-009 +214.95i	-
13.	-1.8993e-001 +215.11i	**-2.4430e-009 +214.95i**	-
14.	-2.0136e-001 +215.08i	-	-
15.	-1.9306e-001 +215.12i	-	-
16.	-1.9534e-001 +215.07i	-	-
17.	-1.9727e-001 +215.12i	-	-
18.	-1.9825e-001 +215.11i	-	-
19.	-1.9932e-001 +215.11i	-	-
20.	-1.9970e-001 +215.10i	-	-
21.	**-1.9970e-001 +215.10i**	-	-

Table 3.3: Intermediate iteration steps for: -1.50e-001 +214.98i

Iteration	Determinant search	Alternate approach	FO Newton's method
1.	-1.5000e-001 +214.98i	-1.5000e-001 +214.98i	-1.5000e-001 +214.98i
2.	-1.4435e-001 +215.17i	-4.2158e-002 +215.08i	-4.2507e-002 +215.00i
3.	-2.2328e-001 +214.99i	-9.9700e-002 +215.04i	-3.9306e-002 +215.01i
4.	-9.4535e-002 +215.15i	-6.3212e-002 +214.97i	-3.9295e-002 +215.01i
5.	-1.7349e-001 +215.14i	-5.3786e-002 +215.04i	-3.9292e-002 +215.01i
6.	-2.1236e-001 +214.98i	-5.0876e-002 +215.03i	-3.9291e-002 +215.01i
7.	-2.2658e-001 +215.13i	-4.6443e-002 +215.01i	-3.9291e-002 +215.01i
8.	-2.1848e-001 +214.99i	-4.2862e-002 +215.00i	-3.9291e-002 +215.01i
9.	-1.8518e-001 +215.11i	-4.0877e-002 +215.01i	**-3.9291e-002 +215.01i**
10.	-2.1017e-001 +215.06i	-4.0115e-002 +215.01i	-
11.	-2.0959e-001 +215.01i	-3.9987e-002 +215.01i	-
12.	-1.8914e-001 +215.00i	-3.9645e-002 +215.01i	-
13.	-1.9623e-001 +215.09i	-3.9457e-002 +215.01i	-
14.	-1.9734e-001 +215.10i	-3.9294e-002 +215.01i	-
15.	-1.9972e-001 +215.10i	**-3.9294e-002 +215.01i**	-
16.	**-1.9971e-001 +215.10i**	-	-

Table 3.4: Intermediate iteration steps for: -3.00e-001 +214.97i

Iteration	Determinant search	Alternate approach	FO Newton's method
1.	-3.0000e-001 +214.97i	-3.0000e-001 +214.97i	-3.0000e-001 +214.97i
2.	-2.5246e-001 +215.15i	-2.3676e-001 +215.01i	-1.9383e-001 +215.07i
3.	-1.7235e-001 +214.98i	-2.0926e-001 +215.09i	-1.9976e-001 +215.10i
4.	-2.2568e-001 +215.14i	-1.8235e-001 +215.15i	-1.9983e-001 +215.10i
5.	-1.8246e-001 +214.97i	-1.9545e-001 +215.12i	-1.9985e-001 +215.10i
6.	-1.8635e-001 +215.02i	-1.9813e-001 +215.11i	-1.9985e-001 +215.10i
7.	-2.1868e-001 +215.05i	-1.9895e-001 +215.11i	-1.9985e-001 +215.10i
8.	-1.9373e-001 +215.14i	-1.9933e-001 +215.11i	-1.9985e-001 +215.10i
9.	-2.1077e-001 +215.07i	-1.9961e-001 +215.10i	-1.9985e-001 +215.10i
10.	-2.0990e-001 +215.12i	-1.9981e-001 +215.10i	**-1.9985e-001 +215.10i**
11.	-2.0393e-001 +215.09i	-1.9985e-001 +215.10i	-
12.	-2.0135e-001 +215.11i	**-1.9985e-001 +215.10i**	-
13.	-1.9974e-001 +215.10i	-	-
14.	**-1.9974e-001 +215.10i**	-	-

Table 3.5: Intermediate iteration steps for: -1.00e-002 +215.08i

Iteration	Determinant search	Alternate approach	FO Newton's method
1.	-1.0000e-002 +215.08i	-1.0000e-002 +215.08i	-1.0000e-002 +215.08i
2.	-2.3436e-001 +215.09i	-5.2235e-002 +215.19i	-2.3739e-002 +215.11i
3.	-2.1459e-001 +215.21i	-8.2348e-002 +215.17i	-2.3562e-002 +215.12i
4.	-2.2251e-001 +215.17i	-1.2342e-001 +215.15i	-2.3563e-002 +215.12i
5.	-2.1773e-001 +215.10i	-1.5341e-001 +215.12i	-2.3563e-002 +215.12i
6.	-1.8015e-001 +215.07i	-1.7242e-001 +215.11i	-2.3563e-002 +215.13i
7.	-1.8589e-001 +215.13i	-1.9045e-001 +215.11i	-2.3563e-002 +215.13i
8.	-1.9011e-001 +215.12i	-1.9541e-001 +215.10i	-2.3563e-002 +215.13i
9.	-1.9227e-001 +215.09i	-1.9741e-001 +215.11i	**-2.3563e-002 +215.13i**
10.	-1.9452e-001 +215.20i	-1.9953e-001 +215.10i	-
11.	-1.9681e-001 +215.15i	-1.9983e-001 +215.10i	-
12.	-1.9812e-001 +215.13i	**-1.9983e-001 +215.10i**	-
13.	-1.9919e-001 +215.10i	-	-
14.	-1.9967e-001 +215.10i	-	-
15.	**-1.9967e-001 +215.10i**	-	-

Table 3.6: Intermediate iteration steps for: -1.00e-002 +215.19i

Iteration	Determinant search	Alternate approach	FO Newton's method
1.	-1.0000e-002 +215.19i	-1.0000e-002 +215.19i	-1.0000e-002 +215.19i
2.	-5.5679e-002 +215.25i	-1.0234e-001 +215.09i	-2.2555e-002 +215.22i
3.	-8.2348e-003 +215.29i	-2.1123e-001 +215.12i	-2.2448e-002 +215.23i
4.	-4.1458e-002 +215.18i	-1.6342e-001 +215.11i	-2.2452e-002 +215.23i
5.	-9.3489e-003 +215.28i	-1.8399e-001 +215.10i	-2.2453e-002 +215.23i
6.	-3.7346e-002 +215.21i	-2.0002e-001 +215.10i	-2.2453e-002 +215.23i
7.	-9.9235e-003 +215.34i	-1.9823e-001 +215.11i	-2.2453e-002 +215.23i
8.	-3.1225e-002 +215.29i	-1.9135e-001 +215.10i	-2.2453e-002 +215.23i
9.	-1.7853e-002 +215.32i	-1.9323e-001 +215.10i	**-2.2453e-002 +215.23i**
10.	-2.9595e-002 +215.31i	-1.9724e-001 +215.10i	-
11.	-2.0936e-002 +215.31i	-1.9917e-001 +215.10i	-
12.	-2.1575e-002 +215.31i	-1.9983e-001 +215.10i	-
13.	-2.2989e-002 +215.32i	**-1.9983e-001 +215.10i**	-
14.	-2.3779e-002 +215.32i	-	-
15.	**-2.3772e-002 +215.32i**	-	-

Table 3.7: Intermediate iteration steps for: -1.00e-002 +215.31i

Iteration	Determinant search	Alternate approach	FO Newton's method
1.	-1.0000e-002 +215.31i	-1.0000e-002 +215.31i	-1.0000e-002 +215.31i
2.	-3.5958e-002 +215.42i	-2.5679e-002 +215.32i	-2.3802e-002 +215.31i
3.	-4.0567e-002 +215.38i	-1.7238e-002 +215.31i	-2.3798e-002 +215.32i
4.	-2.7488e-002 +215.27i	-2.4211e-002 +215.32i	-2.3797e-002 +215.32i
5.	-2.1545e-002 +215.30i	-2.2792e-002 +215.32i	-2.3796e-002 +215.32i
6.	-3.6013e-002 +215.35i	-2.3023e-002 +215.32i	-2.3796e-002 +215.32i
7.	-2.2015e-002 +215.34i	-2.3268e-002 +215.32i	-2.3796e-002 +215.32i
8.	-2.2588e-002 +215.37i	-2.3515e-002 +215.32i	**-2.3796e-002 +215.32i**
9.	-2.4881e-002 +215.30i	-2.3646e-002 +215.32i	-
10.	-2.3992e-002 +215.33i	-2.3773e-002 +215.32i	-
11.	-2.2977e-002 +215.33i	-2.3795e-002 +215.32i	-
12.	-2.3590e-002 +215.32i	**-2.3795e-002 +215.32i**	-
13.	-2.3607e-002 +215.32i	-	-
14.	-2.3780e-002 +215.32i	-	-
15.	**-2.3780e-002 +215.32i**	-	-

Table 3.8: Intermediate iteration steps for: -1.00e-002 +215.61i

Iteration	Determinant search	Alternate approach	FO Newton's method
1.	-1.0000e-002 +215.61i	-1.0000e-002 +215.61i	-1.0000e-002 +215.61i
2.	-1.4557e-001 +215.94i	-1.4112e-002 +215.62i	-1.2472e-002 +215.62i
3.	-2.5350e-001 +216.39i	-1.1713e-002 +215.61i	-1.2471e-002 +215.62i
4.	-2.0349e-001 +216.59i	-1.2902e-002 +215.62i	-1.2471e-002 +215.62i
5.	-1.7850e-001 +216.15i	-1.2018e-002 +215.61i	-1.2471e-002 +215.62i
6.	-1.8346e-001 +216.28i	-1.2237e-002 +215.62i	-1.2471e-002 +215.62i
7.	-1.8948e-001 +216.39i	-1.2351e-002 +215.62i	-1.2471e-002 +215.62i
8.	-2.0048e-001 +216.51i	-1.2410e-002 +215.62i	**-1.2471e-002 +215.62i**
9.	-1.8932e-001 +216.49i	-1.2468e-002 +215.62i	-
10.	-1.9591e-001 +216.40i	-1.2471e-002 +215.62i	-
11.	-1.9779e-001 +216.51i	**-1.2471e-002 +215.62i**	-
12.	-1.9855e-001 +216.45i	-	-
13.	-1.9898e-001 +216.50i	-	-
14.	-1.9999e-001 +216.47i	-	-
15.	-1.9903e-001 +216.48i	-	-
16.	**-1.9903e-001 +216.48i**	-	-

Table 3.9: Intermediate iteration steps for: -1.50e-001 +215.62i

Iteration	Determinant search	Alternate approach	FO Newton's method
1.	-1.5000e-001 +215.62i	-1.5000e-001 +215.62i	-1.5000e-001 +215.62i
2.	-2.5232e-001 +216.09i	-5.1235e-002 +215.65i	-2.8481e-002 +215.64i
3.	-1.9664e-001 +216.54i	-2.9457e-002 +215.64i	-2.3306e-002 +215.65i
4.	-2.4236e-001 +216.23i	-2.7678e-002 +215.65i	-2.3308e-002 +215.65i
5.	-2.3076e-001 +216.49i	-2.1856e-002 +215.65i	-2.3309e-002 +215.65i
6.	-2.2459e-001 +216.39i	-2.2664e-002 +215.65i	-2.3309e-002 +215.65i
7.	-2.4897e-001 +216.52i	-2.2912e-002 +215.65i	-2.3309e-002 +215.65i
8.	-1.9460e-001 +216.50i	-2.3074e-002 +215.65i	-2.3309e-002 +215.65i
9.	-1.9735e-001 +216.42i	-2.3193e-002 +215.65i	**-2.3309e-002 +215.65i**
10.	-2.1783e-001 +216.48i	-2.3300e-002 +215.65i	-
11.	-2.1047e-001 +216.48i	-2.3306e-002 +215.65i	-
12.	-2.0602e-001 +216.47i	-2.3308e-002 +215.65i	-
13.	-1.9459e-001 +216.47i	**-2.3308e-002 +215.65i**	-
14.	-1.9699e-001 +216.47i	-	-
15.	-1.9839e-001 +216.48i	-	-
16.	-1.9623e-001 +216.48i	-	-
17.	-1.9892e-001 +216.48i	-	-
18.	**-1.9893e-001 +216.48i**	-	-

rad/s). Each value in the imaginary domain is summed-up with -0.5, -0.3, -0.15 and -0.01 respectively in the real domain in order to produce four complex initial guesses. Hence, in 1 Hz there are 1600 initial guesses[7].

The solution of TEVP using the FO NEWTON's method results in 3928 eigenvalues. The obtained eigenvalues are plotted against their damping ratios in the figure 3.7 on a linear scale. In the figure 3.8 damping ratios are plotted on the log-scale against the frequency. The effect of attaching 6 spacer dampers, well distributed along the conductor bundle span, is clearly noticeable in the plots. The damping ratios corresponding to the frequencies below 35 Hz are increased considerably, as compared to the first benchmark problem. It means that the spacer dampers are more effective in this frequency region. Moreover, it is to be noticed that unlike in the first benchmark problem, the damping ratios are more scattered in the plot for this benchmark problem, which is normally desirable for a good conductor bundle design.

As a next step, the energy balancing is performed in order to obtain the actual subconductor vibration amplitudes corresponding to each eigenfrequency, which is described in the next chapter.

[7] [1/0.0025 (step size)] $\times$ 4 (for each imaginary guess)=1600

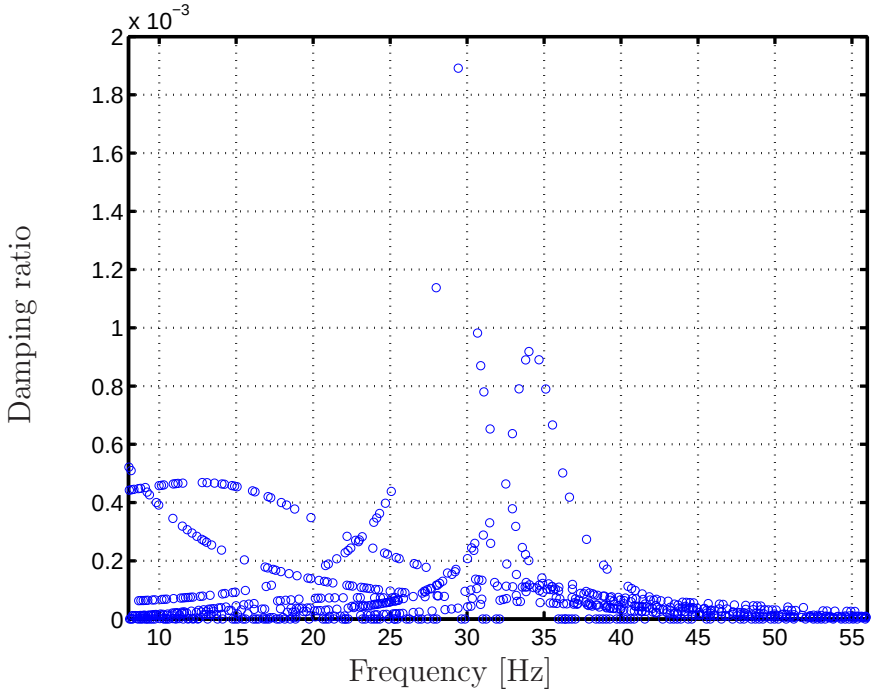

Figure 3.1: Solution of TEVP for benchmark problem-1 using determinant search method (1005 eigenvalues found)

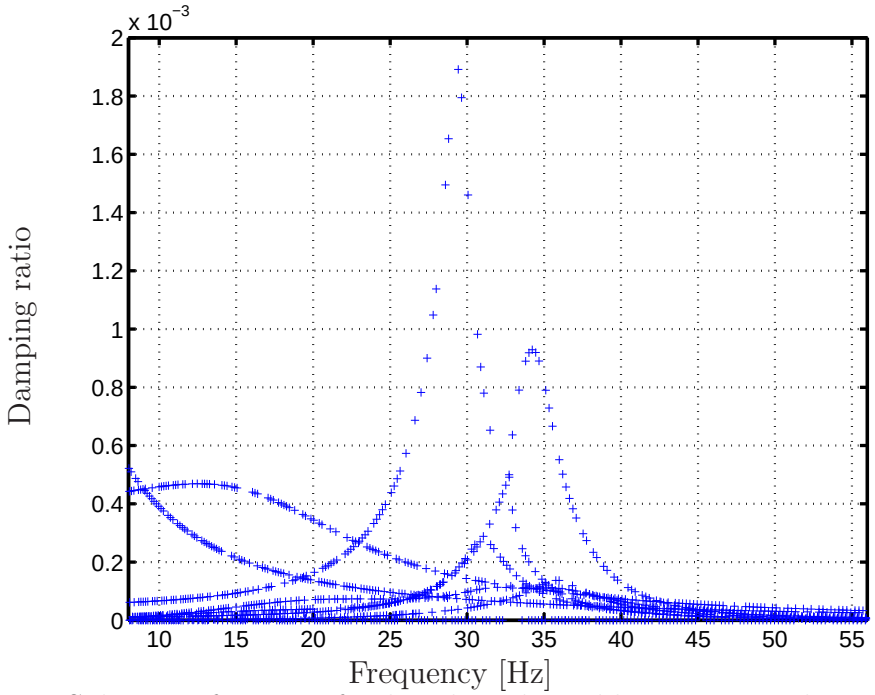

Figure 3.2: Solution of TEVP for benchmark problem-1 using alternate method by converting homogeneous set of equations in to nonhomogeneous set (1786 eigenvalues found)

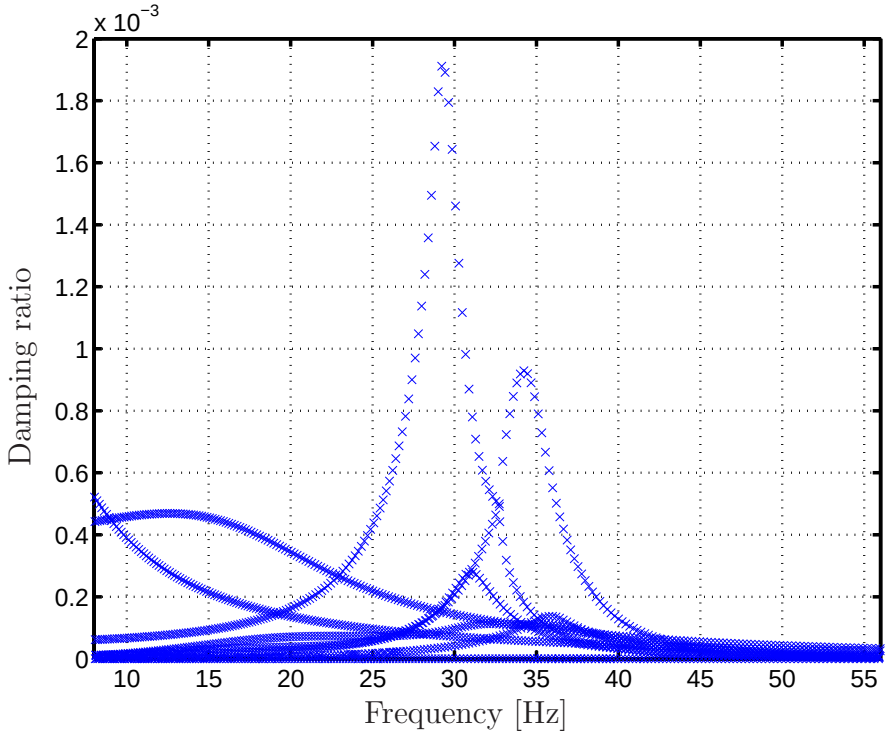

Figure 3.3: Solution of TEVP for benchmark problem-1 using FO NEWTON's method (2546 eigenvalues found)

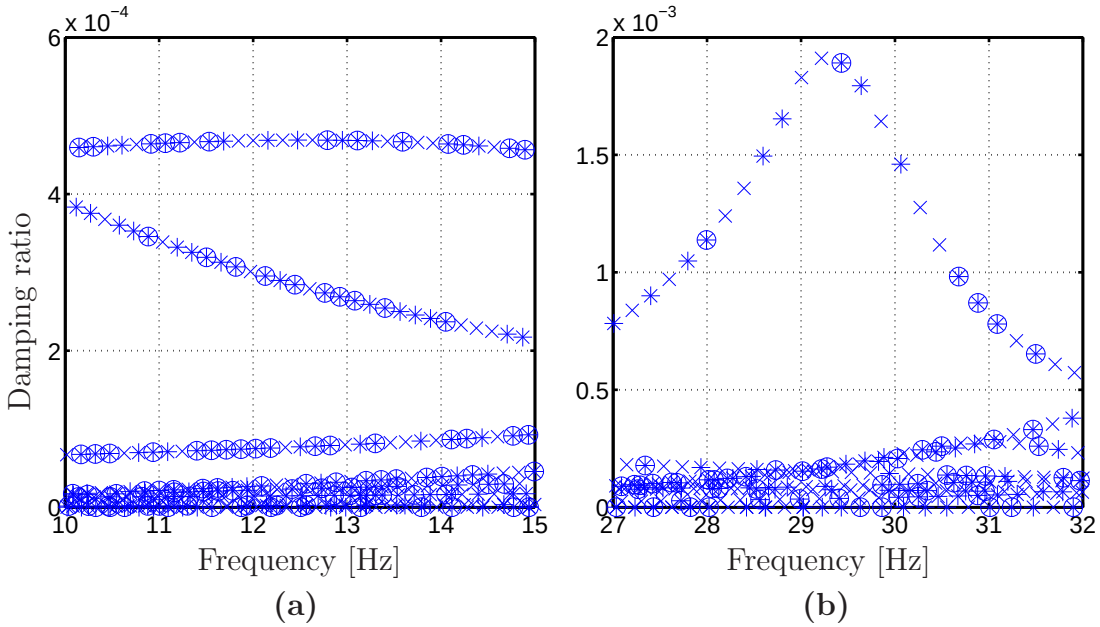

Figure 3.4: Solution of TEVP for benchmark problem-1: Comparison of different solution methods (◯: Determinant search; +: Alternate approach; ×: NEWTON's method) (**a**): From 10-15 Hz; (**b**): From 27-32 Hz

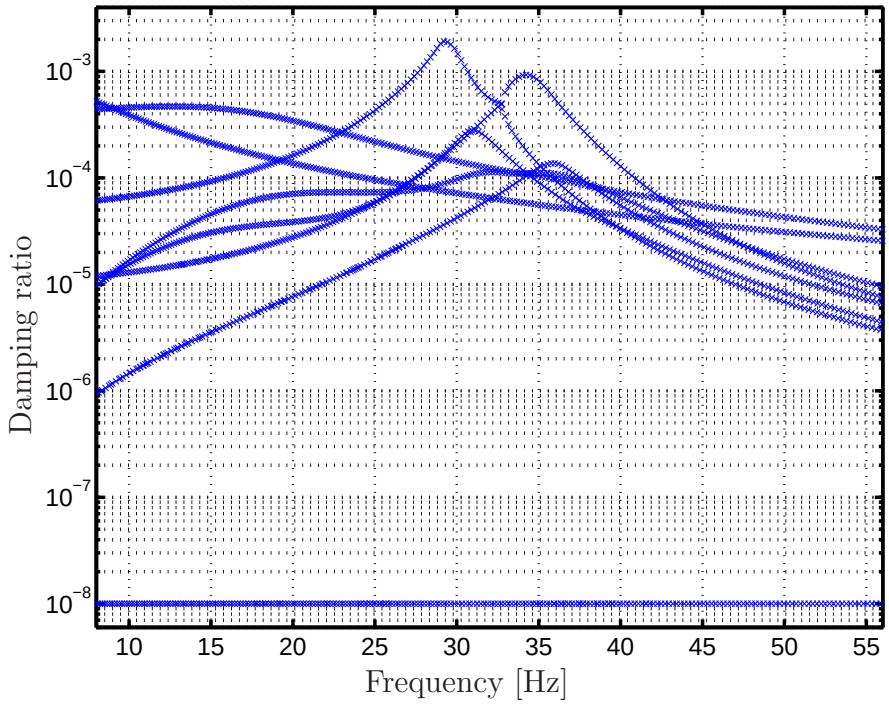

Figure 3.5: Solution of TEVP for benchmark problem-1 using FO NEWTON's method (y-axis plotted on log-scale)

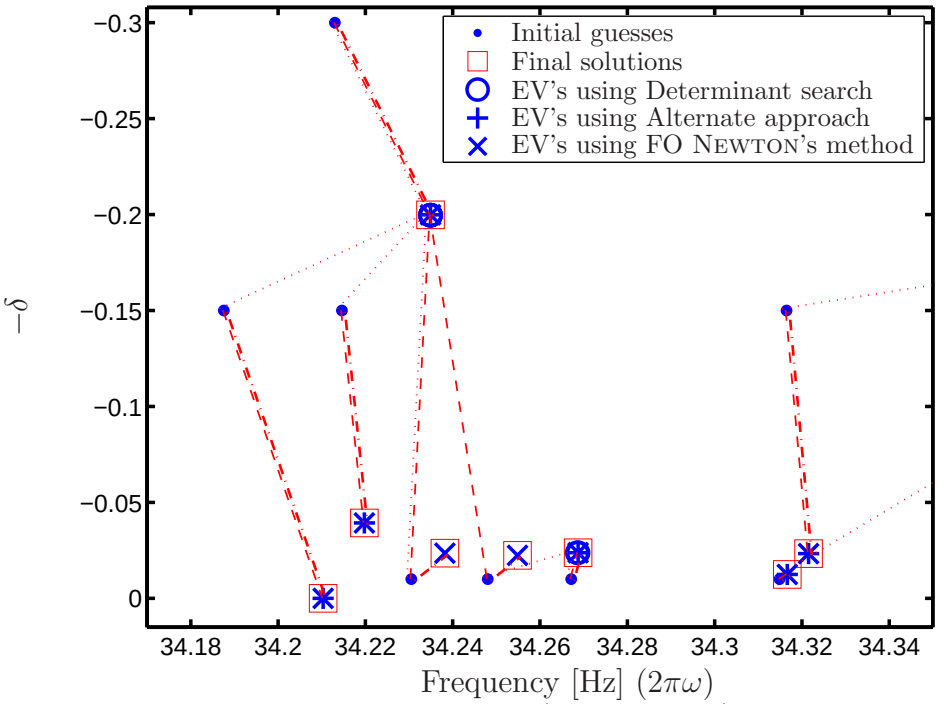

Figure 3.6: Comparison of obtained eigenvalues ($s = -\delta + \mathrm{i}\omega$) for benchmark-1 from different methods. Different lines show the representative convergence path using: $\cdots$: Determinant search; - - -: Alternate approach; -.-.-: NEWTON's method

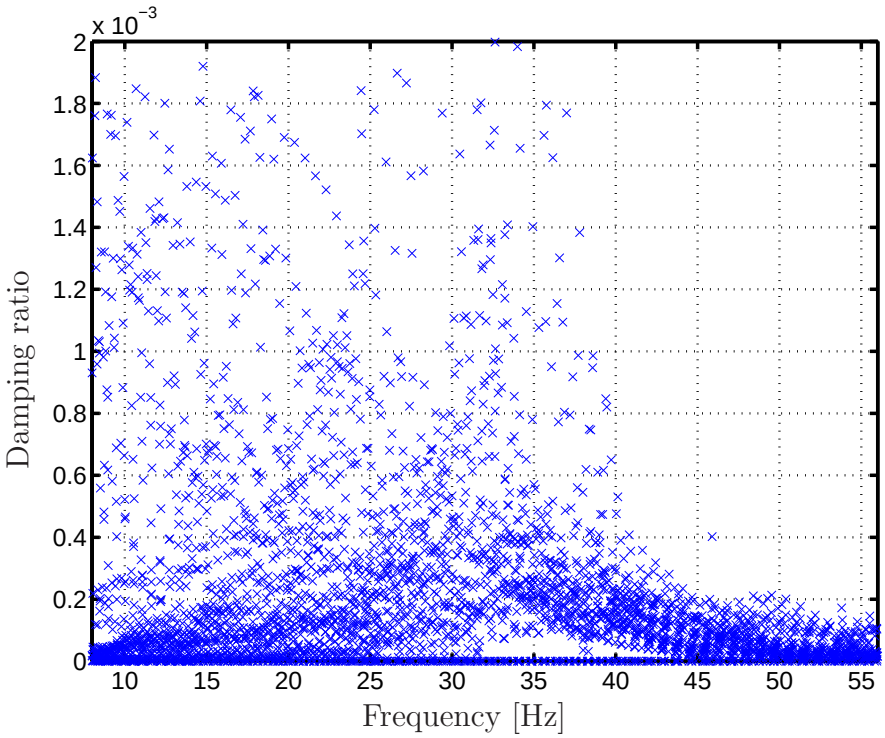

Figure 3.7: Solution of TEVP for benchmark problem-2 using FO NEWTON's method (3928 eigenvalues found)

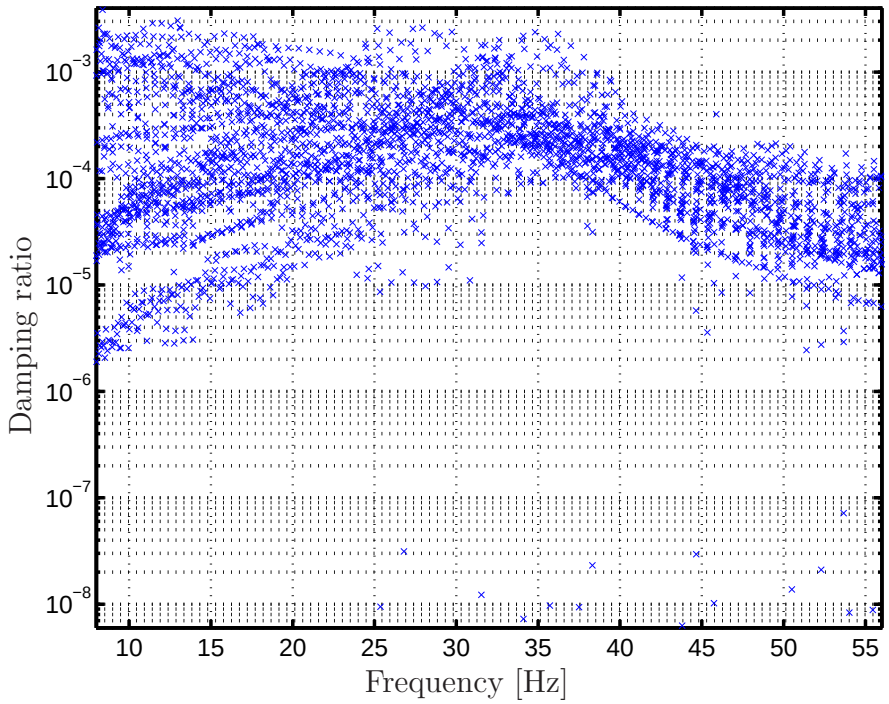

Figure 3.8: Solution of TEVP for benchmark problem-2 using FO NEWTON's method (y-axis plotted on log-scale)

Chapter 4

Energy balance approach

Summary: After obtaining the system's eigenvalues and eigenmodes, as described in chapters 2 and 3, the next step is to scale the obtained mode shapes in order to obtain the actual conductor's vibration amplitudes corresponding to each vibration frequency. This chapter describes an energy balancing approach to obtain the scaling factor, in which the energy input into the system is equated with the energy dissipated in the system.

4.1 Introduction

The right hand side of (2.1) contains the aerodynamic forces and the structural damping, which normally are not well defined. Although there are experimental data available on the cylinder oscillations with relatively large amplitudes (i.e., of the order of one conductor diameter) in a planar stationary flow, and some data concerning the conductor's self-damping are also available, but both data are still far from being complete. Moreover, the wind velocity as a function of space and time is not exactly known, and hence, the rate and the direction of the wind is considered to be a stochastic function of time and space, and is described by their average values. An *energy balance principle* (EBP) is used in [111, 1, 38], in order to obtain the average amplitude of the conductor vibrations, which states

$$P_W = P_D + P_C, \tag{4.1}$$

where P_W is the power imparted by aerodynamic forces, P_D is the power corresponding to the mechanical energy dissipated in the STOCKBRIDGE dampers and in the spacer dampers, and P_C is the power dissipated by material and inter-strand frictional damping in the conductor, also sometimes referred as "conductor's self damping"[8]. These power terms are functions of the amplitudes and the frequencies of conductor vibrations [112, 113, 114].

As shown in the previous chapter, a conductor bundle has a very dense spectrum of system frequencies. Many frequencies are present in a vibrating conductor bundle in the field at any time instant. However, assuming a constant wind velocity through out the span length, energy balance analysis is performed for steady-state oscillation corresponding to each system eigenfrequency. Oscillations corresponding to any eigenfrequency are defined by the eigenmodes obtained after the solution of transcendental eigenvalue problem (TEVP), as shown in the section 3.4. In reality, oscillations of a

[8]For high-tension transmission lines the power dissipation due to interstrand friction is relatively small. Hence, sometimes energy dissipated due to the conductor's self damping is neglected in the energy balancing, and (4.1) becomes: $P_W = P_D$.

conductor bundle with a number of spacer dampers are not completely harmonic in nature [115]. They can, however, be approximated by nearly harmonic oscillations. With such an assumption, one can neglect the dependency of the solution on the time and can approximate the oscillations of the traveling waves in each subspan by characteristic amplitudes of the standing waves in the respective subspans $\hat{A}^c_{m,v}$.

In (4.1), wind power input and conductor's self damping are computed along the span length, whereas the power dissipated by external damping devices is computed only at the points of their attachment. Hence, (4.1) can be written as

$$\sum_{m=1}^{2M}\sum_{v=1}^{N+1} P_{W_{m,v}}(\hat{A}^c_{m,v},\Omega) = \sum_{n=1}^{N} P_{D_n}(K\mathbf{W}_{D_n},\Omega) + \sum_{m=1}^{2M}\sum_{v=1}^{N+1} P_{C_{m,v}}(\hat{A}^c_{m,v},\Omega), \tag{4.2}$$

where N is the number of attached spacer dampers and M is the number of subconductors in the conductor bundle. Here, $P_{W_{m,v}}$ and $P_{C_{m,v}}$ are the contribution of the wind power input and the conductor's self damping from each subspan, and P_{D_n} is the power dissipated by each external damping device. $\hat{A}^c_{m,v}$ are the characteristic amplitudes of equivalent standing waves in each subspan, Ω is the vibration frequency of the system[9]. K is the scaling factor for the respective Ω, which we intend to compute from energy balance analysis. It is to be noted here that the factor K is also intrinsically present in $\hat{A}^c_{m,v}$ terms, as will be shown in the next section. The displacement vector at the damper clamps of the n-th damper is

$$\mathbf{W}_{D_n} = \left\{ \begin{array}{c} W_{1,n}(x)|_{x=\Delta l_n} \\ W_{2,n}(x)|_{x=\Delta l_n} \\ \vdots \\ W_{m,n}(x)|_{x=\Delta l_n} \end{array} \right\}, \tag{4.3}$$

where $W_{m,n}$ is same as in (2.7). Obtaining different power terms in (4.2) will be shown in the section 4.3. Computing the equivalent standing wave characteristic amplitude $\hat{A}^c_{m,v}$ is described in the section 4.2.

4.2 Equivalent standing wave amplitude

Unlike to a standing wave, the amplitude of a traveling wave varies along the span for different wave-loops. Hence, power terms in (4.1) need to be computed at many discrete positions in each wave-loop and to be summed up together to obtain their total values. On the other hand, for a standing wave the steady-state amplitude remains constant through out the span. In order to compute the total values of different power terms, one needs only to compute them over one wave-loop, and multiply it with the number of wave-loops present in the span. Hence, computing power terms along the span is much easier for a standing wave than for a traveling wave. This fact is crucial here, as the

[9]For a dense frequency spectrum of a conductor bundle, the vibration frequency Ω is assumed to be $\Omega = \omega$, where ω is the imaginary part of complex system eigenvalue $s = -\delta + \mathrm{i}\omega$.

power terms are computed for each iteration in the energy balance analysis. Hence, for faster computations, traveling waves in each subspan are approximated by equivalent standing waves.

An equivalent standing wave is defined as a standing wave possessing the same mechanical energy as the energy of traveling waves. In what follows, it is shown how to obtain the characteristic amplitude $\hat{A}^c_{m,v}$ by equating the energies of traveling waves with that of an equivalent standing wave. In fact, the characteristic amplitudes can be defined in many ways and depending upon it's definition one obtains slightly different final results. A major part of the formulation shown in this section is derived from the work done by HADULLA in [44].

Taking into account that the conductor is in resonance with the eigenfrequency, the corresponding eigenmode is

$$w_{m,v}(x,t) = K\mathbf{Re}\left[W_{m,v}(x)\mathrm{e}^{st}\right], \tag{4.4}$$

where a similar coordinate system as mentioned in chapter 2 is utilized. Combining (2.8) and (4.4) results in

$$w_{m,v}(x,t) = K\mathbf{Re}\left[\left\{\overline{A}_{m,v}\mathrm{e}^{-\frac{\delta x}{c_m}}\mathrm{e}^{\mathrm{j}\left(\frac{\omega x}{c_m}+\alpha_{m,v}\right)} + \overline{B}_{m,v}\mathrm{e}^{\frac{\delta x}{c_m}}\mathrm{e}^{-\mathrm{j}\left(\frac{\omega x}{c_m}-\beta_{m,v}\right)}\right\}\mathrm{e}^{\mathrm{i}\omega t}\right], \tag{4.5}$$

where $A_{m,v} = \overline{A}_{m,v}\mathrm{e}^{\mathrm{i}\alpha_{m,v}}$ and $B_{m,v} = \overline{B}_{m,v}\mathrm{e}^{\mathrm{i}\beta_{m,v}}$ are complex amplitudes of two waves traveling in opposite directions, as stated in (2.8). Both waves in (4.5) are traveling waves because of the terms containing δ. In order to apply the energy balance method, we approximate the above expression in each subspan and in both vibration planes (i.e., horizontal and vertical) by standing harmonic waves of characteristic amplitudes $\hat{A}^c_{m,v}$. The traveling waves for each subspan and both the planes of conductor oscillations in (4.5) are replaced with standing waves of amplitude $\hat{A}^c_{m,v}$ so that the oscillation energy for both the waves are the same. Thereby, we first obtain the combined energy density of the combination of two traveling waves using

$$e(x,t) = \frac{T_m}{2}w'^2_{m,v}(x,t) + \frac{\rho A_c}{2}\dot{w}^2_{m,v}(x,t). \tag{4.6}$$

With (4.5) it becomes,

$$e(x,t) = \frac{T_m K^2}{2}\left\{\mathbf{Re}\left[W'_{m,v}(x)\mathrm{e}^{\mathrm{i}\omega t}\right]\right\}^2 + \frac{\rho A_c\omega^2 K^2}{2}\left\{\mathbf{Re}\left[\mathrm{i}W_{m,v}(x)\mathrm{e}^{\mathrm{i}\omega t}\right]\right\}^2. \tag{4.7}$$

Considering that $W_{m,v}(x) = W^R_{m,v}(x) + \mathrm{i}W^I_{m,v}(x)$, we obtain

$$\begin{aligned}\left\{\mathbf{Re}\left[\mathrm{i}W_{m,v}\mathrm{e}^{\mathrm{i}\omega t}\right]\right\}^2 &= \left\{-W^R_{m,v}\sin\omega t - W^I_{m,v}\cos\omega t\right\}^2 \\ &= (W^R_{m,v})^2\sin^2\omega t + (W^I_{m,v})^2\cos^2\omega t + W^R_{m,v}W^I_{m,v}\sin 2\omega t\end{aligned} \tag{4.8}$$

where ρA_c is the mass per unit length of the subconductors and T_m are their respective tension values. Taking the average over one time period we obtain,

$$\begin{aligned}\frac{\omega}{2\pi}\int_0^{\frac{2\pi}{\omega}}\left\{\mathbf{Re}\left[\mathrm{i}W_{m,v}\mathrm{e}^{\mathrm{i}\omega t}\right]\right\}^2\mathrm{d}t &= \frac{1}{2}\left[(W^R_{m,v})^2 + (W^I_{m,v})^2\right] \\ &= \frac{1}{2}W_{m,v}W^*_{m,v},\end{aligned} \tag{4.9}$$

where $(\ )^*$ denotes the complex conjugate. Based on a similar analogy one can also derive the time averaged first term of (4.7) as,

$$\frac{\omega}{2\pi}\int_0^{\frac{2\pi}{\omega}} \left\{\mathbf{Re}\left[W'_{m,v}\mathrm{e}^{\mathrm{i}\omega t}\right]\right\}^2 \mathrm{d}t = \frac{1}{2}W'_{m,v}W'^{*}_{m,v}, \tag{4.10}$$

which together with (4.7) and (4.9) gives the energy density,

$$\bar{e}(x) = \frac{T_m K^2}{4}W'_{m,v}W'^{*}_{m,v} + \frac{\rho A_c \omega^2 K^2}{4}W_{m,v}W^{*}_{m,v}. \tag{4.11}$$

From (4.11) one can now obtain the energy density averaged over one subspan length as,

$$\bar{\bar{e}} = \frac{1}{\Delta l_v - 2b}\left[\int_b^{\Delta l_v - b}\frac{T_m K^2}{4}W'_{m,v}W'^{*}_{m,v}\mathrm{d}x + \int_b^{\Delta l_v - b}\frac{\rho A_c \omega^2 K^2}{4}W_{m,v}W^{*}_{m,v}\mathrm{d}x\right] \tag{4.12}$$

where $2b$ is the clamp width of the spacer dampers combined with characteristic conductor length on both sides of the clamp, as was used in chapter 2. Using the fact that $W_{m,v}(x)$ is a solution of the differential equation

$$T_m W''_{m,v}(x) = \rho A_c s^2 W_{m,v}(x), \tag{4.13}$$

equation (4.12) results in,

$$\bar{\bar{e}} = \frac{K^2}{\Delta l_v - 2b}\left[\frac{T_m}{4}W'_{m,v}W^{*}_{m,v}\Big|_b^{\Delta l_v - b} + \frac{\rho A_c}{4}\left(\omega^2 - s^2\right)\int_b^{\Delta l_v - b}W_{m,v}W^{*}_{m,v}\mathrm{d}x\right]. \tag{4.14}$$

With $s = -\delta + \mathrm{i}\omega$ and having $\omega \gg \delta$ we have $s \approx \mathrm{i}\omega$, which gives

$$\bar{\bar{e}} \approx \frac{K^2}{\Delta l_v - 2b}\left[\frac{T_m}{4}W'_{m,v}W^{*}_{m,v}\Big|_b^{\Delta l_v - b} + \frac{\rho A_c \omega^2}{2}\int_b^{\Delta l_v - b}W_{m,v}W^{*}_{m,v}\mathrm{d}x\right]. \tag{4.15}$$

Considering $\omega \gg \delta$ and $\Delta l_v \gg \lambda$ it is possible to remove the boundary terms from above equation, which are very small because

$$W'_{m,v}(x) =: \frac{\delta}{c}W_{m,v}(x), \tag{4.16}$$

hence

$$TW'_{m,v}W^{*}_{m,v} =: \frac{T_m\delta}{c_m}W_{m,v}W^{*}_{m,v} \quad \Longrightarrow \quad TW'_{m,v}W^{*}_{m,v} =: \frac{T_m\delta}{c_m}\mathcal{O}(W^2_{m,v}) \tag{4.17}$$

where $c_m = \sqrt{\frac{T_m}{\rho A}} = \frac{\omega\lambda}{2\pi}$. With the help of the average value theorem for integral calculus we estimate

$$\int_b^{\Delta l_v - b}W_{m,v}(x)W^{*}_{m,v}(x)\mathrm{d}x \leq \Delta l_v\ \mathcal{O}(W^2_{m,v}) \tag{4.18}$$

and also

$$\omega^2 \Delta l_v \; \mathcal{O}(W_{m,v}^2) \gg \omega\lambda\delta \; \mathcal{O}(W_{m,v}^2) \tag{4.19}$$

for $\omega \gg \delta$ and $\Delta l_v \gg \lambda$. From (4.15) one gets a fairly good approximation of the averaged energy density over time and space as

$$\bar{\bar{e}} \approx \frac{K^2}{\Delta l_v - 2b} \frac{\rho A_c \omega^2}{2} \int_b^{\Delta l_v - b} W_{m,v}(x) W_{m,v}^*(x) \mathrm{d}x. \tag{4.20}$$

From the complex mode shapes $W_{m,v}$, we can obtain the average span amplitude, by taking its quadratic average over the span length as defined by

$$\begin{aligned}
\overline{W_{m,v}^2} &= \frac{1}{(\Delta l_v - 2b)} \int_b^{\Delta l_v - b} W_{m,v}(x) W_{m,v}^*(x) \mathrm{d}x \\
&= \frac{c_m}{2\delta\,(\Delta l_v - 2b)} \Bigg\{ \overline{A}_{m,v}^2 \left(\mathrm{e}^{\frac{-2\delta b}{c_m}} - \mathrm{e}^{\frac{-2\delta(\Delta l_v - b)}{c_m}} \right) - \overline{B}_{m,v}^2 \left(\mathrm{e}^{\frac{2\delta b}{c_m}} - \mathrm{e}^{\frac{2\delta(\Delta l_v - b)}{c_m}} \right) \\
&\qquad + \frac{2\delta}{\omega} \overline{A}_{m,v} \overline{B}_{m,v} \Bigg[\sin\left(\frac{2\omega\,(\Delta l_v - b)}{c_m} + \alpha_{m,v} - \beta_{m,v} \right) \\
&\qquad\qquad - \sin\left(\frac{2\omega b}{c_m} \alpha_{m,v} - \beta_{m,v} \right) \Bigg] \Bigg\}.
\end{aligned} \tag{4.21}$$

It is known that a standing harmonic wave can be represented by two traveling waves with half amplitudes [44]. So, if we transfer this to the view of energy, and replace the wave as expressed in (4.5), in each subspan and in both the directions of oscillations, by *energetically equivalent* standing waves, the following characteristic amplitudes are obtained

$$\hat{A}_{m,v}^c = K \sqrt{2 \overline{W_{m,v}^2}} \tag{4.22}$$

with $v = 1, 2, ..., N+1$ and $m = 1, 2, ..., 2M$, and K as the scaling factor. Hence, if now the wind power input is known, the power dissipation from external damping devices and conductor's self damping as a function of amplitude of conductor vibrations, the energy balance can be performed using (4.2).

The scaling factor K for each vibration frequency can be found using (4.2) and (4.22). The remaining undefined power terms in (4.2) are described in the coming sections. However, if all power terms in (4.2) are known, the computations are made in the following way: the principal modes of oscillations of the bundle in the range of the aeolian vibrations are computed; for each of those modes, assuming an amplitude of vibration at a reference point, the energy dissipated by the system is computed by taking into account the dissipations due to the spacer dampers, STOCKBRIDGE dampers and conductor's self damping. For the same amplitudes of vibration, the energy introduced by the wind is calculated. The difference between the two energies is computed and the value of amplitudes of vibrations are iterated till this difference vanishes. This condition gives the steady state amplitude of vibration, which is further utilized in order to compute the transmission line design parameters as mentioned later in section 4.4. A detailed algorithm for obtaining the scaling factor K using energy balancing is described as follows:

Algorithm for the energy balancing

1. Firstly solve the TEVP in (2.25) with the help of any of the methods described in chapter 2, and obtain the complex system eigenvalues s in the frequency range of interest.

2. For any eigenvalue s, compute the system eigenvectors $A_{m,v}$ and $B_{m,v}$ as described in section 3.4.

3. Assume an initial guess for K, e.g., a value in the range $0 - 1.0$, and compute the characteristic amplitude $\hat{A}^c_{m,v}$ for each subspan and both the planes of oscillation using (4.21) and (4.22).

4. Check if the error $P_W - P_D - P_C \leq \nu$ fulfills the convergence criterion, e.g., $\nu = 10^{-6}$, where P_W, P_D and P_C are the corresponding sums of $P_{W_{m,v}}, P_{D_n}$ and $P_{C_{m,v}}$ respectively, as shown in (4.2). For the optimization, ready-made functions can also be utilized, e.g., for the current analysis the nonlinear optimization function `fsolve` of MATLAB is used.

5. Repeat the steps described above for the next system eigenvalue. The initial guess of K for any eigenvalue, can be taken as the optimized value K corresponding to the previous eigenvalue, which makes the convergence faster.

4.3 Obtaining P_D, P_C and P_W values

Till here we have developed the theoretical background for obtaining the average amplitude of conductor vibrations using energy balancing. The basic relation among different power terms is shown in (4.1). This section briefly describes the wind power input P_W, power dissipated by external damping devices P_D and power dissipation due to conductor's self damping characteristics P_C.

4.3.1 Energy input from the wind

The wind power input P_W is normally computed from the experimentally obtained aerodynamic forces from wind tunnel experiments. It is carried out by measuring the drag and the lift forces on the oscillating cylinders, flexible rods or the cables under uniform laminar cross-flow in the wind tunnel. Many experimental data are available in the literature, e.g., [28, 7, 10, 14, 11, 45, 46, 47, 48]. However, since the experiments have been performed under different experimental conditions and on the rods or cables of different flexibilities, the obtained results differ upto a factor 2, as also shown in figure 5.11.

Such wind power input curves are used for the energy balance analysis of single conductor vibrations (e.g., [1, 2, 21, 5]). In the case of conductor bundles, the flow around an individual subconductor is considerably affected by the presence of other subconductors. Therefore, the same wind power input data as for the single conductor should probably not be used in the case of conductor bundles. On the other hand, due to

many possible conductor bundle combinations regarding the number of the subconductors, their spacing as well as their orientations, wind tunnel tests for the cylinders in bundle configuration are very expensive and formidable. As a result, not enough wind tunnel data is available for conductor bundles. Consequently, in the past, the energy balance analysis of conductor bundles was also performed using the wind power inputs of a single conductor (e.g., [44]). Hence, it is practical to replace the wind tunnel tests by the numerical simulations, which yield a good insight into the dynamic and aerodynamic behavior of the problem. In the present work, numerical studies of wind power input on the single as well as two oscillating cylinders are presented in chapter 5. Presented numerical simulations of the flow around vibrating cylinders use the finite-volume method. Further details of the wind power input computation can be found in chapter 5.

The obtained results for the single cylinder, as shown in figure 5.11 and represented by (5.49), are used for calculating the wind power input on the upstream subconductors. More wind power input curves are obtained for the power input on a downstream cylinder in a cylinder group, as shown in figure 5.24 and represented by (5.55). These curves have been used in the current analysis for obtaining the wind power input on the downstream subconductors.

4.3.2 Energy loss due to external damping devices

As described in chapter 2, the current model incorporates two types of external damping devices attached to the bundle conductor, i.e. spacer damper and groups of Stockbridge dampers. Their respective complex impedance matrices are given, (i.e., Stockbridge damper: [44]; spacer damper: appendix B), relating the forces developed at the damper clamps with the harmonic oscillation velocity of the clamp. The real part of the impedance corresponds to the damping, and causes a phase difference between the oscillation velocities and the forces at the damper clamps. If $\mathbf{F}_{D_n}(t)$ is the vector of the harmonic forces generated at the clamps of n-th damper and $\dot{\mathbf{w}}_{D_n}(t)$ is vector of corresponding harmonic clamp velocities, vibrating with the frequency ω, then the power dissipated by the damper is given by [44]

$$\begin{aligned} P_{D_n} &= \frac{\omega}{2\pi}\int_0^{\frac{2\pi}{\omega}} \left[\mathbf{F}_{D_n}(t)\right]^T \dot{\mathbf{w}}_{D_n}(t)\mathrm{d}t = \frac{\omega}{2\pi}\int_0^{\frac{2\pi}{\omega}} \mathbf{Re}\left[\hat{\mathbf{F}}_{D_n}\mathrm{e}^{\mathrm{i}\omega t}\right]^T \mathbf{Re}\left[\hat{\dot{\mathbf{w}}}_{D_n}\mathrm{e}^{\mathrm{i}\omega t}\right]\mathrm{d}t, \\ &= \frac{1}{2}\mathbf{Re}\left[\hat{\mathbf{F}}^*_{D_n}\hat{\dot{\mathbf{w}}}_{D_n}\right], \end{aligned} \tag{4.23}$$

where $\hat{\mathbf{F}}_{D_n}$ and $\hat{\dot{\mathbf{w}}}_{D_n}$ respectively are the force and the velocity amplitudes at the damper clamps, which using (2.13) and (2.7) respectively become

$$\hat{\mathbf{F}}_{D_n} = \mathbf{Z}_n\hat{\dot{\mathbf{w}}}_{D_n} \qquad \text{and} \qquad \hat{\dot{\mathbf{w}}}_{D_n} = s\hat{\mathbf{w}}_{D_n}. \tag{4.24}$$

Finally the term $P_{D_n}(K\mathbf{W}_{D_n})$ of (4.2) for each spacer damper is computed as

$$P_{D_n} = \frac{(sK)^2}{2}\mathbf{Re}\left[(\mathbf{W}_{D_n})^*\ \mathbf{Z}^*_n\ \mathbf{W}_{D_n}\right] \tag{4.25}$$

where the asterisk stands for "transposed complex conjugate".

Table 4.1: Parameters for the conductor's self-damping

Parameter	Value
N_f	2.91
N_b	1.95
N_t	0.66
C	4.368e-11
P	91710

4.3.3 Power dissipated by conductor's self damping

The power dissipated by the structural damping in conductors is measured by conductor manufacturers and other vibration laboratories. Conductor's self damping is not only a function of amplitude and frequency of vibrations but also of conductor tension. For higher tension the structural damping usually decreases. P_C has been investigated by several authors e.g., [116, 117]. Different laboratories use distinct empirical formulas obtained by the performing experiments with different conductor types. For the present computations the following empirical expression, obtained by the RIBE Electrical Fittings, Germany [17], is used

$$P_{C_{m,v}}(\hat{A}^c_{m,v}) = 2160 \left\{\frac{2\pi}{\omega}\right\}^{N_f} \left\{\frac{180}{\pi} B_{m,v}\right\}^{N_b} \left\{\frac{1}{T_m}\right\}^{N_t} P\ \Delta l_v\ C. \tag{4.26}$$

It is usually assumed that N_f, N_b and N_t are constants for a particular conductor and that C characterizes the damping properties of the particular conductor being considered. The variable $B_{m,v}$ is the vibration angle in radians $\left(= \frac{\pi}{180}\beta = \frac{\pi}{180}\frac{\omega}{c_m}\hat{A}^c_{m,v}\right)$, and is a function of the subspan amplitude and P is the rated tensile strength of the conductor in Newton. $\hat{A}^c_{m,v}$ is the *local* vibration amplitude of the conductor given by (4.22) and ω is the circular frequency corresponding to any system eigenvalue s under consideration. For the current computations, the adopted values of above mentioned parameters are shown in the table 4.1.

4.4 Transmission line design parameters

The scaling factor for each eigenmode of the conductor bundle is obtained using the energy balancing shown in section 4.1. Different transmission line design parameters can now be obtained, after having computed the actual conductor vibrations for each eigenfrequency. Following are the main criteria which are normally used by the transmission line engineers in order to assess the effectiveness of the damping and/or the proneness of the transmission line conductors to fatigue failure:

1. Maximum subspan amplitude A_{max} in each subspan of the transmission line system,

2. $A_{max}f$-value in different subspans of the transmission line system, where $f = 2\pi\omega$,
3. Vibration angles in different subspans,
4. Conductor strains at critical locations, i.e., at clamp-ends and at the points of damper/spacer damper attachment.

Maximum subspan amplitude gives an idea about the severity of vibrations of the conductor in different subspans. Sometimes, it is also normalized by the conductor diameter D. However, it does not directly give any clue of the conductor's stress level. $A_{max}f$-value, which is the multiplication of maximum subspan amplitude to the vibration frequency in Hz, on the other hand, gives an estimate of the velocity of conductor motion corresponding to the maximum vibration amplitude. It is normally represented in mm/sec. Due to its simplicity, it is a popular parameter among transmission line engineers. A nominal value of 118 mm/sec is accepted as a target value [17] for $A_{max}f$. A similar parameter called "vibration angle" ($\beta = 2\pi A_{max}f/c$) is also used as a design parameter, where c is the wave velocity defined in (2.8). It is also referred as bending angle of the conductor corresponding to the maximum subspan amplitudes, given in radians. Although $A_{max}f$ and β do not directly give the actual stress levels in the conductor, yet when plotted against vibration frequencies they have a similar trend as the conductor strains. Conductor strain, however, is the only parameter among all mentioned above, which can directly be interpreted in terms of conductor stress levels, and hence, gives the closest estimation of the severity of conductor motion at the critical positions. A detailed description of the computation of strain levels at critical locations on the subconductors is given in the next section.

4.4.1 Computation of conductor strains at critical locations

For the calculation of eigenfrequencies and eigenmodes it is assumed in (2.3) and in (2.4) that the string is as usual clamped at the suspensions. Thus, kinks, as explained in [1], are caused in a string at the suspension positions and also at the points of damper clamps attachment. Perturbation techniques presented by Hagedorn [2] compute the bending strains not only at those locations, but also in the free field[10], where stationary vibrations with certain amplitude are caused. It was also shown in [2] that extremely simple formulas obtained by perturbation techniques can be used to correct the results obtained from the string equation in the neighborhood of concentrated forces, where bending boundary layers occur. The perturbation analysis presented in [2] will not be repeated here. Instead we directly take the results obtained for computing the bending strains at the suspension clamps and at the points of damper attachments.

Bending strains are obtained in the outer strand of the conductor using

$$\varepsilon(x,t) = \frac{d}{2}w''(x,t), \tag{4.27}$$

[10]The term "bending boundary layer" refers to the localized zones of bending stresses and deformations where the effect of bending is predominant. Bending boundary layers are caused by the edge support conditions; by localized mechanical loads, heating, or cooling, or by abrupt changes in the stiffness. Any location at the conductor which is out of bending boundary layer is called to be in the "free field".

where d is the diameter of the outer conductor strand and w'' is the curvature of the conductor at the point where strains are being computed. Using the perturbation technique described in [2], strains at any point in the free field (4.27) is

$$\varepsilon_1 = \hat{A}\left(\frac{2\pi}{\lambda}\right)^2 \frac{d}{2} \tag{4.28}$$

where ε_1 denotes the maximum strain at any point located in the free field for an oscillation amplitude $\hat{A}$, and λ is the wave length given by the relation $\lambda = 2\pi c/\omega$.
Strains at the points located in vicinity either of the suspension clamps or of the points of damper attachments are given by

$$\varepsilon_2 \cong A\left(\frac{2\pi}{\lambda}\right)\sqrt{\frac{T}{EI}}\left(\frac{d}{2}\right), \tag{4.29}$$

where T is the conductor tension and EI is its bending stiffness. An analogy with (4.29) gives the strains at the critical positions for damped system as,

$$\varepsilon_2 \cong \frac{w'_{eff}}{l_{char}}\left(\frac{d}{2}\right), \tag{4.30}$$

where w'_{eff} is the effective slope at the suspension clamps or at the damper clamps, and l_{char} is the characteristic conductor length. The effective slope is given for different conditions as:

- for fixed end-clamps: $(w'_{eff})_{0,L} = W'|_{x=0,L}$,
- for r-th STOCKBRIDGE damper with zero clamp width:
  $(w'_{eff})_r = W'_r|_{x=l_r} - W'_{r-1}|_{x=l_r}$,
- for n-th spacer damper clamp with a clamp width of $2b$:
  $(w'_{eff})_n = W'_n|_{x=l_n} - (W'_{clamp})_n$, where $W'_{clamp} = \frac{W_n|_{x=(l_n+b)} - W_{n-1}|_{x=(l_n-b)}}{2b}$.

In (4.29) EI is an equivalent bending stiffness which is obtained experimentally. The value EI normally is between two extreme conductor stiffness values, one which is obtained with an assumption of no inter-strand movement in the conductor EI_{max} and the other which corresponds to free inter-strand movement EI_{min}. However, in the current analysis $EI = EI_{min}$ is considered in order to obtain the strain values in the outer most strand of the conductor, which has a diameter of d.
As already mentioned in section 2.1.1, in the case of a conductor bundles, the conductors vibrate not only in the vertical plane but also in the horizontal plane. Because of such a situation, the conductor vibrations and, hence, the strains at the critical locations in both the planes need to be combined together in order to obtain the resultant strains. However, because of a phase difference between the horizontal and the vertical waves obtaining the resultant amplitudes or the strains is not very straight forward. The following section explains how to compute the resultant amplitudes of two mutually perpendicular waves with same frequency but different phases. Resultant strains can also be obtained by calculating resultant effective angle in the similar way as explained in the next section and using (4.30).

4.4.2 Computation of the resultant amplitude

This section shows how to obtain the resultant amplitude of two waves oscillating in perpendicular planes. A similar approach can also be used when one wants to obtain the resultant strain due to two mutually perpendicular motions of the conductor. It is to be noted in the current case that since we are interested in obtaining the resultant amplitude and the strains for each eigenfrequency, we shall consider two waves with the same vibration frequency but with a finite phase difference. If two mutually perpendicular simple harmonic motions are defined by,

$$x = a\sin(\omega t), \qquad \text{and} \qquad y = b\sin(\omega t + \delta), \tag{4.31}$$

as shown in figure 4.3a, where x is the motion of the horizontal wave and y is the motion of the vertical wave at any time instant t. The resultant path of a particle possessing motions in both the perpendicular directions will be elliptical, as shown in figure 4.3b, if both the separate waves oscillate with vibration frequency ω and a phase difference δ.

Two waves in (4.31) are compound by the elimination of time t, which results in the equation of an ellipse tilted by an angle φ:

$$\frac{x^2}{a^2} - \left(\frac{2xy}{ab}\right)\cos\delta + \frac{y^2}{b^2} - \sin^2\delta = 0, \tag{4.32}$$

as is shown in figure 4.4. It is also called as Lissajous figure, which is a plot of y versus x as t is varied. It can be noted that for zero phase difference between the two waves (i.e., $\delta = 0$) or the opposite phase between them (i.e., $\delta = \pi$) the ellipse of (4.32) degenerates into a straight line, as shown in figure 4.1a and b:

$$\frac{x}{a} \pm \frac{y}{b} = 0, \tag{4.33}$$

for which the resultant amplitude of the motion is simply given by

$$R = \sqrt{a^2 + b^2}. \tag{4.34}$$

On the other hand, for $\delta = \pi/2$, the expression (4.32) results in:

$$\frac{x^2}{a^2} + \frac{y^2}{b^2} = 1, \tag{4.35}$$

which is an ellipse whose major and minor axes coincide with either of x and y axes, with the lengths of major and minor axes being either of a and b, as shown in figure 4.2a and b. Hence, the resultant amplitude of the combined motion is

$$R = \max(a, b). \tag{4.36}$$

Difficulty arises with $0 < \delta < \pi/2$, when the resulting ellipse of Lissajous figure is tilted with an angle φ, as shown in figure 4.3 and 4.4. As one can see in figure 4.4 that the resultant amplitude is no longer given by (4.34), and rather is half of the major axis of rotated ellipse. However, in order to determine the length of major axis of the

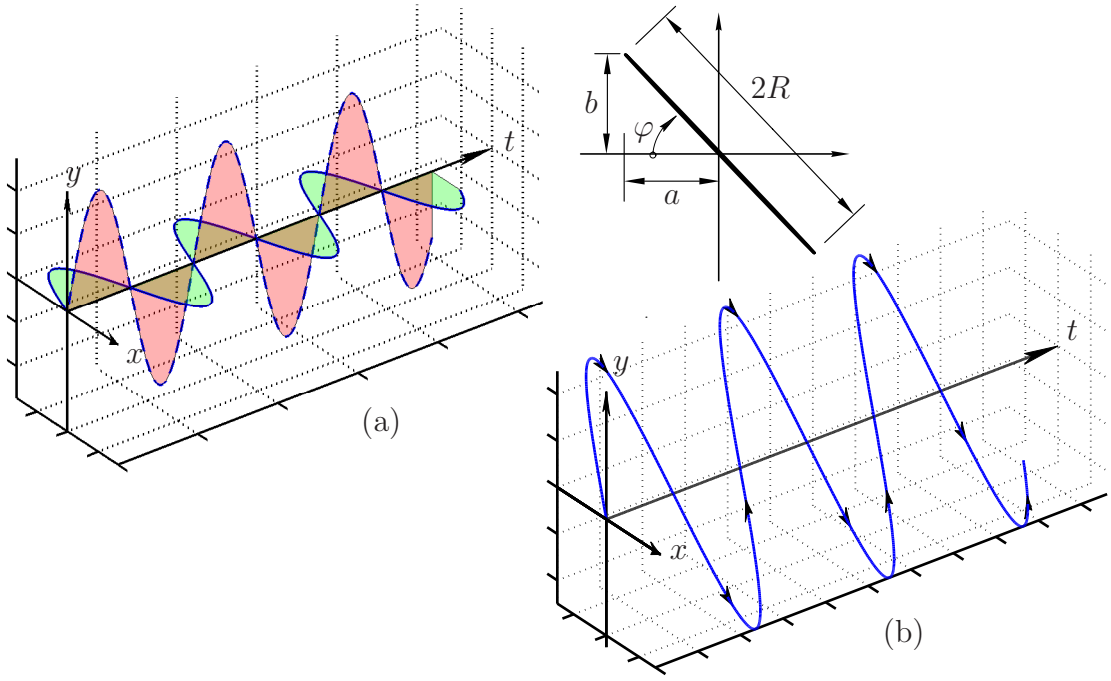

Figure 4.1: A horizontal and a vertical wave for $\delta = 0$

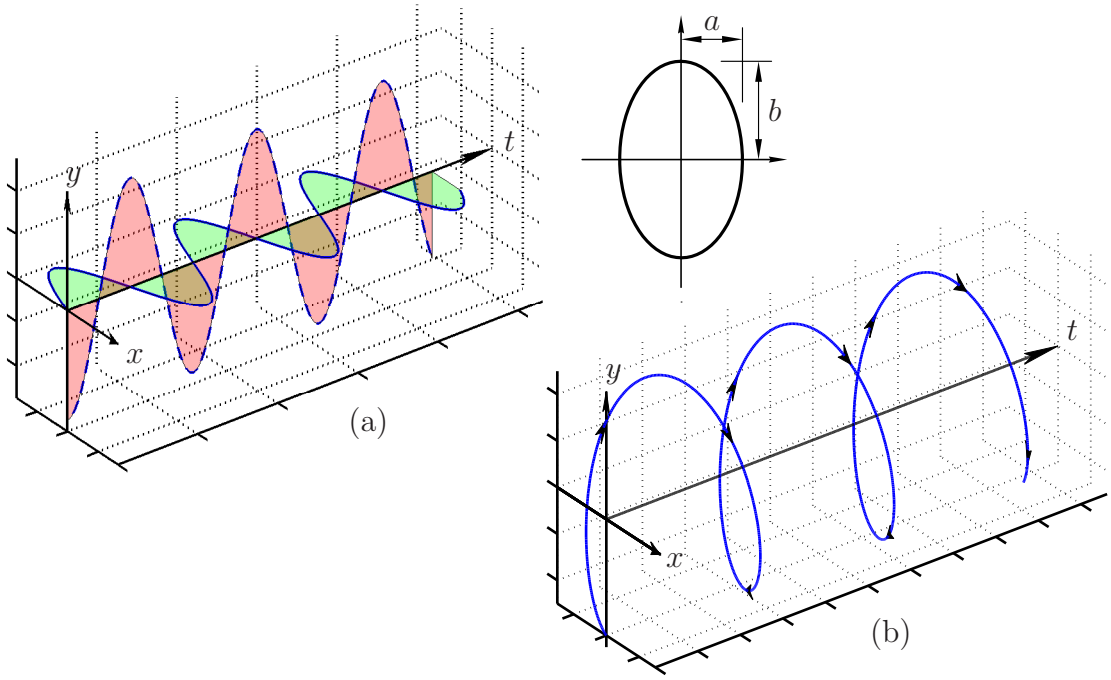

Figure 4.2: A horizontal and a vertical wave for $\delta = \pi/2$

rotated ellipse it is now required to rotate the axis system x, y by an angle φ to x_1, y_1. When the axis system is so rotated, the equation of ellipse (4.32) written in terms of x_1 and y_1 will only be containing the terms having x_1^2, y_1^2 and the constant term, and it will be free from the term containing the multiplication $x_1 y_1$. The rotated coordinate

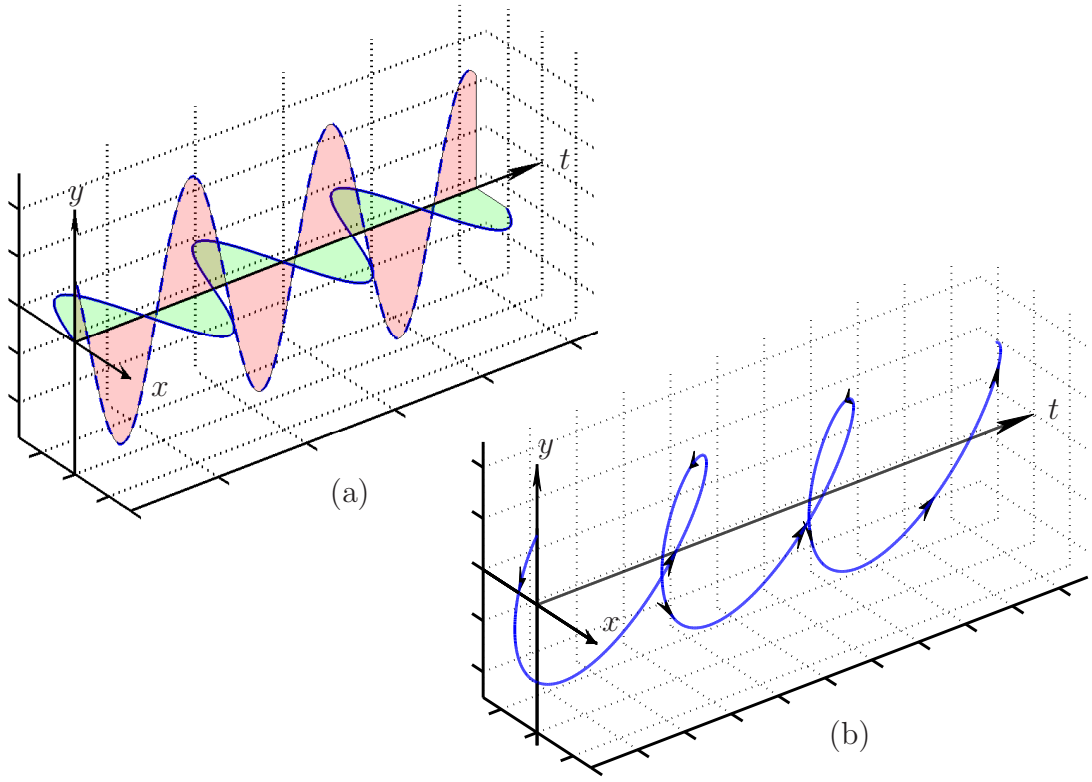

Figure 4.3: A horizontal and a vertical wave for $0 < \delta < \pi/2$

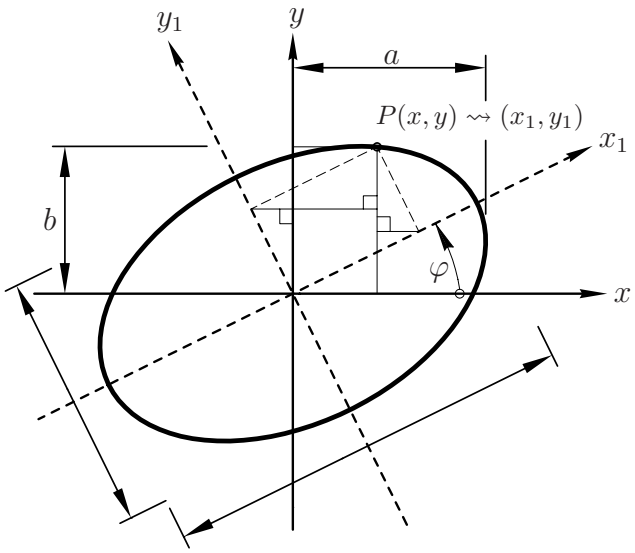

Figure 4.4: LISSAJOUS plot for $0 < \delta < \pi/2$

system is related to the original system by (refer figure 4.4)

$$x = x_1 \cos\varphi - y_1 \sin\varphi, \tag{4.37}$$

$$y = x_1 \sin\varphi + y_1 \cos\varphi. \tag{4.38}$$

Let us write (4.32) as

$$Ax^2 + Bxy + Cy^2 + F = 0, \tag{4.39}$$

where

$$A = \frac{1}{a^2}; \quad B = -\left(\frac{2\cos\delta}{ab}\right); \quad C = \frac{1}{b^2}; \quad \text{and} \quad F = -\sin^2\delta. \tag{4.40}$$

Substituting the values of x and y from (4.37) and (4.38) gives the equation in terms of rotated axes coordinates as:

$$\begin{aligned} &x_1^2[A\cos^2\varphi + B\sin\varphi\cos\varphi + C\sin^2\varphi] \\ &+x_1y_1[-A\sin 2\varphi + B\cos 2\varphi + C\sin 2\varphi] \\ &+y_1^2[A\sin^2\varphi - B\sin\varphi\cos\varphi + C\cos^2\varphi] + F = 0. \end{aligned} \tag{4.41}$$

Since, rotating the axes by an angle φ should result in zero multiplication factor for x_1y_1-term. Equating the multiplier of x_1y_1 to zero in (4.41) results:

$$\tan 2\varphi = \frac{B}{A - C}. \tag{4.42}$$

The tilting angle φ of the ellipse can now be obtained using (4.42). Moreover, (4.42) also result in

$$\sin 2\varphi = \frac{B}{\sqrt{(A-C)^2 + B^2}}; \quad \text{and} \quad \cos 2\varphi = \frac{(A-C)}{\sqrt{(A-C)^2 + B^2}}, \tag{4.43}$$

which further gives

$$\sin\varphi = \sqrt{\frac{1}{2}\left[1 - \frac{(A-C)}{\sqrt{(A-C)^2 + B^2}}\right]}; \quad \cos\varphi = \sqrt{\frac{1}{2}\left[1 + \frac{(A-C)}{\sqrt{(A-C)^2 + B^2}}\right]}. \tag{4.44}$$

Now, with the values of $\sin\varphi$ and $\cos\varphi$ in (4.41) one can finally obtain the equation of tilted ellipse with request to x_1 and y_1 axes, which coincides with the major and minor axes of the ellipse, in the form

$$A_1x_1^2 + C_1y_1^2 + F_1 = 0, \tag{4.45}$$

where

$$A_1 = [A\cos^2\varphi + B\sin\varphi\cos\varphi + C\sin^2\varphi]; \tag{4.46}$$

$$C_1 = [A\sin^2\varphi - B\sin\varphi\cos\varphi + C\cos^2\varphi]; \tag{4.47}$$

$$\text{and} \quad F_1 = F. \tag{4.48}$$

Relation (4.45) is the equation for an ellipse with major and minor axes length of $2\sqrt{-F_1/A_1}$ and $2\sqrt{-F_1/C_1}$ respectively. Finally, the resultant amplitude of two mutually perpendicular waves having a finite phase difference between them is the half of the length of major axis of this ellipse, which is

$$R = \max\left[\sqrt{\frac{-F_1}{A_1}}, \sqrt{\frac{-F_1}{C_1}}\right]. \tag{4.49}$$

Using (4.40), (4.44), (4.46), (4.47) and (4.48) one can now obtain the resultant R.

The same approach can also be used to obtain the resultants of the effective angles at the critical locations on the conductor (i.e., at the end-clamps and at the points of damper attachment). After obtaining the resultant effective angles at the critical positions, strains can be easily computed using (4.30).

4.5 Results for the benchmark problem-2

Section 3.6.2 shows the obtained eigenvalues for the second benchmark problem. The respective mode shapes are obtained using the approach described in section 3.4. Energy balancing is performed and scaling factors are obtained in order to compute the actual conductor vibration amplitudes in horizontal and vertical planes of motion, for each eigenfrequency. Using the approach shown in section 4.4.2, resultant amplitudes are then computed. Different transmission line design parameters, as described in the section 4.4, are obtained for the benchmark problem-2. In order to demonstrate the effectiveness of the attached spacer dampers, similar design parameters are also obtained for the same benchmark problem but without any spacer damper. The obtained results are compared in figures 4.5-4.8.

Figure 4.5 shows the obtained maximum of resultant span amplitudes corresponding to each eigenfrequency. In the plot discrete points correspond to the maximum span amplitude of the conductor bundle with spacer dampers, whereas, the continuous line corresponds to the maximum span amplitude when no spacer damper is attached. It can be seen that even when there is no spacer damper attached, the maximum span amplitude decreases for increasing frequencies. This is mainly due to the higher conductor curvature for higher vibration frequencies, which causes more inter-strand motions. Hence, the conductor's self damping increases because of the energy loss due to friction in the inter-strand motion. However, in the low frequency zone, where conductor's self damping is not high enough, the maximum amplitudes are much higher when no spacer damper is attached. Figure 3.7 shows that the presence of spacer dampers results in higher damping ratios in the lower frequency zone. Hence, attaching spacer dampers helps to keep the amplitudes smaller, which is clearly noticeable in the figure 4.5. On its right y-axis figure 4.5 also shows the ratio of maximum span amplitude with the conductor diameter, for each frequency.

Figures 4.6 and 4.7 respectively compare the $A_{max}f$-value and vibration angle for the conductor bundle with spacer dampers and without spacer damper. Figure 4.8 shows the maximum strains at critical points with respect to the vibration frequencies. All figures show that the incorporation of the spacer dampers helps controlling the transmission line design parameters, and hence helps in extending the conductor life by avoiding the fatigue failures. It is to be noticed here that, although, the $A_{max}f$-value is under prescribed limit (i.e., 118 mm/sec) even without any spacer dampers, yet maximum strains are well above the desirable limit of 150 μm/m, when no spacer damper is attached. Hence, it is required to attach the additional spacer dampers in order to keep the conductor strains and, hence, the stresses under the desirable limits.

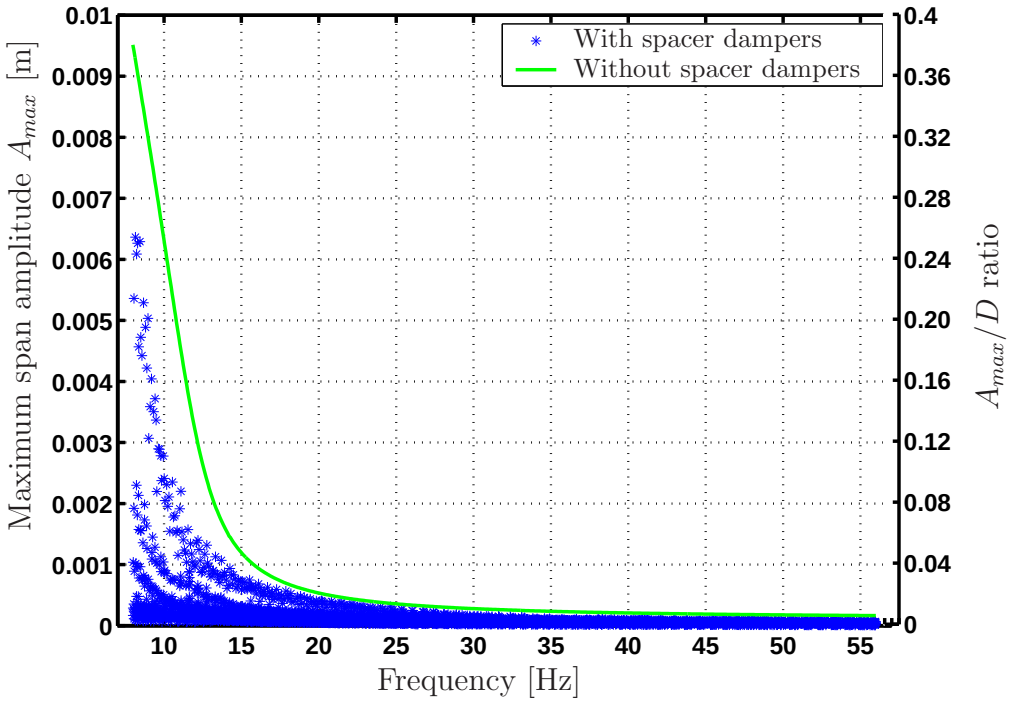

Figure 4.5: Comparison of maximum span amplitude for conductor bundle system with and without spacer dampers

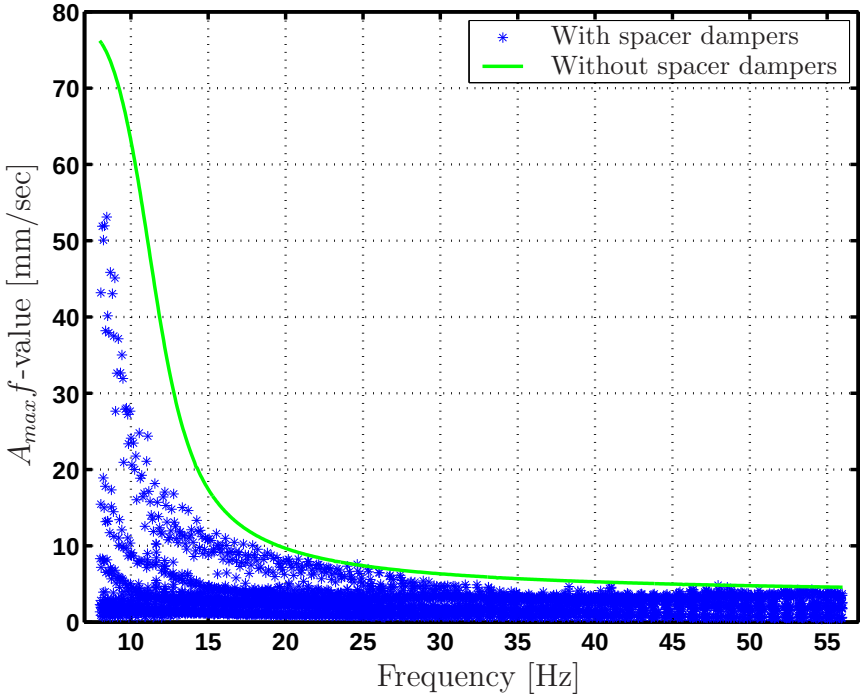

Figure 4.6: Comparison of $A_{max}f$-value for conductor bundle system with and without spacer dampers

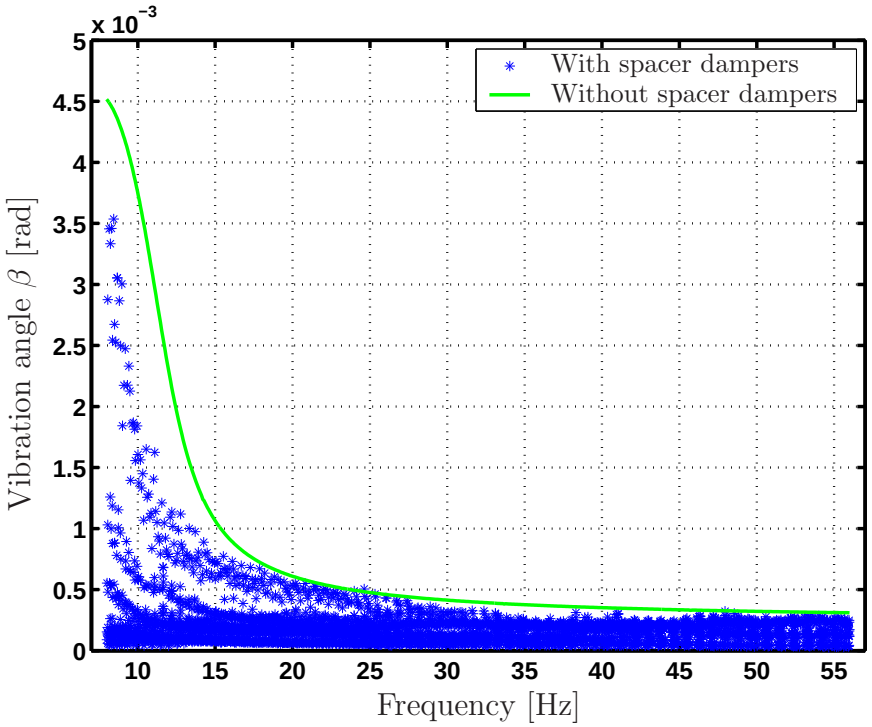

Figure 4.7: Comparison of vibration angle for conductor bundle system with and without spacer dampers

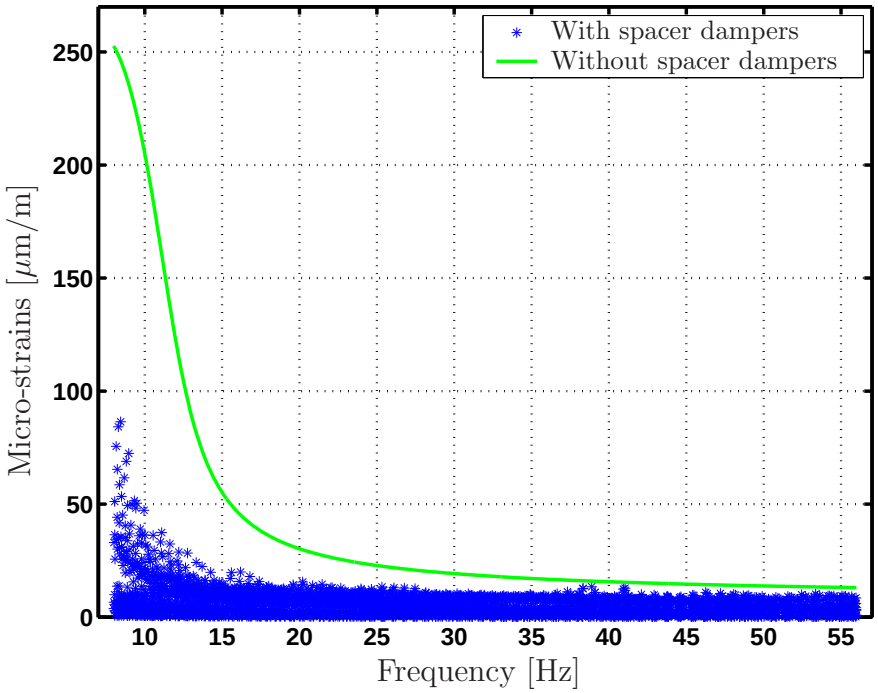

Figure 4.8: Comparison of maximum strains at critical points for conductor bundle system with and without spacer dampers

Chapter 5

Numerically obtaining the wind power input

Summary: This chapter presents a numerical approach to compute the power imparted by wind on oscillating cylinders. Flow around rigid and moving cylinders is modeled using computational fluid dynamics. After solving the Navier-Stokes *equation for the flow, drag and lift forces are computed on the surface of the oscillating cylinder, for different frequencies and amplitudes of the cylinder oscillations. Firstly, the flow around a single cylinder is analyzed and the obtained wind power input is compared with available experimental data. Two cylinders in a tandem arrangement are analyzed next in order to obtain the wind power input on the oscillating downstream cylinder. In the end, the wind power input from the single cylinder is compared with that of the downstream cylinder in a tandem arrangement, and the results are discussed.*

5.1 Introduction

The study presented in this chapter is a first step toward numerically obtaining the power imparted by wind on the different configurations of two vibrating cylinders in a tandem arrangement. The flow around cylinders is simulated using the finite-volume method. The present work is concerned only with the 2D analysis in order to make the study simpler. A parallel version of finite volume flow solver Fastest2d [118, 119, 120] is utilized for the solution of the fluid dynamics problem, which is developed in the Technische Universität Darmstadt, Germany[11]. Moving grids are used to incorporate the cylinder motion, which at each time step adapt to a new configuration.

An essential task in introducing the numerical simulation in this field is the experimental validation of the reliability of the numerical data. In this regard, firstly the reliability of the program is tested by solving the flow around a rigid (i.e., not moving) single cylinder. The drag and the lift forces are computed and compared to available experimental test data. In the next step a forced sinusoidal motion in cross-flow direction is given to the cylinder in order to study the interaction of the cylinder motion with the fluid (i.e., the wind). The drag and the lift forces are, then, calculated by integrating the pressure and the shear values over the cylinder boundary, which cause the impartation of the wind power. The numerically obtained wind power input is later compared to that obtained by different researchers in wind tunnel tests [121].

A good match between the experimental and the numerical results for the wind power input is found, which is shown in the coming sections (refer figure 5.11). In the third step, a more complicated problem of the flow around two rigid cylinders in a

[11] in the group of Prof. M. Schäfer.

tandem arrangement is simulated. Experimental data for the time averaged drag and lift coefficients, for different configurations of two cylinders in a tandem, are available [122]. Numerically computed time-averaged lift and drag forces are compared to available experimental data, in order to understand the interaction of the wake coming from the upstream cylinder with the downstream one. In the last part of the analysis, both the cylinders in a tandem are oscillated with a sinusoidal motion with finite phase differences. Wind power input is, then, computed on the oscillating downstream cylinder using a similar technique, as was done in the previous case of a single cylinder. The wind power input of an isolated cylinder is compared to the power input on the downstream cylinder of a tandem configuration. A major difference in the two wind power inputs is noticed. Results are discussed in detail, which makes it clear why it is not appropriate to use the wind power input data of an isolated cylinder for the analysis of the conductor bundles.

5.2 Elementary equations of the fluid flow

The numerical analysis of fluid flow is based on the discretization of the fundamental fluid equations. This section summarizes the basic equations as they are needed for the understanding of the subject. Fundamental equations for fluid dynamics are based on the conservation of mass, momentum and energy, which altogether lead to the Navier-Stokes equations. These equations are comprised of a number of coupled, nonlinear partial differential equations with no general solution. Analytical solutions can only be found for a very small class of special problems, so that numerical solutions have to be sought in general. Detailed derivations of these equations can be found in fundamental books on fluid dynamics, e.g., [123, 124]. The coming section gives a brief idea about Navier-Stokes equations.

5.2.1 Conservation laws

The conservation law for an extensive property relates the rate of change of its amount in a given quantity of matter (e.g., mass, volume etc.) to externally determined effects. It is derived by considering a given quantity of matter, called *control mass* (CM), and its extensive properties, i.e., mass, momentum and energy. However, in fluid flow it is difficult to follow a part of matter (i.e., CM), which quickly passes through the region of interest. Therefore, in the case of fluids it is more convenient to deal with the flow within a certain spatial region called *control volume* (CV). This method of analysis is called the *control volume approach* and in such an approach, the property balance is formulated for a closed CV. The flux properties are then related in turn to the corresponding material characteristics by means of the constitutional laws, which ultimately leads to the Navier-Stokes equations. These equations are later simplified under appropriate circumstances, pertaining to the compressibility or thermal activities etc., of the flow.

In what follows, the energy equation is skipped, because this particular case is of no interest for the present problem, as we neglect changes related to temperature. It is to be noted here that the nomenclature used in this chapter is standard as used in fluid

dynamics text books. It should not to be confused with what is used in the previous chapters.

Conservation of the mass

The principle of mass conservation states that mass is neither created nor destroyed. Hence, the rate of change of mass in time for a system is equal to the rate of change of mass within the CV taking into account the net flux through the system boundaries. The equation of mass conservation is expressed by the *continuity equation*

$$\frac{\partial \rho}{\partial t} + (\nabla . \rho \boldsymbol{v}) = 0, \tag{5.1}$$

where t stands for time, $\boldsymbol{v}$ for velocity and ρ for the fluid density. ∇ is the standard NABLA operator. Finite volume methods use the integral form of (5.1), which is written as

$$\frac{\mathrm{d}}{\mathrm{d}t} \int_{\Omega} \rho \mathrm{d}\Omega + \int_{S} \rho \boldsymbol{v} \cdot \boldsymbol{n} \mathrm{d}S = 0, \tag{5.2}$$

where Ω stands for the volume occupied by the CV, S is the surface enclosing CV and $\boldsymbol{n}$ is the unit vector orthogonal to the surface S, directed outward.

Conservation of the momentum

Momentum can be changed by the action of forces and its conservation equation is given by NEWTON's second law of motion. The momentum equation relates the rate of change of momentum of a fluid system to the sum of the body forces and the surface forces acting on the system. It is an empirical equation where the surface forces are included in CAUCHY's stress tensor $\mathbf{T}$, which is composed of a diagonal normal stress tensor, pressure and the shear tensor, as

$$\frac{\partial \rho \boldsymbol{v}}{\partial t} + [\nabla \cdot \rho (\boldsymbol{v}\boldsymbol{v})] = [\nabla \cdot \mathbf{T}] + \rho \boldsymbol{b}. \tag{5.3}$$

Although, in the present problem there are no body forces $\boldsymbol{b}$, yet for the sake of completeness they are being included here. Applying the GAUSS divergence theorem to (5.3), a coordinate-dependent integral form is obtained as

$$\frac{\mathrm{d}}{\mathrm{d}t} \int\limits_{\Omega} \rho \boldsymbol{v} \mathrm{d}\Omega + \int\limits_{S} \left[\rho \boldsymbol{v}\boldsymbol{v} \cdot \boldsymbol{n}\right] \mathrm{d}S = \int\limits_{S} \mathbf{T} \cdot \boldsymbol{n} \mathrm{d}S + \int\limits_{\Omega} \rho \boldsymbol{b} \, \mathrm{d}\Omega. \tag{5.4}$$

The surface forces due to the pressure and the stresses, from the molecular point of view, are the microscopic momentum flux across a surface. If these fluxes can not be written in terms of the properties whose conservation equations govern (i.e., density and velocity), the system of equation is not closed. It means that there are fewer equations than dependent variables, and hence, the solution is not possible. It is avoided by formulating constitutive relations. It is assumed here that the fluid is Newtonian. For

Newtonian fluids, the stress tensor $\mathbf{T}$, which is the molecular rate of transport of the momentum, is written as

$$\mathbf{T} = -\left[p + \frac{2}{3}\mu\left(\nabla \cdot \boldsymbol{v}\right)\right]\mathbf{I} + 2\mu\mathbf{D}, \tag{5.5}$$

where μ is the dynamic viscosity of fluid, $\mathbf{I}$ is the unit tensor, p is the static pressure and $\mathbf{D}$ is the deformation tensor, given by

$$\mathbf{D} = \frac{1}{2}\left[\nabla \cdot \boldsymbol{v} + \left(\nabla \cdot \boldsymbol{v}\right)^T\right]. \tag{5.6}$$

5.2.2 The Navier-Stokes equations

This section summarizes the conservation equations and derives the Navier-Stokes equations in a differential form. For incompressible fluids the time derivative of the density vanishes, and in index notation the continuity equation is written as

$$\frac{\partial u_j}{\partial x_j} = 0, \tag{5.7}$$

where x_j and u_j (j=1,2,3) are the cartesian coordinates and the components of the velocity vector respectively. The corresponding momentum conservation equation for the i-th component is

$$\frac{\partial(\rho u_i)}{\partial t} + \frac{\partial\left(\rho u_i u_j\right)}{\partial x_i} = \frac{\partial T_{ij}}{\partial x_i} + \rho b_i \qquad \forall j = 1, 2, 3. \tag{5.8}$$

Equations (5.5) and (5.6) are written in index notation in as

$$T_{ij} = -\left[p + \frac{2}{3}\mu\frac{\partial u_j}{\partial x_j}\right]\delta_{ij} + 2\mu D_{ij}, \tag{5.9}$$

and

$$D_{ij} = \frac{1}{2}\left[\frac{\partial u_i}{\partial x_j} + \frac{\partial u_j}{\partial x_i}\right], \tag{5.10}$$

where δ_{ij} is the Kronecker delta[12] symbol . The material law (5.9) is combined with the equation of motion (5.8), in order to give the differential form of the Navier-Stokes equations for incompressible fluids as

$$\rho\left[\frac{\partial u_i}{\partial t} - u_j\frac{\partial u_i}{\partial x_j}\right] - \frac{\partial}{\partial x_j}\left[\mu\left(\frac{\partial u_i}{\partial x_j} + \frac{\partial u_j}{\partial x_i}\right)\right] + \frac{\partial p}{\partial x_i} = \rho b_i. \tag{5.11}$$

5.3 Introduction to the finite volume methods

This section deals with the basics of finite volume methods (FVM) as employed in Fastest2d [118, 119, 120] code. The first step in obtaining a numerical solution is to discretize the generic domain, i.e., a numerical grid is defined. For the sake of simplicity an equidistant cartesian grid is taken, as shown in figure 5.1.

[12]Kronecker delta is defined as: $\delta_{ij} = 1$ for $i = j$; $\delta_{ij} = 0$ for $i \neq j$.

Discretization of the flow field

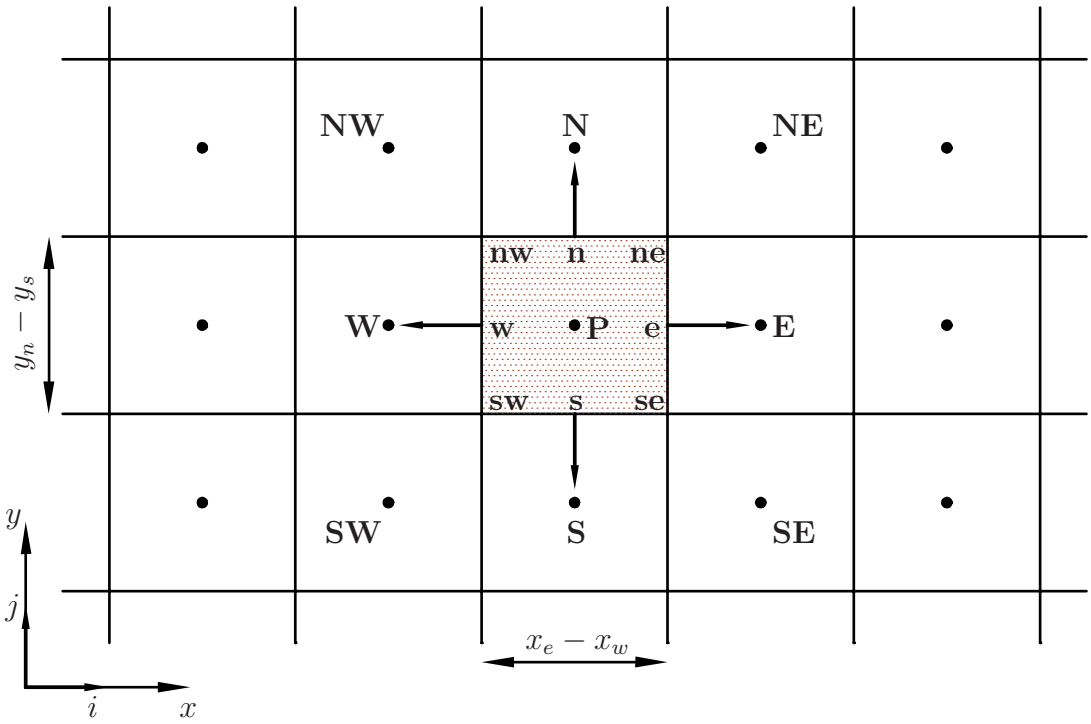

Figure 5.1: 2D cartesian grid: CV, its neighbor edge and corner points

The starting point of the analysis is the integral form of the Navier-Stokes equations (5.11), obtained through the integration over a CV. The solution domain is subdivided into a finite number of small CVs by the grid. The usual practice is to define CVs using a suitable grid and assign the computational nodes to the centers of CV's. The equations are solved for each CV in the fluid domain. This gives rise to the important characteristic of the finite volume discretization, which is the conservation of the applied discretization. Conservation is maintained for each CV and thus consequently on the global level.

For discretization-methods used the in Fastest2d, the grid is locally structured, i.e. each grid node may be considered as the origin of a local coordinate system, where axes coincide with the grid lines [120]. It implies that two grid lines belonging to the same family do not intersect, and also, any pair of the grid lines belonging to different families intersect only once, as shown in figure 5.1. Each node is uniquely identified by a set of indices, which define the grid lines that intersect at it, i.e. (i, j) for a grid in two dimensional (2D) domain. The neighboring nodes are implicitly defined by increasing or decreasing one of the indices by unity.

Different approximation schemes are used in order to evaluate the diffusive (i.e., viscous) and convective parts of the surface integrals, and the volume integral. The volume integral is approximated by the second-order midpoint rule. The diffusive term is approximated using a Central-Differencing Scheme (CDS) [120]. For the convective part an Upwind-Differencing Scheme (UDS), CDS or any user-defined blending of both schemes [120] can be employed by the Fastest2d in order to achieve high stability and accuracy at the same time. CDS provides a second-order accurate solution and

is used in the present work. In what follows, the discretization of the convective and the diffusive terms is briefly explained. The characteristics of the the analyzed flow are unsteady. The time discretization strategy is presented thereafter. The second-order CRANK-NICHOLSON [120] scheme is employed for all computations in the coming sections.

Discretization of the continuity equation

The discretized continuity equation is developed by expressing the terms $\boldsymbol{v}$ and $\boldsymbol{n}$ in the cartesian coordinates and approximating the surface integral as a sum of the related values on the CV faces-e, w, s and n (viz., east, west, south and north), as indicated in the figure 5.1. If velocity components in i and j directions, for $i = j = 1, 2$, in the index notations are expressed as u and v, then

$$\int_S \rho \left(u n_1 + v n_2\right) \mathrm{d}S = \sum_c \underbrace{\rho \left(u n_1 + v n_2\right) \delta S_c}_{m_c} = 0, \tag{5.12}$$

where the term δS_c defines the face length of the CV and subscript c stands for the cell faces (i.e., e, w, s and n). Considering geometrical dimensions of the CV and applying the second order mid-point-rule, final assembly of the continuity equation results in

$$\left(u_E - u_W\right) \Delta y + \left(u_N - u_S\right) \Delta x = 0. \tag{5.13}$$

Discretization of the momentum equation

The discretization of the momentum equation is shown here only for the x-direction, the same applies for the y-direction. The temperature effect is assumed to be negligible, and hence, the viscosity μ is constant. Discretization of (5.4) leads to

$$\underbrace{\rho \int_\Omega \frac{\partial u}{\partial t} \mathrm{d}\Omega}_{(I)} + \underbrace{\rho \int_S \left(u u n_1 + v u n_2\right) \mathrm{d}S}_{(II)} - \underbrace{\mu \int_S \left(\frac{\partial u}{\partial x} n_1 + \frac{\partial u}{\partial y} n_2\right) \mathrm{d}S}_{(III)} = - \underbrace{\int_\Omega \frac{\partial p}{\partial x} \mathrm{d}\Omega}_{(IV)} + \underbrace{\rho \int_\Omega b_1 \mathrm{d}\Omega}_{(V)}. \tag{5.14}$$

Description of the terms:

Transient term (I) An unsteady flow is considered as the sequential solution of steady levels. As mentioned earlier, the second order CRANK-NICHOLSON scheme, with an equal blending of the implicit and the explicit methods, is used for all calculations. Hence,

$$\rho \int_\Omega \frac{\partial u}{\partial t} \mathrm{d}\Omega \approx \rho \frac{\partial u_P}{\partial t} \delta\Omega \approx \rho \frac{u_P^{n+1} - u_P^n}{\Delta t_n} \delta\Omega, \tag{5.15}$$

where $\Delta t = (t_{n+1} + t_n)/2$. Rearranging the terms and putting the values of $\delta\Omega = \Delta x \Delta y$ yield

$$\rho \int_\Omega \frac{\partial u}{\partial t} \mathrm{d}\Omega \approx \underbrace{\frac{\rho \Delta x \Delta y}{\Delta t_n} u_P^{n+1}}_{a_P^{T,u}} - \underbrace{\frac{\rho \Delta x \Delta y}{\Delta t_n} u_P^n}_{b_P^{T,u}}. \tag{5.16}$$

Convective term (II) The convective term is discretized similarly to the continuity equation

$$\int_S \rho \left(uun_1 + vun_2\right) \mathrm{d}S \approx \sum_c \left[\rho \left(uun_1 + vun_2\right)\right]_c \delta S_c = \sum_c m_c u_c, \tag{5.17}$$

where the subscript c stands again for the cell faces. The mass flux m_c, e.g., through the south cell face, is approximated by

$$(m_c)_s = \rho v_s \left(x_{sw} - x_{se}\right), \tag{5.18}$$

where $v_s = (v_P + v_S)/2$. Multiplying both sides by $(m_c)_s$ yields

$$(m_c)_s v_s = \underbrace{\frac{1}{2}(m_c)_s v_P}_{a_P^{C,v}} + \underbrace{\frac{1}{2}(m_c)_s v_S}_{a_S^{C,v}}. \tag{5.19}$$

Diffusive term (III) In order to approximate the diffusive term a (CDS) is applied, which leads to a second order approximation error as

$$\int_S \left(\mu \frac{\partial u}{\partial x} n_1 + \mu \frac{\partial u}{\partial y} n_2\right) \mathrm{d}S \approx \sum_c \left(\mu \frac{\partial u}{\partial x} n_1 + \mu \frac{\partial u}{\partial y} n_2\right)_c \delta S_c, \tag{5.20}$$

where, e.g., for the south cell face

$$\mu \frac{\partial u}{\partial y} n_2 \; \delta S_c \approx \mu \frac{v_S - v_P}{\Delta y} \Delta x = \underbrace{\mu \frac{\Delta x}{\Delta y} v_S}_{a_S^{D,v}} - \underbrace{\mu \frac{\Delta x}{\Delta y} v_P}_{a_P^{D,v}}. \tag{5.21}$$

Pressure term (IV) The pressure gradient term is approximated by the pressure on the cell faces. Since they are also not known, they are evaluated first using the values on the cell centers. The volume of the cell is given by $\delta\Omega = \Delta x \Delta y$. Hence, the discretized equation becomes

$$\int_\Omega \frac{\partial p}{\partial x} \mathrm{d}\Omega \approx \frac{p_e - p_w}{\Delta x} \delta\Omega \approx \underbrace{\frac{1}{2} \Delta y \left(p_e - p_w\right)}_{a_P^{P,u}}. \tag{5.22}$$

Source term (V) The mid point rule is applied for the source term as

$$\rho \int_\Omega b_1 \mathrm{d}\Omega \approx \underbrace{\rho \left(f_1\right)_P \Delta x \Delta y}_{b_P^{S,u}}. \tag{5.23}$$

Assembling all the coefficients: The coefficients introduced above were given exemplarily for each case, i.e., either for the u- or for the v-equations. After assembling each respective term, one obtains the following equations

$$a_P^u u_P - \sum_c a_c^u u_c + a_P^{P,u} (P_E - P_W) = b_P^u, \tag{5.24}$$

$$a_P^v v_P - \sum_c a_c^v v_c + a_P^{P,v} (P_N - P_S) = b_P^v, \tag{5.25}$$

where the coefficients are defined for u-equations as

$$a_P^u = a_E^{C,u} + a_W^{C,u} + a_N^{C,u} + a_S^{C,u} + a_E^{D,u} + a_W^{D,u} + a_N^{D,u} + a_S^{D,u} + a_P^{i,u}, \tag{5.26}$$

$$a_c^u = a_c^{C,u} + a_c^{D,u}, \tag{5.27}$$

$$b_P^u = b_P^{S,u} + b_P^{i,u}, \tag{5.28}$$

and for v-equations as

$$a_P^v = a_E^{C,v} + a_W^{C,v} + a_N^{C,v} + a_S^{C,v} + a_E^{D,v} + a_W^{D,v} + a_N^{D,v} + a_S^{D,v} + a_P^{i,v}, \tag{5.29}$$

$$a_c^v = a_c^{C,v} + a_c^{D,v}, \tag{5.30}$$

$$b_P^v = b_P^{S,v} + b_P^{i,v}. \tag{5.31}$$

Boundary conditions

To close the system of equations described in the preceding section, different boundary conditions of the domain, i.e. initial values and, if required, the initial flow field, are defined. There are two boundary types, i.e., the DIRICHLET conditions and the NEUMANN conditions. At the nodes where variable values are given (i.e., as in DIRICHLET conditions) no additional equation is required. However, when the boundary conditions involve derivatives (i.e., as in NEUMANN conditions) the boundary conditions are discretized to provide the required equations.

After omitting the heat and the mass transportation effects, four boundary types are defined in FASTEST2D. These are the inlet boundary, the outflow boundary, the symmetry line and the fixed wall boundary condition. For the symmetry boundary condition, all fluxes in the direction normal to the boundary are considered to be zero, and there is no shear force on the plane owing to the velocity gradient normal to the symmetry plane. On the walls, the no-slip[13] condition is assumed, which in the case of not-moving boundary equals to zero. In the case of a restart from a previous run, flow field variables, i.e., the pressure and the velocity, are initialized. The inlet conditions are provided by the user, while at the outflow zero gradient for all variables, and the mass conservation are assumed. Inputs of the initial and the boundary conditions specific to our problem are shown in the coming sections.

[13]For no-slip condition velocity of the fluid particle on the wall is equal to the velocity of the wall.

Pressure correction

The pressure term appears for incompressible flows only in the momentum equations. A direct solution requires extensive numerical efforts. FASTEST2D employs a pressure-correction method of the SIMPLE (Semi-Implicit Method for Pressure-Linked Equations) [125] type to emend this problem. In such an approach, the idea is to calculate the velocity component using the momentum equation which does not satisfy the continuity equation. Later the pressure term is corrected iteratively so that the continuity condition is fulfilled. Firstly, using the known field values for the pressure at $(k+1)$-th step, the momentum equation is solved in addition to the continuity equation. Corresponding velocity terms are computed. In the next step, the relation between the velocity corrections and the corresponding pressure components are determined by setting up an error between the actual equations and the uncoupled equations. Now, using an appropriate method (for the present case, the SIMPLE method) velocity corrections are determined in terms of the pressure correction. They are then put into the continuity equation, through which the pressure correction is achieved, which ascertain the velocity corrections and, hence, the velocities for the $(k+1)$-th time step. For more details on the pressure corrections see [125].

5.4 Moving grids

In the current study we are interested in the flow around oscillating cylinders. Hence, the solution domain changes in time due to the movement of the cylinder boundaries. In order to consider such movement of the cylinder, a moving grid approach is used, where the grid moves with the cylinder boundaries. If the grid moves, the transport equations defined in the Eulerian form, as shown in section 5.2, need to be modified for incorporating the grid movement. If the base vectors remain fixed, the only change in the conservation equations is the appearance of a relative velocity in convective terms. Additionally, mass conservation is obtained by enforcing a so-called *space conservation law* (SCL) [120, 126], which is described in the section 5.4.2. In what follows, we describe briefly the derivation of equations for a moving grid system.

5.4.1 Conservation laws for moving grids

Integration of the governing equations (5.1) and (5.3), over a CV with moving boundaries, yields a time dependent integral equation, which is evaluated using the LEIBNIZ's rule [127]. This section describes the resulting transport equations [120] for the mass and the momentum conservations, extended to incorporate the grid movement.

Continuity equation for moving grids

The right hand side of (5.2) stands for the mass of the fluid flowing through the cell surfaces. The implication of a moving surface finally gives an added velocity u_i^g to the

cell surface

$$\underbrace{\frac{\mathrm{d}}{\mathrm{d}t}\int_{\Omega}\rho \mathrm{d}\Omega}_{(I)} + \underbrace{\int_{S}\rho\left(u_j - u_j^g\right)n_j \mathrm{d}S}_{(II)} = 0, \tag{5.32}$$

where term-(I) is the rate of change of mass within the CV and term-(II) is the convective term. Term-(II) is further divided into two parts in (5.33), one of which (i.e., term-(III)) is due to the velocity of the fluid, and the other (i.e., term-(IV)) is due to the grid-velocity:

$$\frac{\mathrm{d}}{\mathrm{d}t}\int_{\Omega}\rho \mathrm{d}\Omega + \underbrace{\int_{S}\rho u_j n_j \mathrm{d}S}_{(III)} - \underbrace{\int_{S}\rho u_j^g n_j \mathrm{d}S}_{(IV)} = 0. \tag{5.33}$$

Momentum conservation equation for moving grids

The velocity in the convective term of the momentum conservation equation (5.4) is replaced by a relative velocity term. It is then treated similarly as for the continuity equation. However, the diffusive term in the momentum conservation equation does not require a correction, since the neighbors of a cell are deferred with the same rate. The integral form of the momentum conservation equation takes the form

$$\frac{\mathrm{d}}{\mathrm{d}t}\int_{\Omega}\rho u_i \mathrm{d}\Omega + \underbrace{\int_{S}\left[\rho u_i\left(u_j - u_j^g\right) - T_{ij}\right]n_j \mathrm{d}S}_{(V)} = \int_{\Omega}\rho b_i \mathrm{d}\Omega. \tag{5.34}$$

Term (V) in (5.34) is divided further into two terms, as shown below, to give the momentum conservation equation for the moving grids as

$$\frac{\mathrm{d}}{\mathrm{d}t}\int_{\Omega}\rho u_i \mathrm{d}\Omega + \underbrace{\int_{S}\left(\rho u_i u_j - T_{ij}\right)n_j \mathrm{d}S}_{(VI)} - \underbrace{\int_{S}\rho u_i u_j^g n_j \mathrm{d}S}_{(VII)} = \int_{\Omega}\rho b_i \mathrm{d}\Omega, \tag{5.35}$$

where term-(VI) and (VII) are attributed to the fluid-velocity and to the grid-velocity respectively.

5.4.2 Space conservation law (SCL)

The space conservation law is used for correcting the continuity equation where the grid velocity is taken into account. In such a case mass fluxes result through the surfaces of the distorted CV, causing an artificial mass source due to the change of the CV volume. In such a case, the conservation of mass (and all other conserved quantities) is not necessarily ensured, if the grid velocities are used for calculating the mass fluxes. Artificial mass sources may cause undesirable oscillations in the results. In such a case, mass conservation is achieved by enforcing the SCL, which can be thought of as the continuity equation for zero fluid velocity.

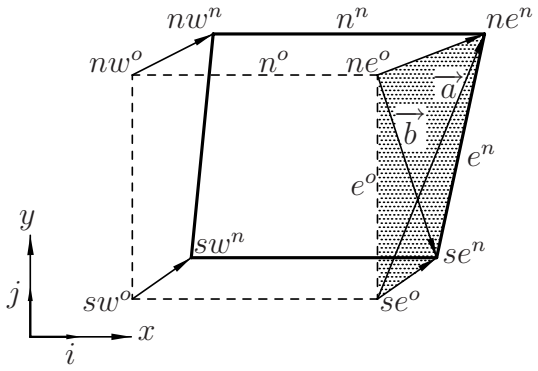

Figure 5.2: Moving two-dimensional CV with swept volume $\delta\Omega_e$

The term (IV) in (5.33) is interpreted as an artificial mass source m. Applied to (5.33), the SCL is deduced from a not-moving, incompressible fluid, $u_j = 0$ as

$$\frac{\mathrm{d}}{\mathrm{d}t}\int_{\Omega}\rho \mathrm{d}\Omega = \rho\int_{S} u_i^g n_i \mathrm{d}S = m. \tag{5.36}$$

In line with [120], the correction of the convective term in the final relation is calculated using the volume swept by the boundary of a CV during time Δt. On the basis of the CV in figure 5.1, the distorted CV and its geometric data are presented exemplarily for its east face in the figure 5.2. The swept volume for the face-e is calculated using the product of the diagonal vectors, $\delta\Omega_e = 1/2(\overrightarrow{a}.\overrightarrow{b})$. The SCL for the east face is obtained as

$$m_e = \rho\int_{S} u_i^g n_i \mathrm{d}S = \rho\frac{\delta\Omega_e}{\Delta t} \tag{5.37}$$

$$\sum_{N}\sum_{e} m_{c,N} = 0, \tag{5.38}$$

where $c = e, w, n, s$ and N is the number of CVs.

5.5 Block structured grid

In the current study, the flow field is discretized using block structured grids. Block structured grids provide a useful compromise between the simplicity and wide variety of solvers available for structured grids and at the same time ability to handle complex geometries, that normally unstructured grids allow. The basic idea of block structured grids is to use a regular data structure within, while constructing the blocks of such regular geometries in order to fill the irregular domains. Among different possible approaches mentioned in [120], we use the non-overlapping blocks to construct the block structured grid. In this approach, grids in two neighboring blocks are strictly required to match at the interfaces, and so-called "hanging nodes" are not allowed. The solution domain is subdivided into several subdomains so that each subdomain can be fitted with a structured grid having good properties, i.e., the grids are not too nonorthogonal and individual CV aspect ratios not too large.

The current study uses a parallel processing version of FASTEST2D, in order to reduce the overall computation time. The parallelization of the fluid domain is achieved by a grid-partitioning technique based on the block-structured grids. Depending on the number of processors, the block structures according to the geometry are configured so that the resulting subdomains can be assigned suitably to the individual processors.

For the current numerical investigations a two-dimensional discretization is used to compute the flow over the stationary or the moving cylinders. As described in section 5.6.3, the numerical study consists of two cases, first where the flow around a single cylinder is analyzed and another where the flow around two cylinders in a tandem is studied. Numerical grids for both the cases are described in sections 5.7.2 and 5.9.2 respectively. The motion of the moving cylinders is prescribed by the time dependent boundary conditions using moving grids, which at each time step adapt to a new configuration according to the cylinder movement.

5.6 Some useful definitions

Some standard terminologies are stated in this section, which are used frequently in the coming part of this chapter.

5.6.1 Dimensionless numbers

Following dimensionless numbers are frequently used in fluid dynamics:

1. **Reynolds number:** The REYNOLDS number is the ratio of inertial forces to viscous forces, and consequently, it quantifies the relative importance of these two types of forces for particular flow conditions. It is a dimensionless number, usually denoted by Re. For the flow around the cylinders it is defined as [15]

$$\mathrm{Re} = \frac{\rho V_0 D}{\mu} \tag{5.39}$$

where ρ is the fluid density, V_0 is the free stream fluid velocity, D is cylinder diameter and μ is the dynamic viscosity of the fluid.

2. **Strouhal number:** The STROUHAL number is a dimensionless number describing the oscillating flow mechanisms. It is the relationship between the vortex shedding frequency, the cylinder (hydraulic) diameter and the free stream fluid velocity [128, 15]. It is usually denoted by St and is expressed as

$$\mathrm{St} = \frac{f_s D}{V_0} \tag{5.40}$$

where f_s is the vortex shedding frequency. One of the most interesting characteristics of fluid-body interaction is "lock-in" [15], between the vortex shedding and vibration frequencies. The STROUHAL number is related, particularly with regard to the lock-in phenomena, to the vortex strength [129]. For a circular cylinder the STROUHAL number has a value between 0.18 to 0.23. A weak change of STROUHAL number over a wide range of REYNOLDS number is noticed, as shown in figure 5.3 [15].

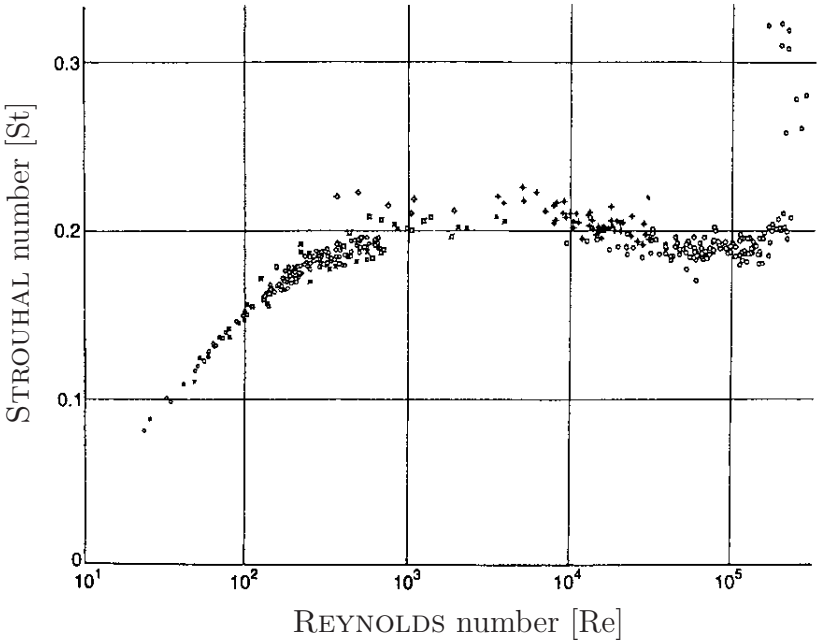

Figure 5.3: Experimentally obtained variation of STROUHAL number with REYNOLDS number for the flow around cylinders [15]

5.6.2 Fluid forces on a cylinder

A cylinder in a cross-flow is subjected to steady and fluctuating drag (in the direction of flow) and the lift (in the direction orthogonal to flow) forces. These forces are responsible for the oscillation of a free cylinder in longitudinal and in transversal directions respectively. Both forces are functions of REYNOLDS number, turbulence characteristics of the main flow, cylinder surface characteristics and the cylinder oscillation amplitudes. Drag and lift coefficients are the dimensionless numbers, which for a circular cylinder are respectively defined as

$$C_D = \frac{F_D}{\frac{1}{2}\rho V_0^2 D}; \tag{5.41}$$

$$C_L = \frac{F_L}{\frac{1}{2}\rho V_0^2 D} \tag{5.42}$$

where F_D and F_L are total drag and lift forces respectively. The total drag force is the sum of the pressure and the shear forces in downstream direction. Similarly, the total lift force is the sum of the pressure and the shear forces in the direction normal to the fluid flow. The shear forces are the results of the viscous effect of the fluid, and the pressure forces are the results of the pressure difference over the cylinder surface.

5.6.3 Specific wind power input

The amount of the power imparted by wind on the vibrating conductor is necessarily a function of the wind velocity, its turbulence, geometry of the conductor and also of

how the vibrating conductor is interacting with the wind. From the consideration of principles of similitude, which had been found useful in investigations of airfoil flutter and galloping of suspension bridges, FARQUHARSON and MCHUGH [28] found that the expression governing the wind power input has the form

$$\frac{P_W}{f^3 D^4 L} = \text{Func}\left(\frac{Y}{D}\right), \tag{5.43}$$

where P_W is total wind power input in Watts, f is the vibration frequency in Hertz, D is the diameter of conductor in meters and L is the conductor length in meters[14]. Using such a relation of wind power input on the normalized amplitude of conductor vibrations (Y/D), they were able to avoid a great number of tests, which would have been necessary to evaluate the wind power for all available conductor diameters at all practical values of frequency.

Expression (5.43) for the power input is only applicable to a conductor that is vibrating with the same amplitude over its entire span length. However, conductors in the field specially in the long-span transmission lines are most often found to vibrate in standing waves with nodes having very small amplitudes and antinodes having relatively large amplitudes. It is evident that Func $\left(\frac{Y}{D}\right)$ is different for different parts of a vibration loop [130]. To make the expression suitable for such a case, the average of the function over a loop is determined by integration for a conductor vibrating in standing sinusoidal loops. This gives an equation for determining the average power per unit length of the conductor in terms of the antinode vibration amplitude $Y_{\max}$. Function Func $\left(\frac{Y_{\max}}{D}\right)$, when shown in terms of the free-loop amplitudes, is referred as "specific wind power input" and is denoted by p_W. Total wind power input P_W in whole span length L is, hence, obtained by using the local relation

$$P_W = p_W f^3 D^4 L, \tag{5.44}$$

and integrating over the span. Experimentally obtained curves for specific wind power input from different researchers are shown in figure 5.11. These experimental curves have been utilized for energy balance analysis of single conductors, as mentioned in [1, 2, 44, 89]. However, the same curves may not be used for conductor bundles, and are required to be modified.

This chapter aims to numerically obtain such wind power input curves which can be utilized for the energy balancing analysis of a conductor bundle. However, the analysis has been performed in different steps. First the performance of the CFD code FASTEST2D is validated by solving the comparatively simpler problem of the flow around a single cylinder. Results for single cylinder analysis are compared with the available wind tunnel data for the similar cases. After achieving a good agreement for the single cylinder case, flow analysis around two cylinders in a tandem is performed. The analysis in the current chapter is performed in the following four major steps:

1. **Single stationary cylinder:** It is the very first step, where the flow around a single stationary cylinder is analyzed. The flow velocity is kept so that vortex

[14]It is to be noted that during their investigations FARQUHARSON and MCHUGH [28] used FPS system of units; conductor diameter and the length were taken in foot.

shedding around the stationary cylinder occurs. The frequency of the vortex shedding, and the time history of the drag and the lift forces are validated with the experimental data.

2. **Single oscillating cylinder:** In the second step, a single cylinder is subjected to the forced harmonic oscillations, with a frequency close to the STROUHAL frequency. Drag and lift forces on the cylinder are obtained. Wind power input on the cylinder is finally computed for different amplitudes of the cylinder oscillations. The numerically obtained wind power input is compared to the power input measured by different researchers in the wind tunnel.

3. **Two stationary cylinders in tandem arrangement:** In this step the flow around two stationary cylinders in a tandem arrangement is analyzed. The analysis is performed for different cylinder orientations, i.e., different lateral and longitudinal spacings between the cylinders. Time averaged lift and drag forces on the downstream cylinder are computed. They are then compared with the same obtained experimentally by different researchers.

4. **Two oscillating cylinders in tandem:** In the last step, both cylinders in the tandem arrangement are harmonically oscillated with the same frequencies, but different phases and amplitudes of vibrations, similar to the analysis done in the step 2. The lift and the drag forces, and ultimately the wind power input on the downstream cylinder are obtained for different amplitudes of the cylinder vibrations. Finally, the obtained wind power inputs are compared to the wind power input of a single isolated oscillating cylinder (as obtained in the step 2).

The numerical analysis for each mentioned step is presented in details in the coming sections. The obtained results are simultaneously discussed. The fluid is treated as incompressible and Newtonian in the complete analysis.

5.7 Flow around a single stationary cylinder

5.7.1 Problem description

In the first step the wind flow around a stationary cylinder, having a diameter D=0.06667 m, is analyzed numerically. A uniform laminar inflow fluid velocity of 0.1 m/sec is taken, which corresponds to a REYNOLDS number of 460. As the fluid, *air* is specified for the current study, with the density of 1.23 kg/m^3 and the dynamic viscosity of 1.78×10^{-5} kg/m.sec. Other relevant data related to the fluid properties are shown in the table 5.1. Although time stepping does not play a very crucial role over a limit value [131], the frequency of the vortex shedding is covered mostly by around 900 time steps, with a time step size of $\Delta t = 0.05$ sec. For the numerical implementation to be complete, the definition of the numerical constants is required in the FASTEST2D. To stabilize the pressure-correction approach by fractionizing the advance of parameters, the under-relaxation factors associated with velocity are chosen to be $\alpha_u = \alpha_v = 0.5$, while one related to the pressure is kept $\alpha_p = 0.3$. For all computations, a central differencing

scheme is employed, as mentioned in the section 5.3. Factor β is kept as 1. The blending factor for the second order CRANK-NICHOLSON time stepping is taken as $c_k = 0.5$. The α parameter in SIP solver is given as 0.90. The convergence criterion for the flow solver is considered as 10^{-4}. As NEWMARK variables, $\beta = 0.25$ and $\gamma = 0.50$ are specified.

5.7.2 Numerical grid for the single cylinder problem

Figure 5.4 and 5.5 show the block structured finite-volume grid of the fluid domain for a single cylinder. The grid used in the present analysis is composed of 11 blocks numbered from 1 to 11, as shown in the figure 5.4. On the left boundary of the block 1 (i.e., the inflow zone) an inflow is prescribed with a uniform velocity (e.g., for the current study 0.1 m/sec), while on the right boundary of the block 11 (i.e., the outflow zone) a zero gradient condition is assumed. Blocks 2 to 9 are located around the cylinder, as shown in the figure 5.5, out of which, blocks 2 to 5 form a non-distorting zone, of a diameter $10D$, around the cylinder and move together with it for a moving cylinder. A fine discretization in these blocks ensures the accuracy of the calculations, because the flow

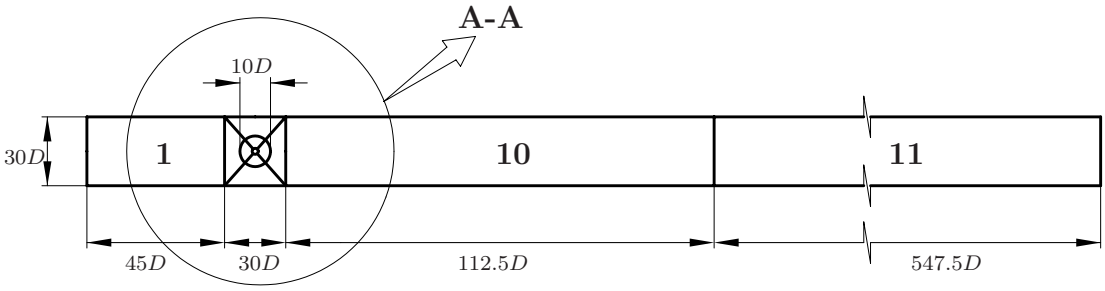

Figure 5.4: Block structured discretization of the numerical domain for one cylinder

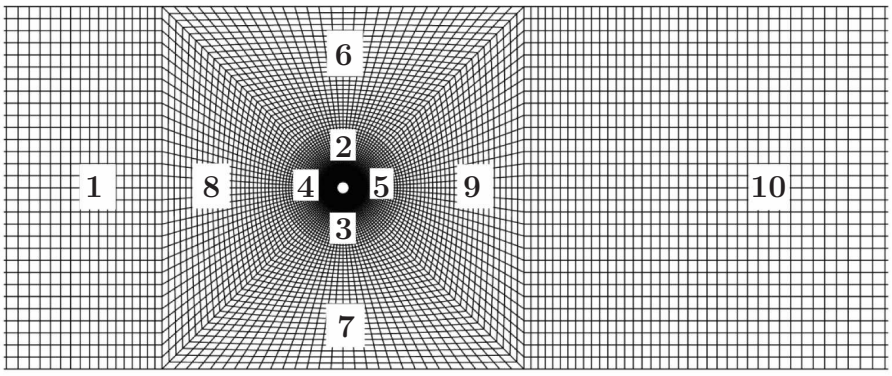

Figure 5.5: Structured finite-volume grid for one cylinder (details at **A-A** of figure 5.4)

field changes abruptly in this zone. In the case of a moving cylinder, only the grids in the outer blocks (e.g., blocks 6 to 9) deform. The flow zones away from the cylinder, where the flow field does not change very abruptly (i.e., blocks 1, 10 and 11), consists of coarser grids to reduce the computational efforts and, hence, to decrease the processing time. In order to minimize the blockage effects [120] from the upper and the lower boundaries on the wake, a large flow channel width of $30D$ is chosen. The inflow zone on the left side of the cylinder is taken as $60D$ and a long outflow region of total length $675D$ is chosen, in order to avoid any influence of the outflow boundary conditions. Symmetry boundary conditions are applied at the upper and the lower boundaries.

Table 5.1: Fluid and grid properties

Fluid properties	
Specific mass (ρ) [kg/m^3]	1.23
Dynamic viscosity (μ) [kg/m.sec]	1.78×10^{-5}
Fluid velocity (V_0) [m/sec]	0.10
Reynolds number (Re)	460
Mach number ($M = V_0/V_{sound}$)	0.0003
Grid properties	
Cylinder's diameter (D) [m]	0.06667
Longitudinal grid dimension (from inflow to cylinder)	$60D$
Longitudinal grid dimension (from outflow to cylinder)	$675D$
Transverse grid dimension	$30D$

Table 5.2: Properties of discretization-blocks for single cylinder grid

Block number	Number of CVs	Assigned processor
Block-1	1200	1
Block-2	1500	1
Block-3 to 5	3×1500	2
Block-6	780	1
Block-7 to 8	2×780	3
Block-9	780	4
Block-10	2700	3
Block-11	3000	4
Total	**16020**	

In order to reduce the computational time, the current analysis is performed on a parallel computer cluster available at TU Darmstadt, the *Hessischer Hochleistungs Rechner* (Hessian High Performance Computer or HHLR) [132]. The present numerical analysis is performed using four processors in parallel. The block-structured grid partitioning technique, on which the parallel implementation strategy of Fastest2d is based, leads in a natural way to an efficient parallelization, see [119, 124, 131]. The blocks are

grouped with respect to the load balance of the processors. Each block shown in figure 5.4 is assigned to one of the four processors, in such a way that the computational load is distributed as uniformly as possible among them, to achieve the highest computational efficiency. Table 5.2 shows the number of CVs in each block and the corresponding processor to which the block is assigned. Out of a total of 16020 CVs (for the coarsest grid), processor 2 is assigned with maximum of 4500 CVs, which leads to a maximum achieved computational efficiency[15] of 89%.

5.7.3 Result for the flow around a stationary cylinder

In what follows, the numerically obtained results are compared to the experimental results from different studies, corresponding to a Reynolds number of 460. Different aspects of the fluid dynamics around a stationary cylinder are also described.

It is well-known that for a Reynolds number more than 40, the wake of a circular cylinder in the steady flow consists of two staggered rows of vortices [66, 133]. The vortices of each row shed alternately from each side of the body. As the vortices shed, a periodic force is exerted on the cylinder. The component of this periodic force in the transverse direction (i.e., the lift force) has the same frequency as the vortex-shedding cycle, while its streamwise component (i.e., the drag force) has a frequency twice that of the shedding frequency [66, 133]. Figure 5.6 shows qualitatively the shedding vortices

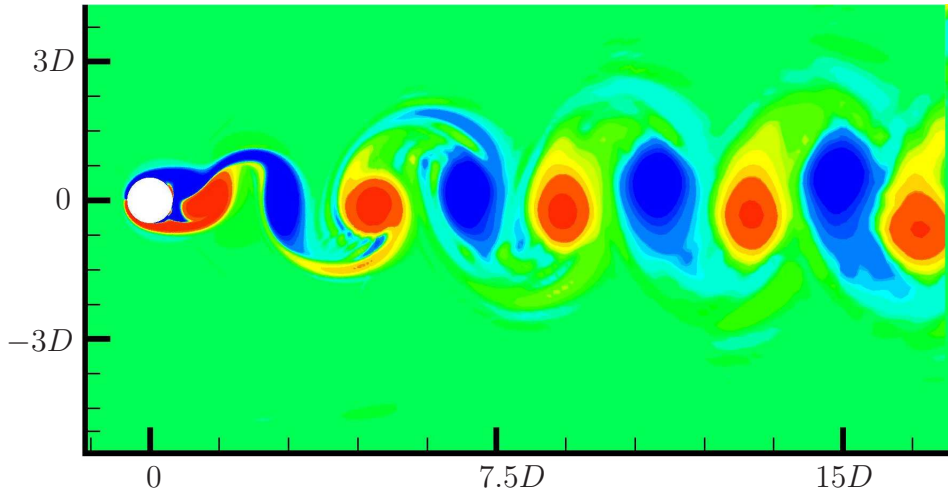

Figure 5.6: Vortex shedding for single stationary cylinder

around a stationary cylinder in a laminar flow field. In [66] experimentally obtained shapes of the vortices for the similar Reynolds number range is pictured, which is similar to what is obtain here numerically. Williamson and Govardhan mentioned in [134] that for a Reynolds number in the range of 460, the mode of vortex shedding is of the type 2S, which is also true for the numerically obtained results in figure 5.6. Hence, qualitatively similar vortex shedding is obtained numerically and experimentally.

[15] Computational efficiency $= \frac{\text{Ideal number of CVs to distribute the load equally}}{\text{Maximum number of CVs assigned to any processor}} \times 100 = \frac{4000}{4500} \times 100 = 89\%$.

In order to compare the results quantitatively, time histories of the numerically obtained lift and drag coefficients are plotted in figures 5.7 (a) and (b). Figure 5.7 (c) shows the power spectra for the lift coefficient obtained using FFT analysis. The frequency of the lift (i.e., frequency of the vortex shedding) is 0.3516 Hz. Figure 5.7 (d) shows the limit cycle (i.e., the LISSAJOU figure) for C_D and C_L. It is seen in this figure that, for one cycle of the lift there are two cycles of the drag. Hence, the frequency of drag component is double (i.e., 0.7080 Hz) of the frequency of the lift component, as is also mentioned in the experimental results from [66, 133]. Moreover, the time-average value of the lift

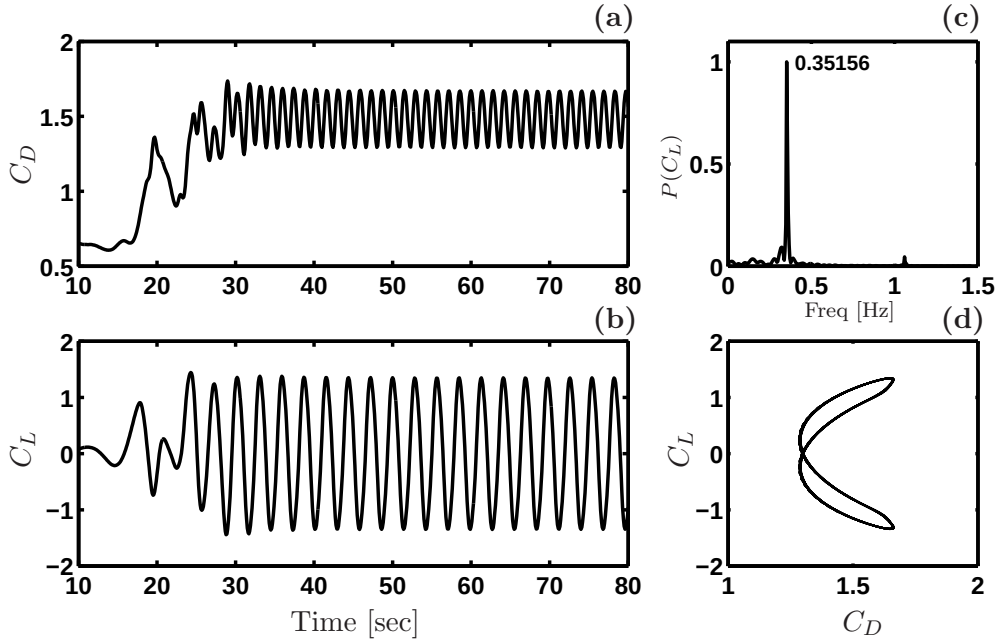

Figure 5.7: Lift and drag coefficients for a single stationary cylinder (Re=460)
(a) Drag coeff.; **(b)** Lift coeff.; **(c)** Power spectra for C_L; **(d)** Limit cycle C_D-C_L

force (and hence of the lift coefficient) is zero, which is obtained in the experimental studies. The average value of the drag coefficient is 1.49, and is close to the value obtained for a similar REYNOLDS number in [135, 131]. Using the current cylinder diameter D=0.06667 m, the fluid velocity V_0=0.1 m/sec and the obtained shedding frequency f_s=0.3516 Hz, the STROUHAL number is calculated using (5.40). The value obtained for the STROUHAL number for the present case is 0.235, which is also close to the STROUHAL number corresponding to a REYNOLDS number of 460, from the figure 5.3.

Based on the above mentioned comparison, it is now clear that the used grid type, the time step size and the time discretization techniques result in a good simulation of the flow. These values are, hence, used further for the analysis of an oscillating cylinder.

5.8 Flow around a vertically oscillating cylinder

Vortex shedding is dramatically changed when a cylinder oscillates in the cross-flow direction of a flow stream. In certain ranges of the amplitude and the frequency of os-

cillations, the cylinder motion controls the instability mechanism leading to the vortex-shedding. One of the most interesting characteristics of the fluid-body interaction is the "*lock-in*" phenomenon [128, 15, 133], between the vortex shedding and the cylinder oscillations. BLACKBURN and HANDERSON in [136] described *lock-in* as a result of an entrainment process, in which the vortex shedding is entrained by the cylinder motion in such a way that its frequency matches with the cylinder's oscillation frequency. They also discussed how the entrainment or the lock-in behavior for the oscillations of the elastically mounted cylinder differs from that for the forced cylinder oscillations. It was shown in [137] that the wind power input to an oscillating cylinder is maximum when it vibrates in its *lock-in* state.

When the cylinder is elastically mounted and is set free to oscillate in the fluid-flow, it interacts with the fluid and starts oscillating slowly, to finally reach the *lock-in* state. Huge computational efforts are, however, required to numerically simulate *fluid-structure interaction* phenomena, even for a single elastically-mounted cylinder. On the other hand, if the cylinder is forcefully oscillated to a frequency exactly same as its *lock-in* frequency, the dynamics of the fluid around the cylinder remains same as it was oscillating in the *lock-in* state. Hence, in such a condition, the forced oscillations of the cylinder are equivalent to that of a elastically mounted cylinder. Using this fact, the current analysis intends to simulate the flow around a moving cylinder, forcefully oscillated with the *lock-in* frequency. However, since the exact value of the *lock-in* frequency is not known, we use the fact that it always remains in proximity of the vortex-shedding frequency of the stationary cylinder [15]. Hence, in the current analysis the cylinder is forcefully oscillated with different frequencies in proximity of the frequency of the vortex-shedding obtained in the section 5.7.3.

5.8.1 Problem description

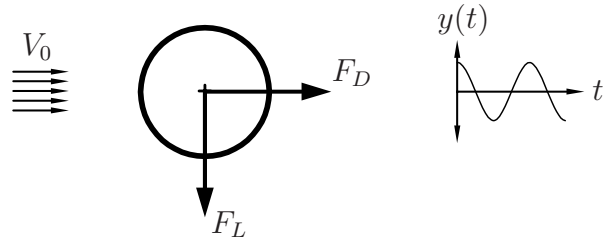

Figure 5.8: Schematic diagram of flow around a stationary cylinder

Figure 5.8 shows the schematic diagram of a harmonically oscillating cylinder of the unit length. The adopted sign conventions for the lift and the drag forces are also shown in this figure. Upward motion $y(t)$ of the cylinder is considered to be positive. The cylinder is forcefully oscillated with different frequencies in the proximity of the vortex-shedding frequency, obtained in the section 5.7.3. The primary characterization of the results is made in terms of the frequency ratio $F_R = f_0/f_s$ and the amplitude ratio $A_R = y_{\max}/D$, where f_0 and $y_{\max}$ are the prescribed frequency and the amplitude of the simple harmonic cross-flow oscillations of the cylinder respectively, f_s is the fixed-cylinder vortex shedding frequency and D is the cylinder diameter.

Similar to the last section, the REYNOLDS number is based on the free-stream flow speed V_0=0.1 m/sec and the cylinder diameter D=0.06667 m, i.e., Re=460. The fixed-cylinder vortex shedding frequency is taken as 0.3516 Hz, as obtained in the section 5.7.3. A *reduced velocity* is defined as $V_r = V_0/f_0D$. The inverse of the reduced velocity V_r is an equivalent STROUHAL number St_e, for any oscillation frequency f_0. The lift and the drag forces F_L and F_D are non-dimensionalized with a factor $\frac{1}{2}\rho V_0^2 D$ to give the lift and the drag coefficients C_L and C_D using (5.41) and (5.42).

For the current analysis, cross-flow amplitudes of the cylinder oscillations[16] range from $0.1D$ to $1.0D$. In fact, the amplitude of the cylinder oscillations is a factor affecting its *lock-in* frequency. To make sure of capturing the *lock-in* frequency and, hence, obtaining the maximum possible wind power input for a particular vibration amplitude, the analysis is performed in a frequency range in proximity of the vortex-shedding frequency f_s of a single rigid cylinder, obtained in section 5.7.3. The frequency range in which the analysis is performed ranges from 0.2693 Hz to 0.3591 Hz, which corresponds to an equivalent STROUHAL number range of $\mathrm{St}_e = 0.18$ to 0.24, and a frequency ratio-range of $F_R = 0.766$ to 1.02.

The grid and the flow field properties are kept same as in the case of a stationary single cylinder in section 5.7.3. However, moving grids are now used for incorporating the cylinder oscillations. The cylinder is oscillated in cross-flow direction with a prescribed sinusoidal motion

$$y(t) = y_{\max} \sin(2\pi f_0 t) \tag{5.45}$$

at any time instant t. Hence, the velocity of the oscillating cylinder is

$$\dot{y}(t) = 2\pi y_{\max} f_0 \cos(2\pi f_0 t). \tag{5.46}$$

Our prime interest in this analysis step lies in computing the wind power input on a single oscillating cylinder, and to compare it to the experimentally obtained wind power input from the wind tunnel experiments [5]. For any prescribed amplitude of cylinder oscillations, the time averaged power of the aerodynamic forces acting on the moving cylinder is computed. The time averaged wind power input on a harmonically oscillating cylinder of unit length is calculated by integrating the product of the lift force and the cross-flow velocity of the cylinder, and averaging it over a cycle of the cylinder oscillation

$$(P_W)_{\mathrm{num}} = \frac{1}{T}\int_{t_1}^{t_2} \dot{y}(t) \cdot F_L(t)\mathrm{d}t \tag{5.47}$$

where $(P_W)_{\mathrm{num}}$ represents the numerically obtained wind power input and T is the time period of cylinder oscillations. For a cylinder of unit length, the specific wind power

[16]It is known from the field observations that the amplitude of the aeolian vibrations rarely exceeds one conductor diameter. Wind tunnel testings provide an explanation for this property of the aeolian vibrations. Different researchers have determined that for a vibration amplitude of up to approximately $0.7D$, the wind imparts energy to the vibrating conductor, and hence, the wind power input is positive. For higher amplitudes than $0.7D$, the conductor starts giving energy back to the wind, as can be seen from the downfall of the experimentally obtained wind power input curves in figure 5.11. This is equivalent of having damping, and hence the vibration amplitude starts decreasing and normally does not go beyond approximately $0.7D$.

input can now be obtained using (5.44) as

$$(p_W)_{\text{num}} = \frac{(P_W)_{\text{num}}}{f_0^3 D^4}. \tag{5.48}$$

5.8.2 Result for the flow around an oscillating cylinder

As mentioned in the previous section, the cylinder is oscillated for each amplitude in a prescribed frequency range, close to the vortex-shedding frequency f_s of the stationary cylinder. Lift and drag forces are obtained and, specific wind power input for all combinations of the amplitudes and the frequencies are computed using (5.47) and (5.48). As expected, the wind power input varies slightly for different oscillation frequencies f_0 even for the same amplitude of cylinder motion. Values of obtained specific wind power inputs for each case are shown in the table 5.3, and are plotted in figure C.14 of appendix C. The maximum specific wind power input for each case is underlined in table 5.3. It is noted that for most of the cases frequency corresponding to the maximum wind power input is lower than the vortex-shedding frequency f_s of the stationary cylinder. As the amplitude increases, the frequency corresponding to the maximum power input decreases. This also goes in-line with the experimental study by KOOPMANN[17] in [138], where it is shown that the lower bound *lock-in* frequency decreases with increasing amplitudes of the cylinder oscillations. Additionally, it is to be noted here that for most of the amplitudes above $0.1D$, the maximum wind power corresponds to an equivalent STROUHAL number of $\text{St}_e = 0.2$, which also confirms the value of STROUHAL number used for an oscillating cylinder in different text books, e.g., [15, 66].

The lift and the drag coefficients

Figure 5.9 (a) and (b) show respectively the time histories of lift and drag coefficients of a cylinder oscillating with an amplitude of $0.5D$ and a frequency of 0.2843 Hz, which corresponds to the maximum wind power input for this amplitude. Figure 5.9 (c) shows the power spectra for the lift coefficient obtained using FFT analysis, stating the frequency of the lift occurrence (i.e., the vortex-shedding frequency). It is noticed that for all the periodic results, the vortex-shedding frequency, obtained from the power spectrum for lift coefficients, is same as the frequency of the cylinder oscillation (refer section C.1 for more results). It shows that the *lock-in* is achieved corresponding to the maximum wind power inputs for different oscillation amplitudes. However, for the smaller amplitudes, i.e., $A_R \leq 0.05$, a quasi-periodic behavior of the lift and drag time histories is observed in figures C.1 and C.2. This is a typical behavior for the lower oscillation amplitudes of the cylinder, also observed by ANAGNOSTOPOULOS in [133], and by MENEGHINI and BEARMAN in [139].

Figure 5.10 shows numerically obtained vortex shedding around the oscillating cylinder at different time instants of a complete cycle of the cylinder oscillation, for $A_R = 0.5$ and $f_0 = 0.2843$ Hz. Formation of one vortex in each cycle of cylinder motion is observed in

[17] Although the study was done for even lower REYNOLDS number of 100.

Table 5.3: Specific wind power input for a single oscillating cylinder

f_0[Hz]⇒	0.2693	0.2843	0.2991	0.3142	0.3292	0.3516	0.3591
F_R ⇒	0.766	0.809	0.851	0.894	0.936	1.00	1.021
St_e ⇒	0.18	0.19	0.20	0.21	0.22	0.235	0.24
A_R ⇓	⇓	⇓	⇓	⇓	⇓	⇓	⇓
0.01	0.0079	0.0085	0.0101	0.0096	**0.0144**	0.0106	0.0118
0.015	0.0154	0.0279	0.0286	**0.0329**	0.0253	0.0215	0.0217
0.02	0.0607	0.0614	0.0593	0.0633	0.0645	**0.0685**	0.0634
0.03	0.0917	0.1280	0.1243	**0.1411**	0.1331	0.1143	0.1215
0.04	0.1921	0.2134	0.2376	0.2321	**0.2467**	0.2130	0.2016
0.05	0.3035	0.2938	0.2738	0.3145	0.3262	**0.3581**	0.3349
0.06	0.4727	0.4826	**0.5005**	0.4785	0.4801	0.4673	0.4581
0.07	0.6683	0.6792	0.6723	0.6803	**0.7163**	0.7031	0.6735
0.08	0.7834	0.8036	0.8173	0.8358	**0.8478**	0.8242	0.8286
0.09	0.9300	0.9205	**0.9542**	0.9145	0.9385	0.8863	0.8623
0.10	1.4367	1.3934	**1.6263**	1.3540	1.3272	1.2033	1.2854
0.20	2.7429	2.6940	2.7852	**3.1726**	2.9452	3.0710	2.8484
0.30	5.2347	6.1498	**6.4763**	6.3245	5.7823	5.2453	4.9623
0.40	13.8384	13.4571	**14.4746**	12.9359	13.1548	12.6323	12.1673
0.50	24.4526	**26.5971**	22.6547	24.2624	21.6473	19.3752	20.2467
0.60	24.6742	26.3424	**29.3646**	27.7643	23.2365	23.8542	21.4374
0.70	33.8534	32.7428	**36.5824**	34.1467	32.1653	31.3452	31.3535
0.80	31.2462	30.1235	**38.5858**	29.2344	25.2521	27.6352	24.4353
0.90	19.6334	20.5252	29.3451	**34.3230**	32.2352	21.4357	18.6342
1.00	16.7434	27.1345	**32.0136**	22.8753	20.7648	22.2733	14.7642

the picture, meaning that the vortex formation is *locked-in* with the cylinder oscillation frequency.

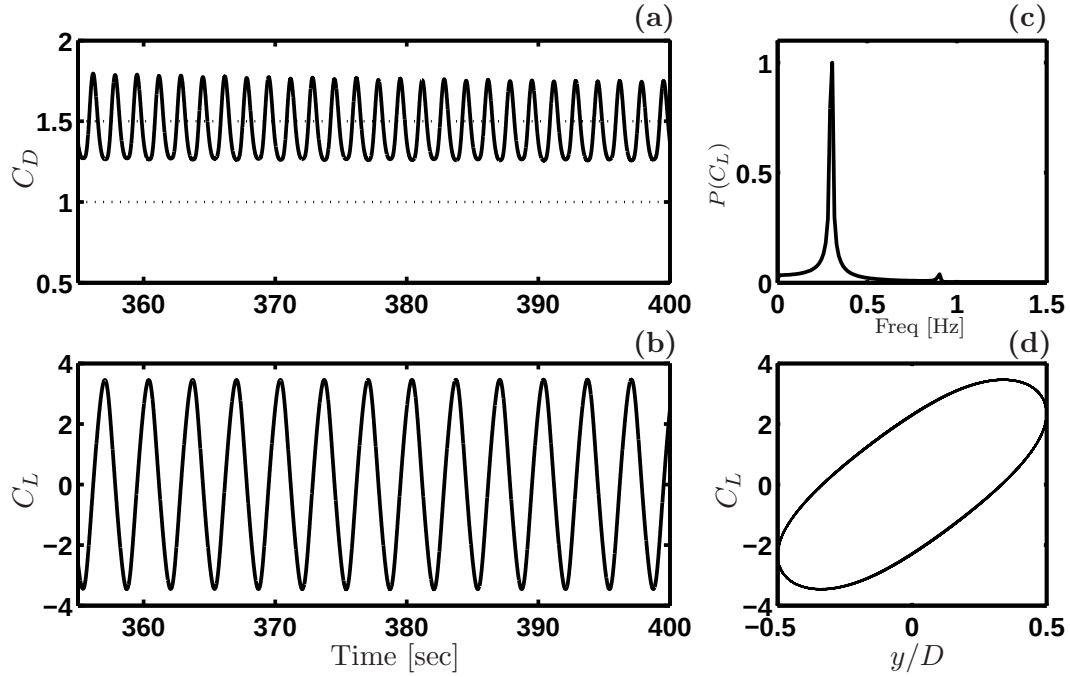

Figure 5.9: $A_R = 0.50$, $f_0 = 0.2843$Hz (i.e., $S_R = 0.19$, $F_R = 0.809$)
(a) Drag coeff.; **(b)** Lift coeff.; **(c)** Power spectra for C_L; **(d)** Limit cycle $\frac{y}{D}$-C_L

Wind power input

For a positive wind power input on the cylinder from wind, there is positive work done on the cylinder by the lift force; and for this to be true the time-average phase angle between the lift force and the cylinder displacement must lie in a range[18] of π to 2π radian. The average work done on the cylinder by the lift forces is assessed by examining the area enclosed by a limit-cycle plot (i.e., phase-plane plot) between the normalized cylinder motion y/D and the lift coefficient C_L and [60]. Figure 5.9 (d) shows the limit cycle plot for y/D and C_L. On the C_L versus y/D trajectory, the sense of traverse is counterclockwise, hence, the lift coefficients and the cylinder motion are in phase, as it should be for a transfer of energy from the fluid to the cylinder. On the other hand, a clockwise limit cycle trajectory means the negative energy transfer[19]. Similar plots for different amplitudes of the cylinder oscillations are shown in appendix C. It is noticed that for A_R ranging from 0.01 to 0.7, the limit cycle of y/D versus C_L are rotating counterclockwise. It shows that the wind power input to the cylinder is positive. Whereas, for the higher A_R values ranging from 0.70 to 1.0, such limit cycles

[18]Note that the direction of the positive motion is opposite to the direction of positive lift force in the current sign convention, as shown in figure 5.8. Hence, a phase difference of π radian between them in the limit cycle diagram means being in the same direction.

[19]It is to be noted that in current case the sign convention for the lift force is opposite to what was used by Blackburn and Henderson in [60].

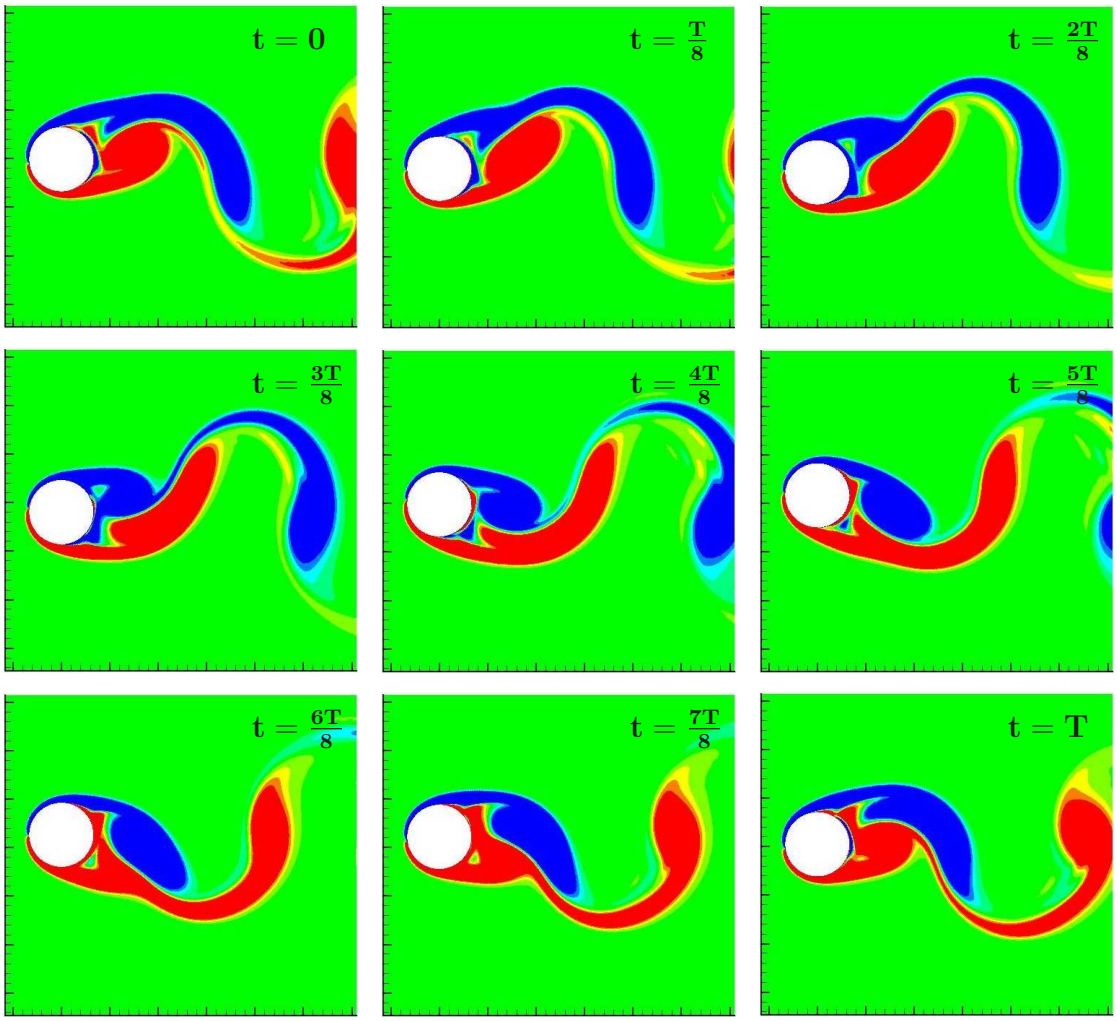

Figure 5.10: Vortex-shedding around an oscillating cylinder; $F_R = 0.809$, $A_R = 0.5$

tend to move clockwise (refer plots in appendix C), which shows that the corresponding wind power inputs tend to decrease.

Figure 5.11 compares the numerically obtained maximum specific wind power inputs for each different amplitudes obtained in the current study, with experimentally obtained wind power inputs by different researchers. The figure shows that the numerically obtained wind power input is in good match with what was obtained experimentally, for A_R values ranging from 0.01 to 0.4. However, for the higher amplitudes, the current numerical analysis gives higher wind power inputs than the experimental data. The prime reason for such a behavior is that, the current analysis is done in a laminar flow region with Re=460, whereas the experimental data corresponds to different percentages of turbulence in the flow field. It is well known from the field experiences that the degree of turbulence highly affects the formation of vortices [15, 66]. Higher turbulence decreases the intensity of the vortex formation[20], resulting in the reduced power inputs

[20]Also from the experiences of the transmission line engineers it is known that those transmission lines which are located in the regions where wind flow is smooth and laminar (e.g., open fields, river crossings etc.) are more prone to the aeolian vibrations.

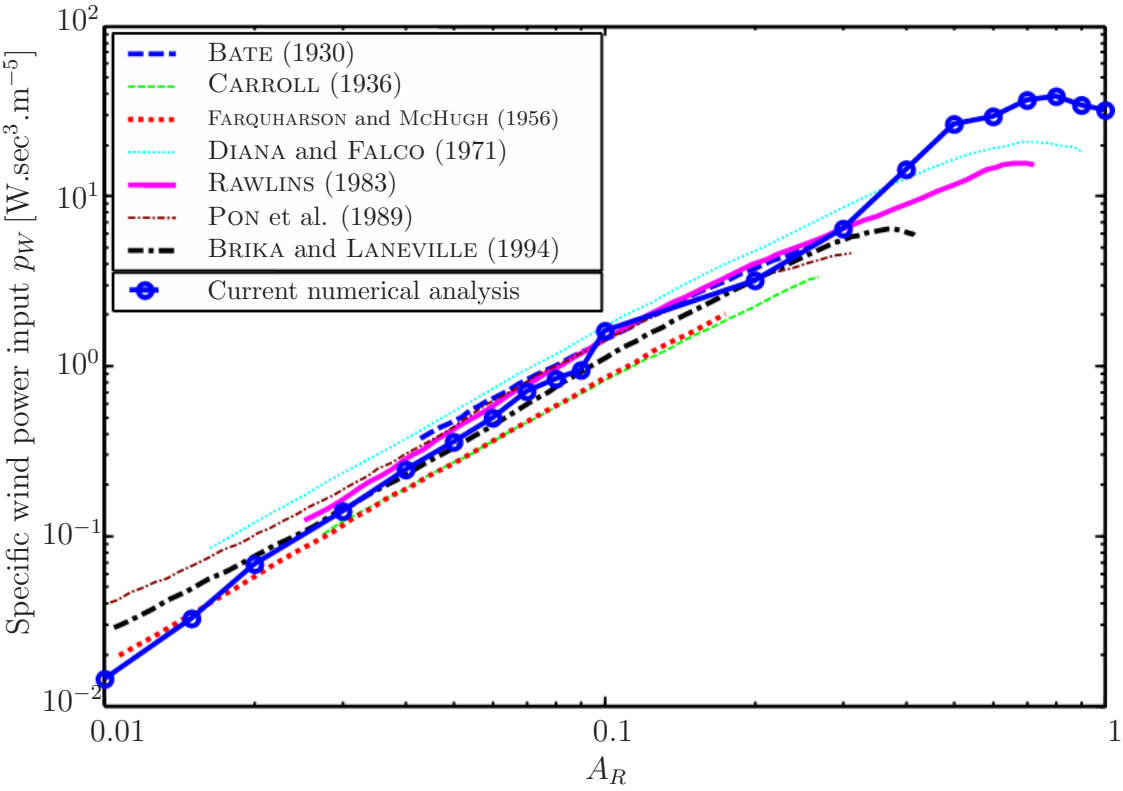

Figure 5.11: Comparison of numerically obtained wind power with experimental curves for a single oscillating cylinder

from the wind. Due to the laminar flow, used in the current analysis a higher power input is achieved, as compared to the experimental studies.

However, the behavior of the numerically obtained wind power curve is similar to the experimental curves. Similar to the experimental data, numerically obtained wind power input also has low values for the smaller vibration amplitudes, and shows a steep increase as the amplitude increases. After a certain value of the amplitude of the cylinder oscillations, the wind power input starts decreasing. Normally, this decrement takes place at around A_R=0.4 to 0.5 in the experimental curves. However, because the current numerical analysis corresponds to a laminar flow, the decrement starts at around A_R=0.8. The wind power input keeps on further decreasing and reaches a negative value after a certain vibration amplitude. In the current analysis the negative wind power occurs for A_R >1.0, which is not shown in the figure 5.11. It can be seen in the figures C.12 and C.13 that for A_R in the range of 1.10 and 1.20, the limit cycles are on the verge of changing from counterclockwise to clockwise, which means that for these amplitudes the wind power drops abruptly and tends to gain negative values. This decrement for the higher amplitudes is also mentioned by Blackburn and Henderson in [60], showing a similar behavior of the limit cycle between cylinder motion and the lift coefficients, as in the current case.

Figure 5.12 shows a curve fitted on the numerically obtained wind power input for a

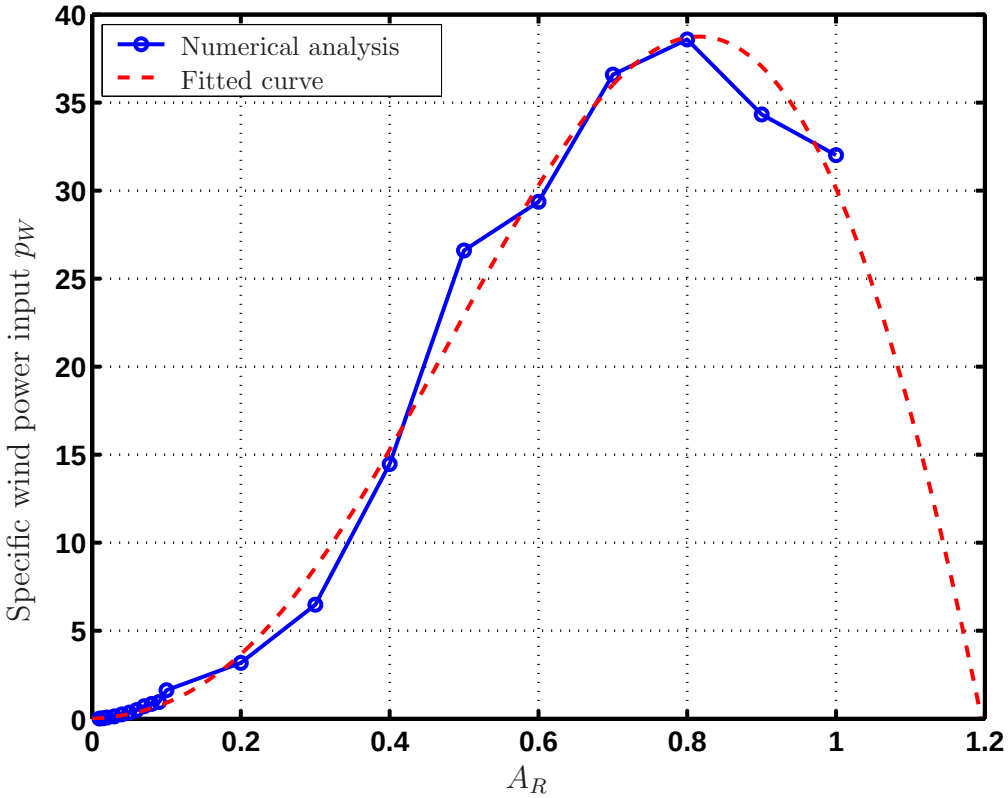

Figure 5.12: Fitted curve on numerically obtained wind power input for a single oscillating cylinder

single oscillating cylinder. The equation of the fitted polynomial is:

$$p_W = 134.39A_R^5 - 411.61A_R^4 + 265.03A_R^3 + 39.3609A_R^2 + 2.9581A_R, \tag{5.49}$$

where $A_R = y_{max}/D$.

The comparison of the numerically obtained results for the lift and the drag coefficients, and for the wind power inputs with those obtained experimentally, validates the numerical techniques used in the current studies. A similar numerical technique is further utilized for solving more complicated problem of the flow around a group of two cylinders in the coming sections.

5.9 Flow around two stationary cylinders in tandem

After analyzing the effect of the laminar wind on a single cylinder, we now investigate the influence of an additional cylinder in the flow path. The presence of an additional upstream cylinder considerably change the properties of the incoming flow on the downstream cylinder. In this section, the flow around two stationary cylinders in a tandem arrangement is analyzed using a similar numerical procedure as used for the the single cylinder, shown in the previous sections. A schematic diagram of the analyzed problem is shown in the figure 5.13, where X represents the cylinder spacing in the in-flow

direction, and Y represents the cylinder spacing in the cross-flow direction. Drag and lift forces are obtained on the downstream cylinder, in order to deduce the effect of the wakes coming from the upstream cylinder on it. Such study is called a wake interference study. Time-averaged lift and drag forces are computed as a function of in-flow and cross-flow spacings between the cylinders. They are later compared to experimental data available in the literature.

5.9.1 Problem description

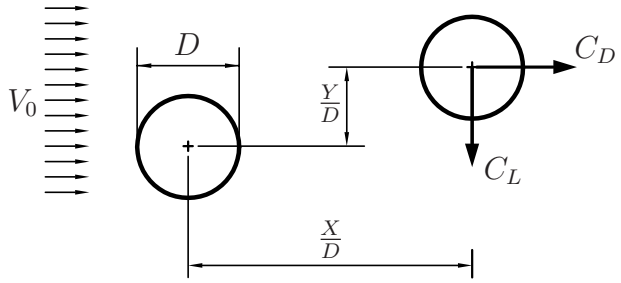

Figure 5.13: Configuration of two stationary cylinders in a tandem arrangement

We are interested in analyzing the problem in the frame of conductor bundles. The present study is performed for two different in-flow spacings between the stationary cylinders, X/D= 15 and 20, which are the usual range of horizontal distances between two subconductors in a conductor bundle. Cross-flow spacings between the cylinders range from Y/D=0 to 4.5. Similar to the single cylinder case shown in previous sections, the diameter of both the cylinders is taken as D=0.06667 m. The fluid is specified as air having a density $\rho = 1.23$ kg/m^3 and a dynamic viscosity $\mu = 1.78 \times 10^{-5}$ kg/ms. The flow field is analyzed under a uniform laminar wind speed of 0.1 m/sec, which corresponds to a Reynolds number of 460. Other data related to the current analysis is shown in the table 5.4.

In order to improve the convergence of iteration during the computations, a smaller time increment $\Delta t = 0.01$ sec is used here. Under-relaxation factors associated with the velocity are chosen to be same as earlier $\alpha_{u,v} = 0.5$, and the factor related to the pressure is kept $\alpha_p = 0.3$. A central differencing scheme is employed, as mentioned in section 5.3. The blending factor for the second order Crank-Nicholson time stepping is taken as $c_k = 0.5$. The α parameter in the SIP solver is 0.90. Newmark variables are specified as $\beta = 0.25$ and $\gamma = 0.50$. The convergence criterion for the flow solver is taken as 10^{-4}.

5.9.2 Numerical grid for the two cylinders problem

The block structured finite-volume grid for two cylinders in a tandem arrangement for X/D=20 is shown in figures 5.14 and 5.15. The flow field in this case is divided into 19 blocks. A similar grid is used for X/D= 15, with small differences in the size of few blocks. Similar to the single cylinder case, on the left side of block 1, a

Table 5.4: Fluid and grid properties

Fluid properties	
Specific mass (ρ) [kg/m^3]	1.23
Dynamic viscosity (μ) [kg/m.sec]	1.78×10^{-5}
Fluid velocity (V_0) [m/sec]	0.10
Reynolds number (Re)	460
Mach number ($M = V_0/V_{sound}$)	0.0003
Grid properties	
Cylinder's diameter (D) [m]	0.06667
In-flow distance between cylinders (X/D)	15, 20
Cross-flow distance between cylinders (Y/D) (for rigid cylinders)	0 - 4.25
Amplitudes of cylinder oscillations (A_R) (for oscillating cylinders)	0 - 0.60
Longitudinal grid dimension (from inflow boundary to cylinder)	$55D$
Longitudinal grid dimension (from outflow boundary to cylinder)	$675D$
Transverse grid dimension	$22.50D$

Table 5.5: Properties of the discretization-blocks for two cylinders grid

Block number	Number of CVs	Assigned processor
Block-1	1200	1
Block-2 to 5	4×1380	2
Block-6 to 9	4×780	1
Block-10 to 13	4×1380	3
Block-14 to 16	3×780	1
Block-17	780	4
Block-18	2700	4
Block-19	3000	4
Total	**24180**	

uniform inflow is prescribed, while at the outflow on the right side of the block 19 a zero gradient condition is assumed. Blocks 2 to 9 are located around the upstream

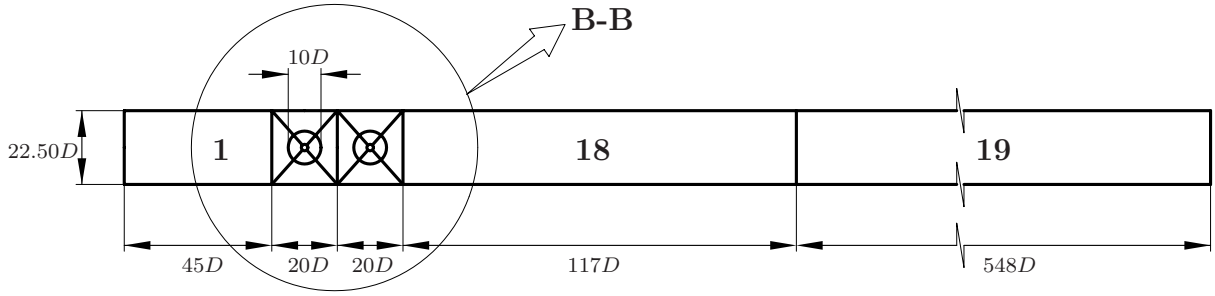

Figure 5.14: Block structured discretization for two identical cylinders in tandem (for X/D=20)

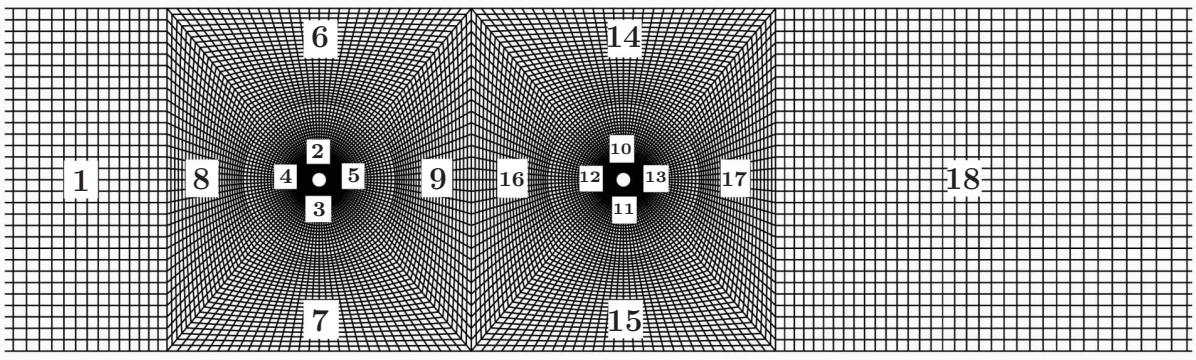

Figure 5.15: Structured finite-volume grid for two cylinders in a tandem (details at **B-B**)

cylinder and 10 to 17 are located around the downstream cylinder. Blocks 2 to 5 form a non-distorting zone around the upstream cylinder and 10 to 13 form the same around the downstream cylinder. For X/D=20, the non-distorting zone has a diameter $10D$, whereas for X/D=15, it is $5D$ in diameter. For moving cylinders (i.e., analysis described in the section 5.10), these non-distorting blocks move together with the cylinders. A fine discretization is used in the blocks close to the cylinders, and the blocks away from the cylinder are coarsely meshed. The width of the inflow zone is kept $55D$ and that of the outflow as $675D$.

In order to avoid generating a new grid for each cross-flow spacing Y/D between the cylinders, a moving grid approach is used, even for the stationary cylinders. However, instead of specifying the time-varying displacements of the cylinders, constant displacements are assigned to both the cylinders. The constant cross-flow displacement of each cylinder is set to half of the desired cross-flow spacing, in opposite directions to each other. In this way, for each separate cross-flow spacing between the cylinders, a new *moved* grid is generated automatically. As an example, figure 5.16 shows a moved grid for $X/D = 15$ and $Y/D = 2.0$.

The total number of CVs in the coarsest grid is 24180. The present analysis is also performed with the parallel computers cluster available at TU Darmstadt [132]. Four parallel processors are used. Each block, as shown in figure 5.14, is assigned to four processors as uniformly as possible, to achieve better computational efficiency. Table 5.5 shows the number of CVs in each block and also the corresponding processors, to

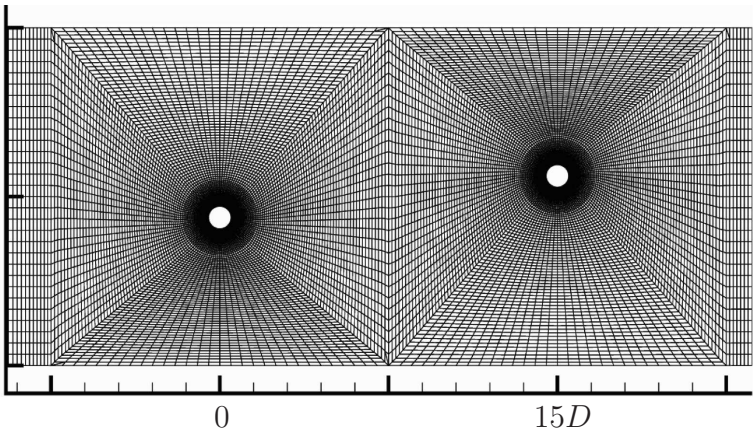

Figure 5.16: Moved grid for two rigid cylinders in tandem ($X/D = 15$ and $Y/D = 2.00$)

which each block is assigned. Out of a total of 24180 CVs, processor 1 is assigned with maximum 6660 CVs, which gives a maximum achieved computational efficiency of 90.77%.

5.9.3 Result for the flow around two stationary cylinders

Dayoub [122] carried out wind tunnel tests for different configurations of two stationary cylinders in tandem arrangement for a high Reynolds numbers of 1.2×10^4, 2.6×10^4, 3.9×10^4 and 5.2×10^4. A similar numerical study was performed by Braun and Awruch in [140] using the finite element method, at a Reynolds number of 2.6×10^4. Braun and Awruch compared their numerical results with the experimental study by Wardlaw and Cooper of [141], and found good agreement. The experimental results obtained by Dayoub are also in a good match with the numerical results of Braun and Awruch. However, unlike these studies, the current analysis is performed for a low Reynolds number of 460. Nevertheless, the results from the current study are compared in this section to the experimental study made by Dayoub in [122], in order to verify the trend of the average aerodynamic forces.

Time-averaged drag and lift forces

In the current case, the emphasis is mainly on the computation of the aerodynamic forces acting on the downstream cylinder. Drag and lift forces acting on the downstream cylinder are computed, and averaged over time. Time-averaged lift and drag forces of the downstream cylinder, obtained for different cylinder arrangements, are presented in the table 5.6. Wake interference studies in terms of the average force coefficients for different configurations of the cylinders are shown in figure 5.17 and 5.18, in which they are compared with the experimentally obtained average force coefficients by Dayoub [122]. Triangular points in these plots correspond to a in-flow spacing between the cylinders of $X/D = 15$, where as square points correspond to $X/D = 20$. Blue continuous lines in the plots represent the fitted curve for the obtained individual points for $X/D = 15$ and blue dash-lines represent the same for $X/D = 20$. Similarly,

the red lines show the results from the experimental studies.

Table 5.6: Numerically obtained time-averaged drag and lift coefficients for two stationary cylinders in a tandem arrangement

Y/D	$X/D = 15$		$X/D = 20$	
	C_D	C_L	C_D	C_L
0.00	0.0610	0.0000	0.1000	0.0000
0.05	0.0930	0.0062	0.1220	0.0045
0.10	0.0963	0.0194	0.1332	0.0160
0.15	0.1125	0.0256	0.1394	0.0180
0.20	0.1321	0.0314	0.1530	0.0223
0.25	0.1362	0.0519	0.1672	0.0450
0.30	0.1417	0.0783	0.1796	0.0545
0.35	0.1578	0.0972	0.2000	0.0855
0.40	0.1752	0.1163	0.2386	0.0980
0.45	0.1896	0.1677	0.2370	0.1200
0.50	0.2054	0.1813	0.2360	0.1260
0.60	0.2419	0.2216	—	—
0.65	0.2915	0.2274	0.3826	0.1700
1.00	0.4631	0.2233	0.6160	0.2103
1.25	0.5892	0.2057	0.6759	0.1958
1.50	0.6672	0.1923	0.7560	0.1578
1.75	0.9136	0.1439	0.8710	0.1793
2.00	1.1449	0.1338	1.0230	0.1000
2.25	1.1603	0.0431	1.1016	-0.0330
2.50	1.1378	0.0266	1.1093	-0.0470
2.75	1.1281	0.0024	1.1190	-0.0575
3.00	1.1321	-0.0132	1.1100	-0.0383
3.25	1.1288	-0.0147	1.1000	-0.0350
3.50	1.1000	-0.0261	1.1180	-0.0340
3.75	1.1058	-0.0267	1.1160	-0.0140
4.00	1.1173	-0.0163	1.1220	-0.0300
4.25	1.1156	-0.0014	1.1140	-0.0260
4.50	1.1324	-0.0023	1.1133	-0.0083

Figure 5.19 presents the time histories of the drag and the lift forces on the down-

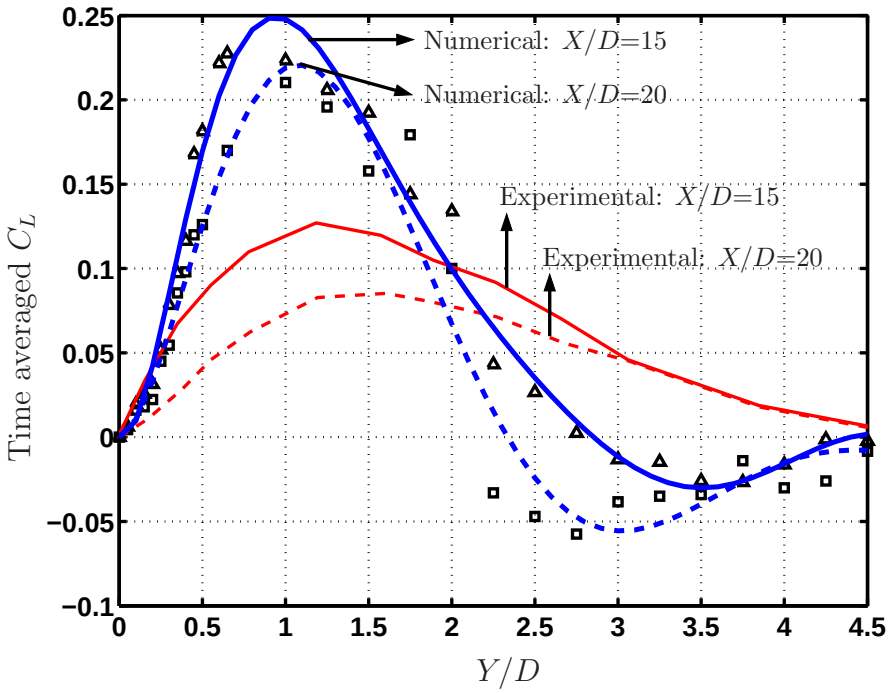

Figure 5.17: Comparison of time averaged lift coefficients for downstream cylinder of two stationary cylinders in a tandem (△: $X/D = 15$, □: $X/D = 20$)

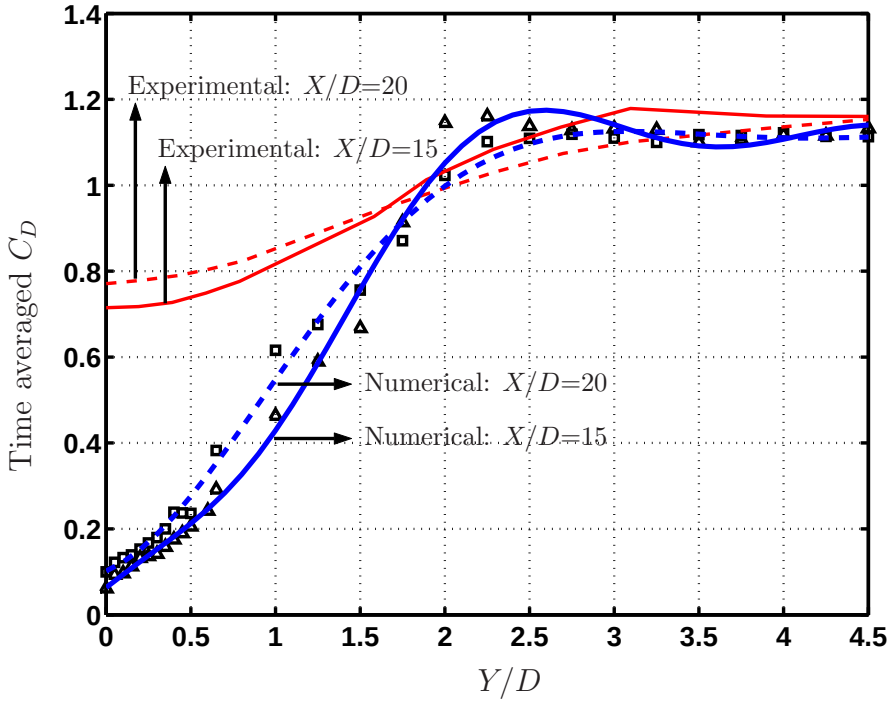

Figure 5.18: Comparison of time averaged drag coefficients for downstream cylinder of two stationary cylinders in a tandem (△: $X/D = 15$, □: $X/D = 20$)

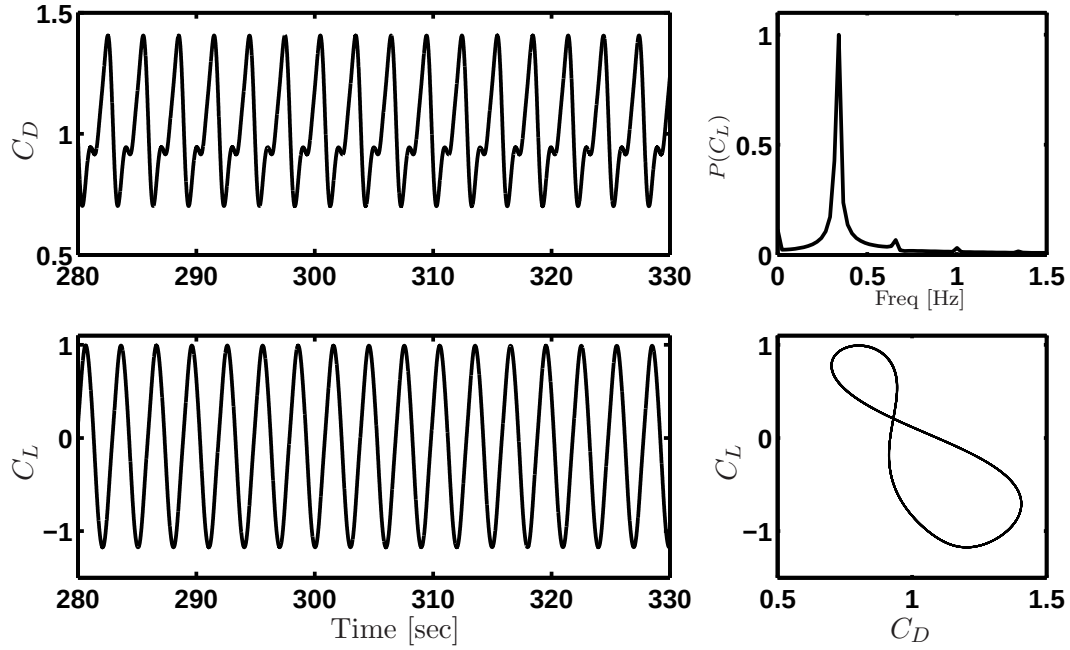

Figure 5.19: $X/D = 20$, $Y/D = 2.00$

stream cylinder, vortex shedding frequency using the FFT and the limit cycle diagram between the lift and the drag forces for $X/D = 20$ and $Y/D = 2.00$. Similar plots are illustrated in section C.2, for other configurations of both the stationary cylinders. Instantaneous rotational fields for fully developed vortices corresponding to different cross-flow cylinder spacings are presented in figure 5.20.

In figure 5.17 average lift coefficient is zero at $Y/D = 0$, where symmetry reproduces the single non-oscillating cylinder situation. It increases till $Y/D \approx 1$, where wake-effects are most intensive[21] (refer figure C.15 and figure 5.17). For higher Y/D values, the lift coefficient begins to decrease due to the reduction of the wake interference (refer figure C.22). In figure 5.19 for $X/D = 20$ and $Y/D = 2.0$ a small presence of lower harmonics is still noticeable. After $Y/D \approx 2.2$ for $X/D = 20$, it is noticed from the figure 5.17 that the average lift forces become negative (refer figure C.20). In the present case, it means that the vortex starts pushing the downstream cylinder away from the upstream cylinder. This is also noticeable in the vortex street representation in figure 5.20(c). This fact is also verified in experimentally obtained vortex street (e.g., as shown on the page 50 of [66]), which shows that the transverse spacing of any vortex from the center of the cylinder is approximately $2D$ to $3D$. The same is also true for the vortex street of the upstream cylinder from its center. Hence, if the downstream cylinder is kept beyond this distance in the cross-flow direction, the vortex street from the upstream cylinder tries to push it outward, causing negative values of the averaged lift force on it. For a low Reynolds number like the one in the current case, when the flow is fairly laminar, the vortex shedding is regular and stronger, which causes negative values of the average lift forces. As the Reynolds number increases, turbulence increases and the vortex shedding starts becoming irregular in its outer region, where it interacts

[21] It is to noted from figure 5.13 that the positive values of lift force stand for pulling down of the downstream cylinder towards the upstream one.

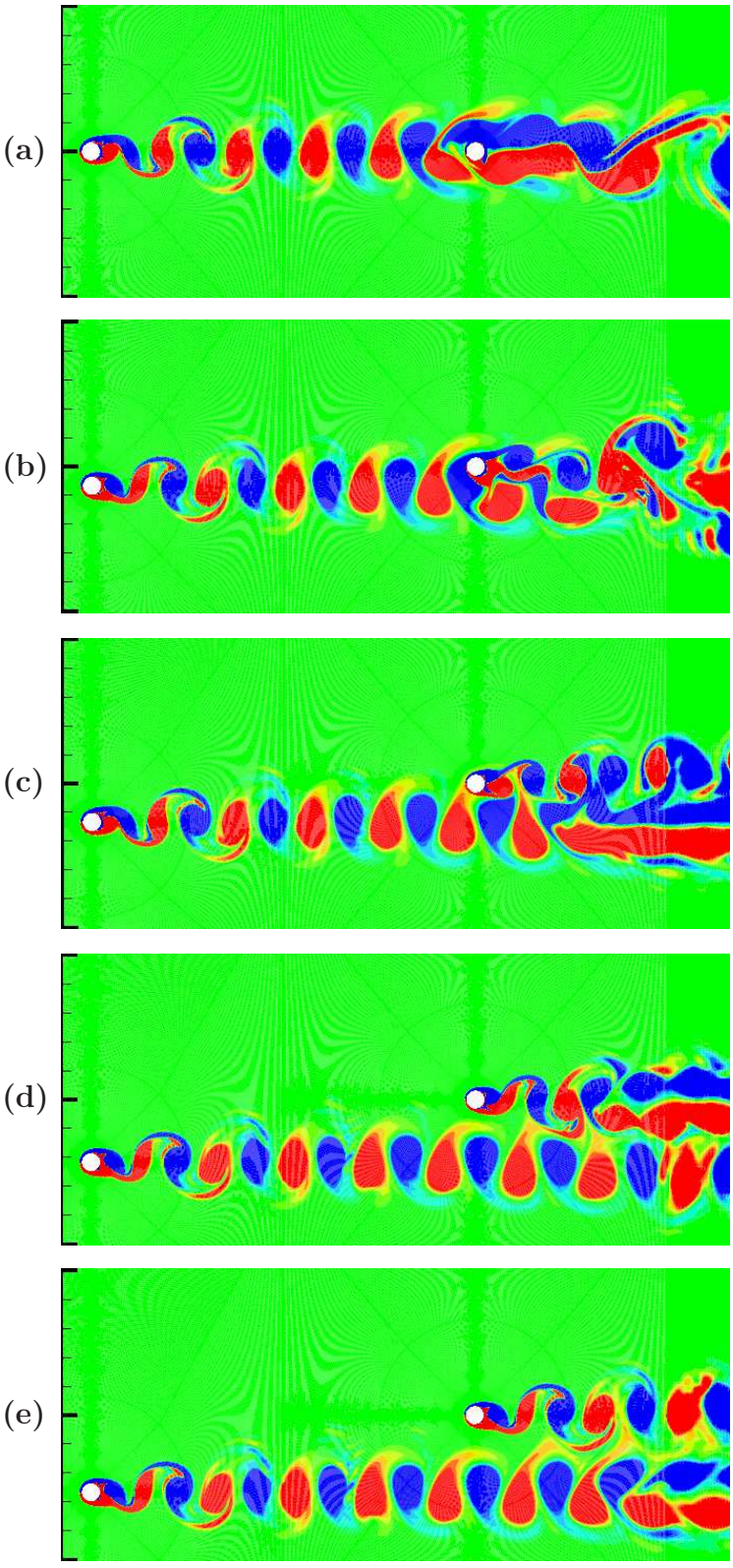

Figure 5.20: Flow around two rigid cylinders in a tandem (rotational field is plotted): **(a)** $Y/D = 0.00$; **(b)** $Y/D = 1.00$; **(c)** $Y/D = 2.00$; **(d)** $Y/D = 3.25$; **(e)** $Y/D = 4.00$

with the turbulent fluid flow. Hence, the average lift forces do not reach the negative values for higher REYNOLDS numbers, like the one used in the experimental data. It is also noted from the figure 5.17 that for a lateral spacing between cylinder $X/D = 15$, negative lift forces occur for larger longitudinal spacings between the cylinders than for $X/D = 20$. This happens because of the fact that, for the smaller X/D values, the vortex street before the downstream cylinder is more intense than for the larger X/D values. This makes a low pressure zone below the cylinder, and causes its pulling downward, even for a comparatively larger Y/D values.

In figure 5.18, the averaged drag coefficient on the downstream cylinder has its lowest value for $Y/D = 0$, due to higher wake-turbulence coming from the upstream cylinder (refer figure C.15 (a), which reduces the intensity of the vortices hitting the downstream cylinder. As the Y/D increases (e.g., $Y/D > 3$ for $X/D = 20$), the downstream cylinder tends to behave like an individual cylinder (refer figure C.20 to figure C.22). It is also noticeable in the figure 5.20(d) and (e) that large Y/D values cause the downstream cylinder to outreach the wake-zone from the upstream cylinder. Hence, the time-averaged lift and drag coefficients approach their corresponding values for a single individual cylinder.

In figures 5.17 and 5.18, numerically obtained time-averaged lift and drag coefficients are plotted with the experimental data by DAYOUB [122]. A large difference between numerically and experimentally obtained average lift and drag coefficients is noticeable. This difference is due to the fact that both studies are performed for different REYNOLDS numbers, as mentioned in the beginning of this section. However, behavior of the numerical results are consistent to the experimental data.

5.10 Flow around two oscillating cylinders in tandem

In sections 5.7.3, 5.8.2 and 5.9.3, numerically obtained results from the simpler cases are compared to different wind-tunnel studies. These comparisons are necessary to verify the quality of the grid and the performance of the adopted numerical schemes. In this section the flow around two oscillating cylinders in tandem is analyzed. Both the cylinders are oscillated in the cross-flow direction with the specified amplitudes, and with the frequencies corresponding to the maximum wind power input of the oscillating single cylinder case, as determined in the section 5.8.2 and shown in the table 5.3.

Although, both cylinders can be oscillated with different phase differences[22], because of the huge computational efforts involved, we confine our study only to two oscillation conditions; the one when both the cylinders oscillate in phase, i.e., $\phi = 0$, and another when both the cylinders oscillate in the opposite phase, i.e., $\phi = \pi$. These two extreme

[22]In an actual twin-bundled transmission line, due to a mechanical coupling of both the subconductors with attached spacer dampers, the whole system vibrates in one of its mode-shapes (or precisely, as a combination of many mode-shapes). Both the subconductors vibrate with some amount of phase shift ϕ in their oscillations. Hence, for different mode-shapes, the downstream conductor will receive a different wind power input than in the case of a single oscillating conductor, even for the same amplitude and the frequency of the cylinder oscillations.

cases give the upper and lower bound for the wind power inputs on the downstream cylinder, for a particular amplitude and the oscillation frequency.

Lift and drag forces are determined on the oscillating downstream cylinder under the wakes from oscillating upstream cylinder. After obtaining the lift and the drag time histories, the wind power input on the downstream cylinder is computed.

5.10.1 Problem description

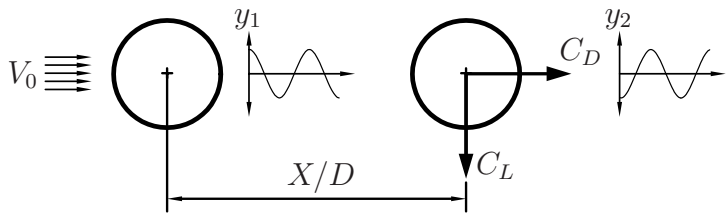

Figure 5.21: Configuration of two stationary cylinders in a tandem arrangement

Figure 5.21 shows two cylinders in a tandem, which are oscillating in cross-flow direction. Time dependent vibrations of the upstream cylinder y_1 and of the downstream cylinder y_2 are specified as

$$y_1 = y_{\max} \sin(2\pi f_0 t) \tag{5.50}$$

$$y_2 = y_{\max} \sin(2\pi f_0 t + \phi) \tag{5.51}$$

where $y_{\max}$ and f_0 are the amplitude and frequency of oscillations for both the cylinders, and ϕ is the phase difference between their oscillations. The present numerical analysis is done for two phase differences, viz., $\phi = 0$ and π. Similar to the previous cases, the diameters of both cylinders are kept as 0.06667 m and the flow field is analyzed under a uniform laminar wind speed of 0.1 m/sec, corresponding to a Reynolds number of 460. Finite-volume grids and the flow properties for the current case are the same as used for the two stationary cylinders case, described in the table 5.1. Details of the grid geometries for $X/D = 15$ and 20 are described in section 5.9.2. A small time step of $\Delta t = 0.01$ sec is chosen in order to capture the abrupt changes in the flow field for the oscillating cylinders. Other numerical parameters for the computations are kept same as for the two stationary cylinders' case, as stated in section 5.9.1. The numerical analysis is performed using the parallel computers cluster available at TU Darmstadt [132], using four parallel processors. The blocks of the discretization, as shown in the figure 5.14, are assigned among four processors as uniformly as possible, in order to achieve a better computational efficiency. Table 5.5 shows the number of CVs in each block and the corresponding processor to which each block is assigned. Out of a total of 24180 CVs (for the coarsest grid), processor 1 is assigned with a maximum of 6660 CVs to process, which results in a maximum achieved computational efficiency of 90.77%.

5.10.2 Result for the flow around two oscillating cylinders

In the current analysis, the main emphasis is on obtaining the wind power input on the oscillating downstream cylinder under the influence of the oscillating upstream cylinder. Both cylinders are forcefully oscillated with A_R ranging from 0.01 to 0.60, where A_R is the oscillation amplitude normalized with the cylinders' diameter, i.e., $A_R = y_{\max}/D$. The frequency of oscillation, for each amplitude is kept equal to the frequency corresponding to the maximum wind power input for the single oscillating cylinder's case, as obtained in the table 5.3. Although, it is true that the maximum wind power inputs on the downstream cylinder may not necessarily correspond to these frequencies of a single cylinder case, they are considered for the present analysis in order to limit the number of required computations. The wind power input is obtained for

Table 5.7: Numerically obtained specific wind power input for two oscillating cylinders in a tandem arrangement

	$X/D = 15$		$X/D = 20$	
$y_{\max}/D \Downarrow$	$\phi = 0$	$\phi = \pi$	$\phi = 0$	$\phi = \pi$
0.00	0.0000	0.0000	0.0000	0.0000
0.01	0.0454	0.0140	0.0252	0.0153
0.02	0.1312	0.0868	—	—
0.03	—	—	0.2500	0.1400
0.05	0.8480	0.4702	0.3152	0.4115
0.10	2.1535	2.2481	3.5977	2.0715
0.15	2.8535	3.7467	3.5976	3.3497
0.20	3.7264	4.8318	2.4956	4.2381
0.25	—	—	2.3546	—
0.30	3.2963	12.4125	2.1207	10.2013
0.35	1.5847	15.5370	2.4414	14.9881
0.40	1.5433	28.2461	1.5409	22.5971
0.45	1.7635	37.5671	1.6346	35.8357
0.50	0.7435	45.3289	—	33.8079
0.55	—	—	0.5408	24.7862
0.60	0.2432	33.3565	0.3183	5.7576

the downstream cylinder by computing the time history of the lift forces on it and using the relation (5.47). Values of the obtained specific wind power inputs for $X/D = 15$ and 20, corresponding to $\phi = 0$ and π for the cylinders' movements, are shown in table 5.7.

In table 5.7 it is noticeable that there are some A_R values for which no studies were made in the single oscillating cylinder case (e.g., 0.25, 0.35, 0.45 and 0.55). However, these

amplitudes are considered in the present case to obtain more data points. The cylinders' oscillation frequencies for such cases are taken equal to the frequencies corresponding to the available lower amplitude in the single oscillating cylinder case[23].

The obtained results of table 5.7, are plotted in the graphical form in figure 5.22 for $X/D = 15$, and in figure 5.23 for $X/D = 20$. In both plots triangular points show the obtained specific wind power input for $\phi = 0$, whereas the square points show the specific wind power input for $\phi = \pi$. In order to show the variation of the wind power inputs with respect to the oscillation amplitude, polynomials are fitted to the data. In figure 5.22 and 5.23, dashed and continuous lines show the fitted curves corresponding to $\phi = 0$ and $\phi = \pi$ respectively.

The equations of the fitted curves are as follows:

$$p_W\Big|_{X/D=15}^{\phi=0} = -218.46A_R^5 + 164.22A_R^4 + 111.35A_R^3 - 149.20A_R^2 + 42.28A_R, \quad (5.52)$$

$$p_W\Big|_{X/D=15}^{\phi=\pi} = 24120A_R^7 - 64198A_R^6 + 52065A_R^5 - 17594A_R^4 + 2996A_R^3 - 214A_R^2 + 24.80A_R, \quad (5.53)$$

$$p_W\Big|_{X/D=20}^{\phi=0} = -489.33A_R^5 + 263.14A_R^4 + 311.01A_R^3 - 273.26A_R^2 + 58.93A_R, \quad (5.54)$$

$$p_W\Big|_{X/D=20}^{\phi=\pi} = 1578A_R^7 - 35111A_R^6 + 48938A_R^5 - 29565A_R^4 + 9784A_R^3 - 1547A_R^2 + 109.93A_R, \quad (5.55)$$

where $A_R = y_{max}/D$.

In figure 5.24 the curves corresponding to both the lateral spacings of the cylinders in tandem are plotted with the wind power input curve for a single cylinder case for comparison. Figure 5.24 and 5.25 clearly show that the wind power inputs for the single oscillating cylinder is altogether different from that for the oscillating downstream cylinder in tandem. Wakes from the upstream oscillating cylinder influence the flow behavior of the downstream cylinder considerably, even at a relatively large in-flow spacing (i.e., $X/D = 20$) between them. It is noticed that for the smaller vibration amplitudes, the wind power input for the oscillating downstream cylinder in tandem is higher than that for the single oscillating cylinder[24], irrespective of their phase differences. Similar to the single oscillating cylinder case, the power input for the oscillating downstream cylinder increases with increasing amplitude of the cylinder oscillations. However, for both the cylinder in tandem oscillating in the same phase (i.e., $\phi = 0$), the power input on downstream cylinder drops relatively faster, for lower vibration amplitudes, i.e. $y_{\max}/D \approx 0.15$. Nevertheless, the power inputs corresponding to $\phi = \pi$ still increase, till the vibration amplitude reaches a value of $y_{\max}/D \approx 0.5$ and then they suddenly drop at $y_{\max}/D = 0.6$. The reason of such sudden drop in the wind power

[23]e.g., for an amplitude of 0.25D in the two cylinders' case, the frequency of oscillation is taken as the one corresponding to maximum WPI for an amplitude of 0.20D in the single cylinder's case.

[24]Note that $\phi = 0$ and $\phi = \pi$ are two extreme cases for the bundled conductors. Practically conductors in a bundle will oscillate with some phase between 0 and π.

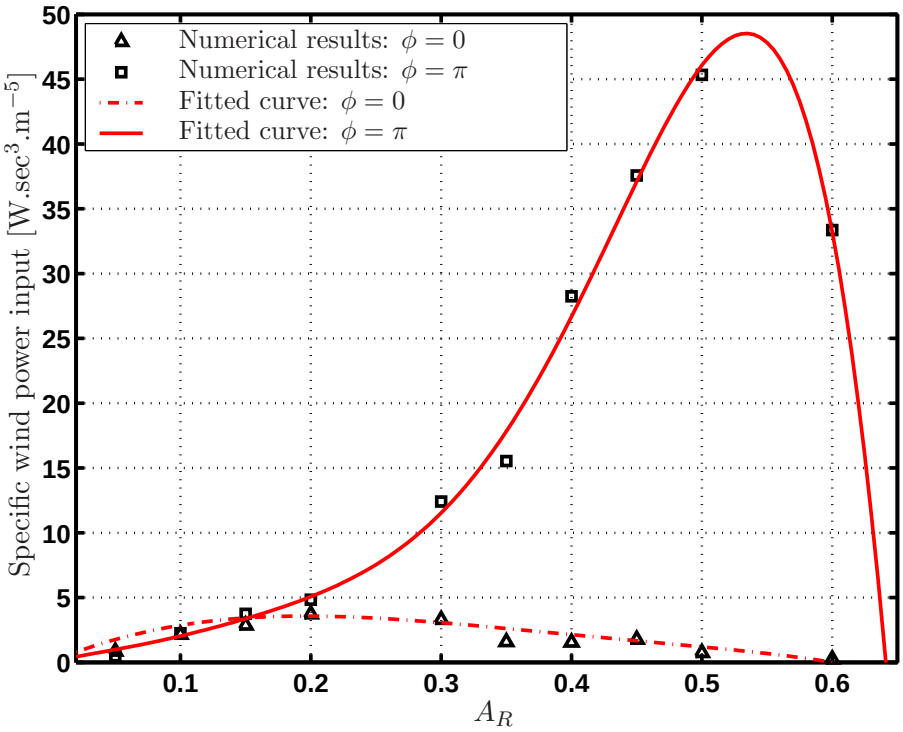

Figure 5.22: Numerically obtained wind power inputs for the downstream cylinder for X/D=15

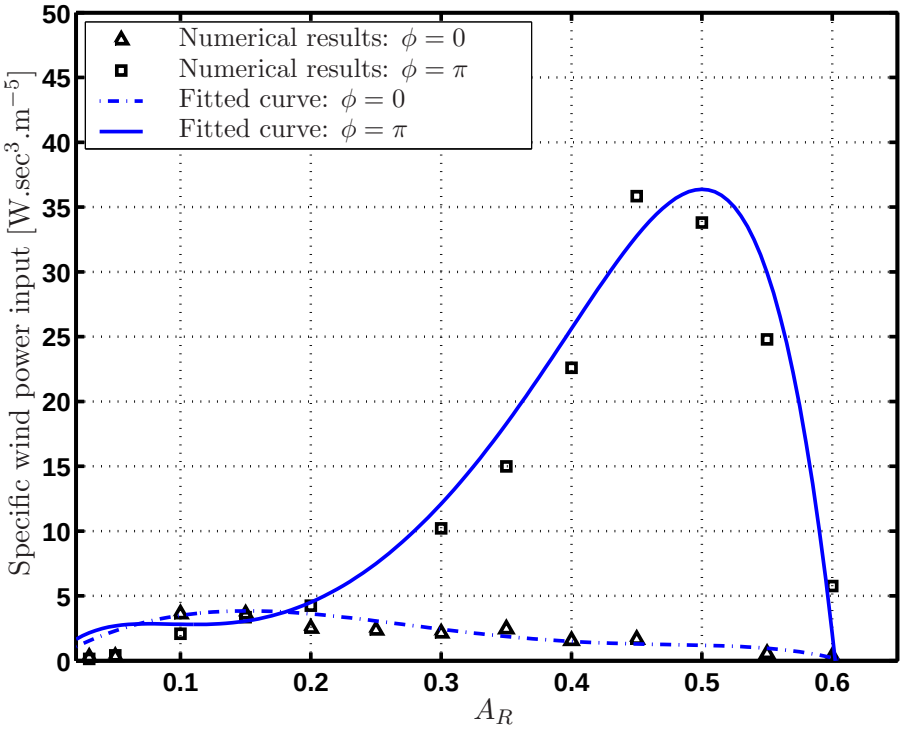

Figure 5.23: Numerically obtained wind power inputs for the downstream cylinder for X/D=20

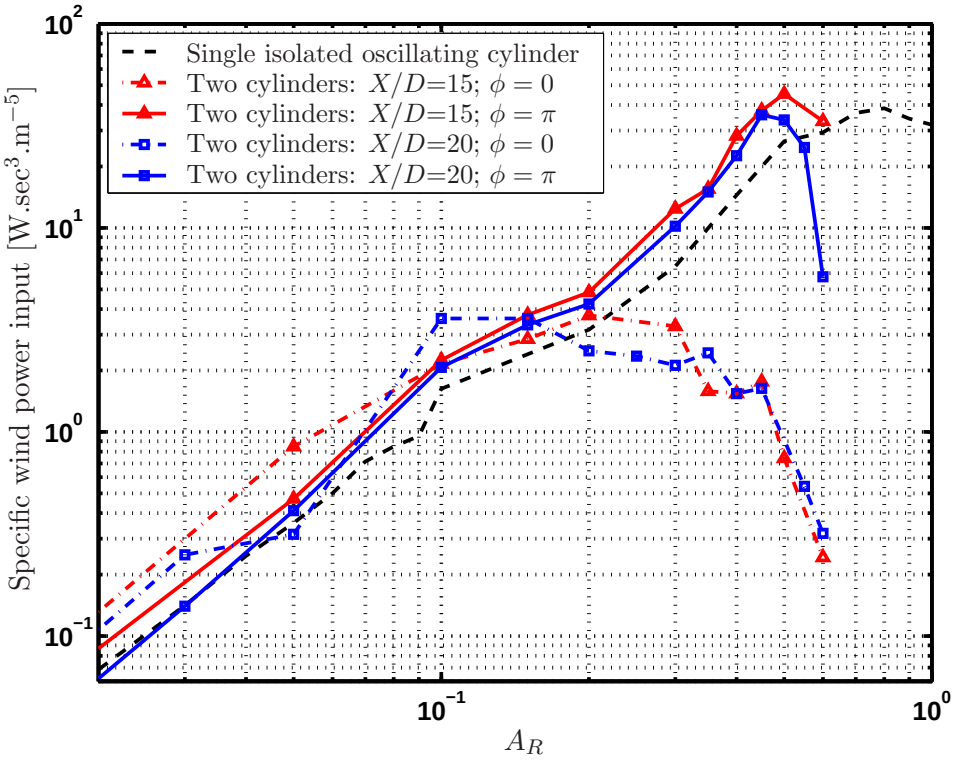

Figure 5.24: Comparison of wind power inputs for the single cylinder and the downstream cylinder of two cylinders in a tandem

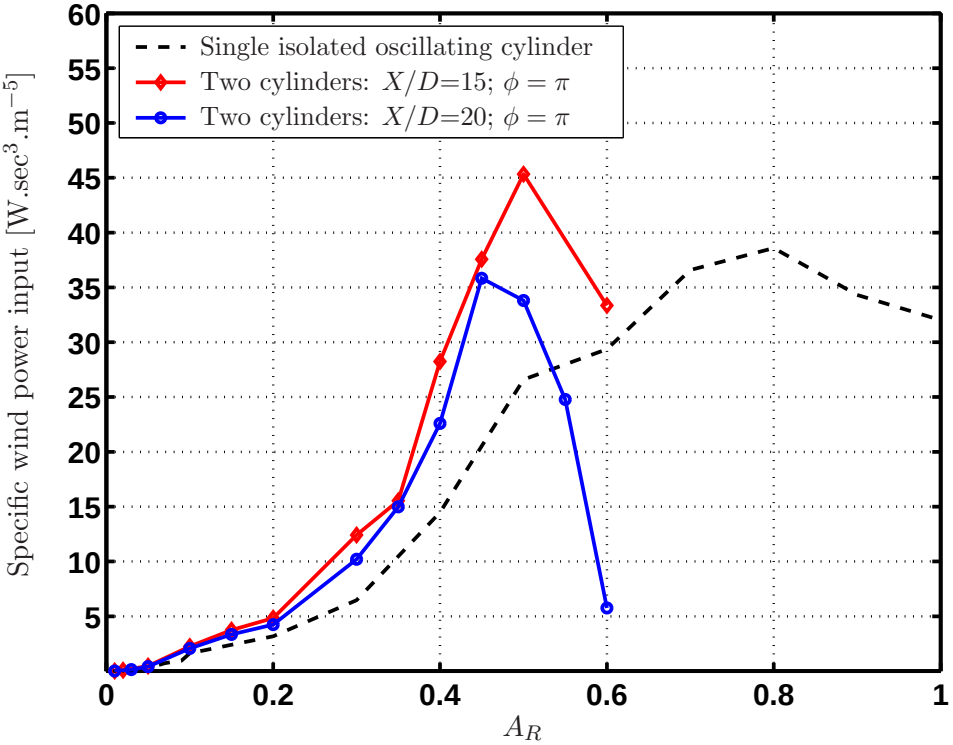

Figure 5.25: Comparison of wind power inputs for the single cylinder and the downstream cylinder of two cylinders in a tandem

input is, that due to the generation of wake-turbulence between both the cylinders, vortices from the wake of upstream cylinder become very weak, causing a low power input on the downstream cylinder.

It is also noticed that the specific wind power input on the downstream cylinder decreases, with an increasing value of X/D and tends toward single isolated cylinder case for a larger X/D values. In figure 5.25, the wind power input for a single oscillating cylinder is plotted against the obtained values for oscillating downstream cylinder on the linear scale. For its highest value, the wind power input for $X/D \approx 15$ is approximately 80% higher than the corresponding value for the single isolated oscillating cylinder.

Brika and Laneville, in [52], presented the results from wind tunnel tests on two cylinders in tandem, and obtained the wind power inputs on the downstream cylinder. Yet in their studies the upstream cylinder was kept fixed, which does not replicate the vibration character of conductor bundles. However, similar trends of the wind power inputs for a cylinder oscillating in the wake of another stationary cylinder are noticed by Pon et al. in [142] and by Brika and Laneville in [52].

Hence, it is concluded that the presence of an upstream cylinder increases significantly the wind power input imparted to the downstream cylinder. Current study shows that, this increase could be as large as, 80% depending on the lateral distance between both the cylinders. Wind power input on the downstream cylinder is higher when both the cylinders oscillate in the opposite phases. It is also noted, however, that for the higher oscillation amplitudes of the cylinders, wind power on the downstream cylinder drops sharply. This also explains why even in undamped bundled conductors, vibration amplitudes are much smaller than those in the single conductor transmission lines.

For the present study, the energy balance analysis given in chapter 4 uses the wind power input curves presented in figure 5.24. In order to obtain the wind power inputs on both the upstream subconductors in the quad bundle benchmark problem, stated in section 3.6.2, the curve corresponding to a single oscillating cylinder in (5.49) is used, as shown in the figure 5.12. As the horizontal distance between upstream and the downstream subconductors is approximately 0.5m, i.e. $20D$, the wind power input curves corresponding to $X/D = 20$, i.e. (5.54) and (5.55), are utilized in order to obtain the power input from the wind on both the downstream subconductors. For each vibration frequency the phase difference between the vertical oscillations of the upstream and the downstream subconductor is computed from the mode shapes, as mentioned in the section 3.4. Wind power input values from the curves corresponding to $\phi = 0$ and $\phi = \pi$ in the figure 5.24, i.e. (5.54) and (5.55), are linearly interpolated for any intermediate phase difference between the vertical motions of both the subconductors.

5.11 Conclusions

In the present chapter a finite volume approach is used to numerically analyze the flow around cylinder(s). At first the flow around a single stationary cylinder is analyzed. Obtained lift and drag time histories, and other aspects of the flow, e.g. frequency of the vortex shedding, Strouhal number etc. are compared to experimental data

in order to check the validity of numerical approach utilized. In the next step single cylinder is oscillated with a synchronous motion of a given amplitude and frequency. The wind power due to lift is obtained numerically and compared to previous wind-tunnel studies performed by many researchers. Although, the REYNOLDS number of the current analysis was far below that of the experimental studies, the wind power input for small vibration amplitudes was found in good agreement. For higher amplitudes of oscillations, the numerically obtained wind power input is higher than the experimental values, the reason for such a behavior are discussed. However, the utilized numerical scheme was validated.

After validation, the same numerical scheme was used to find the wind power input on the downstream cylinder of a tandem arrangement. Firstly the flow is analyzed around two stationary cylinders with different configurations. Numerical results of the time averaged lift and drag forces on the downstream cylinder are compared to experimental wind tunnel data, and were found to agree well. The analysis is then extended to the last step of analyzing the flow around two oscillating cylinders. Two lateral spacings between the cylinders were analyzed, viz., $X = 15D$ and $X = 20D$. The wind power input on the downstream cylinder is computed for different amplitudes of oscillation of the cylinders. A considerable difference between the wind power inputs for single and twin-bundled cylinders was noted.

It is now clear that the use of the same wind power input for single and tandem oscillating cylinders is at least questionable. These results for two cylinders in tandem might also be utilized for analyzing the quad-bundle conductors, as the wake-effects in the transverse direction are negligible for a spacing higher than $4D$, which is normally the case in transmission lines.

Chapter 6

Conclusions and recommendations

Summary: The outcomes of the studies presented in chapter 3 and 5 are evaluated in section 6.1. The evaluations lead to the main conclusions given in section 6.2, in response to the research aim of the present work stated in the section 1.3. The final chapter of the thesis ends with section 6.3, which discusses the recommendations and the suggestions for follow-up research.

6.1 Evaluation of the studies in this thesis

This thesis presents a mathematical-mechanical modeling of the aeolian vibrations in conductor bundles with many spacer dampers and STOCKBRIDGE dampers. Both the structural and the aerodynamic side of the conductor bundle vibration problem are considered in this work. In chapter 2, the conductor bundle with many spacer dampers and STOCKBRIDGE dampers is modeled by treating the conductor as a continuous system. Different external damping devices are incorporated using their impedance matrices. The formulation results in a non-polynomial transcendental eigenvalue problem (TEVP) in the complex domain. It presents several numerical difficulties in order to obtain all the system eigenvalues using traditional solution methods [34, 65, 64, 5].
The aim of this thesis is

1. to find better numerical techniques for the solution of the transcendental eigenvalue problem, which is encountered when modeling conductor bundles by considering subconductors as continuous systems.

2. to numerically obtain the wind power input on the oscillating downstream cylinder under the wake of an oscillating upstream cylinder.

6.1.1 Solution of TEVP

Three methods for the solution of non-polynomial TEVP in the complex domain are presented, viz., the determinant search method, an alternate approach by converting the homogeneous set of equations into a nonhomogeneous set, and a first order NEWTON method. A benchmark problem is solved, and the solutions obtained by the three methods are compared in section 3.6.1. It is shown in section 3.6.1 that the classical determinant search method misses several eigenvalues. The prime reasons for this behavior is a large variation in the order of the elements of the system matrix, and a poor optimization criterion, involving many multiplication operations to calculate the determinants. Such difficulty is avoided in the alternate approach, by converting the homogeneous set of equations into a nonhomogeneous one. The alternate approach

results in a numerically well-behaving optimization criterion. It is able to find many eigenvalues missed by the determinant search. The alternate approach gives a good solution method in the case of single conductor problems, as shown in [5]. However, with the very dense spectrum of the eigenvalues in the case of conductor bundles, it misses many eigenvalues due to the optimization criterion involving the complex domain. NEWTON's method of solving the eigenvalue problems is specially useful for the systems having closely spaced eigenvalues. Comparisons of the obtained results in section 3.6.1, show that even the first order NEWTON method not only requires the least number of iterations and, hence, is the fastest among other presented methods, but also is able to find all the eigenvalues of such a system with densely spaced eigenvalues. The first order NEWTON method for the solution of the eigenvalue problems, is found to be about 2 times faster than the determinant search method and about 1.25 times faster than the alternate approach. The system eigenvalues for a larger benchmark problem, with 6 spacer dampers, are obtained using the first order NEWTON method. The problem is further analyzed using the energy balance approach.

A higher order NEWTON method is also formulated in section 3.3.5, which can be used for system matrices for even bigger conductor bundle problems with many damping devices. A method is also discussed in section 3.5, which gives an estimate of the approximate number of complex eigenvalues presented in a specified frequency range.

6.1.2 Numerical computation of the wind power input

The flow around rigid and moving cylinder(s) is analyzed in chapter 5 using computational fluid dynamics (CFD) analysis. The CFD analysis in the current study is based on the two-dimensional NAVIER-STOKES equations using finite-volume schemes. A parallel version of the finite volume flow solver FASTEST2D [118], developed in the Technische Universität Darmstadt, Germany[25], is used for the solution of the fluid dynamics problem. Moving grids are used, which adapt to a new configuration depending on the cylinder movement at each time step.

Although, this part of the research ultimately aims to obtain the power imparted by wind on the downstream cylinder in a tandem arrangement, CFD analysis is performed in the following steps in order to first compare and validate the numerical results with the experimental findings:

1. flow around a single stationary cylinder,
2. flow around a single oscillating cylinder,
3. flow around two stationary cylinders in tandem, and
4. flow around two oscillating cylinders in tandem,

After finding good agreement between numerical and experimental results for the intermediate analysis, the desired wind power input on the oscillating downstream cylinder

[25] in the group of Prof. M. SCHÄFER.

in a tandem arrangement is obtained in step 4. Detailed outcomes of the studies are discussed in the following sections.

Flow around a single cylinder

In section 5.7.3 the flow around a single stationary cylinder is analyzed first. The study is made for a laminar cross-flow wind velocity corresponding to a REYNOLDS number of 460. As expected, the vortex shedding around the cylinder emerged. The frequencies of lift and drag forces were compared to the experimental results and were found in agreement. In section 5.8, the wind power input on an oscillating cylinder is obtained numerically by integrating the non-stationary NAVIER-STOKES equations of the flow around an oscillating cylinder. Moving grids are used, deforming as the cylinder moves. The flow is analyzed in an amplitude range of $A_R = 0.01$ to 1.0. It was observed that, corresponding to each vibration amplitude, the wind power input varies with the oscillation frequencies. In order to obtain the maximum value of wind power input corresponding to each vibration amplitude, the study is performed in a cylinder oscillation frequency range of $F_R = 0.766$ to 1.021, results for which are shown in table 5.3 and in figure C.14.

Figure 5.11 depicts a comparison of the numerically obtained specific wind power input on a single oscillating cylinder to the same obtained experimentally by other researchers. The results show a good agreement for the lower vibration amplitudes. However, for the higher amplitudes, the numerical wind power input has larger values than the experimental results. Such differences are mainly due to the laminar wind flow used in the numerical studies, whereas the experimental studies are performed for turbulent flows.

Flow around two cylinders in tandem

The flow around two stationary cylinders, under different configurations, are studied next. The study is performed for two in-flow spacings between the cylinders, i.e., $X/D = 15$ and 20. Cross-flow spacings are varied from $Y/D = 0$ to 4.5. The study is performed for a REYNOLDS number of 460. It is observed in section 5.9.3 that after a cross-flow spacing of $Y/D > 3.0$ between two cylinders, there is a small effect of the wakes coming from the upstream cylinder on the flow around the downstream cylinder. Due to this fact, in a quad conductor bundle, it is sufficient to consider the influence of only one upstream cylinder on the downstream cylinder, which is directly in line with it. Hence, in the current study, the obtained wind power input for the two cylinder configuration, as shown in figure 5.21, is also used for obtaining the wind power input on both the downstream cylinders in the benchmark problem for a quad bundle. The time-averaged lift and drag forces on the downstream cylinder are obtained for different in-flow and cross-flow spacings between the two cylinders. The obtained results are compared to the results from experimental studies and found acceptable, as described in section 5.9.3 and shown in figures 5.17 and 5.18.

In the last step of the numerical analysis, the flow around two oscillating cylinders is analyzed. The study is performed for two in-flow spacings between the cylinders, i.e., $X/D = 15$ and 20. Both cylinders are oscillated with the same amplitudes and frequen-

cies. For each amplitude, the frequency is taken equal to the frequency corresponding to the maximum wind power input in the case of a single oscillating cylinder, as shown in table 5.3. In order to limit the computational effort, the flow around two oscillating cylinders is analyzed for two phase differences of the cylinders' oscillations only, i.e., $\phi = 0$ and $\phi = \pi$.

Section 5.10.2 describes the obtained wind power input on the oscillating downstream cylinder under the wakes from an oscillating upstream cylinder. Figures 5.22 and 5.23 show the obtained wind powers respectively for $X/D = 15$ and 20. They are compared to the numerically obtained wind power input on a single oscillating cylinder in figure 5.24 and 5.25.

It is observable from these figures that the wind power input on a single oscillating cylinder behaves different from that on a downstream cylinder in a tandem arrangement. Wake from the upstream cylinder considerably effect the flow behavior of the downstream cylinder, even at a relatively large in-flow spacing (i.e., $X/D = 20$) between them. The obtained wind power inputs, are used for the power input on the downstream subconductors for the energy balance analysis of the benchmark problem in chapter 5.

6.2 Conclusions

In this thesis a modified energy balance principle was developed for estimating the aeolian vibration levels in conductor bundles with many spacer dampers and STOCKBRIDGE dampers. The conclusions are as follows:

1. Modeling of the conductor bundles with many spacer dampers and STOCKBRIDGE dampers, using the presented mathematical-mechanical model, considerably reduces the size of the problem in comparison to the discrete methods. However, the price one pays for the reduced problem-size, are the increased numerical difficulties in the form of a TEVP in the complex domain.

2. NEWTON's eigenvalue iteration method is an efficient technique for solving the TEVP of a sparse-system matrix with very closely spaced complex eigenvalues. It is not only able to determine all of the system eigenvalues for the presented benchmark problem, but also is faster and requires less iterations compared to other solution methods.

3. First efforts are made in the current work to numerically determine the wind power input on oscillating cylinders. Numerical flow analysis is carried out via CFD. Wind power inputs are obtained for the oscillating single cylinder, and for the oscillating downstream cylinder in the wake of oscillating upstream cylinder. The numerical analysis has provided promising results, which are comparable to former experimental data.

4. Numerical analysis of flows around the cylinders show that the flow around an isolated cylinder is considerably different from the flow around the downstream cylinder in a tandem configuration. A significant difference between the wind

power input curves, for an isolated cylinder and the downstream cylinders in tandem arrangement, is observed. The conclusion is, that for the energy balance analysis of conductor bundles, wind-power input curves for a single cylinder must not be used for the downstream conductors.

5. A method for computing the resultant amplitudes of a subconductor undergoing the vertical and the horizontal oscillations, is shown in section 4.4.2. A similar approach is also used for obtaining the effective angles for computing strains at the critical locations on the subconductors.

6.3 Recommendations for follow-up research

The numerical analysis of the flow around a single cylinder and around two cylinders in tandem, has produced promising results in the present work. However, these results are still incomplete due to the present day limitations in computational power. Following recommendations are suggested for the future work:

1. In the current work, the flow around a single oscillating cylinder is investigated for its prescribed motion. Few oscillation frequencies in proximity of the vortex-shedding frequency are chosen, as the lock-in frequency is not known exactly. Hence, the obtained wind power input may not be the maximum, which corresponds to the lock-in frequency. It would be worthwhile to investigate the same using *fluid structure interaction* (FSI), which gives the exact lock-in frequency and, hence, the maximum wind power input.

2. It would be worthwhile to investigate the flow with different percentages of turbulence, which correspond more closely to the conductor bundles in the field.

3. In the present analysis the flow around two oscillating cylinders, considers only two phase differences between the cylinders' oscillations. It is assumed, that the wind power input can be linearly interpolated for any intermediate values of the phase difference. A detailed insight on the dependency of wind power input on the cylinders' phase differences is, thus, necessary.

Appendix A

Transmission line conductor as a string

A general way of modeling a transmission line conductor is to consider it as a beam under an axial tension. This chapter presents the derivation of the equation of motion for such axially tensed beam. It is discussed later how a transmission line conductor can safely be treated as a string in order to reduce the size of the problem.

A.1 Equation of motion of a beam under axial tension

Let us consider conductor as a homogeneous, isotropic, axially-tensed Euler-Bernoulli beam[26] undergoing a planar deflection. Its is considered that its span length is l, cross sectional area is A, moment of inertia is I, and its axial tension is T. The mass density of the beam material is ρ and its Young's modulus is E. Its elementary equation of motion is derived here, by assuming that the motion of the beam is planar and transverse, i.e., longitudinal motion is neglected.

Hamilton's principle is used for obtaining the equation of motion. If $w(x,t)$ is the transverse deflection field at any location x on the beam at any time t, the total kinetic energy $\mathcal{T}$ due to the translation and the rotation of an infinitesimal beam element can be written as [143, 144]

$$\mathcal{T} = \frac{1}{2}\int_0^l \rho A \dot{w}^2 \mathrm{d}x + \frac{1}{2}\int_0^l \rho I \dot{w}'^2 \mathrm{d}x, \tag{A.1}$$

where $(\,)'$ and $\dot{(\,)}$ denote the derivatives with respect to the space coordinate x and to the time coordinate t respectively. The potential energy $\mathcal{V}$ can be written from the theory of elasticity as

$$\mathcal{V} = \frac{1}{2}\int_0^l EI w''^2 \mathrm{d}x + \frac{1}{2}\int_0^l T w'^2 \mathrm{d}x, \tag{A.2}$$

The Lagrangian $\mathcal{L}$ is given by $\mathcal{L} = \mathcal{T} - \mathcal{V}$, and the variational form yields

$$\delta \int_{t_0}^{t_1} \mathcal{L} \mathrm{d}t = 0, \tag{A.3}$$

[26] Euler-Bernoulli hypotheses holds good if the the ratio of the height of the beam's cross section to the radius of curvature of the neutral fibre after the deformation is much smaller compared to unity [143, 144].

or

$$\delta \int_{t_0}^{t_1} \int_0^l \frac{1}{2} \left[\rho A \dot{w}^2 + \rho I \dot{w}'^2 - EI w''^2 - T w'^2 \right] \mathrm{d}x \; \mathrm{d}t = 0. \tag{A.4}$$

Using the variational procedure, we obtain from (A.4)

$$\int_{t_0}^{t_1} \int_0^l \left[\rho A \dot{w} \delta \dot{w} + \rho I \dot{w}' \delta \dot{w}' - EI w'' \delta w'' - T w' \delta w' \right] \mathrm{d}x \; \mathrm{d}t = 0, \tag{A.5}$$

or

$$\begin{aligned} &- \int_{t_0}^{t_1} EI w'' \delta w' \Big|_0^l \mathrm{d}t - \int_{t_0}^{t_1} \left[(EI w'')' - \rho I \ddot{w}' - T w' \right] \delta w \Big|_0^l \mathrm{d}t \\ &+ \int_{t_0}^{t_1} \int_0^l \left[-\rho A \ddot{w} - (EI w'')'' + (\rho I \ddot{w}')' + (T w')' \right] \delta w \; \mathrm{d}x \; \mathrm{d}t = 0, \end{aligned} \tag{A.6}$$

where the variations of the field variable and its spatial derivatives at the initial and the final time instants are taken as zero, i.e., $\delta w \Big|_{t_0}^{t_1} = \delta w' \Big|_{t_0}^{t_1} \equiv 0$. The condition in (A.6) holds for an arbitrary variation δw, if and only if all three integral terms vanish identically. The first two terms correspond to the natural and the geometric boundary conditions. The integrand in the last term of (A.6) leads to

$$\rho A \ddot{w} + (EI w'')'' - (\rho I \ddot{w}')' - (T w')' = 0, \tag{A.7}$$

which is the equation of motion for a beam under axial tension. For a constant cross section, homogeneous material and a constant tension in the beam, (A.7) takes the form

$$\rho A \ddot{w} + EI w'''' - \rho I \ddot{w}'' - T w'' = 0. \tag{A.8}$$

Relation (A.8) is the equation of motion for a homogeneous, cylindrical beam with a constant axial tension, vibrating in a transverse plane, with rotational inertia included.

A.2 Transmission line conductor as a string

A string is defined as an one-dimensional elastic continuum that does not transmit or resist bending moment and shear force. Such an idealization may also be utilized for a beam or a cable-like element when its slenderness ratio[27] is large as compared to unity. Using the non-dimensional variables

$$\tilde{x} = \frac{x}{l}; \; \tilde{t} = \frac{tc}{l} = \frac{t}{l} \sqrt{\frac{T}{\rho A}}; \text{ and } \tilde{w} = \frac{w}{r_g} = w \sqrt{\frac{A}{I}},$$

[27] Ratio of length to the transverse dimension.

the equation of motion for a beam under axial tension, as derived in (A.8), is rewritten as

$$\frac{\mathrm{d}^2\tilde{w}}{\mathrm{d}\tilde{t}^2} + \frac{1}{4\pi^2}\left(\frac{\lambda_{beam}}{l}\right)^2 \frac{\mathrm{d}^4\tilde{w}}{\mathrm{d}\tilde{x}^4} - \frac{1}{s_r^2}\frac{\mathrm{d}^4\tilde{w}}{\mathrm{d}\tilde{x}^2\mathrm{d}\tilde{t}^2} - \frac{\mathrm{d}^2\tilde{w}}{\mathrm{d}\tilde{x}^2} = 0, \tag{A.9}$$

where r_g is the radius of gyration of the cross-section about its neutral axis, c is the wave velocity of the traveling wave in the string, $\lambda_{beam} = 2\pi\sqrt{EI/T}$ is a wavelength and $1/s_r^2$ is defined as the slenderness ratio, where $s_r = \sqrt{Al^2/I}$. It is clear from (A.9) that the non-dimensional term $(\lambda_{beam}/l)^2$ decides the relative importance of the fourth-order flexure term, while $1/s_r^2$ reflects the relative importance of the fourth order rotary inertia term. Term $\sqrt{EI/T}$ is called as the *characteristic length* l_{char} of the conductor. For high-tension transmission line conductors, value of l_{char} typically varies between 0.1 and 0.5 m, which as compared to the span length of the transmission line is a very small quantity. A transmission line conductor has a very small flexural stiffness EI as compared to the conductor tension T, and a very large span length l as compared to its transverse dimension, i.e., its diameter D. Hence, for a transmission line conductor

$$\frac{\lambda_{beam}}{l} \ll 1, \tag{A.10}$$

and

$$s_r \gg 1, \tag{A.11}$$

hold good. Moreover, the EI-term has a very little influence on the eigenfrequencies and eigenfunctions of the free vibrations [29], and can, therefore, be neglected in their determination. Considering (A.10) and (A.11), the fourth order differential terms in (A.9) are very small. Hence, they are safely neglected, and the transmission line conductor is considered as a string having no stiffness. Neglecting both the fourth orders terms in (A.9) results in the equation of motion for a string

$$\rho A\ddot{w} - Tw'' = 0. \tag{A.12}$$

By neglecting the fourth order terms, the size of the problem is considerably reduced. Such approximation does not have considerable effect on the system eigenfrequencies [29]. Hence, equation (A.12) is used in the section 2.1.1 to model the subconductors of the conductor bundle. The forth order terms do however become important when computing bending strains (see section 4.4.1).

Appendix B

Impedance matrix for a spacer damper

A spacer damper consists of an aluminium frame, which is considered to be rigid for the purpose of the investigation. Arms are attached to the central body by means of flexible joints containing rubber elements. These joints are treated as *viscoelastic* hinges for the mathematical modeling. At the free end, each of these arms posses a clamp of finite length for gripping one of the subconductor. In principle, the impedance matrix for a spacer damper can be found directly from the laboratory experiments. However, it is a formidable task to experimentally obtain impedance matrix for each new spacer damper. In what follows, shows a procedure to analytically obtain the impedance matrix for a spacer damper with its known design parameters, developed by Anderson and Hagedorn in [21]. In present analysis a four armed spacer damper is considered, as shown in figures 1.3. The procedure is, however, generalized for any number of arms.

A quad spacer damper, as shown in figures 1.2c and 1.3, consists of a central rigid body connected to four arms by viscoelastic hinges. Figure B.1 shows the corresponding coordinate system considered for a quad spacer damper, in the current modeling. In this figure body $\mathbf{C}$ represents the central rigid frame, and bodies $\mathbf{D}_k$, $k = 1, 2, 3, 4$, represent arms of the spacer damper. Each of these 5 rigid bodies have 6 degrees of freedom (DOF), i.e., 3 translational and 3 rotational. The quad-spacer damper is therefore a system of five rigid bodies, i.e., it is a system of $5 \times 6 = 30$ DOF. Motion of each of these five bodies is ruled by the linear and angular momentum equations

$$m_i \ddot{\overrightarrow{r}}_i = \sum_j \mathcal{F}_{i,j}, \qquad \frac{\mathrm{d}}{\mathrm{d}t}\left(\Theta_i \overrightarrow{\omega}_i\right) = \sum_j \mathcal{M}_{i,j}, \qquad i = 1, 2, 3, 4, 5. \tag{B.1}$$

Here m_i is the mass of the i-th body, $\ddot{\overrightarrow{r}}_i$ is the acceleration of its center of mass with respect to an inertial frame of reference, Θ_i is its central inertia tensor and $\overrightarrow{\omega}_i$ is its angular velocity with respect to an inertial frame. The $\mathcal{F}_{i,j}$ are the forces acting on in i-th body; the sums on the right side of (B.1) extend over all these forces and moments respectively.

The configuration of the system is represented at each instant by the values of the generalized coordinates

$$\mathbf{q} = \langle q_1, q_2, ..., q_{30} \rangle^T, \tag{B.2}$$

which can be arbitrarily chosen. Typically, for each body three translational and three rotational co-ordinates about center of gravity of each body are used. Since we are interested only in oscillations of small amplitudes, three rotation angles of each of the

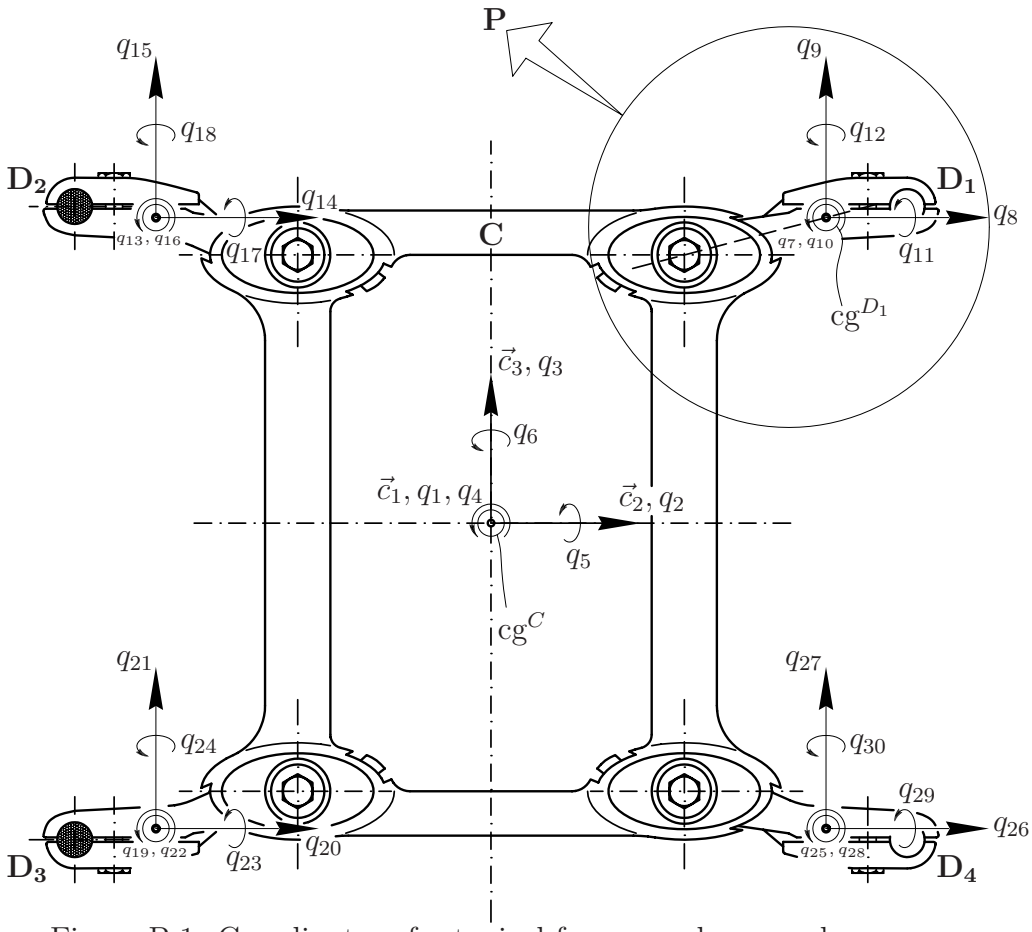

Figure B.1: Coordinates of a typical four armed spacer damper

five bodies about the $x-$, $y-$ and $z-$ axes, as shown in figure B.1, can be used as generalized co-ordinates, and there is no need to use EULER angles or an equivalent representation. In the equations of motion, linearized about the equilibrium position, the left sides of (B.1) is simply a linear combination of the $\ddot{q}_i, i = 1, 2, ..., 30$. Moreover, the forces at the viscoelastic joints in linearized form can also be written as linear combinations of q_i and $\dot{q}_i, i = 1, 2, 3, ..., 30$.

With the system in equilibrium, the transverse forces $F^+_{m,n}$ and $F^-_{m,n}$, $m = 1, 2, ..., 8$, vanish, while the axial $g_m, m = 1, 2, ..., 8$, are equal to the respective tensions in the conductors. For the oscillating system we therefore have

$$g_m = T_m + \bar{g}_m, \qquad m = 1, 2, ..., 8 \tag{B.3}$$

where the $\bar{g}_m, m = 1, 2, ..., 8$, are small of first order in the $\mathbf{q}$. If the arm of figure 2.2c is rotated about its axis PC, it is clear that T_1 and T_2 produce a rotating torque of first order in $\mathbf{q}$, while the torque produced by $\bar{g}_1$ and $\bar{g}_2$ is of the second order.

The linearized equations of motion of the spacer damper are therefore of the type

$$\mathbf{M}\ddot{\mathbf{q}} + \mathbf{D}\dot{\mathbf{q}} + \mathbf{C}\mathbf{q} = \mathbf{L}\mathbf{f} + \mathbf{N}\mathbf{u}, \tag{B.4}$$

with $\mathbf{M}, \mathbf{D}$ and $\mathbf{C}$ as real symmetric 30×30 matrices, $\mathbf{L}$ a real 30×16 matrix and $\mathbf{N}$

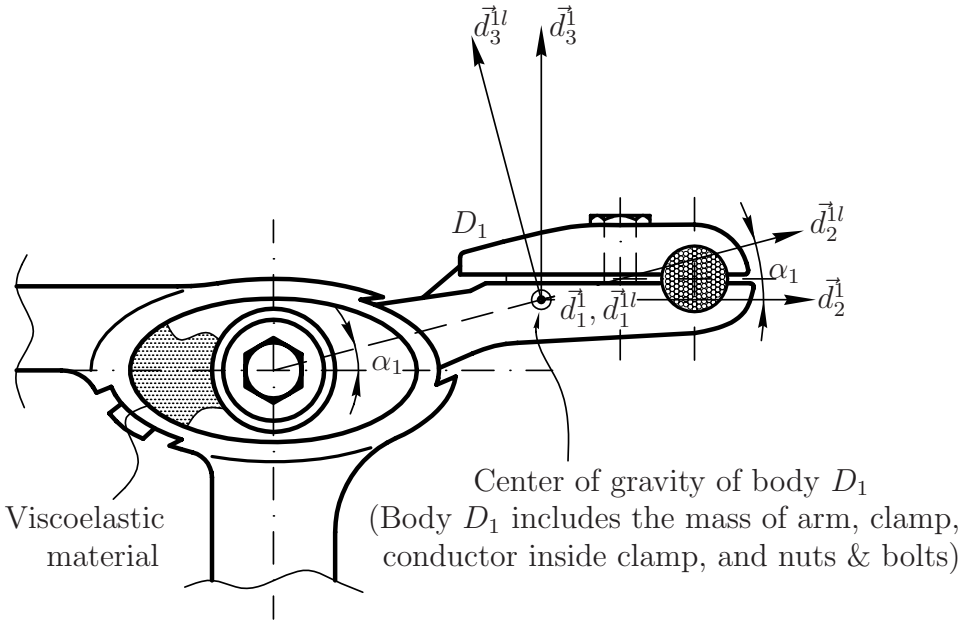

Figure B.2: Details at view-**P** of figure B.1

a real 30×4 matrix. As before,

$$\mathbf{f} = \left\langle F^-_{1,n}, F^-_{2,n+1}, F^+_{1,n+1}, F^+_{2,n}, F^-_{3,n}, F^-_{4,n}, F^+_{3,n+1}, F^+_{4,n+1} \right\rangle^T , \tag{B.5}$$

and

$$\mathbf{f} = \begin{bmatrix} F^-_{1,n} \\ F^-_{2,n} \\ F^+_{1,n+1} \\ F^+_{2,n+1} \\ F^-_{3,n} \\ F^-_{4,n} \\ F^+_{4,n+1} \\ F^+_{4,n+1} \end{bmatrix}, \qquad \mathbf{w}_n = \begin{bmatrix} w^-_{1,n}(\Delta l_n - b, t) \\ w^-_{2,n}(\Delta l_n - b, t) \\ w^+_{1,n+1}(b, t) \\ w^+_{2,n+1}(b, t) \\ w^-_{3,n}(\Delta l_n - b, t) \\ w^-_{4,n}(\Delta l_n - b, t) \\ w^+_{2M-1,n+1}(b, t) \\ w^+_{2M,n+1}(b, t) \end{bmatrix}, \tag{B.6}$$

is the vector of the forces acting at the damper clamps in the directions transverse to the subconductors as shown in figure 2.2(c) and

$$\mathbf{u} = \langle (\bar{g}_1 - \bar{g}_2), (\bar{g}_3 - \bar{g}_4), (\bar{g}_5 - \bar{g}_6), (\bar{g}_7 - \bar{g}_8) \rangle^T , \tag{B.7}$$

contains the forces acting on the clamps in the subconductors' axial direction. Only the differences of the $\bar{g}_i, i = 1, 2, ..., 8$, contained in (B.7) appear in the linearized equations of motion. In (B.4) the mass matrix **M** is easily obtained from the mass and geometry of the spacer damper. The damping matrix **D** and the stiffness matrix **C**, which describe how the forces and moments in the viscoelastic joints are related to the displacements and velocities, contain information on both the viscoelastic properties of the joints and

the geometry of the spacer damper. In addition, the matrix $\mathbf{C}$ contains the coefficients of the restoring torques due to $T_i, i = 1, 2, ..., 8$. The matrices $\mathbf{L}$ and $\mathbf{N}$ contain geometric information only.

Since the clamps are not free to move in the axial direction of the conductors, we assume that the axial stiffness of the conductor is such that the clamps are rigidly fixed in this direction. This corresponds to four conditions of constraint, which in the linearized form are written as,

$$\mathbf{A}\mathbf{q} = \mathbf{0}, \tag{B.8}$$

where 4×30 real matrix $\mathbf{A}$ contains geometric parameters only. The constraint equation (B.8) is used for eliminating $\mathbf{u}$ from (B.4). Since we are interested only in the harmonic oscillations of the type

$$\mathbf{q}(t) = \mathrm{Re}\left[\hat{\mathbf{q}}\mathrm{e}^{\mathrm{i}\Omega t}\right], \tag{B.9}$$

with complex amplitude $\hat{\mathbf{q}}$, (B.4) is reduced to

$$\left[-\Omega^2\mathbf{M} + \mathrm{i}\Omega\mathbf{D} + \mathbf{C}\right]\hat{\mathbf{q}} = \mathbf{L}\hat{\mathbf{f}} + \mathbf{N}\hat{\mathbf{u}}, \tag{B.10}$$

where $\hat{\mathbf{f}}$ and $\hat{\mathbf{u}}$ are the complex force amplitudes corresponding to (B.5) and (B.7) respectively. Solving (B.10) for $\hat{\mathbf{q}}$ yields

$$\hat{\mathbf{q}} = \left(-\Omega^2\mathbf{M} + \mathrm{i}\Omega\mathbf{D} + \mathbf{C}\right)^{-1}\left(\mathbf{L}\hat{\mathbf{f}} + \mathbf{N}\hat{\mathbf{u}}\right), \tag{B.11}$$

and substituting it into

$$\mathbf{A}\hat{\mathbf{q}} = \mathbf{0}, \tag{B.12}$$

yields

$$\mathbf{A}\left(-\Omega^2\mathbf{M} + \mathrm{i}\Omega\mathbf{D} + \mathbf{C}\right)^{-1}\left(\mathbf{L}\hat{\mathbf{f}} + \mathbf{N}\hat{\mathbf{u}}\right) = \mathbf{0}. \tag{B.13}$$

These are four scalar equations, which can be solved for $\hat{\mathbf{u}}$:

$$\hat{\mathbf{u}} = \left[-\mathbf{A}\left(-\Omega^2\mathbf{M} + \mathrm{i}\Omega\mathbf{D} + \mathbf{C}\right)^{-1}\mathbf{N}\right]^{-1}\left[\mathbf{A}\left(-\Omega^2\mathbf{M} + \mathrm{i}\Omega\mathbf{D} + \mathbf{C}\right)^{-1}\mathbf{L}\right]\hat{\mathbf{f}}. \tag{B.14}$$

The vector $\hat{\mathbf{u}}$ is therefore known as a linear function of $\hat{\mathbf{f}}$, and if it is substituted into (B.10) this equation can be solved for $\hat{\mathbf{q}}$, giving

$$\hat{\mathbf{q}} = \mathbf{E}(\Omega)\hat{\mathbf{f}}. \tag{B.15}$$

The explicit form of complex 30×16 matrix $\mathbf{E}(\Omega)$ is not given here for simplicity, but it follows easily from the equation above.

If w_i and f_i are the elements of the corresponding displacement vector and the force vector, shown in (B.6), the geometric displacements w_i in the direction of $f_i, i = 1, 2, ..., 16$,

at the end points of the clamps is written as a linear combination of $q_j, j = 1, 2, ..., 30$, such as

$$\mathbf{w} = \mathbf{Q}\mathbf{q}, \tag{B.16}$$

where the real 16×30 matrix $\mathbf{Q}$ contains only geometric information. For the harmonic oscillations, (B.16) is written in terms of the complex amplitudes as

$$\hat{\mathbf{w}} = \mathbf{Q}\hat{\mathbf{q}} \tag{B.17}$$

which, together with (B.15), leads to

$$\hat{\mathbf{f}} = (\mathbf{Q}\mathbf{E}(\Omega))^{-1}\,\hat{\mathbf{w}}. \tag{B.18}$$

It finally yields

$$\hat{\mathbf{f}} = \left(\frac{1}{\mathrm{i}\Omega}\right)(\mathbf{Q}\mathbf{E}(\Omega))^{-1}\,\hat{\dot{\mathbf{w}}}, \tag{B.19}$$

so that the complex impedance matrix is

$$\mathbf{Z}(\Omega) = \left(\frac{1}{\mathrm{i}\Omega}\right)(\mathbf{Q}\mathbf{E}(\Omega))^{-1}. \tag{B.20}$$

It is to be noted here that impedance matrix $\mathbf{Z}(\Omega)$ contains not only the information of mass, damping and stiffness of the spacer damper, but also of the conductor tensions, due to the finite length $2b$ of the conductor clamp.

Mass matrix M:

In order to obtain the mass matrix $\mathbf{M}$ in (B.4), the mass and geometrical properties of the central frame and the spacer damper arms are determined. Moment of inertias of each rigid body about their local principal axes, are determined experimentally using *torsion pendulum* experiments [145]. In the current case, mass, locations of the CG's for each rigid body and their respective moment of inertias are provided by Ribe Electrical Fittings GmbH [17].

Stiffness and damping matrices C and D:

To compute $\mathbf{C}$ and $\mathbf{D}$ matrices, in (B.4), mechanical stiffness and damping parameters of the viscoelastic joints are determined in the laboratory. Since the damping is provided by the attached rubber elements at the arm-hinges, the damping matrix $\mathbf{D}$ is frequency-dependent. The term *viscoelastic* used so far to describe the properties of the joint is therefore somewhat misleading. In the present context it simply means that the joints has linear elastic and damping properties.

In order to obtain the damping and stiffness matrices $\mathbf{D}$ and $\mathbf{C}$, a *dynamic characteristic test* is carried out for each viscoelastic joints. The purpose of this test is to obtain the damping and the stiffness characteristics of the viscoelastic joints of a spacer damper. In such a test, the central rigid body is held fixed and a low-frequency sinusoidal movement (i.e., transverse or rotational) is applied on each joint along the axes

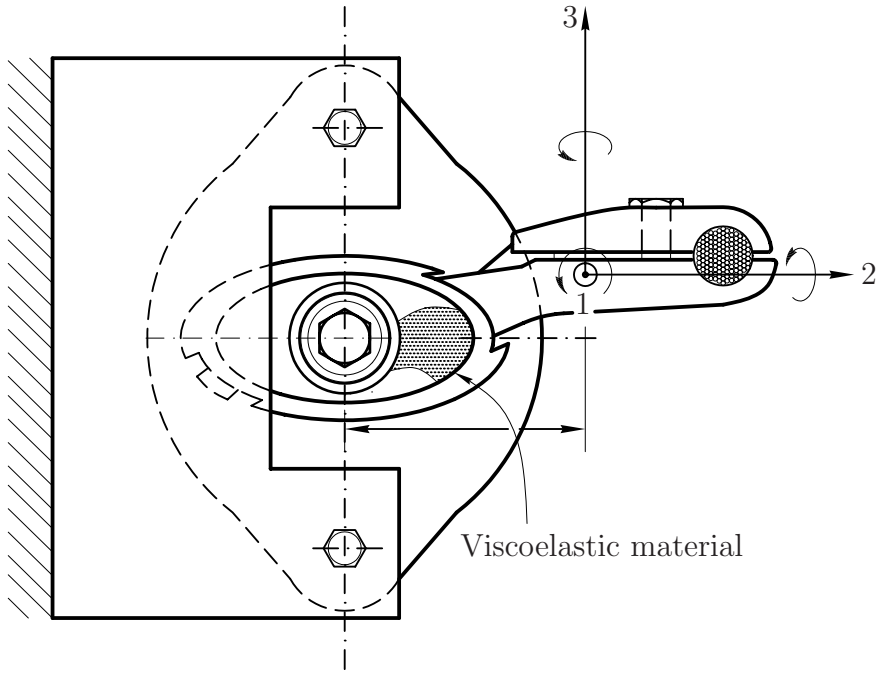

Figure B.3: Testing of the stiffness and damping characteristics of viscoelastic hinge

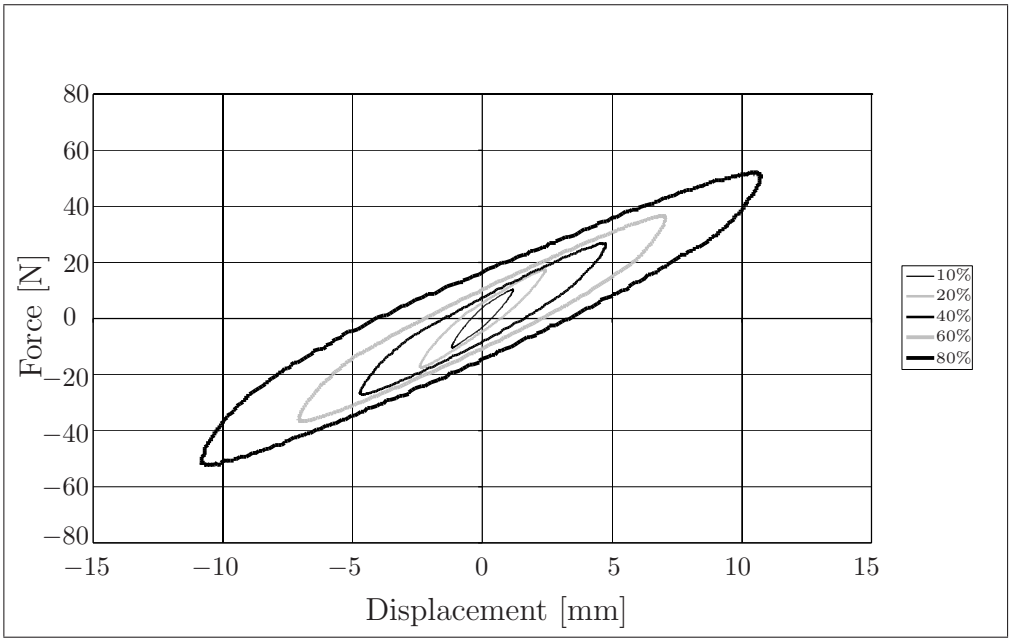

Figure B.4: Testing of the stiffness and damping characteristics of viscoelastic hinge (translational direction)

about which its characteristics are desired (i.e., along $\vec{d}_j^i, i = 1, 2, ..., M; j = 1, 2, 3$), as shown in the figure B.3. Forces F_j^i for a transverse movement (or moment for an rotational movement), corresponding displacement x_j^i (or the angle for rotational movement) and the phase angle $\varphi_{j,\text{trans}}^i$ (or $\varphi_{j,\text{rot}}^i$ for rotational movement) between the two are measured. From these measurements, the stiffness $C_{j,\text{trans}}^i$ (or $C_{j,\text{rot}}^i$) and the *damping factor* or the *loss factor* $\eta_{j,\text{trans}}^i$ (or $\eta_{j,\text{rot}}^i$) are calculated using[28]

$$C_{j,\text{trans}}^i = \frac{F_j^i \cos\varphi_{j,\text{trans}}^i}{x_j^i}, \tag{B.21}$$

$$\eta_{j,\text{trans}}^i = \tan\varphi_{j,\text{trans}}^i. \tag{B.22}$$

Table B.1: Testing results corresponding to figure B.4

Percentage of maximum displacement	Peak displacement	Peak Force	Phase Angle	Stiffness	Loss Factor
[-]	x [mm]	F [N]	φ [degrees]	K [N/mm]	η [-]
10	1.2	10.5	16.8	8.43	0.303
20	2.4	17.6	16.2	6.96	0.290
40	4.7	27.1	17.3	5.46	0.311
60	7.1	36.6	17.3	4.92	0.311
90	10.8	52.2	18.3	4.58	0.330

Figure B.4 shows a typical hysteresis plot between the displacement and the force (courtesy: RIBE Electrical Fittings GmbH [17]). For this test the central rigid frame is fixed and the arm is rotated around the axis of the hinge in a plane perpendicular to the subconductor. The excitation frequency is kept as a low value of 2 Hz. The test is performed at five different displacement amplitudes. The amplitudes are selected such

[28] If $m\ddot{x} + \frac{k}{\pi\Omega}\dot{x} + cx = \hat{f}\cos\Omega t$,

is the equation of motion for a damped system excited with a frequency Ω, where k is the structural damping of the system, then a dimensionless quantity *loss factor* is defined as $\eta = \tan\nu = \frac{k}{\pi c}$, where ν is called as the *loss angle* [143]. If φ is the phase difference between excitation force and the steady state response of the system, then it relates to the loss factor η as

$$\tan\varphi = \eta\left[1 - \left(\frac{\Omega}{\Omega_0}\right)^2\right]^{-1}.$$

For small excitation frequency Ω as compared to the natural frequency Ω_0 of the hinge-arm system, term $(\Omega/\Omega_0)^2$ becomes very small and can be neglected. Thus, for small excitation frequency relations $\eta = \tan\nu = \tan\varphi$, and hence, $\nu = \varphi$ holds good.

as to reproduce 10%, 20%, 40%, 60% and 90% of the maximum displacement permitted by the spacer damper design.

It is to be noted here that this test simulates the rotation of the damper-arm about axis 1 (refer figure B.3). This is the motion, which primarily causes the rubber (or viscoelastic) joint to dissipate most of the energy. Table B.1 shows the obtained values of the displacements, forces, phase angles, computed stiffness and loss factors. From the corresponding length of the spacer arm, one can compute the rotation angle and corresponding moment required to move it; and ultimately are obtain the corresponding loss factor.

In the current study, structural damping from the viscoelastic joints is incorporated in terms of the complex stiffness matrix $\mathbf{C}_{\text{struct}}$, where

$$\mathbf{C}_{\text{struct}} = \mathbf{C}(1 + i\eta). \tag{B.23}$$

B.1 Data for the benchmark problem

For the benchmark problem mentioned in the section 3.6, spacer dampers of the type RIBE-454-465-3 [17] are considered. Relevant data for this spacer damper are given in the table B.2.

Table B.2: Geometric data for quad spacer damper the type RIBE-454-465-3

Parameter	Value
Number of arms	4
Horizontal distance between two hinges	0.18 m
Vertical distance between two hinges	0.34 m
Distance from hinge point to center of mass of the corresponding arm (all 4 arms)	0.064 m
Distance from hinge point to center of mass of the conductor in corresponding arm (all 4 arms)	0.114 m
Angle between horizontal direction and center-line of arm ($\alpha_1, \alpha_2, \alpha_3$ and α_4)	0.247 rad
Mass of the frame with hinges and bolts	2.8 kg
Mass of each arm	0.5 kg
Inertia tensor of the frame including bolts, nuts and damper elements (regarding center of mass of the frame)	$\begin{bmatrix} 83.7 & 0 & 0 \\ 0 & 65.8 & 0 \\ 0 & 0 & 22.3 \end{bmatrix}$ $\times 10^{-3}$ kg.m^2
Inertia Tensor of each arm (regarding center of mass of the arm)	$\begin{bmatrix} 1.15 & 0 & 0 \\ 0 & 0 & 0 \\ 0 & 0 & 1.15 \end{bmatrix}$ $\times 10^{-3}$ kg.m^2

Appendix C

Lift and drag curves for single and two oscillating cylinder(s)

C.1 Single oscillating cylinder

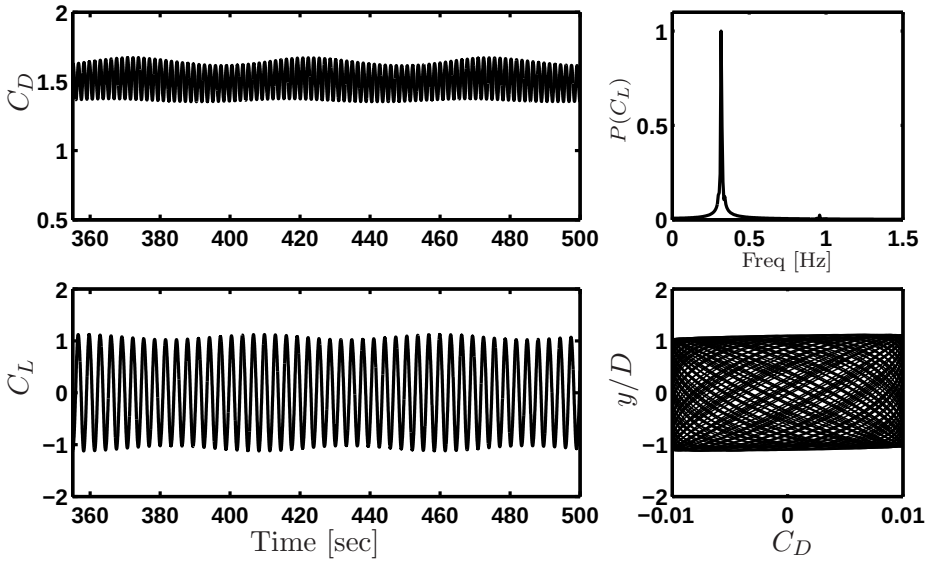

Figure C.1: $A_R = 0.01$, $f_0 = 0.3292$Hz (i.e., $S_R = 0.22$, $F_R = 0.936$)

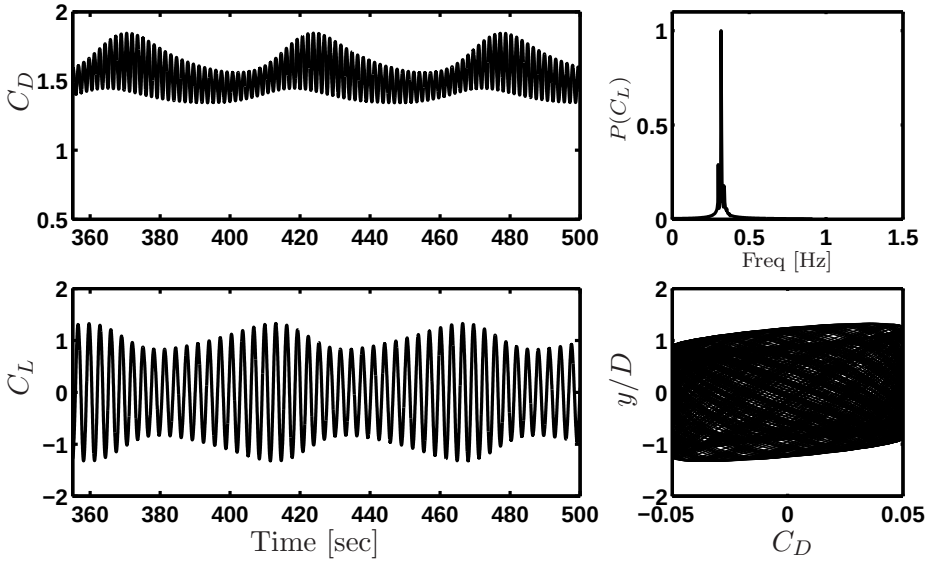

Figure C.2: $A_R = 0.05$, $f_0 = 0.3516$ Hz (i.e., $S_R = 0.235$, $F_R = 1.00$)

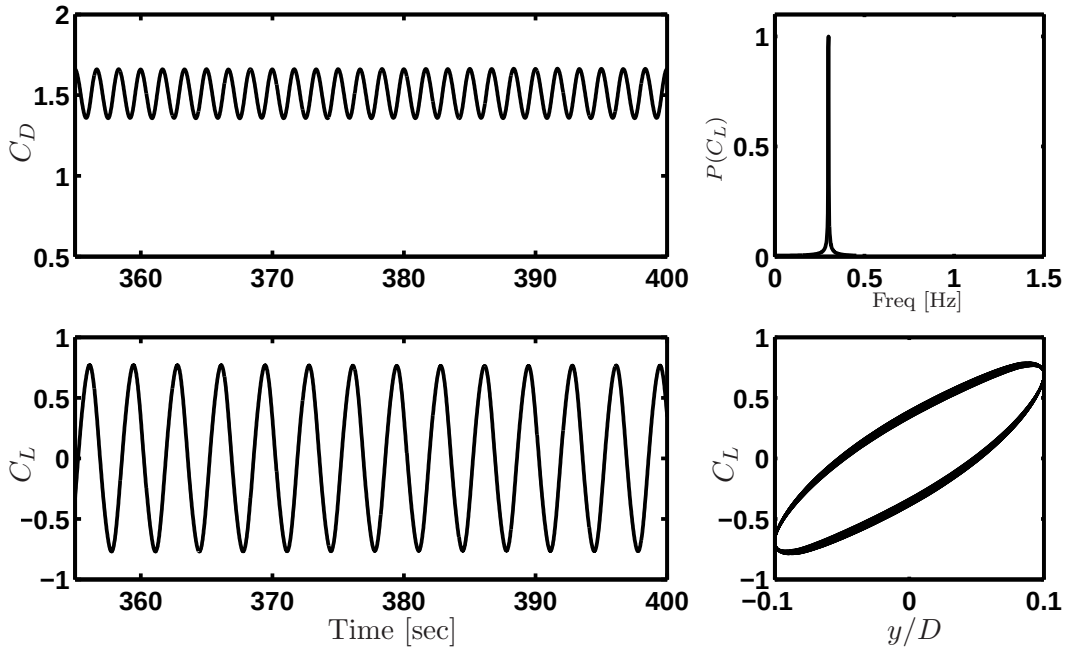

Figure C.3: $A_R = 0.10$, $f_0 = 0.2991$ Hz (i.e., $S_R = 0.20$, $F_R = 0.851$)

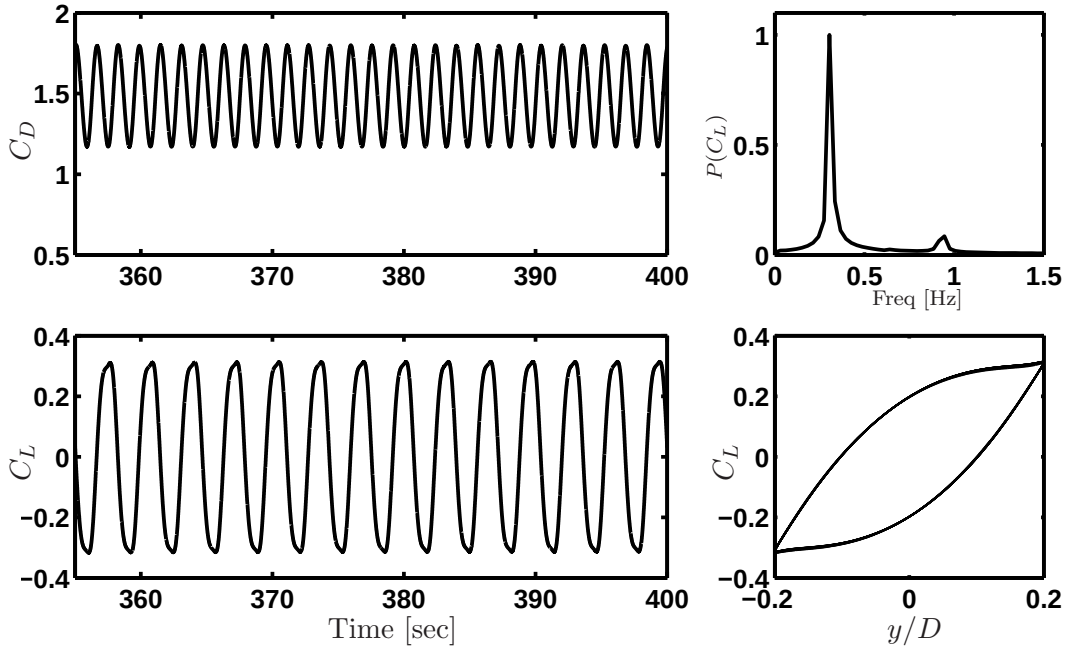

Figure C.4: $A_R = 0.20$, $f_0 = 0.3142$ Hz (i.e., $S_R = 0.21$, $F_R = 0.894$)

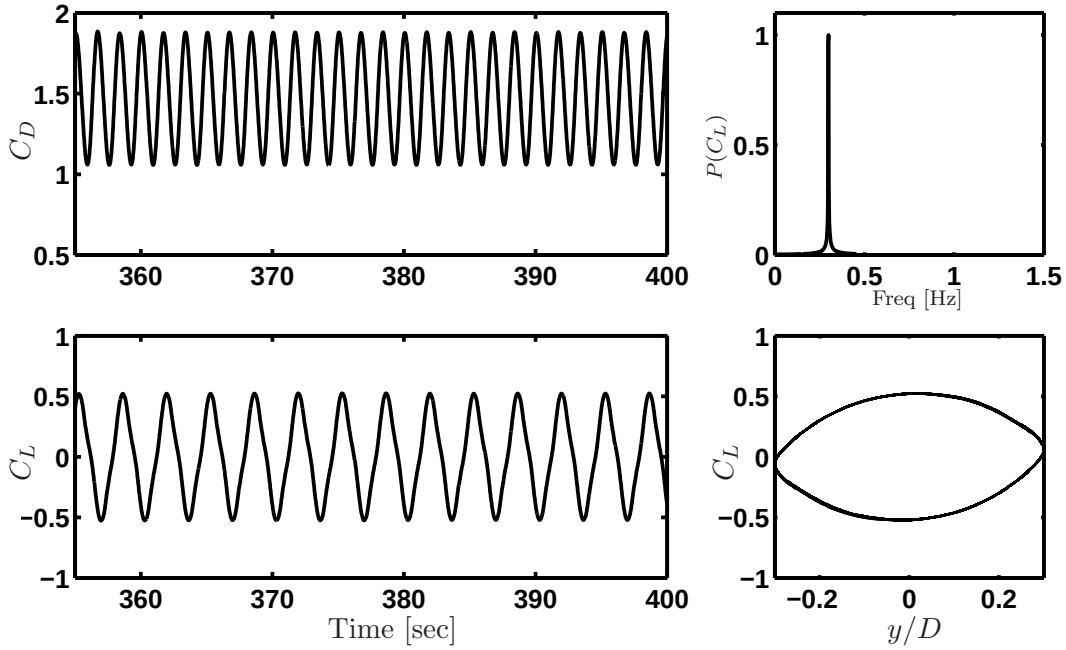

Figure C.5: $A_R = 0.30$, $f_0 = 0.2991$ Hz (i.e., $S_R = 0.20$, $F_R = 0.851$)

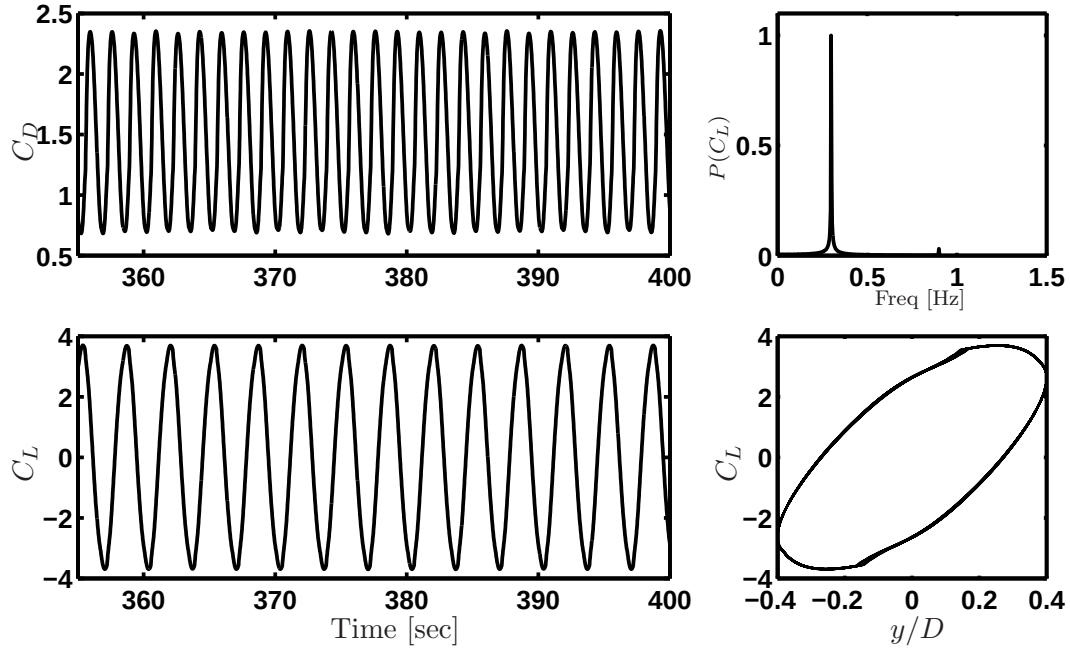

Figure C.6: $A_R = 0.40$, $f_0 = 0.2991$ Hz (i.e., $S_R = 0.20$, $F_R = 0.851$)

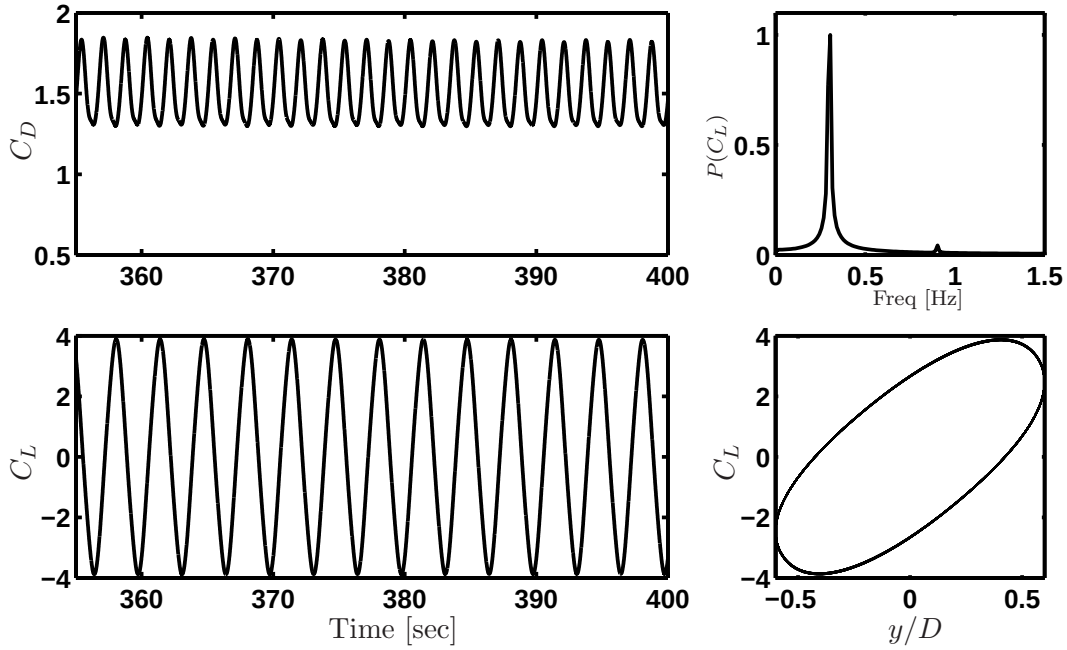

Figure C.7: $A_R = 0.60$, $f_0 = 0.2991$ Hz (i.e., $S_R = 0.20$, $F_R = 0.851$)

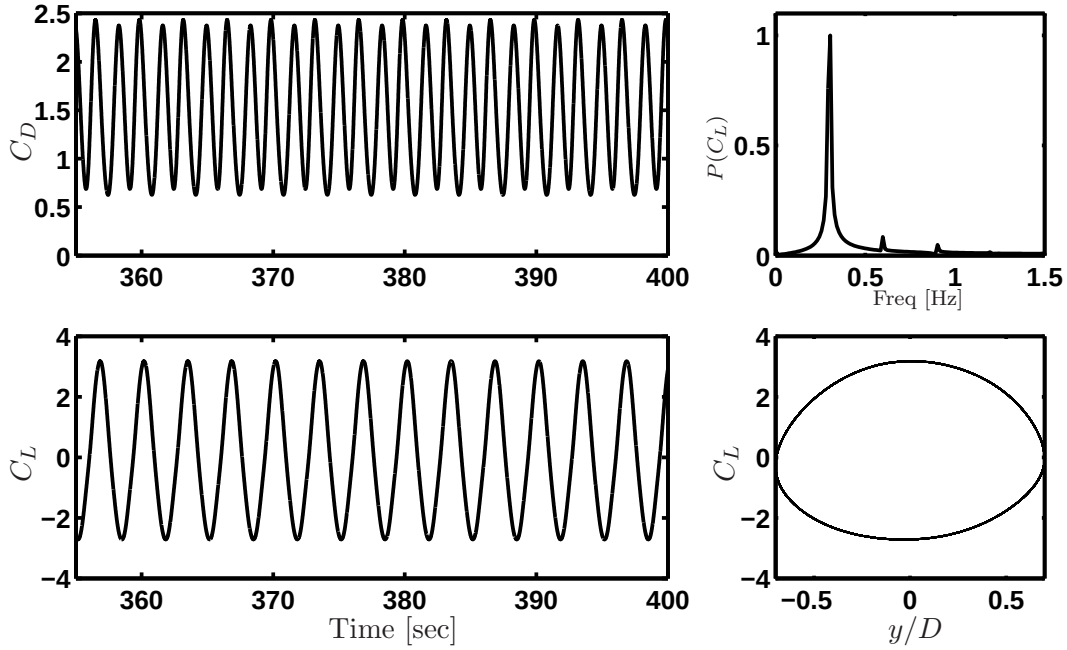

Figure C.8: $A_R = 0.70$, $f_0 = 0.2991$ Hz (i.e., $S_R = 0.20$, $F_R = 0.851$)

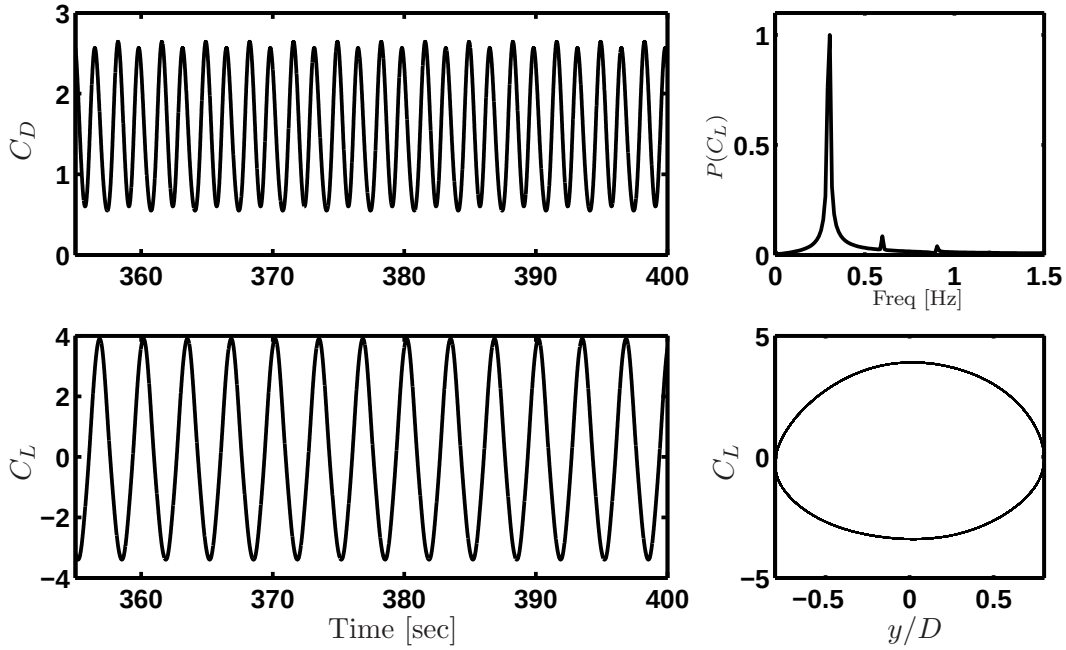

Figure C.9: $A_R = 0.80$, $f_0 = 0.2991$ Hz (i.e., $S_R = 0.20$, $F_R = 0.851$)

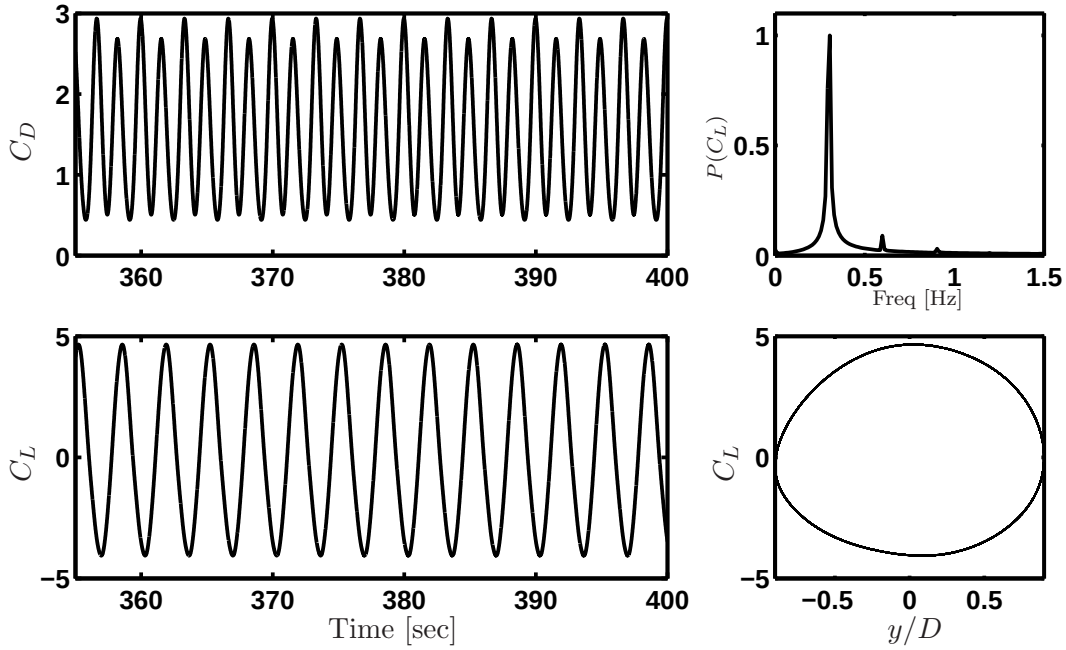

Figure C.10: $A_R = 0.90$, $f_0 = 0.3142$ Hz (i.e., $S_R = 0.21$, $F_R = 0.894$)

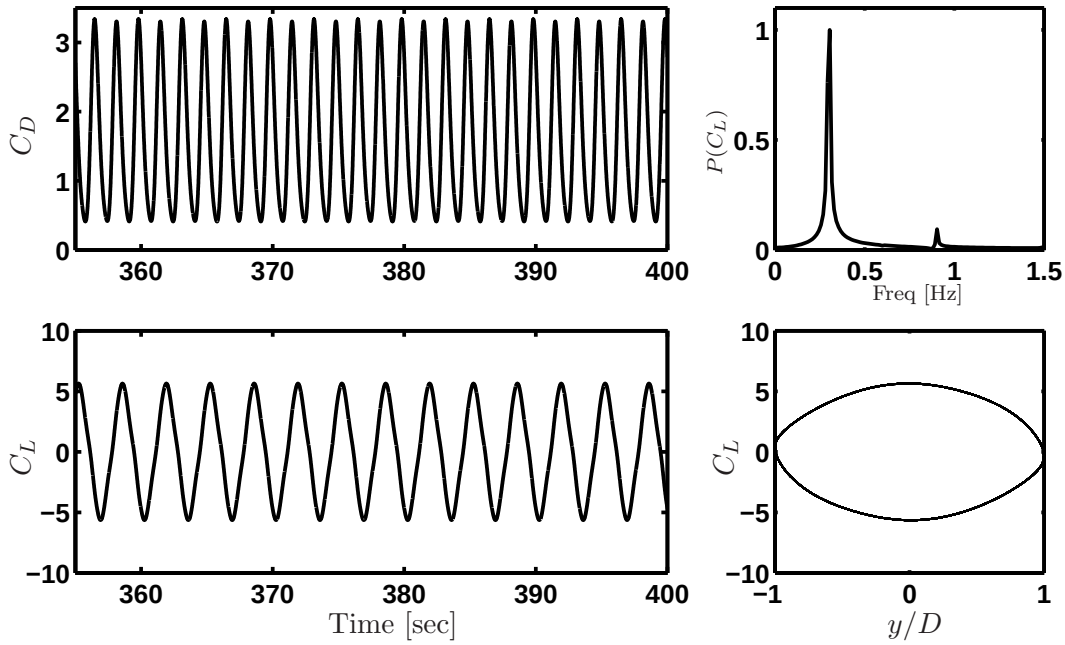

Figure C.11: $A_R = 1.00$, $f_0 = 0.2991$ Hz (i.e., $S_R = 0.20$, $F_R = 0.851$)

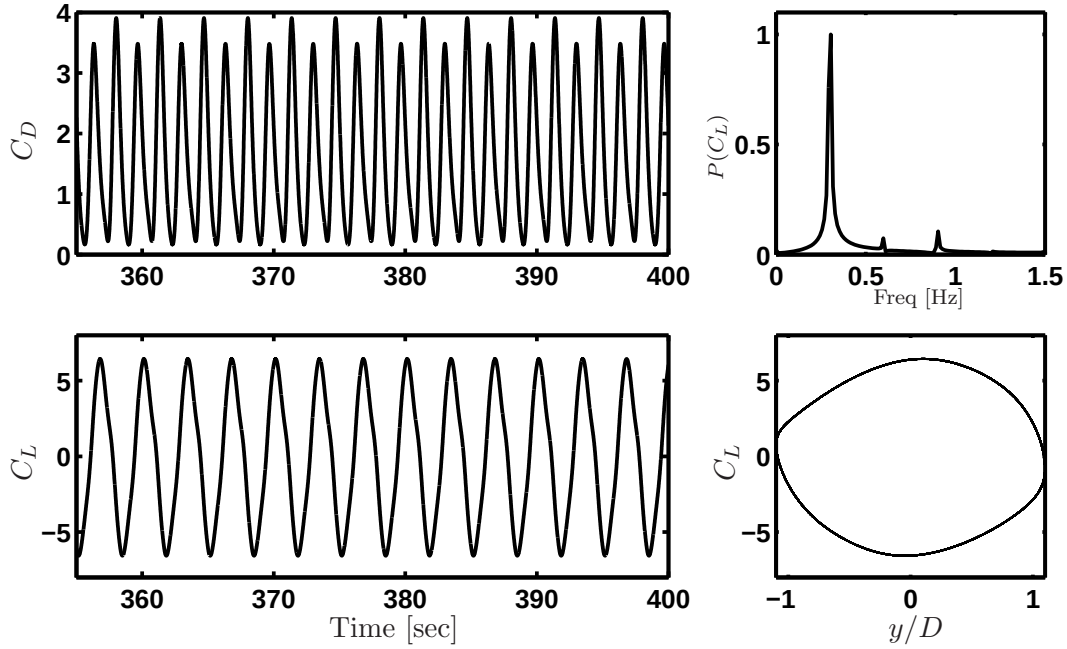

Figure C.12: $A_R = 1.10$, $f_0 = 0.2991$ Hz (i.e., $S_R = 0.235$, $F_R = 1.00$)

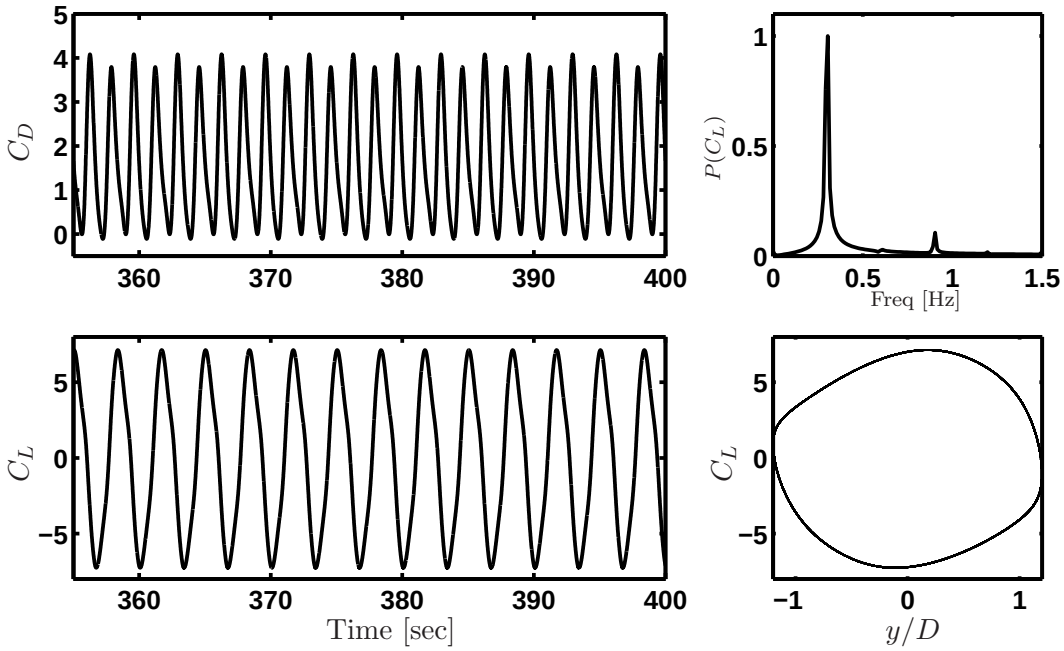

Figure C.13: $A_R = 1.20$, $f_0 = 0.2991$ Hz (i.e., $S_R = 0.235$, $F_R = 1.00$)

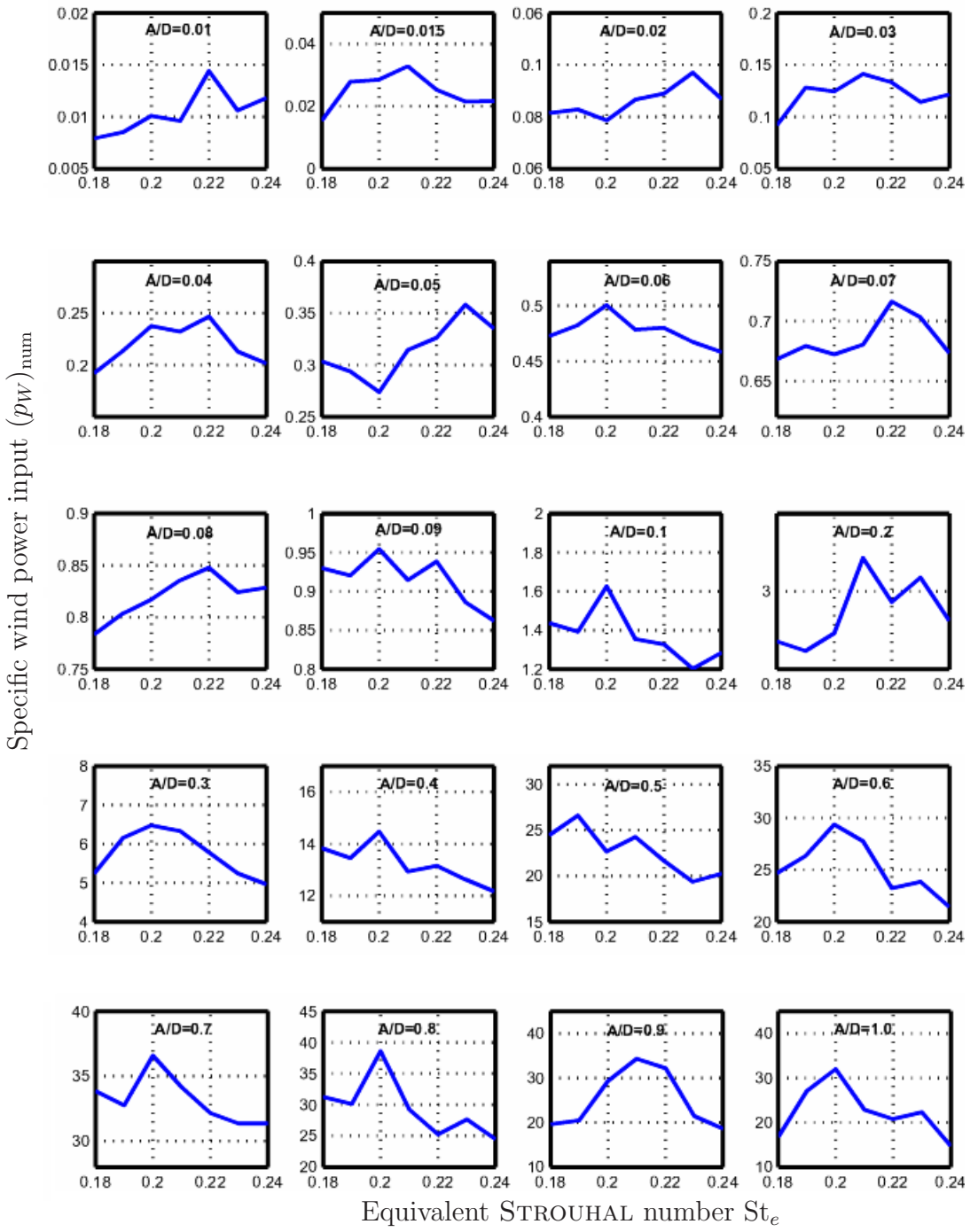

Figure C.14: Specific wind power input on a single oscillating cylinder as a function of oscillation frequencies

C.2 Two stationary cylinders in a tandem

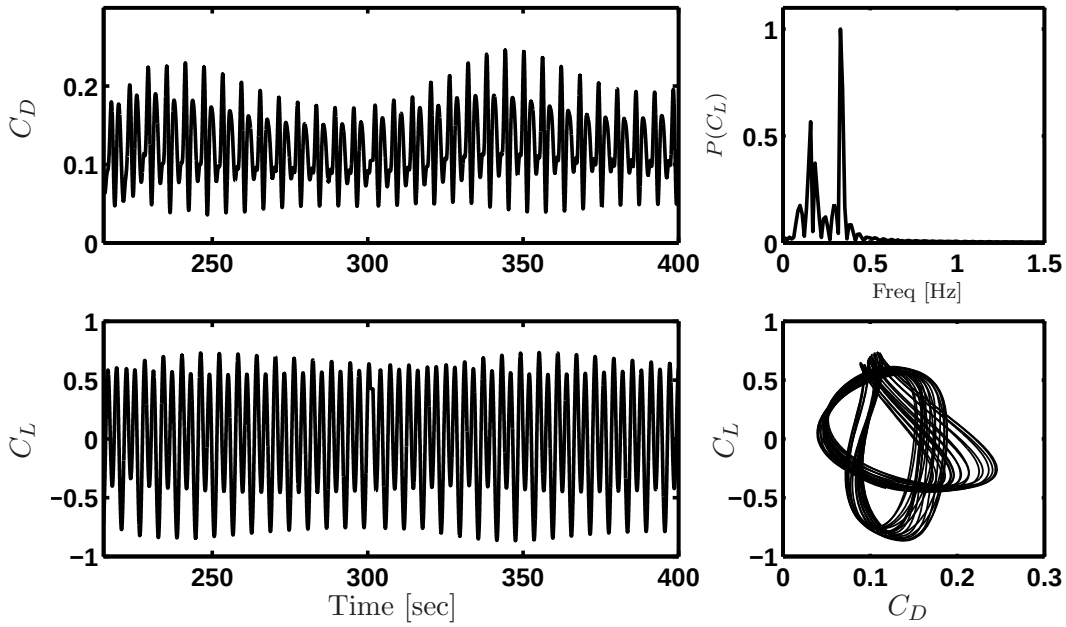

Figure C.15: $X/D = 20$, $Y/D = 0.00$

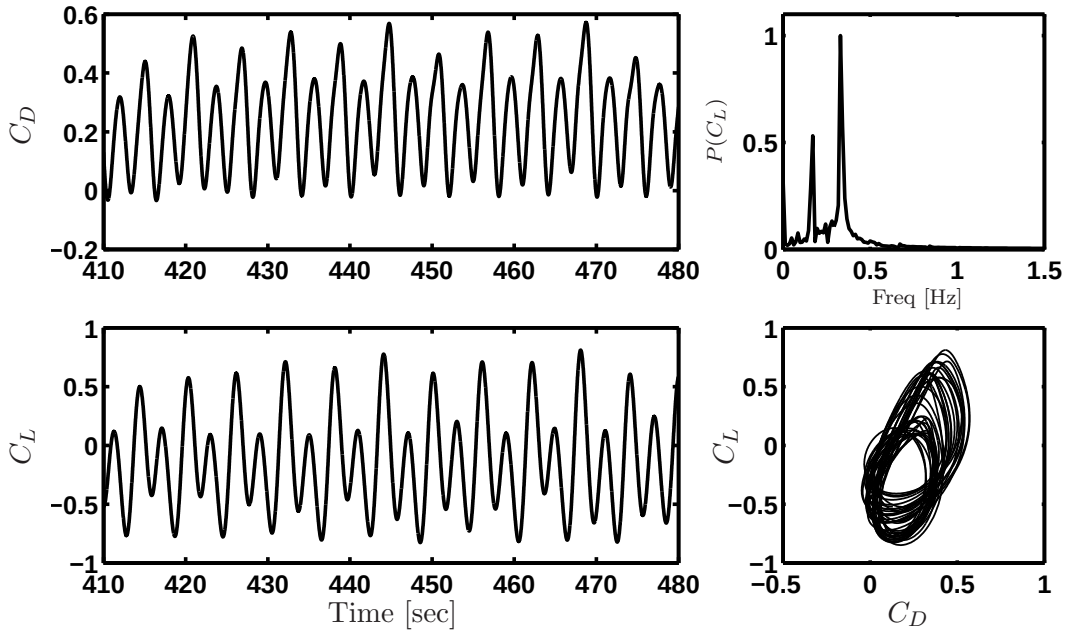

Figure C.16: $X/D = 20$, $Y/D = 0.50$

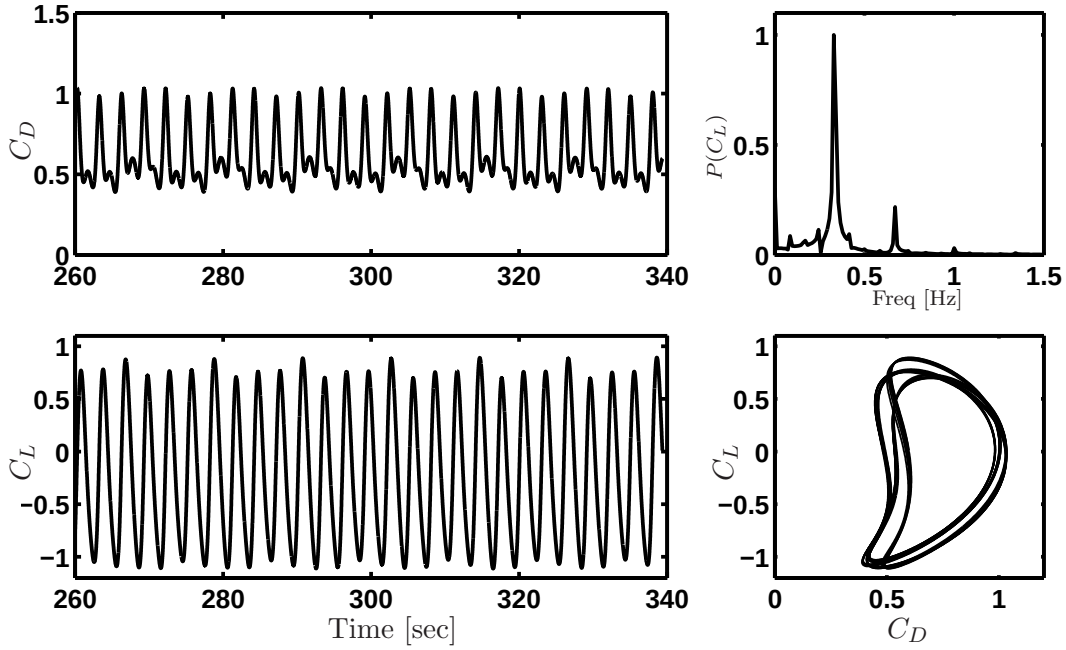

Figure C.17: $X/D = 20$, $Y/D = 1.00$

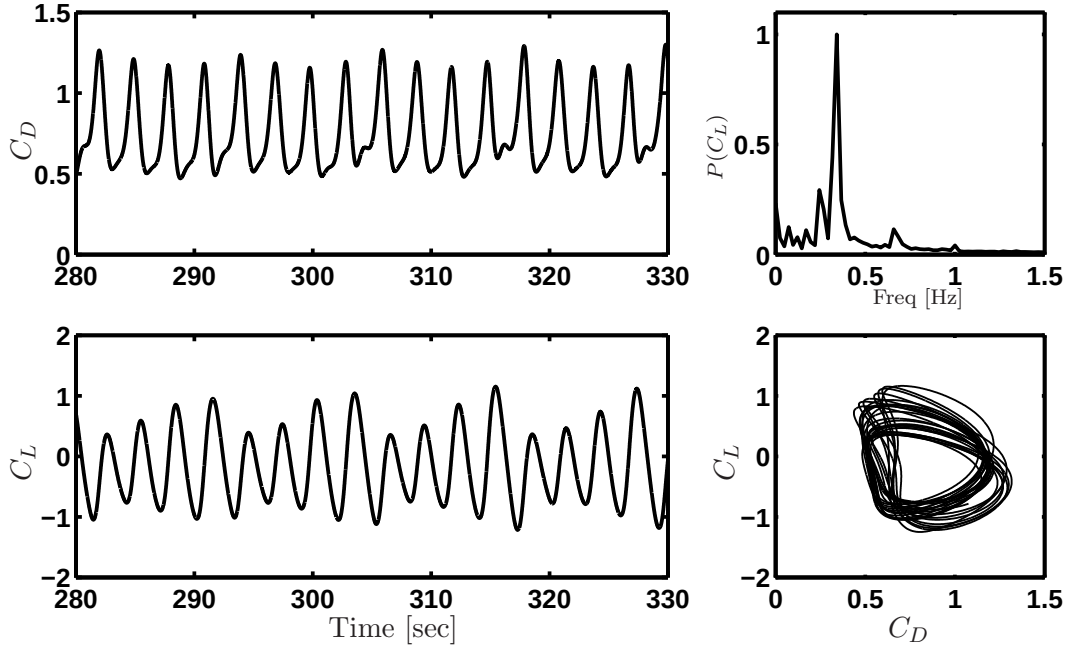

Figure C.18: $X/D = 20$, $Y/D = 1.50$

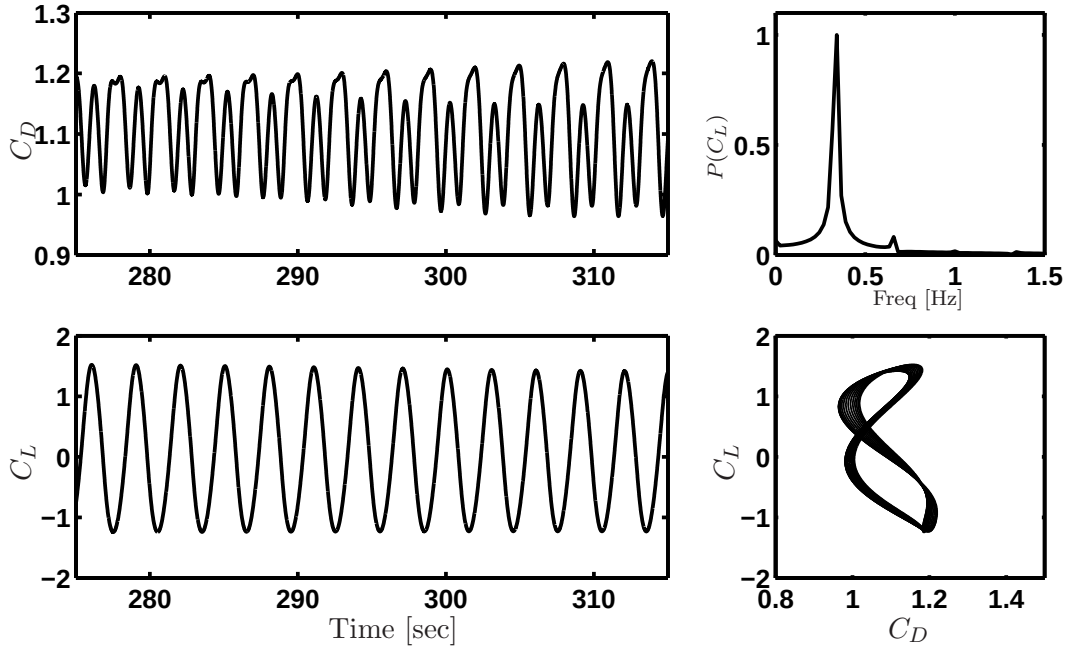

Figure C.19: $X/D = 20$, $Y/D = 2.50$

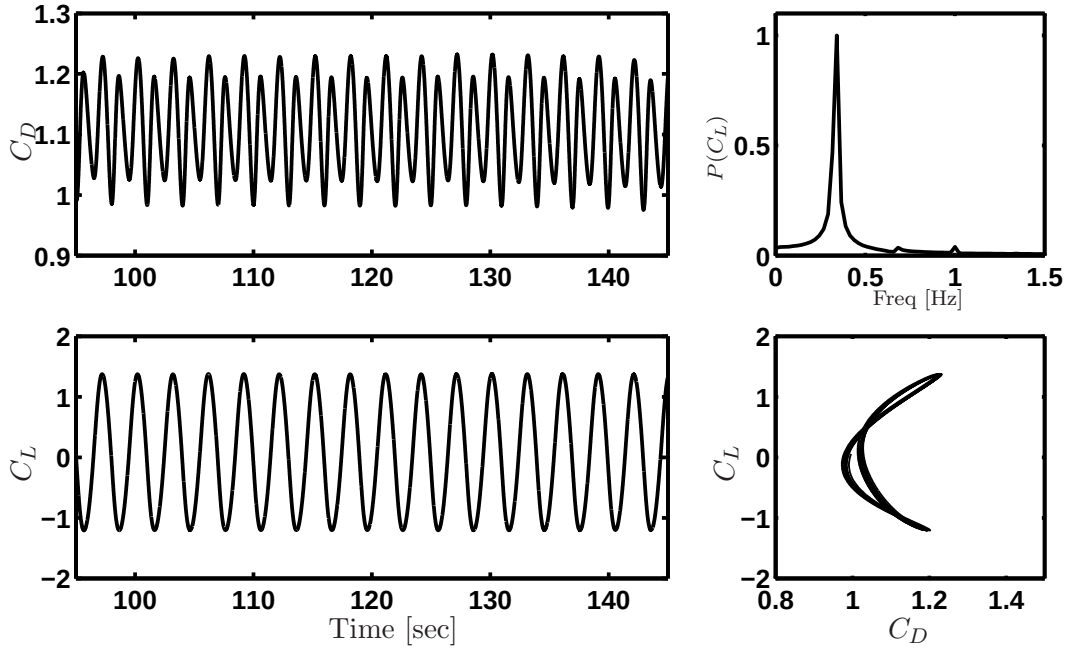

Figure C.20: $X/D = 20$, $Y/D = 3.00$

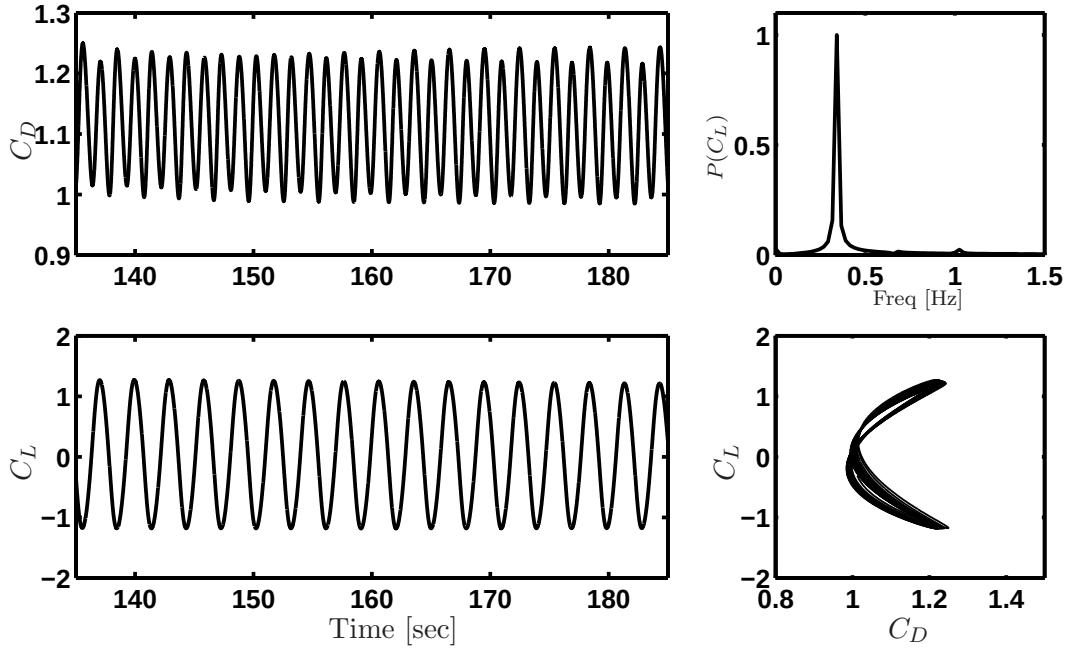

Figure C.21: $X/D = 20$, $Y/D = 3.50$

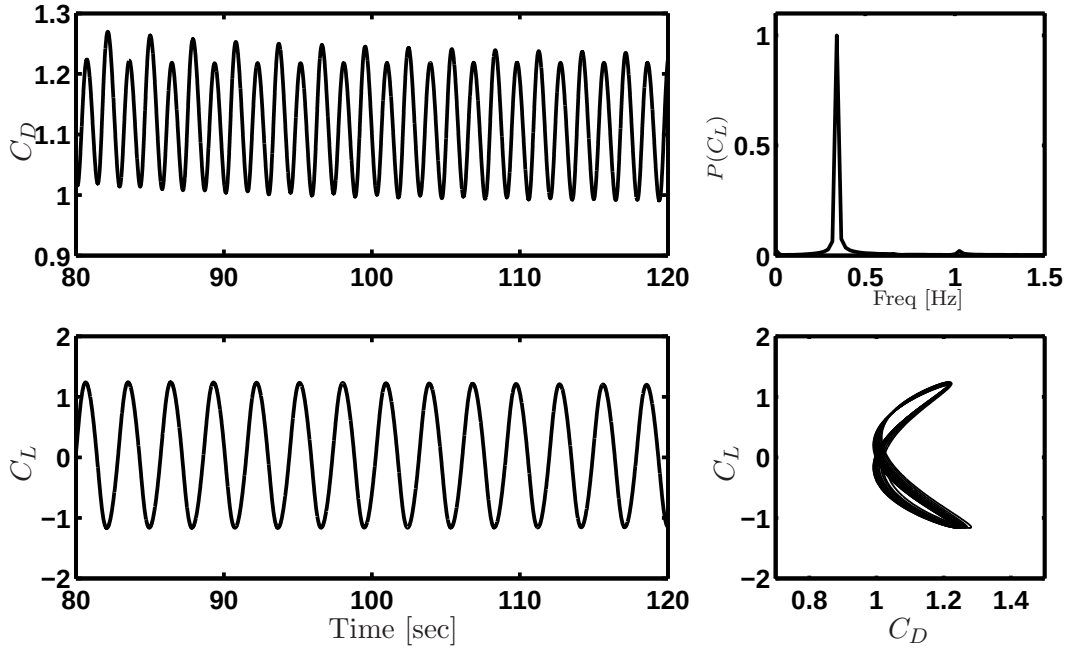

Figure C.22: $X/D = 20$, $Y/D = 4.00$

Bibliography

[1] P. Hagedorn. Ein einfaches Rechenmodell zur Berechnung winderregter Schwingungen an Hochspannungsleitungen mit Dämpfern. *Ingenieur-Archiv*, 49:161–177, 1980.

[2] P. Hagedorn. On the computation of damped wind excited vibrations of overhead transmission lines. *Journal of Sound and Vibration*, 83(2):253–271, 1982.

[3] J. Vecchiarelli, I.G. Currie, and D.G. Harvard. Simulation of aeolian vibration of a conductor span with a STOCKBRIDGE damper. In *Third International Symposium on Cable Dynamics, Trondheim, Norway*, 1999.

[4] H. Verma, G. Chakraborty, H. Krispin, and P. Hagedorn. On the modeling of wind induced vibrations of long span electrical transmission lines. In *Proceedings of Fifth International Symposium on Cable Dynamics, Santa Margherita, Italy*, pages 53–60, September 2003.

[5] H. Verma and P. Hagedorn. Wind induced vibrations of long electrical overhead transmission line spans: A modified approach. *Wind and Structures*, 8(2):89–106, March 2005.

[6] T. Staubli. An investigation of the fluctuating forces on a transverse-oscillating circular cylinder. In *EUROMECH-Colloquium 119, London*, 1979.

[7] R.E.D. Bishop and A.Y. Hassan. The lift and drag forces on a circular cylinder in a flowing fluid. In *Proceedings of the Royal Society of London 277 (Series A)*, pages 51–75, 1964.

[8] D. Brika and A. Laneville. A laboratory investigation of the aeolian power imparted to a conductor using a flexible circular cylinder. In *Proceedings of the Royal Society of London 277(Series A)*, pages 23–27, July 1995.

[9] S.S. Chen. *Flow-Induced Vibration of Circular Cylindrical Structures*. Washington, New York, London : Hemisphere Publishing Corporation, 1987.

[10] G. Diana and M. Falco. On the forces transmitted to a vibrating cylinder by a blowing fluid. *Mechanica*, 6:9–22, 1971.

[11] C.B. Rawlins. Model of power imparted to a vibrating conductor by turbulent wind. Technical report, Alcoa Conductor Products Company, Technical Note No. 31, 1983.

[12] C.B. Rawlins. Model of power imparted to a vibrating conductor by turbulent wind. *Alcoa Conductor Products Company, Technical Note No. 31*, 1998.

[13] *Transmission Line Reference Book 345 KV and Above.* Palo Alto, California: Electrical Power Research Institute, 1987.

[14] *Transmission Line Reference Book, Wind Induced Conductor Motion.* Palo Alto, California: Electrical Power Research Institute, 1979.

[15] R.D. Blevins. *Flow-Induced Vibrations.* Second ed., Van Nostrand Reinhold, New York, 1990.

[16] A.T. Edwards and J.M. Boyd. Bundle-conductor-spacer design requirements and development of "spacer-vibration damper". *IEEE Transactions on Power Apparatus and Systems*, PAS-84, 10:924–929, October 1965.

[17] Personal communication. (H.J. Krispin). *Ribe Electrical Fittings GmbH, Schwabach, Germany*, 2000-2006.

[18] A. Bürklin, F. Busemann, W.v. Mangoldt, G. Markt, and F. Kromer. Bündelleitungen. Technical report, Berlin/Germany: Siemens-Schuckert-Werke, SGO-Nr. 4520/1.1 143, 1942.

[19] L. Möcks. Bilung von Schwingungsinseln in Bündelleitern. *Elektrizitätswirschaft*, 69:709–710, 1970.

[20] R. Claren, G. Diana, and P. Nicolini. Vibrations in multi conductor bundles. In *CIGRE*, volume 22-08, 1974.

[21] K. Anderson and P. Hagedorn. On the energy dissipation in spacer-dampers in bundled conductors of overhead transmission lines. *Journal of Sound and Vibration*, 180(4):539–556, 1995.

[22] R.G. Sturm. Vibrations of cables and dampers part-1. *Electrical Engineering*, May 1936.

[23] R.A. Monroe and R.L. Templin. Vibration of overhead transmission lines. *AIEE Transactions*, 51:1052–1058, December 1932.

[24] J.G. Allnut and M.D. Rowbottom. Damping of aeoline vibration on overhead lines by vibration dampers. *Proceeding of Institute of Electrical and Electronic Engineers*, 121:1175–1178, 1974.

[25] M.S. Dhotarad, N. Ganesan, and B.V.A. Rao. Transmission line vibration. *Journal of Sound and Vibration*, 60(2):217–327, 1978.

[26] A. Simpson. Determination of the natural frequencies of multiconductor overhead transmission lines. *Journal of Sound and Vibration*, 20(4):417–449, 1972.

[27] M. Ervik. Estimating aeolian vibration level based on energy balance principle. Technical report, CIGRE SC-22, WG-1, 1975.

[28] F.B. Farquharson and R.E. McHugh. Wind tunnel investigation of conductor vibration using rigid models. *AIEE Bimonthly Publication: Power Apparatus and Systems*, 75, Pt. III:871–877, October 1956.

[29] R. Claren and G. Diana. Vibrazioni dei conduttori. *L'Energia Elettrica*, 10, 1966.

[30] R. Hartlen and I. Currie. Lift oscillator model for vortex-induced vibrations. In *Americal Society of Civil Engineers*, volume 96, pages 577–591, 1970.

[31] W.D. Iwan. The vortex induced oscillations of elastic structural elements. *Journal of Engineering for Industry*, 97:1378–1382, 1975.

[32] R.A. Skop and O.M. Griffin. On a theory for the vortex excited oscillations of flexible cylindrical structures. *Journal of Sound and Vibration*, 41:263–274, 1975.

[33] M.S. Dhotarad, N. Ganesan, and B.V.A. Rao. Transmission line vibration with 4r dampers. *Journal of Sound and Vibration*, 60(4):604–608, 1978.

[34] R. Claren, G. Diana, , F. Giordana, and E. Massa. The vibrations of transmission line conductor bundles. In *IEEE Winter Power Meeting, Ney York, N.Y., Paper-71TP 158-PWR*, pages 1796–1814, January-February 1971.

[35] L. Möcks and J. Schmidt. Bemessung und Anordnung von selbstdämpfenden Feldabstandhaltern in Bündelleitern. *Elektrizitätswirschaft*, 87, H.21:1044–1048, 1988.

[36] P. Hagedorn. The control of vibrations in bundled conductors via self-damping spacers. In *Proceedings of the 1st International Conf. on Motion and Vibration Control, Yokohama*, pages 846–851, September 1992.

[37] P. Hagedorn and T. Hadulla. On the mathematical modelling of vortex excited vibrations in bundled conductors. In *Proceedings of the 7th. International Conference on Fluid Induced Vibration - FIV 2000, Lucerne, Switzerland*, pages 19–22, June 2000.

[38] P. Hagedorn, N. Mitra, and T. Hadulla. Vortex-excited vibrations in bundled conductors: A mathematical model. *Journal of Fluids and Structures*, 16(7):843–854, 2002.

[39] H. Verma, A. M. Dighe, and P. Hagedorn. On the solution of transcendental eigenvalue problem in transmission line bundled conductors. *Proceedings of International Mechanical Engineering Congress, ASME, Anaheim, CA*, 2004.

[40] D. Hearnshaw. Spacer damper performance, a function of in-span positioning. In *IEEE*, paper-T 74 061-8, 1974.

[41] S. Houle, C. Hardy, A. Lapointe, and M. St-Louis. Experimental assessment of spacer-damper system performance with regard to control of wind-induced vibrations of high-voltage transmission lines. In *IEEE/CSEE Joint Conference on High Voltage Syst., Beijing, China*, 87JC-39, 1987.

[42] P. Bourdon, J. Brunelle, and P. Lavigne. Methods of evaluating dynamic characteristics of dampers, spacers and spacer dampers. In *CAE Research Report*, contract no. 145 T 327, 1987.

[43] P. Hagedorn and M. Kraus. On the performance of spacer dampers in bundled conductors. In *European Transactions on Electrical Power Engineering*, volume 3(4), pages 305–311, July-August 1993.

[44] T. Hadulla. *Wirbelerregte Schwingungen in Freileitungsbündeln.* PhD thesis, Institut für Mechanik, Technische Universität Darmstadt, Germany, 2000.

[45] D. Brika and A. Laneville. A laboratory investigation of the aeolian power imparted to a conductor using a flexible circular cylinder. *IEEE Transections on Power Delivery*, 11(2):1145–1152, 1996.

[46] A. Khalak and C.H.K. Williamson. Fluid forcesand dynamics of a hydroelastic structure with very low mass and damping. *Journal of Fluids and Structures*, 11:973–982, 1997.

[47] K. Nakagawa, K. Kishida, and K. Igarashi. Vortex-induced oscillation and lift of yawed circular cylinders in cross-flow. *Journal of Fluids and Structures*, 12:759–777, 1998.

[48] A. Khalak and C.H.K. Williamson. Motions, forces and mode transitions in vortex-induced vibrations at low mass-damping. *Journal of Fluids and Structures*, 13:813–851, 1999.

[49] M. Belloli, A. Cigada, G. Diana, and D. Rocchi. Wind tunnel investigation on vortex induced vibration of a long flexible cylinder. In *Proceedings of Fifth International Symposium on Cable Dynamics, Santa Margherita, Italy*, pages 247–254, September 2003.

[50] A. Khalak and C.H.K. Williamson. Dynamics of a hydroelastic cylinder with very low mass and damping. *Journal of Fluids and Structures*, 10:455–472, 1996.

[51] D. Brika and A. Laneville. Vortex-induced vibrations of a long flexible circular cylinder. In *Journal of Fluid Mechanics*, volume 250, pages 481–508, 1993.

[52] D. Brika and A. Laneville. The power imparted by wind to a flexible circular cylinder in the wake of another stationary cylinder. *IEEE Transections on Power Delivery*, 12(1):398–405, 1997.

[53] A. Laneville and D. Brika. The fluid and mechanical coupling between two circular cylinders in tandem arrangement. *Journal of Fluids and Structures*, 13(7/8):967–986, 1999.

[54] D. Brika and A. Laneville. The flow interaction between a stationary cylinder and a downstream flexible cylinder. *Journal of Fluids and Structures*, 13:579–606, 1999.

[55] R. Claren, G. Diana, and P. Nicolini. Vibration in multiple conductor bundles. In *Proceedings of International Conference on Large High Voltage Systems (CIGRÉ), Paper No. 22-08*, pages 1–24, 1974.

[56] M. Gaydon and D. Rockwell. Vortices incident upon an oscillating cylinder: Flow structure and loading. *Journal of Fluids and Structures*, 13:709–722, 1999.

[57] J.-C. Lin, Y. Yang, and D. Rockwell. Flow past two cylinders in tandem: Instantaneous and averaged flow structure. *Journal of Fluids and Structures*, 16(8):1059–1071, 2002.

[58] D.J. Newman and G.E. Karniadakis. Simulations of flow past a freely vibrating cable. *Journal of Fluid Mechanics*, 344:95–136, 1997.

[59] H.M. Blackburn and W.H. Melbourne. Sectional lift forces for an oscillating circular cylinder in smooth and turbulent flows. *Journal of Fluids and Structures*, 11:413–431, 1997.

[60] H. M. Blackburn and R. D. Henderson. A study of two-dimensional flow past an oscillating cylinder. *Journal of Fluid Mechanics*, 385:255–286, 1999.

[61] C. Evangelinos, D. Lucor, and G.E. Karniadakis. DNS-derived force distribution on flexible cylinders subject to vortex-indeced vibration. *Journal of Fluids and Structures*, 14:429–440, 2000.

[62] D. Shiels, A. Leonard, and A. Roshko. Flow-induced vibration of a circular cylinder at limiting structural parameters. *Journal of Fluids and Structures*, 15:3–21, 2001.

[63] A.L. Braun and A.M. Awruch. Aerodynamic and aeroelastic analysis of bundled cables by numerical simulation. *Journal of Sound and Vibration*, 284(1–2):51–73, 2005.

[64] N. Mitra. On the control of vortex excited vibrations of conductors of overhead transmission lines. Master's thesis, Indian Institute of Technology, Kharagpur: Department of Ocean Engineering and Naval Architecture, 2001.

[65] S.S. Ranmale. Solution of transcendental eigenvalue problem in overhead conductors. Master's thesis, Department of Civil Engineering, Indian Institute of Technology Bombay, Mumbai, India, 1996.

[66] M.M. Zdravkovich. *Flow Around Circular Cylinders, Volume-1.* Oxford University Press, 1997.

[67] D. Sauter and P. Hagedorn. On the hysteresis of wire cables in STOCKBRIDGE dampers. *International Journal of Nonlinear Mechanics*, 37(8):1453–1459, 2002.

[68] J.H. Wilkinson. *The Algebraic Eigenvalue Problem.* Oxford University Press, London, 1965.

[69] D.A. Gignac. Solution of a complex quadratic eigenvalue problem. *International Journal for Numerical Methods in Engineering*, 11:99–106, 1977.

[70] H.A. Smith, R.K. Singh, and D.C. Sorensen. Formulation and the solution of the nonlinear damped eigenvalue problem for skeletal systems. *International Journal for Numerical Methods in Engineering*, 38:3071–3085, 1995.

[71] J. Ye and F.W. Williams. Bounding properties for eigenvalues of a transcendental dynamic stiffness matrix by using a quadratic matrix pencil. *Journal of Sound and Vibration*, 185(1):173–183, 1995.

[72] I. Gohberg, P. Lancaster, and L. Rodman. *Matrix Polynomials*. Academic Press, New York, 1982.

[73] D.C Sorensen. Implicitly restarded arnoldi/lanczos methods for large scale eigenvalue calculations. *Technical Report*, Department of Computational and Applied Mathematics, Rice University, Houston, Texas, 1995.

[74] D.C Sorensen. Implicit application of polynomial filters in a k-step Arnoldi method. *SIAM J. Matrix Anal. Appl.*, 13(1):357–385, 1992.

[75] R.B. Lehoucq and D.C Sorensen. Deflation techniques for an implicitly restarted Arnoldi iteration. *SIAM J. Matrix Anal. Appl.*, 17(4):789–821, 1996.

[76] R.B. Lehoucq, D.C Sorensen, and C. Yang. Solution of large-scale eigenvalue problems with implicitly restarted Arnoldi methods. *ARPACK User's Guide*, SIAM, 1998.

[77] J. W. Demmel. *Applied Numerical Linear Algebra*. SIAM, Philadelphia, 1997.

[78] R.J. Radke. *A Matlab Implimentation of the Implicitly Restarted Arnoldi Method for Solving Large-Scale Eigenvalue Problems*. PhD thesis, Department of Computational and Applied Mathematics, Rice University, Houston, Texas, 1996.

[79] D.R. Fokkema, G.L.G. Sleijpen, and H.A. Van der Vorst. Jacobi-Davidson style QR and QZ algorithms for the reduction of matrix pencils. *SIAM J. Sci. Comput.*, 20(1):94–125, 1998.

[80] G.L.G. Sleijpen, H.A. Van der Vorst, and Ellen Meijerink. Efficient expansion of subspaces in the Jacobi-Davidson method for standard and generalized eigenproblems. *Electronic Transactions on Numerical Analysis*, 7:75–89, 1998.

[81] G.H. Golub and C.F. Van Loan. *Matrix Computations*. The Johns Hopkins University Press, London, 1989.

[82] J.H. Wilkinson. Convergence of the LR, QR and related algorithms. *Comput. J.*, 8:77–84, 1965.

[83] V.N. Kublanovskaja. On an application of newton's method to the determination of eigenvalues of λ-matrices. *Dokl. Akad. Nauk SSSR*, 188:1004–1005, 1969.

[84] V.N. Kublanovskaja. On an approach to the solution of the generalized latent value problem for λ-matrices. *SIAM J. Numer. Anal.*, 7:532–537, 1970.

[85] A. Ruhe. Algorithms for the nonlinear eigenvalue problem. *SIAM J. Numer. Anal.*, 10(4):674–689, 1973.

[86] B.N. Parlett and W. Kahan. On the convergence of a practical QR algorithm. *Proc. IFIP Congress*, pages 25–30, 1968.

[87] F.W. Williams, S. Yuan, K. Ye, D. Kennedy, and M.S. Djoudi. Towards deep and simple understanding of the transcendental eigenproblem of structural vibrations. *Journal of Sound and Vibration*, 256(4):681–693, 2002.

[88] C.B. Moler and G.W. Stewart. An algorithm for generalized matrix eigenvalue problems. *SIAM J. Number. Anal.*, 10(2), 1973.

[89] H. Verma and P. Hagedorn. Wind induced vibrations of long electrical overhead transmission line spans: A modified approach. *Wind and Structures*, 8(2):89–106, 2005.

[90] F.W. Williams and W.H. Wittrick. An automatic computational procedure for calculating natural frequencies of skeletal structures. *International Journal of Mechanical Sciences*, 12:781–791, 1970.

[91] W.H. Wittrick and F.W. Williams. A general algorithm for computing natural frequencies of elastic structures. *Quarterly Journal of Mechanics and Applied Mathematics*, 24:263–284, 1971.

[92] W.H. Wittrick and F.W. Williams. An algorithm for computing critical buckling loads of elastic structures. *Journal of Structural Mechanics*, 1:497–518, 1973.

[93] W.H. Wittrick and F.W. Williams. Buckling and vibration of anisotropic or isotropic plate assemblies under combined loadings. *International Journal of Mechanical Sciences*, 16:209–239, 1974.

[94] F.W. Williams. Natural frequencies of repetitive structures. *Quarterly Journal of Mechanics and Applied Mathematics*, 24:285–310, 1971.

[95] M.S. Djoudi, D. Kennedy, F.W. Williams, S. Yuan, and K. Ye. Exact substructuring in recursive Newton's method for solving transcendental eigenproblems. *Journal of Sound and Vibration*, 280:883–902, 2005.

[96] H. Verma, A. M. Dighe, and P. Hagedorn. On the dynamics of bundled conductors in overhead transmission lines. *Proc. Appl. Math. Mech.*, 4:115–116, 2004.

[97] W. H. Yang. A method for eigenvalues of sparse λ-matrices. *Short Communication, Int. J. Num. Meth. Eng.*, 19:943–948, 1983.

[98] K. V. Singh and Y. M. Ram. Transcendental eigenvalue problem and its applications. *AIAA Journal*, 40:1402–1407, 2002.

[99] L.B. Rall. *Computational Solution of Nonlinear Operator Equations*. Wiley, London and New York, 1969.

[100] P. Venkataraman. *Applied Optimization with MATLAB Programming*. John Wiley & Sons, Inc., 2002.

[101] E. Anderson, Z. Bai, C. Bischof, S. Blackford, J. Demmel, J. Dongarra, J. Du Croz, A. Greenbaum, S. Hammarling, A. McKenney, and D.C. Sorensen. *LAPACK User's Guide*. SIAM, Philadelphia, Third Edition, 1999.

[102] S.V. Kartyshov. Numerical method for solving the eigenvalue problem for sparse matrices depending non-linearly on a spectral parameter. *Computational Mathematics and Mathematical Physics*, 29(6):209–213, 1989.

[103] S.V. Kartyshov. Numerical method for solving an eigenvalue problem for sparse matrices with a nonlinear spectral parameter. *Zh. Vychisl. Mat. Fiz.*, 29(12):1898–1903, 1989.

[104] M.A. Aslanyan and S.V. Kartyshov. A modification of a numerical method for solving a nonlinear eigenvalue problem. *Computational Mathematics and Mathematical Physics*, 38(5):683–687, 1998.

[105] M.R. Spiegel. *Theory and Problems of Complex Variables*. Schaum's Outline Series, McGraw-Hill Book Company, New York, 1964.

[106] N. Wagner and L. Gaul. Eigenpath analysis of transcendental two-parameter eigenvalue problems. *In proceedings of European Congress on Computational Methods in Applied Sciences and Engineering*, 2004.

[107] P. Kravanja and M. Van Barel. A derivative-free algorithm for computing zeros of analytical functions. *Computing*, 63:69–91, 1999.

[108] J.S. Jo, H.J. Jung, M.G. Ko, and I.W. Lee. Eigenvalue-counting methods for non-proportionally damped systems. *International Journal of Solids and Structures*, 40(23):6457–6472, 2003.

[109] H. J. Jung, D.H. Kim, and I.W. Lee. Technique of checking missed eigenvalues for eigenproblem with damping matrix. *Int. J. Numer. Meth. Engng.*, 50:55–66, 2001.

[110] P. Lancaster. *Lambda-Matrices and Vibrating Systems*. Dover Publications, 2002.

[111] J.S. Tompkins, L.L. Merrill, and B.L. Jones. Quantitative relationships in conductor vibration damping. *AIEE Transactions on Power Apparatus & Systems*, 75, pt. 111:879–894, 1956.

[112] E.S. Doocy, A.R. Hard, R. Ikegami, and C.B. Rawlins. *Transmission Line Reference Book*. Electrical Power Research Institute, Palo Alto, California, 1979.

[113] M. Tunstall. Wind-induced vibrations of overhead transmission lines: An overview. In *Proceedings of the International Seminar on Cable Dynamics, Tokyo, Japan*, pages 13–26, 1997.

[114] E. Bahtovska. The energy balance for wind-excited vibrations. *Facta Universitatis, Series: Mechanical Engineering*, 1(7):769–773, 2000.

[115] C.B. Rawlins. The long span problem in the analysis of conductor vibration damping. *IEEE Transactions on Power Delivery*, 15-2:770–776, 2000.

[116] U. Gutzer and P. Hagedorn. On laboratory measurements of damping and bending stiffness of the conductors of overhead transmission lines. *Proceedings of the Int. Symposium on Cable Dynamics, Liège, Belgium*, pages 529–536, October 19-21, 1995.

[117] D.U. Noiseux. Similarity laws of the internal damping of stranded cables in transverse vibrations. *IEEE Transections on Power Apparatus and Delivery*, 7(3):1574–1581, 1992.

[118] *FASTEST-Parallel Multigrid Solver for Flows in Complex Geometries: Manual*. INVENT Computing GmbH, 1994.

[119] F. Durst and M. Schäfer. A parallel block-structured multigrid method for the prediction of incompressible flows. *Journal for Numerical Methods in Fluids*, 22:549û565, 1996.

[120] H. Ferziger and M. Perić. *Computational Methods for Fluid Dynamics*. Springer, Berlin, 2nd edition, 1997.

[121] S. Meynen, H. Verma, P. Hagedorn, and M. Schäfer. On the numerical simulation of vortex-induced vibrations of oscillating conductors. *Journal of Fluids and Structures*, 21:41–48, 2005.

[122] A.H. Dayoub. *Mean Flow Effects on a Circular Cylinder in a Wake*. PhD thesis, Department of Mechanical Engineering, University of Waterloo, Canada, 1974.

[123] C.A.J. Fletcher. *Computational Techniques for Fluid Dynamics, Volume-1*. Springer, Berlin, 1991.

[124] M. Schäfer. *Numerik im Maschinenbau*. Springer-Verlag, Berlin, 1999.

[125] S.V. Patankar and D.B. Spalding. A calculation procedure for heat, mass and momentum transfer in three dimensional parabolic flows. *Int. J. Heat Mass Transfer*, 15:1787–1806, 1972.

[126] I. Demirdžić and M. Perić. Space conservation law in finite volume calculations of fluid flow. 8:1037–1050, 1988.

[127] P.D. Thomas and C.K. Lombard. Geometric conservation law and its application to flow computations on moving grids. *AIAA Journal*, 17:1030–1037, 1979.

[128] V. Strouhal. Über eine besondere Art der Tonerregung. *Ann. d. Phys. u. Chem. N. F. (Leipzig)*, 5(10):216–251, 1878.

[129] T. Sarpkaya. Vortex-induced oscilaltions. *Journal of Applied Mechanics*, 46:241–258, 1979.

[130] C.B. Rawlins. Recent developments in conductor vibration research. Technical report, Alcoa Research Laboratories, Technical Paper No. 13, 1958.

[131] O. Yaman. Numerical simulation of vortex-induced vibrations. Master's thesis, Fachgebiet Numerische Berechnungsverfahren im Maschinenbau, Technische Universität Darmstadt, Germany, 2003.

[132] http://www.tu-darmstadt.de/hrz/hhlr/.

[133] P. Anagnostopoulos. Numerical study of the flow past a cylinder excited transversely to the incident stream. part 1: Lock-in zone, hydrodynamic forces and wake geometry. *Journal of Fluids and Structures*, 14:819–851, 2000.

[134] C.H.K. Williamson and R. Govardhan. Vortex-induced vibrations. *Annual Review of Fluid Mechanics*, 413-455:413–455, 2004.

[135] R.D. Henderson. Nonlinear dynamics and pattern formation in turbulent wake transition. *Journal of Fluid Mechanics*, 352:65–112, 1997.

[136] H.M. Blackburn and R.D. Henderson. A study of two-dimensional flow past an oscillating cylinder. *Journal of Fluid Mechanics*, 385:255–286, 1999.

[137] H. Verma, P. Hagedorn, and T. David. Computing the power imparted by the fluid on an oscillating cylinder in cross-flow: Some results and many questions. In *Presented in Fourth Conference on Bluff Body Wakes and Vortex-Induced Vibrations, Santorini, Greece*, June 21-24 2005.

[138] G.H. Koopmann. The vortex wakes of vibrating cylinders at low reynolds numbers. *Journal of Fluid Mechanics*, 27:501–512, 1967.

[139] J.R. Meneghini and P.W. Bearman. Numerical simulation of high amplitude osillatory flow about a circular cylinder. *Journal of Fluids and Structures*, 9:435–455, 1995.

[140] A.L. Braun and A.M. Awruch. Aerodynamic and aeroelastic analysis of bundled cables by numerical simulation. *Journal of Sound and Vibration*, 284(1-2):51–73, 2005.

[141] R.L. Wardlaw and K.R. Cooper. Mechanism and alleviation of wind-induced structural vibrations. In *Proceedings of Second Symposium on Applications of Solid Mechanics, McMaster University, Hamilton, Canada*, page 369û399, 1974.

[142] C.J. Pon, D.G. Havard, J.G. Currie, and R. MacDonald. Aeolian vibration excitation of bundled conductors. *Canadian Electrical Association*, I and II, 1989.

[143] P. Hagedorn and S. Otterbein. *Technische Schwingngungslehre*. Springer Verlag, Heidelberg, 1987.

[144] P. Hagedorn and A. DasGupta. *Vibrations and Waves in Continuous Mechanical Systems*. Wiley, 2007.

[145] C.E. Crede. Determining moment of inertia. *Machine Design*, page 138, August 1948.

Lebenslauf

Himanshu Verma

Geburtsdatum:	24.06.1979
Geburtsort:	Ambah, Indien
Staatsangehörigkeit:	Inder

Schulische Bildung:

1983-1991	Grundschule in Ambah, Indien
1991-1993	Higher school in Ambah, Indien
1994-1995	Higher secondary school in Ambah, Indien

Studium:

1996-2000	Bachelor of Engineering / Civil Engg., SGSITS Indore, Indien
2000-2002	Master of Technology / Structural Engg., IIT Bombay, Indien
2001-2002	Studium an der TU Darmstadt, Deutschland als DAAD Stipendiat

Berufliche Tätigkeit:

seit 09/2006	Statiker-A380, Airbus Deutschland GmbH, Hamburg, Deutschland

Eidesstattliche Erklärung

Hiermit erkläre ich, Himanshu Verma, an Eides statt, daß ich die vorliegende Dissertation selbständig angefertigt und keine anderen als die angegebenen Quellen und Hilfsmittel verwendet habe.

Hamburg, 15. November 2008 Himanshu Verma